

International Journal of Antennas and Propagation

Advanced Modeling and Simulation Methods for Multiphysics and Multiscale Problems

Lead Guest Editor: Su Yan

Guest Editors: Yumao Wu, Huapeng Zhao, and Han Guo





Advanced Modeling and Simulation Methods for Multiphysics and Multiscale Problems

International Journal of Antennas and Propagation

**Advanced Modeling and Simulation Methods for
Multiphysics and Multiscale Problems**

Lead Guest Editor: Su Yan

Guest Editors: Yumao Wu, Huapeng Zhao, and Han Guo



Copyright © 2017 Hindawi. All rights reserved.

This is a special issue published in “International Journal of Antennas and Propagation.” All articles are open access articles distributed under the Creative Commons Attribution License, which permits unrestricted use, distribution, and reproduction in any medium, provided the original work is properly cited.

Editorial Board

Ana Alejos, Spain
Mohammad Ali, USA
Jaume Anguera, Spain
Rodolfo Araneo, Italy
Alexei Ashikhmin, USA
Herve Aubert, France
Paolo Baccarelli, Italy
Xiulong Bao, Ireland
Toni Björninen, Finland
Stefania Bonafoni, Italy
Paolo Burghignoli, Italy
Shah Nawaz Burokur, France
Giuseppe Castaldi, Italy
Luca Catarinucci, Italy
Felipe Catedra, Spain
Marta Cavagnaro, Italy
Shih Yuan Chen, Taiwan
Yu Jian Cheng, China
Renato Cicchetti, Italy
Riccardo Colella, Italy
Laura Corchia, Italy
Lorenzo Crocco, Italy
Claudio Curcio, Italy
Francesco D'Agostino, Italy
María Elena de Cos Gómez, Spain
Tayeb A. Denidni, Canada

Giuseppe Di Massa, Italy
Michele D'Urso, Italy
Francisco Falcone, Spain
Miguel Ferrando Bataller, Spain
Flaminio Ferrara, Italy
Vincenzo Galdi, Italy
Claudio Gennarelli, Italy
Farid Ghanem, Algeria
Sotirios K. Goudos, Greece
Rocco Guerriero, Italy
Kerim Guney, Turkey
Song Guo, Japan
Tamer S. Ibrahim, USA
M. R. Kamarudin, UK
Slawomir Koziel, Iceland
Luis Landesa, Spain
Ding-Bing Lin, Taiwan
Angelo Liseno, Italy
Pierfrancesco Lombardo, Italy
Lorenzo Luini, Italy
Atsushi Mase, Japan
Diego Masotti, Italy
Ch. F. Mecklenbräuker, Austria
A. T. Mobashsher, Australia
Ananda S. Mohan, Australia
J.-M. Molina-Garcia-Pardo, Spain

Giuseppina Monti, Italy
Giorgio Montisci, Italy
N. Nasimuddin, Singapore
Mourad Nedil, Canada
Symeon Nikolaou, Cyprus
Giacomo Oliveri, Italy
Ikmo Park, Republic of Korea
Josep Parrón, Spain
Matteo Pastorino, Italy
Xianming Qing, Singapore
Ahmad Safaai-Jazi, USA
Safieddin Safavi-Naeini, Canada
Magdalena Salazar-Palma, Spain
Stefano Selleri, Italy
Raffaele Solimene, Italy
Gino Sorbello, Italy
Seong-Youp Suh, USA
Sheng Sun, Hong Kong
Larbi Talbi, Canada
Luciano Tarricone, Italy
Parveen Wahid, USA
Chien-Jen Wang, Taiwan
Wen-Qin Wang, China
Mustapha C E Yagoub, Canada
Shiwen Yang, China
Yuan Yao, China

Contents

Advanced Modeling and Simulation Methods for Multiphysics and Multiscale Problems

Su Yan, Yumao Wu, Huapeng Zhao, and Han Guo
Volume 2017, Article ID 3051476, 2 pages

Multiband Radar Signal Coherent Processing Algorithm for Motion Target

Tingjing Wang, Ying Zhang, Hua Zhao, and Yanxin Zhang
Volume 2017, Article ID 4060789, 8 pages

Calculation Algorithm for Diffraction Losses of Multiple Obstacles Based on Epstein–Peterson Approach

Ahmad S. Abdulrasool, Jabir S. Aziz, and Sadiq J. Abou-Loukh
Volume 2017, Article ID 3932487, 9 pages

Full Wave Modeling of Array Structures Using Generalized Single-Source Tangential Equivalence Principle Algorithm

Hanru Shao, Jianfeng Dong, and Jun Hu
Volume 2017, Article ID 4903906, 10 pages

A Truncated Singular Value Decomposition Enhanced Nested Complex Source Beam Method

Lianning Song and Zaiping Nie
Volume 2017, Article ID 9072421, 7 pages

High Performance Computing of Complex Electromagnetic Algorithms Based on GPU/CPU Heterogeneous Platform and Its Applications to EM Scattering and Multilayered Medium Structure

Zhe Song, Xing Mu, and Hou-Xing Zhou
Volume 2017, Article ID 9173062, 12 pages

Acceleration of Augmented EFIE Using Multilevel Complex Source Beam Method

Lianning Song, Yongpin Chen, Ming Jiang, Jun Hu, and Zaiping Nie
Volume 2017, Article ID 9640136, 8 pages

Tolerance Analysis of Antenna Array Pattern and Array Synthesis in the Presence of Excitation Errors

Ying Zhang, DanNi Zhao, Qiong Wang, ZhengBin Long, and Xiaofeng Shen
Volume 2017, Article ID 3424536, 6 pages

Full-Wave Analysis of the Shielding Effectiveness of Thin Graphene Sheets with the 3D Unidirectionally Collocated HIE-FDTD Method

Arne Van Londersele, Daniël De Zutter, and Dries Vande Ginste
Volume 2017, Article ID 5860854, 8 pages

Numerical Simulations of the Lunar Penetrating Radar and Investigations of the Geological Structures of the Lunar Regolith Layer at the Chang'E 3 Landing Site

Chunyu Ding, Yan Su, Shuguo Xing, Shun Dai, Yuan Xiao, Jianqing Feng, Danqing Liu, and Chunlai Li
Volume 2017, Article ID 3013249, 11 pages

A Robust Method to Suppress Jamming for GNSS Array Antenna Based on Reconstruction of Sample Covariance Matrix

Yanyun Gong, Ling Wang, Rugui Yao, and Zhaolin Zhang
Volume 2017, Article ID 9764283, 12 pages

High Precise Scattering Centers Models for Cone-Shaped Targets Based on Induced Currents

Qi-Feng Li, Kun-Yi Guo, Xin-Qing Sheng, and Tian-Shu Liu
Volume 2017, Article ID 7482895, 12 pages

Editorial

Advanced Modeling and Simulation Methods for Multiphysics and Multiscale Problems

Su Yan,¹ Yumao Wu,² Huapeng Zhao,³ and Han Guo⁴

¹Department of Electrical and Computer Engineering, University of Illinois at Urbana-Champaign, Urbana, IL 61801-2991, USA

²School of Information Science and Technology, Fudan University, Shanghai 200433, China

³School of Electronic Engineering, University of Electronic Science and Technology of China, Chengdu 611731, China

⁴Department of Electrical Engineering and Computer Science, University of Michigan, Ann Arbor, MI 48109, USA

Correspondence should be addressed to Su Yan; suyan@illinois.edu

Received 29 October 2017; Accepted 30 October 2017; Published 22 November 2017

Copyright © 2017 Su Yan et al. This is an open access article distributed under the Creative Commons Attribution License, which permits unrestricted use, distribution, and reproduction in any medium, provided the original work is properly cited.

With great success being achieved in electromagnetic (EM) modeling and simulation, EM scientists and researchers are turning their concentration towards much more challenging multiphysics and multiscale problems, which have a greater range of applications in sciences and technologies. Problems that involve large-scale and multiscale features in both space and time, that are nonlinear and multiphysics in nature, and that lack unique solutions for mathematical or engineering reasons are encountered routinely in many applications such as the design of integrated circuits and packages, the modeling of natural or artificial materials, the simulation of large-scale antenna arrays, the deterministic and stochastic investigation of EM and particle interactions, the analysis of EM compatibility in complex environments, and the optimization of geometrical and material parameters in inverse problems. In this special issue, many of these important topics have been covered and discussed.

Real-world medium exhibits complex hierarchical structures and randomness on different length scales. To capture the multiscale feature as well as the random characteristic of the real-world medium, one article in this special issue hybridized a statistical model based on the random medium theory with the deterministic method, the finite-difference time-domain (FDTD) method, to simulate the radar signal reflected by the lunar regolith layer. A unidirectionally collocated hybrid implicit-explicit FDTD method was proposed to simulate the planar structure of graphene to increase the time step by utilizing an implicit method for structures under the critical dimension.

Modern wireless systems are often operated in complex EM environments. To achieve satisfactory performance, it is critical to consider the effect of the environment when designing wireless systems. The scale difference between wireless systems and its working environment poses a very challenging multiscale problem. Two articles in this special issue discussed the fast modeling of complex EM environments and explored the environmental effect on the design of wireless systems. One work presented an algorithm to calculate total diffraction losses for multiple obstacle objects using Epstein–Peterson approach. Another article concerned the antijamming performance of receiving antennas in satellite navigation systems, where a robust method to suppress jamming for satellite navigation by reconstructing sample covariance matrix without main-lobe nulling has been proposed.

Several articles in this special issue present advanced methods in modeling and simulation of large and complex objects, which are usually encountered in multiphysics and multiscale problems. To improve the computational efficiency, high-frequency asymptotic methods, high-efficiency full-wave methods, and high-performance computing techniques can be developed. In this special issue, a high precision scattering center model was proposed based on induced currents of cone-shaped targets. To address the scattering problem from large objects, one article presented an efficient matrix compression algorithm for the nested complex source beam (CSB) method based on the truncated singular value decomposition. The computation of the augmented electric

field integral equation was accelerated by using the multilevel CSB method. A generalized single-source tangential equivalence principle algorithm was proposed to solve the EM scattering of array structures with very small distance or even connected elements. One article introduced recent work on high-performance computing based on GPU/CPU heterogeneous platform.

Acknowledgments

The editors thank all the contributors and the anonymous reviewers for their contributions to this special issue.

*Su Yan
Yumao Wu
Huapeng Zhao
Han Guo*

Research Article

Multiband Radar Signal Coherent Processing Algorithm for Motion Target

Tingjing Wang, Ying Zhang, Hua Zhao, and Yanxin Zhang

College of Electronic Engineering, University of Electronic Science and Technology of China, Chengdu, Sichuan 611731, China

Correspondence should be addressed to Ying Zhang; zhying@uestc.edu.cn

Received 24 April 2017; Revised 6 June 2017; Accepted 22 June 2017; Published 20 November 2017

Academic Editor: Yumao Wu

Copyright © 2017 Tingjing Wang et al. This is an open access article distributed under the Creative Commons Attribution License, which permits unrestricted use, distribution, and reproduction in any medium, provided the original work is properly cited.

In real application, most aerial targets are movable. In this paper, an effective multiple subbands coherent processing method is proposed for moving target. Firstly, an echoed signal model of motion target based on geometrical theory of diffraction is established and the influence of velocity on range profile of the target is analyzed. Secondly, a method based on minimum entropy principle is used to compensate velocity. Then, incoherent factors including a quadratic phase term, a linear phase factor, a fixed factor, and an amplitude difference term are analyzed. Subsequently, efficient methods are applied to estimate other incoherent factors, except that the quadratic term is small enough to be ignored. Finally, the feasibility and performance of the proposed method are investigated through numerical simulation.

1. Introduction

Multiple radar subband fusion is effective to obtain ultra-wide bandwidth so that the range resolution of radar target can be improved. Compared with real ultra-wideband radar, it reduces the manufacture costs and the complexity of system design. Since the received echoes with respect to different radars differ in time delay, amplitude, and so forth, coherent compensation between subbands is essential before multiband fusion [1–5].

In [2], Cuomo et al. obtained the target echoed signal from distributed radars. Then, a nonlinear optimization problem was established to estimate the pole rotation angle and the complex amplitude coefficient. However, the procedure of solving the function was rather complicated. Besides, Wang [5] proposed to use modern spectral estimation methods including modified root-multiple signal classification (MUSIC) algorithm and estimated signal parameters via rotational invariance technique (ESPRIT) to estimate the incoherent factors. However, these methods require overlapped observation frequency bands. In [6, 7], all-phase fast Fourier transform (apFFT) spectral analysis was proposed to obtain the phase factor between subbands. It shows good performance when estimating incoherent factors without the prior information of scattering centers numbers. However,

the estimation precision of the coherent factor is limited by the sampling frequency. *A coherent processing method based on sparse representation was present in [8]; genetic algorithm (GA) was adopted to obtain optimal parameters. GA can simultaneously optimize multiple parameters and solve out superior estimates but it is computationally demanding when parameters increase.*

The aforementioned algorithms assumed that the target is static or with low speed. However, most aerial targets tend to be fast moving in real applications [9]. In this paper, in order to take a more practical situation into account, a new subband coherent compensation method is presented. The proposed method consists of the following steps. Firstly, an echoed signal based on geometrical theory of diffraction (GTD) model of constant high speed target is built and the influence of velocity on range profile is analyzed. Then, an effective method using minimum entropy principle is applied to compensate the velocity. Considering the residual of velocity compensation and difference of time delays and amplitudes between subbands, the incoherent factors are analyzed, which are shown to include a quadratic phase term, a linear phase factor, a fixed factor, and an amplitude difference term. Quadratic term is so small which can be ignored. Subsequently, a modified cross-correction method is applied to estimate the linear phase factor. As

TABLE 1: Scattering structures and the corresponding geometry parameters.

Scattering field	Corner	Edge	Point	Single curved surface	Flat plate
α	-1	-0.5	0	0.5	1

for the fixed phase factor, the one-dimension optimization problem is transformed to nonlinear least square fitting problem to improve the estimation precision. Taking amplitude difference into account, golden section method is applied to seek an appropriate amplitude factor. To verify validity of the proposed algorithm, computer simulation is conducted.

The rest of this paper is organized as follows: in Section 2, radar echo model of motion target is established and the influence of the velocity on range resolution is analyzed. Velocity compensation and incoherent parameters estimation are elaborated in Section 3. After that, computer simulation result is shown in Section 4. Finally, discussion and conclusion are drawn in Section 5.

2. Analysis of Radar Echoed Signal of Motion Target

Without considering the resonance behavior of a target to wideband systems, it is generally believed that the target scattering characteristics of two radars are approximately in agreement. The frequency response of echoed signal is described by the following GTD model:

$$S_{Ri}(f_i) = S_i(f_i) \sum_{m=1}^M A_{mi} \left(j \frac{f_i}{f_{ci}} \right)^{\alpha_m} \exp \left(-j \frac{4\pi R_{mi} f_i}{c} \right), \quad (1)$$

where $S_i(f)$ denotes the frequency spectrum of the transmitted signals of the i th radar, $i = 1, 2$. $f_i = f_0 + n_i \Delta f_i$, where f_0 represents the initial frequency, n_i is the n_i th frequency point, and the frequency step is denoted by Δf_i . f_{ci} denotes the carrier frequency. A_{mi} and R_{mi} denote the complex amplitude and range of the m th scattering center for the i th radar, respectively. Geometry parameter of the m th scattering center is denoted by α_m . In particular, Table 1 shows the scattering structures and the corresponding geometry parameters. c is the light speed.

Then, (1) can be rewritten as

$$S_{Ri}(f_i) = \sum_{m=1}^M A_{mi} \left(j \frac{f_i}{f_{ci}} \right)^{\alpha_m} S'_i(f_i), \quad (2)$$

$$S'_i(f_i) = S_i(f_i) \exp \left(-j \frac{4\pi R_{mi} f_i}{c} \right); \quad (3)$$

(4) is transformed to time domain, namely,

$$S'_i(t) = S_i \left(t - \frac{2R_{mi}}{c} \right). \quad (4)$$

When radar target is static or with low speed, the distance between target and radar can be considered invariant within the pulse duration. However, when target is fast moving,

this assumption does not hold. Supposing that v_m is the radial velocity of the m th scattering centers, the instantaneous distance \bar{R}_{mi} at time t is given by $\bar{R}_{mi} = R_{mi} + v_m t$.

Substituting (4) into (3) yields

$$S'_i(t) = \text{rect} \left(\frac{a_m t - b_{mi}}{T_i} \right) \cdot \exp \left(\left[j 2\pi \left(f_{ci} (a_m t - b_{mi}) + \frac{1}{2} K_i (a_m t - b_{mi})^2 \right) \right] \right), \quad (5)$$

$$a_m = 1 - \frac{2v_m}{c},$$

$$b_{mi} = \frac{2R_{mi}}{c};$$

therefore,

$$S_{Ri}(f_i) = \sum_{m=1}^M A_{mi} \left(j \frac{f_i}{f_{ci}} \right)^{\alpha_m} \cdot F(S'_i(t)). \quad (6)$$

$F(\cdot)$ is Fourier transform. $S_{Ri}(f_i)$ can be further induced by stationary phase principle and let $f_i = f_i + f_{ci}$;

$$S_{Ri}(f_i) = \sum_{m=1}^M \bar{A}_{mi} \left(j \frac{f_i + f_{ci}}{f_{ci}} \right)^{\alpha_m} \cdot \text{rect} \left(\frac{f_i + (2v_m/c) f_{ci}}{a_m B_i} \right) \exp(j\Phi_{mi}(f_i)), \quad (7)$$

where

$$\Phi_{mi}(f) = -\frac{\pi (f_i + (2v_m/c) f_{ci})^2}{K_i a_m^2} - \frac{2\pi b_{mi}}{a_m} (f_i + f_{ci}) + \frac{\pi}{4}, \quad (8)$$

and $\bar{A}_{mi} = (1/a_m \sqrt{K_i}) A_{mi}$, and the pulse widths and bandwidth are denoted by T_i and B_i , respectively. $K_i = B_i/T_i$ is the frequency modulated rate. Process the echoed signal with matching filter,

$$M_{Ri}(f_i) = S_{Ri}(f_i) \cdot S_{\text{ref},i}^*(f_i) \quad (9)$$

and $S_{\text{ref},i}(f_i)$ is the spectrum of conference signal $S_{\text{ref},i}(t)$.

$$S_{\text{ref},i}(t) = \exp \left([j\pi K_i t^2] \right). \quad (10)$$

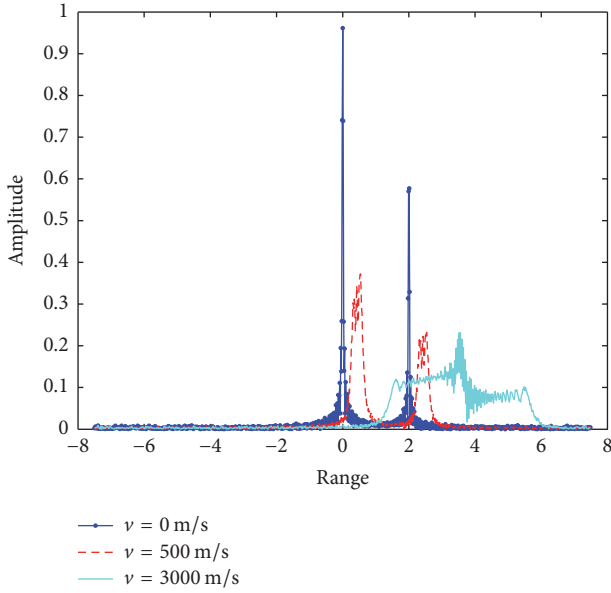


FIGURE 1: The influence of varied target velocity on range profile.

Then the echoed signal after matching filter can be expressed as

$$M_{Ri}(f_i) = \sum_{m=1}^M \bar{A}_{mi} \text{rect} \left(\frac{f_i + (2v_m/c) f_{ci}}{(1 - 2v_m/c) B_i} \right) \left(j \frac{f_i + f_{ci}}{f_{ci}} \right)^{\alpha_m} \exp(j\Phi'_{mi}(f_i)), \quad (11)$$

$$\begin{aligned} \Phi'_{mi}(f_i) &= -\frac{4\pi v_m (c - v_m)}{K_i (c - 2v_m)^2} f_i^2 - \frac{4\pi v_m c f_{ci}}{K_i (c - 2v_m)^2} f_i \\ &\quad - \frac{4\pi v_m^2 f_{ci}^2}{K_i (c - 2v_m)^2} - \frac{4\pi R_{mi}}{c - 2v_m} (f_i + f_{ci}) \\ &\approx -\frac{4\pi v_m}{K_i (c - 2v_m)} f_i^2 - \frac{4\pi v_m c f_{ci}}{K_i (c - 2v_m)^2} f_i \\ &\quad - \frac{4\pi v_m^2 f_{ci}^2}{K_i (c - 2v_m)^2} - \frac{4\pi R_{mi}}{c - 2v_m} (f_i + f_{ci}), \end{aligned} \quad (12)$$

where $v_m \ll c$ and $\bar{A}_{mi} = (1/a_m K_i) A_{mi}$. From (12), when the target moves, the change of scale and location of the range profile occur. When the speed is low or frequency modulated rate is high, the second-order term in (12) can be ignored. On the contrary, serious influence may be triggered by high speed or low frequency modulated rate. Processing the echoed signal using inverse fast Fourier transform (IFFT) to obtain range profile, the quadratic term in (12) may lead to distortion of range profile of target, which is shown as reduction of peak values and broadening of waveform. Besides, the second term in (12) may give rise to the shift of range profile. Figure 1 shows the influence of varied target velocity on range profile. It is observed that the range profile deteriorates as the increase of target velocity.

3. Coherent Processing Algorithm with Velocity Compensation

The procedure of multiband coherent processing is presented in Figure 2. The steps include the following:

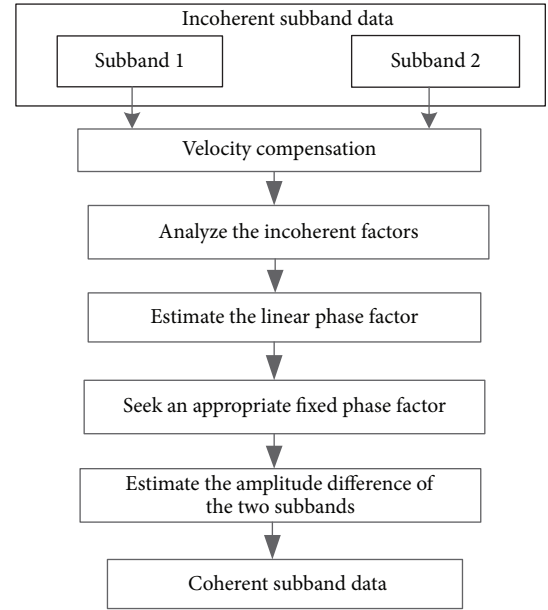


FIGURE 2: The flow of multiple subband coherent processing.

- (1) Estimate target moving speed and apply velocity compensation to subband signals.
- (2) Analyze the incoherent factors and establish a nonlinear optimization function to estimate the factors.
- (3) Estimate the linear phase term by cross-correlation method.
- (4) Solve a nonlinear least square fitting problem to seek the fixed phase factor.
- (5) Estimate the amplitude difference between the subbands by golden section method.
- (6) Coherent recovery using the estimated incoherent factors.

3.1. Velocity Compensation and Phase Residual Analysis. From the aforementioned analysis, it is pretty critical to eliminate or decrease the influence of target velocity before coherent processing.

Assume that $\varphi_i(f_i)$ is the compensatory phase which includes estimation velocity. $y_i(f_i)$ represents $M_{Ri}(f_i)$ which is compensated by $\varphi_i(f_i)$. The one-dimension range profile of $y_i(f_i)$ is $Y_i = \{Y_i(h) \mid h = 1, 2, \dots, n\}$, and the amplitude distribution of sampling point can be computed as

$$p_{hi} = \frac{|Y_i(h)|^2}{\sum_{l=1}^n |Y_i(l)|^2}. \quad (13)$$

Using p_{hi} to computing the entropy yields

$$H_i = -\sum_{h=1}^n p_{hi} \ln p_{hi}. \quad (14)$$

Then, the required velocity compensation phase $\hat{\varphi}_i$ can be obtained by minimizing

$$\hat{\varphi}_i = \arg \min_{\varphi_i} H. \quad (15)$$

Traversing method is utilized to estimate the velocity [10]. To be specific, search step is set up within the range of certain velocity and entropy of range profile is resolved by compensatory velocity. When H reaches its minimum, the corresponding \tilde{V} is the most appropriate compensatory velocity. In the view of the velocity values of different scattering centers which are almost identical, v_m can be replaced by the uniform estimated velocity \tilde{V} . The echoed signal is then compensated via

$$y_i(f_i) = M_{Ri}(f_i) * \exp(j\hat{\varphi}_i(f_i)), \quad (16)$$

where

$$\begin{aligned} \hat{\varphi}_i(f_i) = & \frac{4\pi\tilde{V}}{K_i(c-2\tilde{V})}f_i^2 + \frac{4\pi\tilde{V}cf_{ci}}{K_i(c-2\tilde{V})^2}f_i \\ & + \frac{4\pi\tilde{V}^2f_{ci}^2}{K_i(c-2\tilde{V})^2}, \quad i = 1, 2. \end{aligned} \quad (17)$$

On the assumption that $\{y_1(f_{1n}), n = 0, \dots, N_1 - 1\}$ and $\{y_2(f_{2n}), n = N - N_2, \dots, N - 1\}$ are the preprocessed echoed signals of two radars. The frequency ranges are within $[f_0, f_{N_1-1}]$ and $[f_{N-N_2}, f_{N-1}]$. Because the sampling frequency of the subbands may be different, uniform resampling [11] is applied to subband data so that the sampling rate of all subbands is identical. Meanwhile, as shown in Figure 3, subbands are extrapolated, where $\bar{y}_1(f)$ and $\bar{y}_2(f)$ represent the extended subband data. $f = f_0 + n\Delta f$, $n = 1, \dots, N$. $\Delta f = \min\{\Delta f_1, \Delta f_2\}$ denotes frequency step of subbands after uniform resampling.

Take $\bar{y}_1(f)$ as the reference signal. Assuming that $v \ll c$ and taking the time delay and the initial phase value difference between two radar echoed signals into account, after velocity compensation and simplification, the phase of radar echoed signals become

$$\begin{aligned} \tilde{\Phi}_1(f) \approx & -\frac{4\pi\Delta v c}{K_1(c-2v)(c-2\tilde{V})}f^2 \\ & + \frac{4\pi\Delta v c f_{c1}}{K_1(c-2v)(c-2\tilde{V})}f - \frac{4\pi R_{m1}}{c-2v}f, \\ \tilde{\Phi}_2(f) \approx & -\frac{4\pi\Delta v c}{K_2(c-2v)(c-2\tilde{V})}f^2 \\ & + \frac{4\pi\Delta v c f_{c2}}{K_2(c-2v)(c-2\tilde{V})}f - \frac{4\pi R_{m1}}{c-2v}f \\ & + \alpha n + \beta, \end{aligned} \quad (18)$$

where $\Delta\hat{v} = v - \tilde{V}$ is velocity estimation error, α denotes the linear phase term caused by time delay difference between the

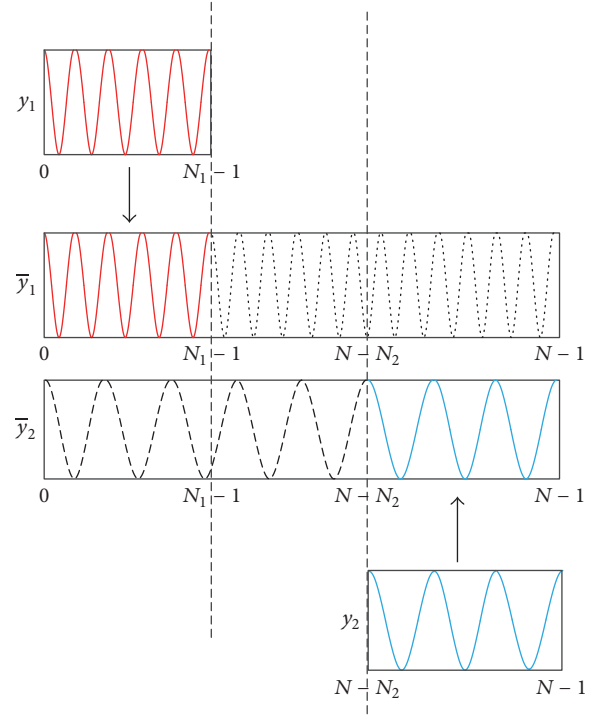


FIGURE 3: Extended subband data for estimation of incoherent factors.

target and the different radars, and β denotes the fixed phase difference between subbands. The phase difference between subbands is computed as

$$\begin{aligned} \delta(f) = & \tilde{\Phi}_1(f) - \tilde{\Phi}_2(f) \\ \approx & -\left(\frac{1}{K_1} - \frac{1}{K_2}\right) \frac{4\pi\Delta v c}{(c-2v)(c-2\tilde{V})}f^2 \\ & + \left(\left(\frac{f_{c1}}{K_1} - \frac{f_{c2}}{K_2}\right) \frac{4\pi\Delta v c}{(c-2v)(c-2\tilde{V})}\right)f - \alpha n \\ & - \beta. \end{aligned} \quad (19)$$

Discretization processing yields

$$\begin{aligned} \delta(n) \approx & -\left(\frac{1}{K_1} - \frac{1}{K_2}\right) \frac{4\pi\Delta v \Delta f^2}{c}n^2 \\ & - \left(\left(\frac{1}{K_1} - \frac{1}{K_2}\right)2f_0 - \left(\frac{f_{c1}}{K_1} - \frac{f_{c2}}{K_2}\right)\right) \frac{4\pi\Delta v \Delta f}{c}n \\ & - \alpha n \\ & - \left(\left(\frac{1}{K_1} - \frac{1}{K_2}\right)f_0 - \left(\frac{f_{c1}}{K_1} - \frac{f_{c2}}{K_2}\right)\right) \frac{4\pi\Delta v}{c}f_0 \\ & - \beta. \end{aligned} \quad (20)$$

It is observed from (20) that the first, second, and fourth items are the incoherence caused by the residual of velocity

compensation. The first item of (20) is the quadratic term, which is usually ignored in most literatures. Assuming that $\Delta v = 1000$ m/s and $\Delta f = 20$ MHz, the bandwidths of two subbands are 1 GHz and 0.8 GHz and the pulse widths are $512 \mu\text{s}$. From the formula $-(1/K_1 - 1/K_2)(4\pi\Delta v\Delta f^2/c)n^2$, the value of quadratic term is about 0.002145 rad. It is obviously small even if the velocity estimation error is large. Therefore, it can be ignored in practical application. A new linear phase factor is composed of second item and initial linear phase factor, which leads to the shift of one-dimension range profile of multiple subbands. The remaining part refers to a new fixed phase, which includes residual term and initial fixed phase factor. It can be concluded that the residual of velocity compensation, as well as time delay, initial phase, and amplitude difference between subbands give rise to the incoherence of the echoed subband signals. It is necessary to estimate the incoherent factors and preprocess the subbands to ensure subband data mutually coherent before subband fusion.

3.2. Incoherent Factors Estimation. In [2], Cuomo et al. proposed that the incoherent factors between different echoed signal spectra can be expressed as linear phase item and fixed phase item when the targets are static or with lower speed. According to (20), besides the linear factor and the fixed factor, amplitude difference and the quadratic term of frequency should also be considered. The following cost function is defined:

$$J_1(\theta, \varphi, \lambda, \rho) = \sum_{n=0}^{N-1} \left| \rho \bar{y}_1(n) e^{j(\theta n^2 + \varphi n + \lambda)} - \bar{y}_2(n) \right|^2, \quad (21a)$$

where

$$\begin{aligned} \theta &= -\left(\frac{1}{K_1} - \frac{1}{K_2}\right) \frac{4\pi\Delta v\Delta f^2}{c}, \\ \varphi &= -\left(\left(\frac{1}{K_1} - \frac{1}{K_2}\right) 2f_0 - \left(\frac{f_{c1}}{K_1} - \frac{f_{c2}}{K_2}\right)\right) \frac{4\pi\Delta v\Delta f}{c} \\ &\quad - \alpha, \\ \lambda &= -\left(\left(\frac{1}{K_1} - \frac{1}{K_2}\right) f_0 - \left(\frac{f_{c1}}{K_1} - \frac{f_{c2}}{K_2}\right)\right) \frac{4\pi\Delta v}{c} f_0 \\ &\quad - \beta. \end{aligned} \quad (21b)$$

In (21a), ρ is the amplitude difference between the two subbands, θ denotes the quadratic phase term, and φ and λ denote new linear phase and fixed phase, respectively.

$J_1(\theta, \varphi, \lambda, \rho)$ should be minimized to obtain the optimal estimation of θ , φ , λ , and ρ . It is straightforward to see that (9) is nonlinear and nonconvex. Standard nonlinear optimization algorithms such as Newton method [12] tend to work out local minimum and genetic algorithm [13] can be used to seek a global optimal solution but the burden of calculation is heavy. From prior analysis in Section 3.1, it is deduced that the quadratic term θ is usually so small, and the value is approximated to zero. Correlation method is applied

to deal with the linear phase factor. On the assumption that $R(n)$ is the correlation function of $\bar{y}_1(n)$, $\bar{y}_2(n)$,

$$R(n) = \bar{y}_1(n) \bar{y}_2^*(n), \quad (22)$$

where $(\cdot)^*$ is the conjugate operator.

The modeling error is ignored:

$$\bar{y}_2(n) \approx \rho \bar{y}_1(n) e^{j(\varphi n + \lambda)}. \quad (23)$$

We obtained the cross-correlation of range profiles $r(k)$ from $R(n)$:

$$\begin{aligned} r(k) &= \frac{1}{N_{\text{FFT}}} \sum_{n=0}^{N_{\text{FFT}}-1} R(n) e^{j(2\pi/N_{\text{FFT}})nk} \\ &= \frac{1}{N_{\text{FFT}}} \sum_{m=0}^{N_{\text{FFT}}-1} \bar{y}_1(n) \bar{y}_2^*(n) e^{j(2\pi/N_{\text{FFT}})nk} \\ &\approx \frac{\rho e^{-j\lambda}}{N_{\text{FFT}}} \sum_{m=0}^{N-1} |\bar{y}_1(n)|^2 e^{j(2\pi/N_{\text{FFT}})n(k - (N/2\pi)\varphi)}, \end{aligned} \quad (24)$$

where N_{FFT} is the number of points in IFFT and $N_{\text{FFT}} \gg N$. Zero-padding is used to expand the length of $R(n)$ to N_{FFT} . When $k = (N/2\pi)\varphi$, $r(k)$ reaches its maximum. Denote this k as k_{max} , and the linear phase is computed as

$$\hat{\varphi} = \frac{2\pi k_{\text{max}}}{N_{\text{FFT}}}. \quad (25)$$

$\bar{y}_1(n)$ is compensated by the linear phase factor in (25); that is,

$$\bar{y}'_1(n) = \bar{y}_1(n) \cdot \exp(j\hat{\varphi}n). \quad (26)$$

A new coherent function is defined to estimate the fixed phase factor:

$$J_2(\lambda) = \sum_{n=0}^{N-1} \left| \frac{\bar{y}'_1(n) e^{j\lambda}}{|\bar{y}'_1(n)|} - \frac{\bar{y}_2(n)}{|\bar{y}_2(n)|} \right|^2. \quad (27)$$

$J_2(\lambda)$ may not be a unimodal function in $[-\pi, \pi]$; in order to gain better coherence, the nonlinear least square problem can be computed by means of MATLAB subroutine *lsqcurvefit* to find the most appropriate $\hat{\lambda}$.

Substitute $\hat{\varphi}$ and $\hat{\lambda}$ into the primary cost function (21a), the constant $\hat{\rho}$ can be worked out by golden section method. Our aim is to minimize the function $J_1(\rho)$ within the interval $[a, b]$, and the two points ρ_1, ρ_2 are calculated by golden section scale as follows:

$$\begin{aligned} \rho_1 &= a + 0.382 * (b - a), \\ \rho_2 &= a + 0.618 * (b - a). \end{aligned} \quad (28)$$

The search interval is chosen as $[a, \rho_2]$, if $J_1(\rho_1) < J_1(\rho_2)$. Otherwise, the interval is $[\rho_1, b]$. Repeat (28) by new points; in this way, search interval is shrinking, and the point is approximated to the minimum $\hat{\rho}$.

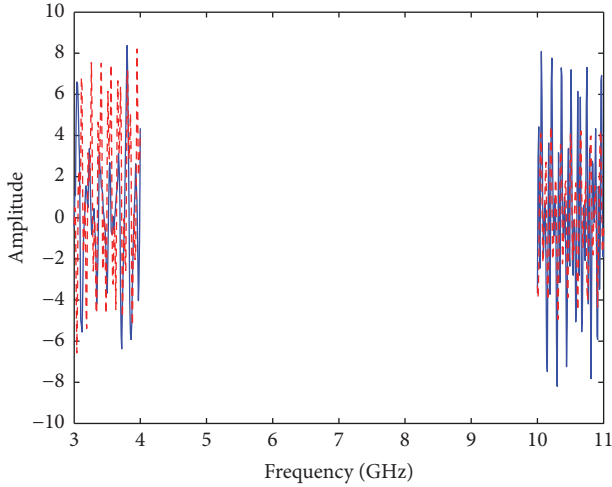


FIGURE 4: Two subband data sets (blue solid lines denote the real coherent subbands. Red dash line denotes the measured incoherent subbands in the condition that target is moving).

The lower subband signal data is rewritten as follows:

$$\tilde{y}_1(n) = \hat{\rho}y_1(n) e^{j(\hat{\varphi}n + \hat{\lambda})}, \quad n = 1, \dots, N_1 - 1. \quad (29)$$

Now the lower frequency band data in $[f_0, f_{N_1-1}]$ is coherent to the upper one. The aforementioned process *assumes implicitly that the upper sideband data is more pristine than the lower subband data. However, in most practical application, the choice of benchmark subband data should be made based on sensor hardware or data equality evaluations. Otherwise, the data may be fused but degraded if the data is from lower quality sensor.*

4. Computer Simulation Result

In this section, the performance and feasibility of the proposed method are verified via numerical simulations. LFM signals are transmitted by two radars, carrier frequencies f_{c1}, f_{c2} are 3.5 GHz and 10.5 GHz, bandwidths B_1, B_2 are 1 GHz and 0.8 GHz, and both the pulse durations are 100 μ s. Supposing there are four scattering centers of target, the range between radar and scattering centers is 200 Km. The echo amplitude of scattering centers is 1, 2, 3, and 1. Geometry parameters of the scattering centers are 0.5, 1, 0, and -1. In particular, velocities are all 3000 m/s. In order to validate the effectiveness of velocity compensation, set lower subband signal as an example. Simulate the effect of mutual incoherence between the subbands; the signal sampled in the lower subband has been attached to a linear phase factor $\alpha = -\pi/9$, a fixed phase factor $\beta = -\pi/4$, and a constant $\rho = 1.5$.

It is observed from Figure 4 that red dash lines are not consistent with blue solid lines, because target velocity makes the original subbands shift on frequency spectra. As shown in Figure 5, it is easily concluded that process incoherent subband data directly without velocity compensation leads to mismatching between real lower subband and the measured

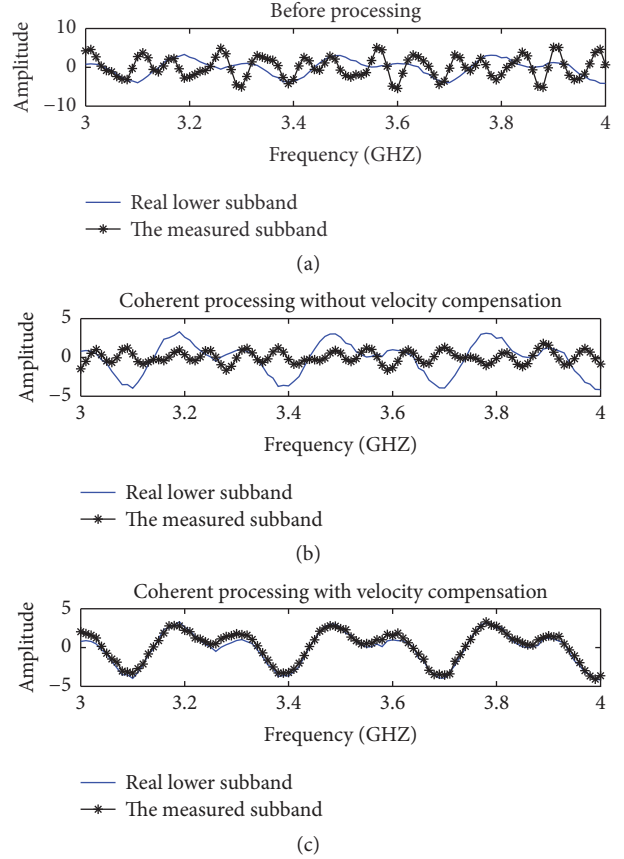


FIGURE 5: Comparison between real lower subband and the measured subband ((a) shows the two subbands before processing, (b) shows velocity compensation is not used to process the measured subband, and (c) shows velocity compensation is used to process the measured subband).

subband. Besides, applying velocity compensation method on the measured subband, it matches well with real lower subband after coherent processing.

Furthermore, to test the antinoise performance of the proposed method, zero mean white noise is added to the original signal. *After velocity compensation*, the pole method proposed in [14] and apFFT method [8] are also applied to process two subband data sets.

Root mean square error (RMSE) is defined as $RMSE = \sqrt{(1/M_{iter}) \sum_{i=1}^{M_{iter}} |\hat{S}_i - s|^2}$, where \hat{S}_i is estimate result and s is real value. RMSE between real incoherent factors and estimated parameters against the value of signal to noise ratio (SNR) under 100 runs of Monte Carlo simulations is shown in Figure 6. As the figure shows, when estimating the linear phase factors, compared with pole method and apFFT method, our method shows preferable performance when SNR is less than 10 dB, and the accuracy of our method is the most outstanding among all methods. With the increase of SNR, the poled method performs better than other methods. As for the fixed phase factor estimation, RMSE curves evaluated by pole method and apFFT method are approximated, and our method outperforms

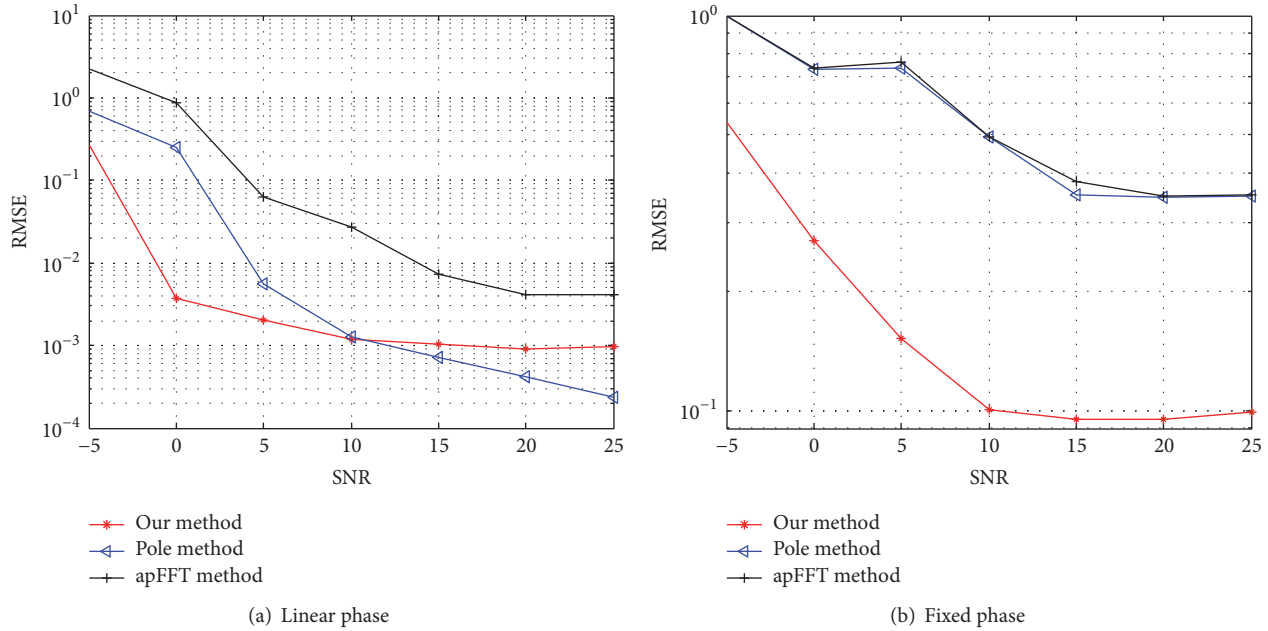


FIGURE 6: Average RMSE comparison at different SNR.

the other methods. In conclusion, our method has better antinoise property and improves the incoherent factors estimate precision essentially; also it is more robust than other methods.

5. Conclusion

In this paper, a multiple subband coherent processing method based on motion target is proposed. This algorithm firstly introduces an effective velocity compensation approach based on minimum entropy to decrease the effects on range profile of the target. Then, a modified correlation method and a nonlinear least square fitting algorithm are applied to estimate the phase difference between the various subbands. Besides, amplitude error is considered, and golden section algorithm is directly used to search the error. Compared with existing coherent processing methods, the proposed method is able to deal with more practical problem. Simulation results show the robustness in the presence of noise.

Conflicts of Interest

The authors declare that they have no conflicts of interest.

Acknowledgments

This paper is supported by a grant from Open Foundation of Key Laboratory of Space Target Measurement, National Science Foundation of China (no. 61671121), Doctoral Fund of Ministry of Education of China (no. 2016M602673), and Doctoral Fund of Jiangxi Province (no. 2016KY15).

References

- [1] S. L. Borison, S. B. Bowling, and K. M. Cuomo, "Super-resolution methods for wideband radar," *The Lincoln Laboratory Journal*, vol. 5, no. 3, pp. 441–461, 1992.
- [2] K. Cuomo, J. Pion, and J. Mayhan, "Ultrawide-band coherent processing," *IEEE Transactions on Antennas and Propagation*, vol. 47, no. 6, pp. 1094–1107, 1999.
- [3] L. D. Vann, K. M. Cuomo, J. E. Piou, and J. T. Mayhan, "Multi-sensor fusion processing for enhanced radar imaging Tech. Rep. TR-1056," Tech. Rep., Lincoln Laboratory, Massachusetts Inst. Technology, Lexington, MA, USA, 2000.
- [4] K. Suwa and M. Iwamoto, "A bandwidth extrapolation technique of polarimetric radar data and a recursive method of polarimetric linear prediction coefficient estimation," in *Proceedings of the 2003 IGARSS: Learning From Earth's Shapes and Colours*, pp. 4329–4331, Toulouse, France, July 2003.
- [5] C. Wang, *Research on radar signal level fusion imaging techniques [Ph.D. thesis]*, National University of Defense Technology, Changsha, China, 2006.
- [6] J. Tian, J. Sun, G. Wang, Y. Wang, and W. Tan, "Multiband radar signal coherent fusion processing with IAA and apFFT," *IEEE Signal Processing Letters*, vol. 20, no. 5, pp. 463–466, 2013.
- [7] Y. Zou, X. Gao, X. Li, and Y. Liu, "Multiband radar signals coherent compensation with sparse representation," in *Proceedings of the 8th International Congress on Image and Signal Processing, CISP 2015*, pp. 1085–1089, Shenyang, China, October 2015.
- [8] H. H. Zhang and R. S. Chen, "Coherent processing and superresolution technique of multi-band radar data based on fast sparse Bayesian learning algorithm," *Institute of Electrical and Electronics Engineers. Transactions on Antennas and Propagation*, vol. 62, no. 12, pp. 6217–6227, 2014.
- [9] M. Xing, R. Wu, and Z. Bao, "High resolution ISAR imaging of high speed moving targets," *Radar, Sonar and Navigation, IEE Proceedings*, vol. 152, no. 2, pp. 58–67, 2005.

- [10] J. Yang, Q. L. Bao, and Z. P. Chen, "The implemental methods of high velocity compensation in isar imaging based on entropy minimization," *Signal Processing*, vol. 25, no. 12, pp. 1861–1866, 2007.
- [11] Y. Zou, X. Z. Gao, and X. Li, "High precision coherent compensation for multiband radar data at low SNR," *IEEE Signal Processing Letters*, vol. 37, no. 1, pp. 48–54, Jan 2015.
- [12] S. Boyd and L. Vandenberghe, *Convex Optimization*, Cambridge University Press, 2004.
- [13] Z. Yu, Y. Chen, Z.-Q. Sun, and Y.-B. Lu, "The super-resolution range imaging based on multiband wideband signal fusion," in *Proceedings of the 2009 Asia-Pacific Conference on Synthetic Aperture Radar, APSAR 2009*, pp. 160–164, chn, October 2009.
- [14] B. Tian, Z. Chen, and S. Xu, "Sparse subband fusion imaging based on parameter estimation of geometrical theory of diffraction model," *IET Radar, Sonar and Navigation*, vol. 8, no. 4, pp. 318–326, 2014.

Research Article

Calculation Algorithm for Diffraction Losses of Multiple Obstacles Based on Epstein–Peterson Approach

Ahmad S. Abdulrasool,¹ Jabir S. Aziz,² and Sadiq J. Abou-Loukh¹

¹Electrical Engineering Department, Baghdad University, Baghdad, Iraq

²Electronics and Communication Engineering Department, Al-Nahrain University, Baghdad, Iraq

Correspondence should be addressed to Ahmad S. Abdulrasool; ahmadsalam5101986@gmail.com

Received 25 April 2017; Revised 2 July 2017; Accepted 27 July 2017; Published 3 October 2017

Academic Editor: Huapeng Zhao

Copyright © 2017 Ahmad S. Abdulrasool et al. This is an open access article distributed under the Creative Commons Attribution License, which permits unrestricted use, distribution, and reproduction in any medium, provided the original work is properly cited.

Applying propagation models with good accuracy is an essential issue for increasing the capacity and improving the coverage of cellular communication systems. This work presents an algorithm to calculate total diffraction losses for multiple obstacles objects using Epstein–Peterson approach. The proposed algorithmic procedure to model the diffracting can be integrated with other propagation mechanisms in ray-tracing for the prediction of received signal level in non-line-of-sight environments. This algorithm can be interpreted into software application to scan large areas with a reasonable simulation time.

1. Introduction

With the rapid development of networks and wireless communication, there is an increasing need for reliable point-to-area prediction tools in the planning of radio communication services. These prediction tools must include the characteristics of the particular zone in which the system is intended to be used [1]. The wireless network sites/cells/access points are distributed based on the traffic and path loss and usually it appears like the one shown in Figure 1.

Propagation mechanisms may generally be attributed to reflection, diffraction, and scattering. Diffraction and scattering occur when the obstructing object is large compared to the wavelength of the radio wave. Diffraction allows radio signals to propagate around the curved surface of the earth, beyond the horizon, and behind obstructions. A complex environment with obstacles may attenuate the electromagnetic waves. If the obstacle will diffract the wave over or around the obstruction, there will be high attenuation through the obstacle [2]. Determination of the diffraction losses with a minimum acceptable error is very challenging for realistic propagation environments such as mountainous regions, so that system design requires a set of statistics that describes the expected performance of a propagation path. Propagation models are employed to provide the required

statistics. A propagation model can be a set of mathematical expressions, diagrams, and/or algorithms used to represent the radio characteristics for a given environment. The path-loss prediction models can be roughly divided into three types, empirical, theoretical, and site-specific [3].

An empirical model is usually a set of equations derived from extensive field measurements. The main advantage of empirical models is their simplicity and computational efficiency. The model accuracy depends on the measurement accuracy and the similarity between the environments where the measurements and predictions are taking place [4]. The input parameters for the empirical models are usually qualitative and not very specific, for example, a dense urban area and a rural area. One of the main drawbacks of empirical models is that they cannot be used for different environments without modification [5].

A theoretical model is based on the principals of physics and may therefore be applied to different environments without affecting the output. The main drawbacks of theoretical models are the wide range error, which is impractical to base networks design and optimization on such models.

A site-specific model is based on numerical methods such as the ray-tracing method and the finite-difference time-domain (FDTD) method. The input parameters can be very detailed. Ray-tracing is a method that uses a geometric

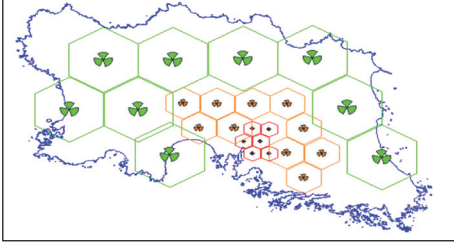


FIGURE 1: Example of cellular network plan.

approach and examines what paths the wireless radio signal takes from transmitter to receiver as if each path was a ray of light (possibly reflecting from the surfaces) as shown in Figure 2 [6]. Ray-tracing predictions are good when detailed information of the area is available, but the predicted results may not be applicable to other locations, thus making these models site-specific. The disadvantages of site-specific models are the large computational overhead that may be prohibitive for some complex environments as stated in [7, 8].

The ray-tracing accuracy and overhead computation is largely dependent on the method of diffraction loss calculation. There are many methods for diffraction calculation purpose; each differs in complexity and accuracy. The most used methods are the Bullington [9], Deygout [10], and Epstein–Peterson [11]. These methods are not presented in algorithmic form that is suitable for software integration; thus it is hard to find diffraction loss for large areas using these methods.

This work focuses on the diffraction loss calculation for multiple obstacles and presents an algorithm for the process of calculation that can be interpreted into software application for coverage prediction tools.

2. Diffraction

Diffraction is the propagation of wave behind obstacle even when the line-of-sight (LOS) is not clear (non-line-of-sight (NLOS)) as shown in Figure 3. Due to diffraction, coverage still presented even when the RF signal is obstructed. The physical and the mathematical explanation of this phenomenon are detailed in [12].

In order to get good result for prediction, the RF diffraction should be taken into consideration. Since coverage will extend behind obstacles (cell size increased), signal level estimation will increase at many points in certain geographical areas. Also the quality of signal at the mobile station will be impacted if it is getting power from cells other than the serving cell (due to coverage extension of the other cells due to diffraction). Capacity will be impacted as well due to this coverage extension as it will serve a larger geographical area and hence more mobile stations under the same serving cell.

The diffraction is dealt with as a kind of loss, usually measured in dB. This amount of loss is directly subtracted from total signal power.

Diffraction loss (DL) is calculated as follows by approximating the shape of obstruction object to knife edge [13]:

$$\nu = h \sqrt{\frac{2(d_1 + d_2)}{\lambda d_1 d_2}}. \quad (1)$$

If $\nu \leq -1$

$$DL = 0. \quad (2)$$

If $-1 < \nu \leq 0$

$$DL = 20 * \log_{10} (0.5 - 0.62 * \nu). \quad (3)$$

If $0 < \nu \leq 1$

$$DL = 20 * \log_{10} (0.5 * e^{-0.95 * \nu}). \quad (4)$$

If $1 < \nu \leq 2.4$

$$DL = 20 * \log_{10} \left(0.4 - \sqrt{0.1184 - (-0.1 * \nu + 0.38)^2} \right). \quad (5)$$

If $2.4 < \nu$

$$DL = 20 * \log_{10} \left(\frac{0.225}{\nu} \right). \quad (6)$$

ν is the diffraction parameter. h is the obstacle height in meters. d_1 is the distance between cell and obstacle in meters. d_2 is the distance between mobile and obstacle in meters. λ is the signal wavelength in meters.

These parameters are medicated in Figure 3.

3. Multiple Obstacles Diffraction

Usually, when the signal propagates from transmitter to receiver it exhibits from zero to n multiple obstacles. Each obstacle will cause diffraction and the received signal level is governed by the net diffracting losses plus other propagation mechanisms effects. Calculation of multiple objects diffraction losses is subjected to many models under the Uniform Theory of Diffraction (UTD). Each model differs in complexity and accuracy that varies from one propagation environment to another. The most famous models are Bullington, Deygout, and Epstein–Peterson.

The Epstein–Peterson [11] is a diffraction model that considers all the obstruction objects. It produces acceptable error, but the error increases when the obstruction objects are closely spaced. Even though Epstein–Peterson model produces less error than Bullington model, it is systematic compared to Deygout model as stated in [3, 14].

The Epstein–Peterson model regards the first obstruction object as new signal source. The next step is to consider the next obstruction object (between the new source and the receiver) as the new source. Every time move one step to the next obstruction object and redo these steps till there is no more obstruction object left. The net diffraction loss is the sum of diffraction lost per each step.

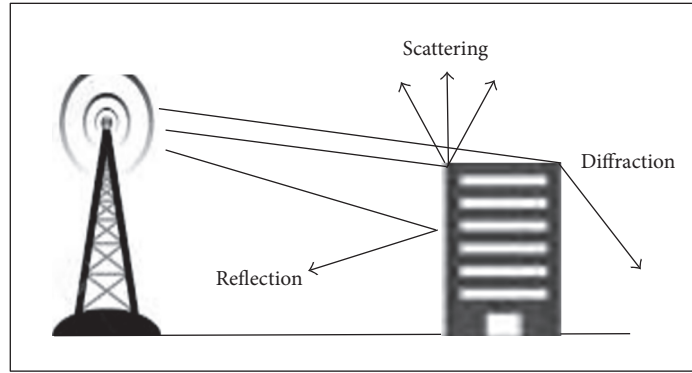


FIGURE 2: Propagation mechanisms in ray-tracing.

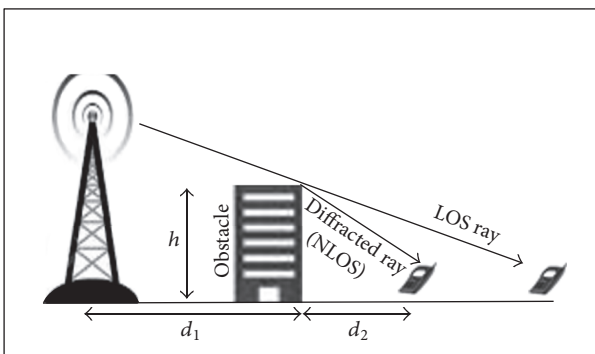


FIGURE 3: Diffraction of rays when line-of-sight is obstructed.

4. Multiple Obstacles Diffraction Losses Calculation Algorithm

As stated in the previous section, the Epstein–Peterson approach is systematic with acceptable error (unless obstruction obstacles are closely spaced). In this work, an algorithm for calculating the total diffraction losses based on Epstein–Peterson approach for a defined geographical area is proposed. The steps of the algorithm are shown in Figure 4.

The following is the summary of the algorithm’s variables in the flow chart with definitions.

DB is the cellular network data base.

cell $_h$ is the specified cell height (antenna height above the ground plus the elevation on 3D map) (in meters).

I and J are the geographical square dimensions (unitless integers).

ms $_h$ is an I by J matrix which represents the mobile height at 3D map (average mobile height plus the elevation on 3D map) (in meters).

$i, j, k,$ and m are counters.

ms(i, j) is the mobile located in i th and j th point on 3D map.

PP(i, j) is the path profile between cell and ms(i, j) (unitless).

K is number of objects (hills, building, houses, trees, and etc.) in PP(i, j) (unitless integers).

M is the number of obstacles in PP(i, j).

h_{ec} is the increase in object height due to earth curvature (in meter).

Obj_loc(k) is the k th object location in PP(i, j) (in meters).

Obj_h is the k th object height in PP(i, j) (in meters).

$A, B, C, D, E,$ and F are temporary variables.

Obst_loc(m) is the m th obstacle location in PP(i, j) (in meters).

Obst_h(m) is the m th obstacle height in PP(i, j) (in meters).

Obst_DL(m) is the diffraction losses resulting from the m th obstacle (in dB).

ms_DL(i, j) is the total diffraction losses experienced by ms(i, j) (in dB).

The following are the footnotes in the flowchart:

(1) Load cellular network data base (DB).

(2) Load the 3D map zone over which the processing will be implemented. The 3D maps are segmented in order to reduce amount of computations by excluding unnecessary areas.

(3) Get geographic square from 3D Map with dimensions equal to max technology coverage multiplied by 2 and have center at the same cell location. This setup will reduce the computation further by excluding the areas which cannot be served by a cell due to technology limitation. For example, GSM technology has max cell radius of 32 Km; thus it is not required to calculate the diffraction loss outside this radius.

(4) Set I and J to be equal to the dimensions of the geographic square dimensions obtained from the previous step.

(5) Extract path profile (PP(i, j)) between cell and ms(i, j) from the 3D map.

(6) Mountains, hills, buildings, tress, and others are objects that may or may not obstruct the LOS.

(7) Object location and object dimension are found from PP(i, j) stored in Obj_loc(k) and Obj_h(k), respectively.

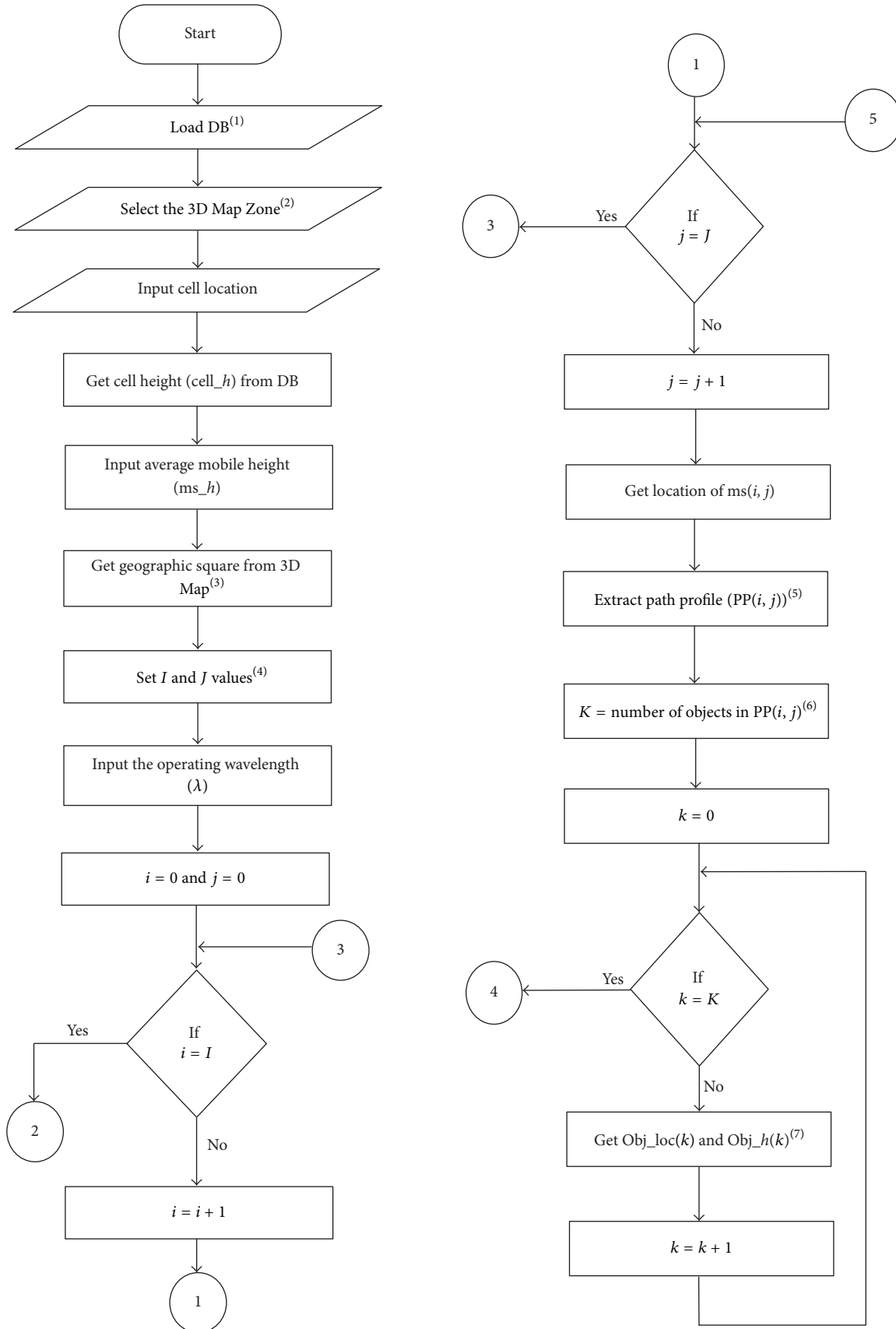


FIGURE 4: Continued.

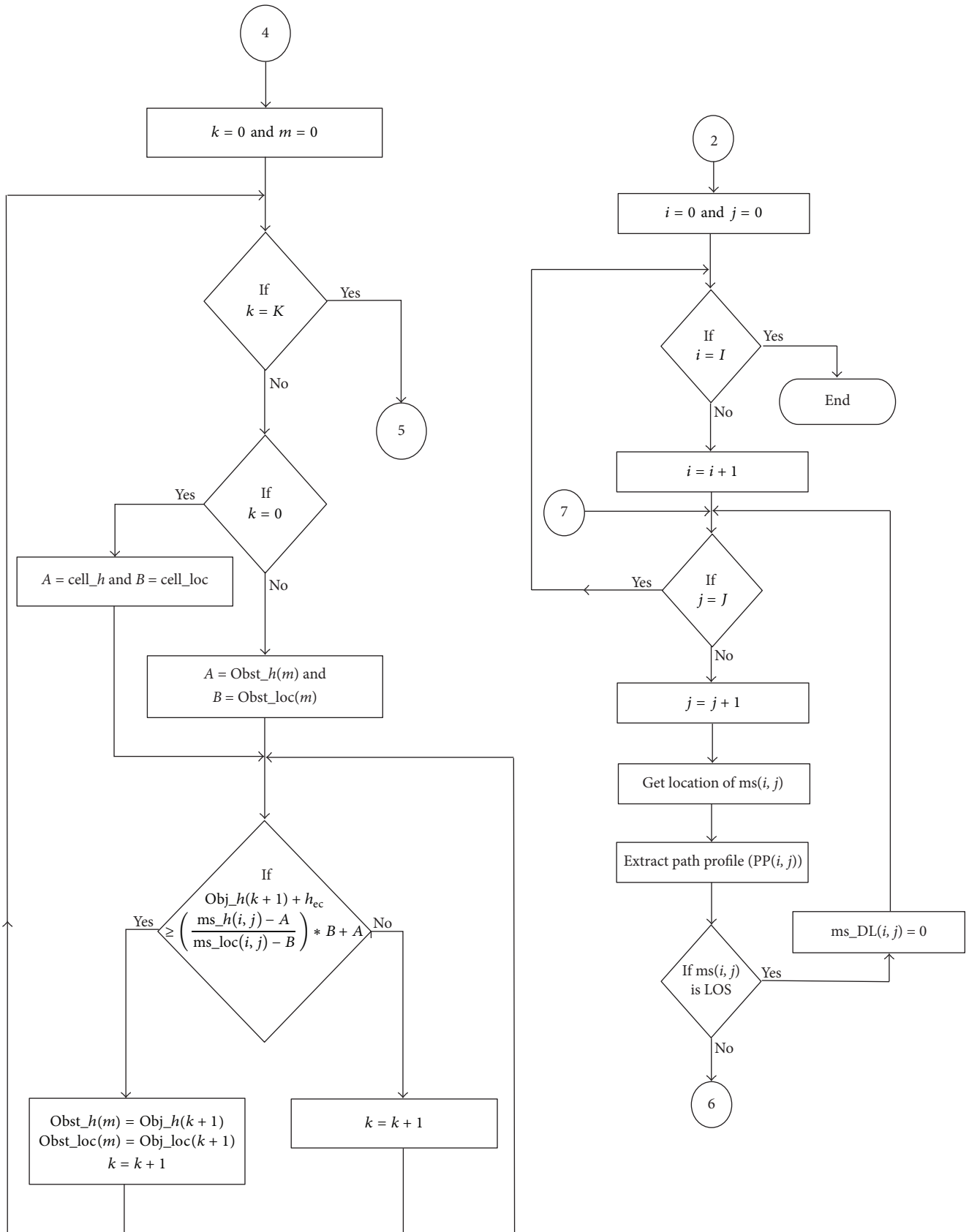


FIGURE 4: Continued.

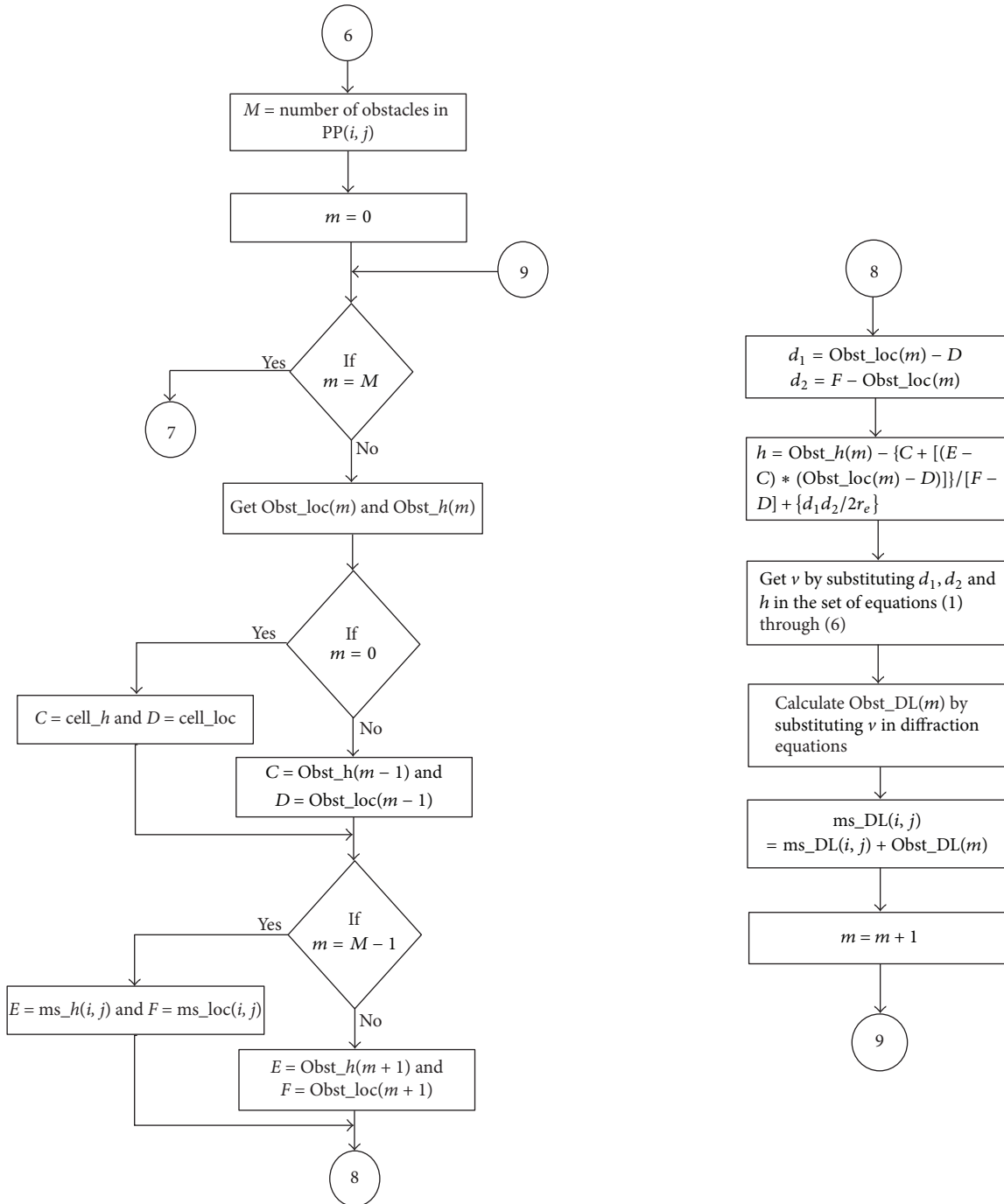


FIGURE 4: Multiple obstacles diffraction losses calculation algorithm flow chart.

5. Practical Implementation of Methodology

In order to validate the proposed diffraction loss calculation methodology, a comparison needs to be made between simulation and practical measurement. It is well known that the diffraction of RF signal cannot be measured directly since it is combined with other propagation mechanisms that contribute to RF signal level through the interaction with propagation environment's elements.

In this work, all the propagation mechanisms (including the diffraction loss) will be simulated under ray-tracing propagation model. The simulated signal level resulting from this model will be used for the comparison with the measured signal level using Root Mean Square Error (RMSE). This comparison will be used to validate the proposed methodology. The RMSE will give an indication of the diffraction mechanism simulation accuracy if other propagation mechanisms are simulated with minimum possible error.

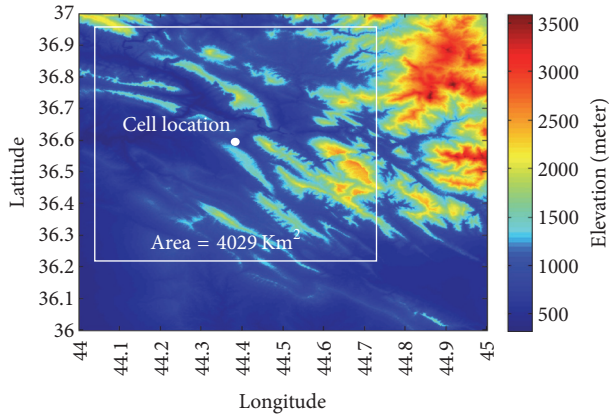


FIGURE 5: Map for the methodology test.

The ray-tracing model was used to simulate signal propagation from GSM cell using the following data:

- (i) Geographical zone is between latitude 36° - 37° and longitude 44° - 45° with an area of 10019 Km^2 . This zone is mountains shown in Figure 5.
- (ii) The foliage density is low.
- (iii) GSM cell is located at latitude 36.6001° and longitude 44.3973° .
- (iv) Operating frequency is within 900 Mhz band (0.33 m wavelength).
- (v) Mobil station sensitivity is -102 dBm (GSM standard).
- (vi) The transmitted pilot signal power is 15 W (41.7 dBm).
- (vii) The used antenna model is Tongyu 182018DE-65P with max gain of 17.8 dBi and horizontal beamwidth of 63° and vertical beamwidth of 7.5° . The provided radiation pattern data is 1° resolution.
- (viii) The antenna physical parameters are 0° mechanical tilt, 1° electrical, and 40° azimuth.
- (ix) Cell antenna height is 39 m height above ground.
- (x) The average mobile station height is 0.5 meter (assuming that the mobile is in user pocket sitting in car).
- (xi) 3D map in DEM format with 90 m resolution.
- (xii) The ray-tracing was simulated using the MATLAB software package.

The diffraction loss calculation will be applied on a part of the 10019 Km^2 area, and the selection is done autonomously by the algorithm based on cell location and the max radius the technology can cover. For example, in GSM, the max cell radius is 32 Km; thus the area on which the simulation is applied is $32 * 2$ by $32 * 2 \text{ Km}^2$ (4029 Km^2 out of 10019 Km^2). This will contribute in a great reduction in simulation time and processing as many points on the 3D map are excluded as operating technology cannot serve.

The signal level measurements were performed on the road intersected with the prediction map. The measurements

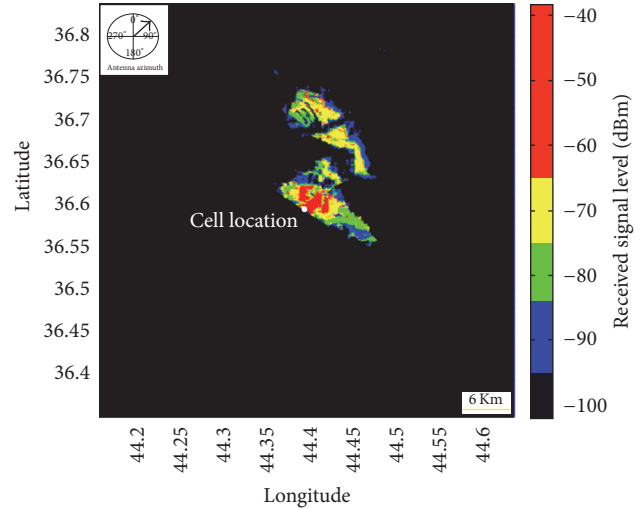


FIGURE 6: Measurement route (pink path) overlaid on prediction map.

were implemented with the mobile station forced-camping on the same cell. Handovers or cell reselections were not allowed; thus the measurement continued on the same cell till there is no more coverage. The resulting measurement route is shown in Figure 6 in the pink route overlaid on the prediction map. The measurement route length is 5.8 Km. A GPS device was connected to capture the coordinates at every measurement in order to compare it with the corresponding predicted value.

It should be noted here that the diffraction losses are not required to be calculated every time for cellular networks optimization process. For example, antenna azimuth, tilt, or pilot signal power changes do not imply to calculate the diffraction losses rather than other propagation mechanisms. Also, if a network site has more than one cell (which is usually the case) and these cells' antennas are at the same height, it is enough to do the diffraction calculation for one cell only and assume that it is the same for the other cells.

6. Results and Discussions

The diffraction loss map obtained using the proposed algorithm is shown in Figure 7 presented in thematic view; each color represents a certain loss value. The diffraction loss data in Figure 7 is one of propagation mechanisms that are required to obtain the prediction map shown in Figure 6.

In order to examine the result, the measured and predicted received signal level need to be compared. Figure 8 shows the measured and predicted received signal level versus distance. The RMSE of the measured and predicted values versus distance is shown in Figure 9. The overall RMSE is 5.34 dB with error ranging from 0.0014 dB to 21.56 dB.

In RF signal propagation, there are two cases for path description for between transmitter and receiver, LOS case and NLOS case. For the NLOS case, the diffraction is the main propagation mechanism that allows RF signal to be intercepted by the receiver. Accordingly, the RMSE will be filtered more.

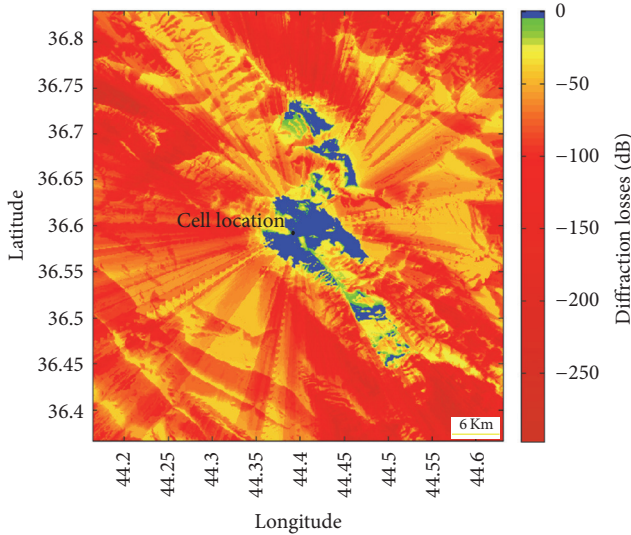


FIGURE 7: Diffraction loss thematic map view (area = 4029 Km²).

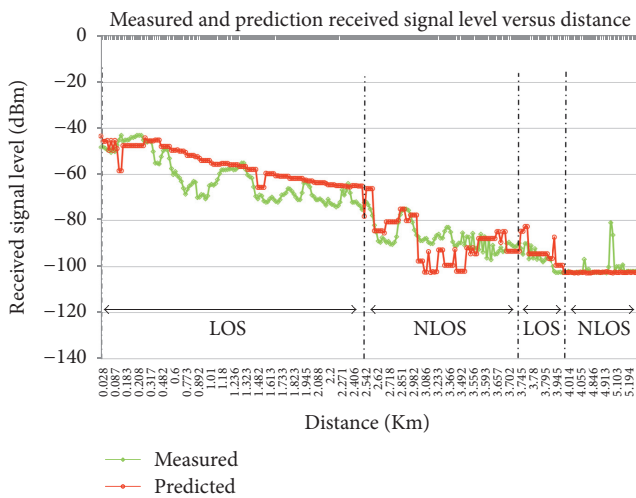


FIGURE 8: Measured and predicted signal level versus distance.

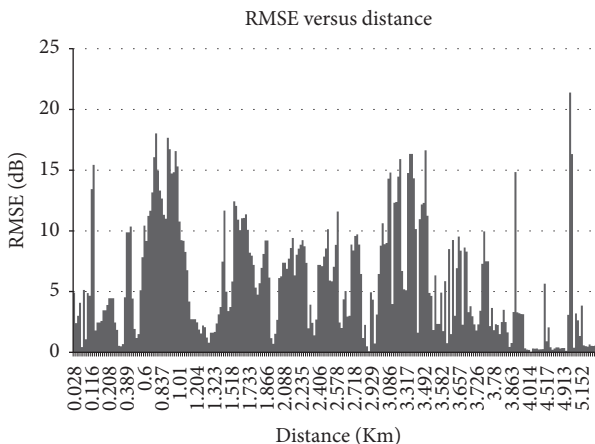


FIGURE 9: Measurement and prediction of RMSE versus distance.

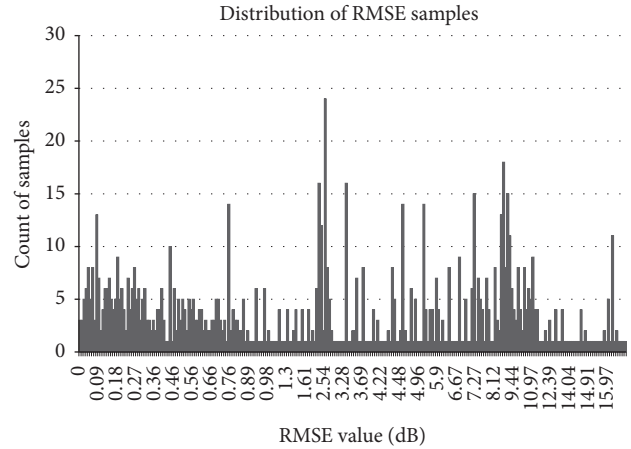


FIGURE 10: RMSE samples distribution for NLOS cases.

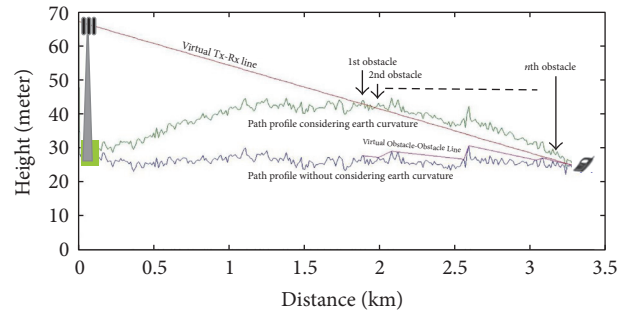


FIGURE 11: Path profile and earth curvature effect.

The RMSE samples distribution is shown in Figure 10. The overall RMSE for NLOS cases is 4.37 dB with error ranging from 0.0014 dB to 21.56 dB. Even though the max error is 21.56 dB, the count of these samples is very less.

It can be noted from Figure 7 that the diffraction losses increase as the distance in the radial direction increases. This effect is due to earth curvature and the possibility of increasing the number of obstruction obstacles as shown in Figure 11.

It was found that same number of obstacles does not give same diffraction loss as shown in Figure 12. This is due to the fact that for a specific number of obstacles there are many possibilities of arrangements (i.e., location of obstacles with respect to each other). The arrangement is parametrized by h , d_1 , and d_2 in (1). This will result in different v values and thus different diffraction loss for the same number of obstacles.

The required simulation time per area of 4029 Km² is 122 minute on PC with core i5 and 8 GB RAM. There is no need to repeat the simulation for a life cellular network optimization purpose.

7. Conclusions

By considering the NLOS cases only, the signal propagation modeling using ray-tracing resulted in RMSE of 4.37 dB. This RMSE is attributed to proposed diffraction loss calculation

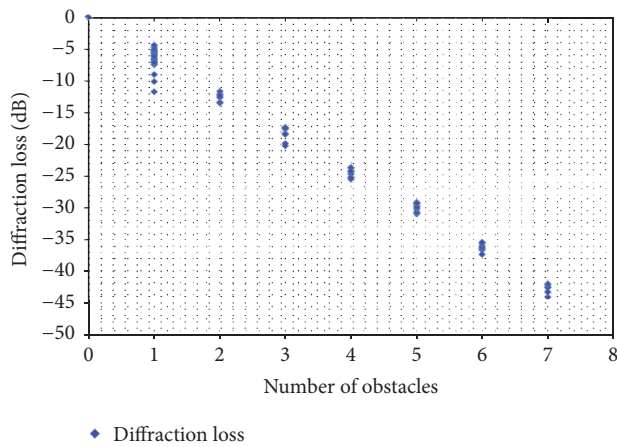


FIGURE 12: Diffraction losses versus number of obstacles.

algorithm and other propagation mechanisms calculation. For RF signal propagation prediction, this error value is acceptable. Thus it can be concluded that the performance of proposed procedure is acceptable.

The structure and systematic property of the algorithm make it very appropriate for software integration. Due to the acceptable error value and the ability of algorithm to cover very wide areas, the inclusion of diffraction mechanism modeling with other propagation mechanisms to do coverage prediction will allow the RF network designers to evaluate the network and enhance coverage, quality, and capacity without the need for costly and extensive drive tests.

Also, it was shown that the diffraction loss and number obstacles are not linearly proportional. The same number of obstacles can result in different diffraction loss due to different arrangement of obstacles. The arrangement of obstacles is parametrized by h , d_1 , and d_2 .

Also, it was seen that the effect of earth curvature has huge impact on diffraction loss if it considered. This is very important fact that should be considered in wireless network design to avoid coverage problems.

It is enough to find the diffraction loss map one time per site with many cells as long as these cells are at the same height. Also, in case of pilot signal power change, antenna tilt, or azimuth change, the diffraction map still valid. Thus the 122 min simulation time will not be required every time.

Conflicts of Interest

The authors declare that they have no conflicts of interest.

References

- [1] K. Paran and N. Noori, "Tuning of the propagation model ITU-R P.1546 recommendation," *Progress in Electromagnetics Research B*, vol. 8, pp. 243–255, 2008.
- [2] R. K. Crane, *Propagation Handbook for Wireless Communication System Design*, CRC Press LLC, 2003.
- [3] D. A. Bibb, J. Dang, Z. Yun, and M. F. Iskander, "Computational accuracy and speed of some knife-edge diffraction models,"

in *Proceedings of the IEEE Antennas and Propagation Society International Symposium*, July 2014.

- [4] E. Ostlin, *On radio wave propagation measurements and modelling for cellular mobile radio networks [Doctoral Dissertation]*, Blekinge Institute of Technology, 2009.
- [5] M. F. Iskander and Z. Yun, "Propagation prediction models for wireless communication systems," *IEEE Transactions on Microwave Theory and Techniques*, vol. 50, no. 3, pp. 662–673, 2002.
- [6] T. Rappaport, *Wireless Communications: Principles and Practice*, Prentice Hall, 2nd, 2001.
- [7] J. W. McKown and R. L. Hamilton, "Ray tracing as a design tool for radio networks," *IEEE Network*, vol. 5, no. 6, pp. 27–30, 1991.
- [8] T. Schwengler, *Wireless & Cellular Communications*, 2010.
- [9] K. Bullington, "Radio propagation at frequencies above 30 megacycles," *Proceedings of the IRE*, vol. 35, no. 10, pp. 1122–1136, 1947.
- [10] J. Deygout, "Multiple knife-edge diffraction of microwaves," *IEEE Transactions on Antennas and Propagation*, vol. 14, no. 4, pp. 480–489, 1966.
- [11] J. Epstein and D. W. Peterson, "An experimental study of wave propagation at 850 MC," *Proceedings of the IRE*, vol. 41, no. 5, pp. 595–611, 1953.
- [12] J. B. Keller, "Geometrical theory of diffraction," *Journal of the Optical Society of America*, vol. 52, pp. 116–130, 1962.
- [13] W. C. Y. Lee, *Mobile Cellular Telecommunications Systems*, McGraw-Hill Book Company, 1988.
- [14] H. R. Anderson, *Fixed Broadband Wireless System Design*, John Wiley & Sons, Chichester, UK, 2003.

Research Article

Full Wave Modeling of Array Structures Using Generalized Single-Source Tangential Equivalence Principle Algorithm

Hanru Shao,¹ Jianfeng Dong,¹ and Jun Hu²

¹Faculty of Electrical Engineering and Computer Science, Ningbo University, Ningbo 315211, China

²School of Electronic Engineering, University of Electronic Science and Technology of China, Chengdu 611731, China

Correspondence should be addressed to Hanru Shao; shaohanru@nbu.edu.cn

Received 28 April 2017; Accepted 28 June 2017; Published 6 August 2017

Academic Editor: Yumao Wu

Copyright © 2017 Hanru Shao et al. This is an open access article distributed under the Creative Commons Attribution License, which permits unrestricted use, distribution, and reproduction in any medium, provided the original work is properly cited.

The generalized single-source tangential equivalence principle algorithm (GSST-EPA) is proposed to solve the electromagnetic scattering of array structures with very small distance or even connected elements. For the traditional EPA scheme, it is difficult to deal with those situations. Based on source reconstruction method (SRM), the new GSST-EPA can be used to solve this problem efficiently. This scheme can also reduce the number of unknowns by half via the extinction theorem and keep the good accuracy by using tangential field projection. Furthermore, the multilevel fast multipole algorithm (MLFMA) is used to accelerate the matrix-vector multiplication in the GSST-EPA. Several numerical results are given to demonstrate the accuracy and efficiency of the proposed method.

1. Introduction

The array structure has a great range of applications in practical engineering, such as antenna arrays, metamaterials, and microwave absorber. As a kind of multiscale modeling, the array structure involving large number of elements and fine components has been the challenge for traditional full wave methods [1]. Therefore, more advanced numerical methods with better efficiency and robustness need to be developed.

In recent years, many efforts have been made to address the above problems. Particularly, the full wave integral equation (IE) solvers have attracted much attention due to high accuracy, relatively small matrices, and ability to be accelerated by fast algorithms. The progress in IE solvers for array structures can be divided into two categories: one is macro basis function methods focusing on reducing the number of unknowns, for instance, the sub-entire-domain (SED) basis function method [2], the characteristic basis function (CBF) method [3], and the synthetic basis function (SBF) approach [4]. These methods are similar to each other except the way of generating macro basis function. The other one is domain decomposition methods based on integral equations, including equivalence principle algorithm (EPA) [5–7], linear embedding via Green's operator (LEGO) [8], and generalized

transition matrix (GTM) [9]. The objectives of these methods are similar by using surface equivalence theorem to transform the unknowns on original objects onto the equivalence surfaces enclosing the objects.

The EPA has been used to solve some multiscale problems. Several efforts have also been made to improve the accuracy and extend the application range. For example, the high-order field point sampling scheme [7] and tangential EPA (T-EPA) [10] have been proposed to improve the accuracy of scattering operator. The efficiency of scattering operator has been improved by hierarchical LU decomposition method [11]. Furthermore, the low-frequency problem [12] and time-domain models [13] have been solved using EPA method. The EPA is also combined with BOR to solve large-scale problems [14].

In this paper, the EPA is implemented to solve large-scale array structures and some important improvements are made to achieve better numerical flexibility and efficiency. Firstly, the single-source EPA is used to reduce the number of unknowns by half via extinction theorem, in which only electric currents or magnetic currents on the equivalence surfaces need to be solved [15]. Secondly, the tangential field projection scheme is applied on equivalence surface to improve the accuracy of single-source EPA, which is

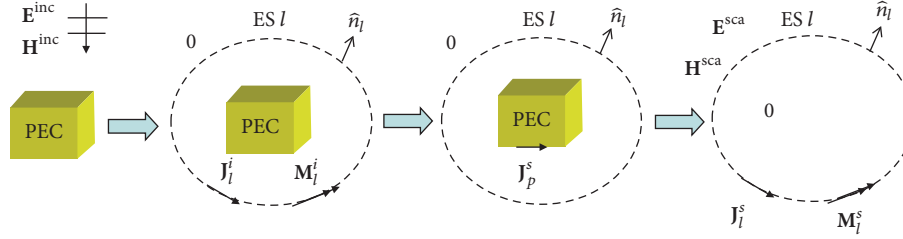


FIGURE 1: A PEC object characterized by equivalence surface with three steps.

called single-source tangential EPA (T-EPA) [16]. Thirdly, the source reconstruction method (SRM) is proposed to solve the case that connected structures intercepted by equivalence surfaces [17]. Using this scheme, the EPA equations are still well-conditioned and only equivalence surface currents are the final unknowns to be solved. Finally, the above three improvements are combined together as a new scheme named generalized single-source tangential EPA (GSST-EPA). The GSST-EPA is more efficient and robust than traditional EPA for solving complicated array problems. To improve the ability of solving large-scale array structures further, the multilevel fast multipole algorithm (MLFMA) [18] is applied to accelerate the translation procedure which is the coupling between nonadjacent equivalence surfaces. Numerical results are shown to validate the accuracy and efficiency of the new method.

2. Equivalence Principle Algorithm

The basic idea of EPA is to transform the original problems into a new equivalent problem with scattering operator and translation operator. The electromagnetic scattering of N nonconnected perfect electric conductor (PEC) objects in free space is considered to illustrate EPA. Each object is enclosed by an artificial equivalence surface $ES\ l$ ($l = 1, \dots, N$). The EPA scheme is based on the following two procedures: the scattering solution of objects via an equivalence surface and the couplings between objects via the equivalence surfaces, corresponding to the scattering operator and translation operator separately. Next, these two operators are defined in detail.

2.1. Scattering Operator. The first procedure can be derived from a PEC object characterized by equivalence surface with three steps as shown in Figure 1. The first step is outside-in propagation. The equivalence incident electric and magnetic currents on the equivalence surface can be obtained by using equivalence principle as follows:

$$\begin{aligned} \mathbf{J}_l^i &= -\hat{\mathbf{n}}_l \times \mathbf{H}^{\text{inc}}, \\ \mathbf{M}_l^i &= \hat{\mathbf{n}}_l \times \mathbf{E}^{\text{inc}}, \end{aligned} \quad (1)$$

where $\hat{\mathbf{n}}_l$ is the unit outer normal vector on the $ES\ l$. The currents \mathbf{J}_l^i and \mathbf{M}_l^i generate the original incident fields inside and zero field outside. Then the electric current on the PEC

can be solved using method of moments (MoM) which is the second step as

$$\eta_0 \mathcal{L}(\mathbf{J}_p^s) = [-\eta_0 \mathcal{L}_{pl} \quad \eta_0 \mathcal{K}_{pl}] \cdot \begin{bmatrix} \mathbf{J}_l^i \\ \frac{1}{\eta_0} \mathbf{M}_l^i \end{bmatrix}. \quad (2)$$

Here, \mathcal{L} and \mathcal{K} are the surface integral operators defined as

$$\begin{aligned} \mathcal{L}(\mathbf{r}, \mathbf{r}') \cdot \mathbf{X}(\mathbf{r}') &= ik \int_s \left[\mathbf{X}(\mathbf{r}') + \frac{1}{k^2} \nabla \nabla' \cdot \mathbf{X}(\mathbf{r}') \right] \\ &\quad \cdot \mathbf{G}_0(\mathbf{r}, \mathbf{r}') ds', \end{aligned} \quad (3)$$

$$\mathcal{K}(\mathbf{r}, \mathbf{r}') \cdot \mathbf{X}(\mathbf{r}') = \text{P.V.} \int_s \nabla G_0(\mathbf{r}, \mathbf{r}') \times \mathbf{X}(\mathbf{r}') ds',$$

where \mathbf{X} is \mathbf{J} or \mathbf{M} ; G_0 is Green's function in free space. η_0 is the wave impedance in free space. P.V. stands for the Cauchy principle value integration. The last step is inside-out propagation. Once the PEC current is solved, the scattering electric and magnetic currents can be computed using equivalence principle as

$$\begin{aligned} \begin{bmatrix} \mathcal{I}_{ll} & 0 \\ 0 & \mathcal{I}_{ll} \end{bmatrix} \cdot \begin{bmatrix} \mathbf{J}_l^s \\ \frac{1}{\eta_0} \mathbf{M}_l^s \end{bmatrix} &= \begin{bmatrix} \hat{\mathbf{n}}_l \times \mathbf{H}^{\text{sca}} \\ -\hat{\mathbf{n}}_l \times \mathbf{E}^{\text{sca}} \end{bmatrix} \\ &= \begin{bmatrix} \hat{\mathbf{n}}_l \times \mathcal{K}_{lp} \\ \mathcal{L}_{lp} \times \hat{\mathbf{n}}_l \end{bmatrix} \cdot [\mathbf{J}_p^s], \end{aligned} \quad (4)$$

where \mathcal{I} is identity operator. The currents \mathbf{J}_l^s and \mathbf{M}_l^s generate the original scattering fields outside and zero field inside. Combining these three steps, the scattering of a PEC object via an equivalence surface can be characterized by the scattering operator \mathcal{S}_{ll} as

$$\begin{aligned} [\mathbf{C}_l^s] &= \begin{bmatrix} \mathcal{I}_{ll} & 0 \\ 0 & \mathcal{I}_{ll} \end{bmatrix}^{-1} \cdot \begin{bmatrix} \hat{\mathbf{n}}_l \times \mathcal{K}_{lp} \\ \mathcal{L}_{lp} \times \hat{\mathbf{n}}_l \end{bmatrix} \cdot [\eta_0 \mathcal{L}_{pp}]^{-1} \\ &\quad \cdot [-\eta_0 \mathcal{L}_{pl} \quad \eta_0 \mathcal{K}_{pl}] \cdot [\mathbf{C}_l^i] = \mathcal{S}_{ll} \cdot [\mathbf{C}_l^i], \end{aligned} \quad (5)$$

where

$$[\mathbf{C}_l^{s/i}] = \begin{bmatrix} \mathbf{J}_l^{s/i} \\ \frac{1}{\eta_0} \mathbf{M}_l^{s/i} \end{bmatrix}. \quad (6)$$

It can be seen that the scattering operator can capture the full physics rigorously. Therefore, the unknowns on the inside object are transferred to the unknowns on the equivalence surface. Because the inside objects always have complex structures and different materials, the number of unknowns on the equivalence surface can be much less than that on the object.

2.2. Translation Operator. The second procedure can be illustrated by the scattering of two PEC objects as shown in Figure 2. The field scattered by \mathbf{J}_k^s and \mathbf{M}_k^s produces new fields on ES l . So these fields can be interpreted as the incident currents from the ES k to ES l and can be expressed by a translation operator \mathcal{T}_{lk} , $l \neq k$, as

$$[\mathbf{C}_{lk}^i] = \mathcal{T}_{lk} \cdot [\mathbf{C}_k^s], \quad (7)$$

where

$$\mathcal{T}_{lk} = \begin{bmatrix} \mathcal{F}_{ll} & 0 \\ 0 & \mathcal{F}_{ll} \end{bmatrix}^{-1} \cdot \begin{bmatrix} -\hat{n}_l \times \mathcal{K}_{lk} & -\hat{n}_l \times \mathcal{L}_{lk} \\ \eta_0 \hat{n}_l \times \mathcal{L}_{lk} & -\eta_0 \hat{n}_l \times \mathcal{K}_{lk} \end{bmatrix}. \quad (8)$$

Therefore, the scattered currents on ES l can be written as

$$[\mathbf{C}_l^s] = \mathcal{S}_{ll} \cdot [\mathbf{C}_l^i] + \mathcal{T}_{lk} \cdot [\mathbf{C}_k^s]. \quad (9)$$

For the generalized scattering of N nonadjacent PEC objects enclosed by N equivalence surfaces separately, the EPA equations can be written as

$$\begin{bmatrix} \mathcal{F} & -\mathcal{S}_{11}\mathcal{T}_{12} & \cdots & -\mathcal{S}_{11}\mathcal{T}_{1N} \\ -\mathcal{S}_{22}\mathcal{T}_{21} & \mathcal{F} & \cdots & -\mathcal{S}_{22}\mathcal{T}_{2N} \\ \vdots & \vdots & \ddots & \vdots \\ -\mathcal{S}_{NN}\mathcal{T}_{N1} & -\mathcal{S}_{NN}\mathcal{T}_{N2} & \cdots & \mathcal{F} \end{bmatrix} \cdot \begin{bmatrix} \mathbf{C}_1^s \\ \mathbf{C}_2^s \\ \vdots \\ \mathbf{C}_N^s \end{bmatrix} = \begin{bmatrix} \mathcal{S}_{11} \cdot \mathbf{C}_1^i \\ \mathcal{S}_{22} \cdot \mathbf{C}_2^i \\ \vdots \\ \mathcal{S}_{NN} \cdot \mathbf{C}_N^i \end{bmatrix}. \quad (10)$$

The matrix form can be obtained by expanding the currents with Rao–Wilton–Glisson (RWG) basis function and using Galerkin's method to discretize the equation [19]. If the array structures have the same element, then each element can be enclosed by the same equivalence surface which leads to the same scattering operator. Therefore, only one scattering operator needs to be solved and stored which can reduce the solving time significantly.

3. Single-Source Equivalence Principle Algorithm

The single-source EPA is similar to original EPA scheme which is based on the above two procedures. The difference is that the equivalence magnetic currents on ES l can be expressed by the equivalence electric currents on ES l in

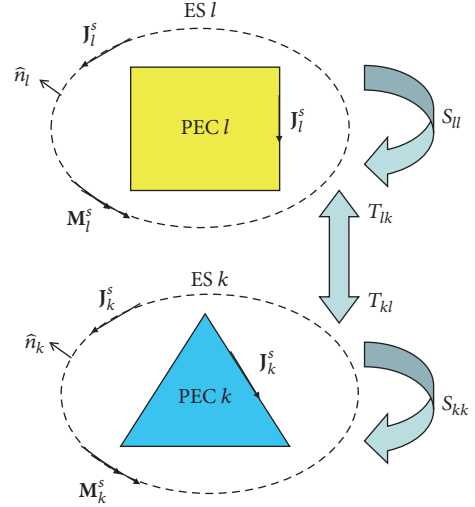


FIGURE 2: The interaction of two PEC objects using EPA scheme.

the single-source EPA. Therefore, only the electric currents on the equivalence surfaces are the final unknowns, which can reduce the number of unknowns by half compared with original EPA.

According to extinction theorem, the equivalence incident currents \mathbf{J}_l^i and \mathbf{M}_l^i generate zero field outside the ES l as shown in Figure 3(a):

$$\begin{aligned} \mathbf{E}^i &= \eta_0 \mathcal{L}_{ll}(\mathbf{J}_l^i) + \frac{1}{2} \mathcal{F}_{ll}^r(\mathbf{M}_l^i) - \mathcal{K}_{ll}(\mathbf{M}_l^i) = 0, & \text{on ES } l^+, \\ \mathbf{H}^i &= -\frac{1}{2} \mathcal{F}_{ll}^r(\mathbf{J}_l^i) + \mathcal{K}_{ll}(\mathbf{J}_l^i) + \frac{1}{\eta_0} \mathcal{L}_{ll}(\mathbf{M}_l^i) = 0, & \text{on ES } l^+, \end{aligned} \quad (11)$$

where ES l^+ denotes the outside surface of ES l . The integral operators \mathcal{L} , \mathcal{K} are defined as (3), and \mathcal{F}^r is defined as

$$\mathcal{F}^r(\mathbf{X}) = \hat{n} \times \mathbf{X}. \quad (12)$$

\mathbf{X} is equivalence incident or scattering surface current $\mathbf{J}^{i/s}$ or $\mathbf{M}^{i/s}$. Then the magnetic current can be expressed by electric current as

$$\frac{1}{\eta_0} \mathbf{M}_l^i = \left[-\frac{1}{2} \mathcal{F}_{ll}^r + \mathcal{K}_{ll} \right]^{-1} \cdot \mathcal{L}_{ll}(\mathbf{J}_l^i) = \mathcal{Z}_E^i(\mathbf{J}_l^i), \quad (13)$$

on ES l^+ ,

$$\frac{1}{\eta_0} \mathbf{M}_l^i = -[\mathcal{L}_{ll}]^{-1} \cdot \left[-\frac{1}{2} \mathcal{F}_{ll}^r + \mathcal{K}_{ll} \right](\mathbf{J}_l^i) = \mathcal{Z}_H^i(\mathbf{J}_l^i), \quad (14)$$

on ES l^+ .

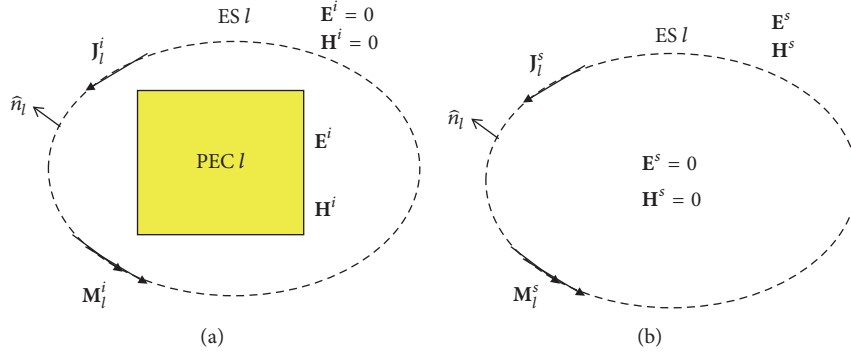


FIGURE 3: (a) Outside-in equivalence process. (b) Inside-out equivalence process.

Similarly, the relation between equivalence scattering currents \mathbf{J}_l^s and \mathbf{M}_l^s can be established via extinction theorem as shown in Figure 3(b):

$$\frac{1}{\eta_0} \mathbf{M}_l^s = \left[\frac{1}{2} \mathcal{L}_{ll}^r + \mathcal{K}_{ll} \right]^{-1} \cdot \mathcal{L}_{ll} (\mathbf{J}_l^s) = \mathcal{L}_E^s (\mathbf{J}_l^s), \quad (15)$$

on $ES l^-$,

$$\frac{1}{\eta_0} \mathbf{M}_l^s = -[\mathcal{L}_{ll}]^{-1} \cdot \left[\frac{1}{2} \mathcal{L}_{ll}^r + \mathcal{K}_{ll} \right] (\mathbf{J}_l^s) = \mathcal{L}_H^s (\mathbf{J}_l^s), \quad (16)$$

on $ES l^+$,

where $ES l^-$ denotes the inside surface of $ES l$. It can be seen that there are two types of expressions for the magnetic current and electric current, which are named as E -type and H -type. Therefore, the scattering operator of single-source EPA on $ES l$ also has two types and can be written as

$$\begin{aligned} \mathbf{J}_l^s &= [\mathcal{L}_{ll}]^{-1} \cdot [\hat{\mathbf{n}}_l \times \mathcal{K}_{lp}] \cdot [\eta_0 \mathcal{L}_{pp}]^{-1} \\ &\cdot [\eta_0 \mathcal{L}_{pl} \quad -\eta_0 \mathcal{K}_{pl}] \cdot \begin{bmatrix} 1 \\ \mathcal{L}_{E/H}^s \end{bmatrix} (\mathbf{J}_l^i) \\ &= \tilde{\mathcal{S}}_{ll}^{E/H} \cdot (\mathbf{J}_l^i). \end{aligned} \quad (17)$$

The definition of scattering operator on $ES k$ is similar to the above. The two types of translation operator from $ES k$ to $ES l$ are defined as

$$\tilde{\mathcal{T}}_{lk}^{E/H} = [\mathcal{L}_{ll}]^{-1} \cdot [-\hat{\mathbf{n}}_l \times \mathcal{K}_{lk} \quad -\hat{\mathbf{n}}_l \times \mathcal{L}_{lk}] \cdot \begin{bmatrix} 1 \\ \mathcal{L}_{E/H}^s \end{bmatrix}. \quad (18)$$

Finally, the single-source EPA equations have two types of expressions as follows:

$$\begin{bmatrix} \mathcal{F} & -\tilde{\mathcal{S}}_{11}^{E/H} \tilde{\mathcal{T}}_{12}^{E/H} & \cdots & -\tilde{\mathcal{S}}_{11}^{E/H} \tilde{\mathcal{T}}_{1N}^{E/H} \\ -\tilde{\mathcal{S}}_{22}^{E/H} \tilde{\mathcal{T}}_{21}^{E/H} & \mathcal{F} & \cdots & -\tilde{\mathcal{S}}_{22}^{E/H} \tilde{\mathcal{T}}_{2N}^{E/H} \\ \vdots & \vdots & \ddots & \vdots \\ -\tilde{\mathcal{S}}_{NN}^{E/H} \tilde{\mathcal{T}}_{N1}^{E/H} & -\tilde{\mathcal{S}}_{NN}^{E/H} \tilde{\mathcal{T}}_{N2}^{E/H} & \cdots & \mathcal{F} \end{bmatrix}$$

$$\begin{bmatrix} \mathbf{J}_1^s \\ \mathbf{J}_2^s \\ \vdots \\ \mathbf{J}_N^s \end{bmatrix} = \begin{bmatrix} \tilde{\mathcal{S}}_{11}^{E/H} \cdot \mathbf{J}_1^i \\ \tilde{\mathcal{S}}_{22}^{E/H} \cdot \mathbf{J}_2^i \\ \vdots \\ \tilde{\mathcal{S}}_{NN}^{E/H} \cdot \mathbf{J}_N^i \end{bmatrix}. \quad (19)$$

Once the electric currents have been solved, the magnetic currents can be obtained using (15) or (16).

4. Single-Source Tangential Equivalence Principle Algorithm

In the single-source EPA, the equivalence surface currents \mathbf{J} are the rotated tangential projections of the fields onto the surface as follows:

$$\mathcal{F} (\mathbf{J}^{s/i}) = \pm \hat{\mathbf{n}} \times \mathbf{H}^{s/i}, \quad (20)$$

where $\mathbf{H}^{s/i}$ is the known field. Therefore both scattering operator and translation operator have identity operator in (17) and (18). Numerical results have shown that the discretization of identity operator using conventional Galerkin's scheme and common divergence-conforming RWG function leads to large error in the field projection procedure [10]. So the accuracy of single-source EPA needs to be improved. In this paper, a different field projection scheme is adopted to improve the accuracy by using surface integral to represent the tangential fields. As shown in Figures 3(a) and 3(b), the equivalent currents are generated from the tangential field projection on the equivalence surface $ES l$ by using Huygens equivalence principle as follows:

$$\eta_0 \mathcal{L}_{ll} (\mathbf{J}_l^i) - \frac{1}{2} \mathcal{L}_{ll}^r (\mathbf{M}_l^i) - \mathcal{K}_{ll} (\mathbf{M}_l^i) = \mathbf{E}^i, \quad \text{on } ES l^-, \quad (21)$$

$$\frac{1}{2} \mathcal{L}_{ll}^r (\mathbf{J}_l^i) + \mathcal{K}_{ll} (\mathbf{J}_l^i) + \frac{1}{\eta_0} \mathcal{L}_{ll} (\mathbf{M}_l^i) = \mathbf{H}^i, \quad (22)$$

on $ES l^+$,

$$\eta_0 \mathcal{L}_{ll}(\mathbf{J}_l^s) + \frac{1}{2} \mathcal{S}_{ll}^r(\mathbf{M}_l^s) - \mathcal{K}_{ll}(\mathbf{M}_l^s) = \mathbf{E}^s, \quad (23)$$

on ES l^+ ,

$$-\frac{1}{2} \mathcal{S}_{ll}^r(\mathbf{J}_l^s) + \mathcal{K}_{ll}(\mathbf{J}_l^s) + \frac{1}{\eta_0} \mathcal{L}_{ll}(\mathbf{M}_l^s) = \mathbf{H}^s, \quad \text{ES } l^+. \quad (24)$$

By submitting (13) and (14) into (21) and (22) and submitting (15) and (16) into (23) and (24), there are four types of expressions for the incident current \mathbf{J}_{ll}^i and scattering current \mathbf{J}_{ll}^s separately, which can be denoted as *TEE*, *TEH*, *THE*, and *THH*. Numerical results have shown that \mathcal{L}_H^i and \mathcal{L}_H^s are more accurate than \mathcal{L}_E^i and \mathcal{L}_E^s when using RWG function as basis and testing functions [15]. It also has been proved that the *THH* type is the same as single-source EPA [16]. Therefore, only the *TEH* is used in this paper.

The single-source tangential EPA (T-EPA) based on the *TEH* type can be derived by submitting (14) into (21) and (16) into (23) as follows:

$$\begin{aligned} \eta_0 \mathcal{L}_{ll}(\mathbf{J}_l^i) - \frac{1}{2} \eta_0 \mathcal{S}_{ll}^r \cdot \mathcal{L}_H^i(\mathbf{J}_l^i) - \eta_0 \mathcal{K}_{ll} \cdot \mathcal{L}_H^i(\mathbf{J}_l^i) \\ = \mathcal{L}_{TEH}^i(\mathbf{J}_l^i) = \mathbf{E}^i, \quad \text{on ES } l^-, \end{aligned} \quad (25)$$

$$\begin{aligned} \eta_0 \mathcal{L}_{ll}(\mathbf{J}_l^s) + \frac{1}{2} \eta_0 \mathcal{S}_{ll}^r \cdot \mathcal{L}_H^s(\mathbf{J}_l^s) - \eta_0 \mathcal{K}_{ll} \cdot \mathcal{L}_H^s(\mathbf{J}_l^s) \\ = \mathcal{L}_{TEH}^s(\mathbf{J}_l^s) = \mathbf{E}^s, \quad \text{on ES } l^+. \end{aligned} \quad (26)$$

Then the scattering operator of single-source T-EPA on ES l can be written as

$$\begin{aligned} \mathbf{J}_l^s = [\mathcal{L}_{TEH}^s]^{-1} \cdot [\eta_0 \mathcal{L}_{lp}] \cdot [\eta_0 \mathcal{L}_{pp}]^{-1} \\ \cdot [\eta_0 \mathcal{L}_{pl} - \eta_0 \mathcal{K}_{pl}] \cdot \begin{bmatrix} 1 \\ \mathcal{L}_H^i \end{bmatrix} \cdot \mathbf{J}_l^i = \tilde{\mathcal{S}}_{ll}^{TEH} \cdot \mathbf{J}_l^i \end{aligned} \quad (27)$$

and the translation operator should be changed as

$$\tilde{\mathcal{T}}_{lk}^{TEH} = [\mathcal{L}_{TEH}^i]^{-1} \cdot [\eta_0 \mathcal{L}_{lk} - \eta_0 \mathcal{K}_{lk}] \cdot \begin{bmatrix} 1 \\ \mathcal{L}_H^s \end{bmatrix}. \quad (28)$$

It can be seen that both of scattering operator and translation operator have the combination of \mathcal{L} and $\pm(1/2)\mathcal{S}^r + \mathcal{K}$ operators instead of using identity operator. So when using conventional Galerkin's scheme and RWG function to discretize the scattering and translation operators, this will lead to a more accuracy result [10]. Finally, the equations of single-source T-EPA are the same as (19) except for the expressions of scattering and translation operators.

5. The Single-Source Tangential Equivalence Principle Algorithm with Source Reconstruction Method (SRM)

In the practical engineering, the elements of array structures may be very close to each other. It is a challenge for EPA because the near fields between the equivalence surfaces

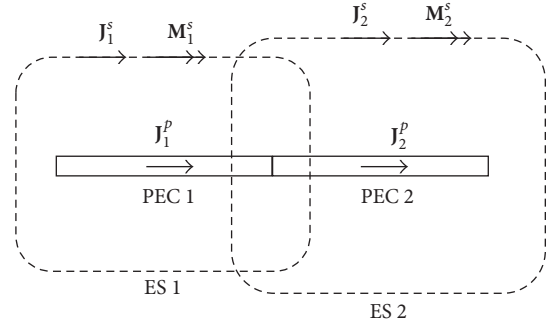


FIGURE 4: A PEC strip solved using source reconstruction method.

and objects are hard to calculate with high accurate. The other situation is that the elements are connected with each other, which can be solved with tap basis method. But this method needs to increase the number of unknowns and deteriorate the conditioning of EPA equations. In this paper, the source reconstruction method (SRM) is combined with single-source T-EPA to deal with the above two challenges. To illustrate this method, a scattering problem of a PEC strip is considered. The strip is divided into two parts as shown in Figure 4. The left part PEC 1 is enclosed by ES 1, and the right part PEC 2 is enclosed by ES 2. \mathbf{J}_1^p is the current on PEC 1; \mathbf{J}_2^p is the current on PEC 2. The MoM equations can be generated as

$$\eta_0 \mathcal{L}_{p_1 p_1} \mathbf{J}_1^p + \eta_0 \mathcal{L}_{p_1 p_2} \mathbf{J}_2^p = -\mathbf{E}_1^i, \quad (29)$$

$$\eta_0 \mathcal{L}_{p_2 p_2} \mathbf{J}_2^p + \eta_0 \mathcal{L}_{p_2 p_1} \mathbf{J}_1^p = -\mathbf{E}_2^i. \quad (30)$$

The equivalence scattering currents \mathbf{J}_1^s on ES 1 can be obtained through inside-out propagation:

$$\mathbf{J}_1^s = [\mathcal{L}_{TEH1}^s]^{-1} \cdot [\eta_0 \mathcal{L}_{s_1 p_1}] \cdot \mathbf{J}_1^p, \quad (31)$$

where the operator \mathcal{L}_{TEH1}^s has been defined in (26). Then substituting (29) into (31) yields

$$\begin{aligned} \mathbf{J}_1^s = [\mathcal{L}_{TEH1}^s]^{-1} \cdot [\eta_0 \mathcal{L}_{s_1 p_1}] \cdot [\eta_0 \mathcal{L}_{p_1 p_1}]^{-1} \\ \cdot (-[\eta_0 \mathcal{L}_{p_1 p_2}] \cdot \mathbf{J}_2^p - \mathbf{E}_1^i). \end{aligned} \quad (32)$$

\mathbf{E}_1^i is the incident plane wave on PEC 1 which is already known, while \mathbf{J}_2^p needs to be solved. Suppose that the equivalence scattering currents \mathbf{J}_2^s and \mathbf{M}_2^s on ES 2 are already known, then the \mathbf{J}_2^p can be got by using source reconstruction method [17] as follows:

$$\mathbf{J}_2^p = [\eta_0 \mathcal{L}_{s_2 p_2}]^+ \cdot [\mathcal{L}_{TEH2}^s] \cdot \mathbf{J}_2^s, \quad (33)$$

where $(\cdot)^+$ denotes the pseudoinverse. In this paper, the pseudoinverse is computed by truncated SVD method. \mathbf{E}_1^i can be replaced by equivalence incident currents as

$$\mathbf{E}_1^i = [\eta_0 \mathcal{L}_{p_1 s_1} - \eta_0 \mathcal{K}_{p_1 s_1}] \cdot \begin{bmatrix} 1 \\ \mathcal{L}_{H1}^i \end{bmatrix} \cdot \mathbf{J}_1^i. \quad (34)$$

Hence, substituting (33) and (34) into (32), we have

$$\mathbf{J}_1^s = \widetilde{\mathcal{F}}_{s_1 s_2}^{\text{SRM}} \cdot \mathbf{J}_2^s + \widetilde{\mathcal{S}}_{s_1 s_1}^{\text{TEH}} \cdot \mathbf{J}_1^i, \quad (35)$$

where

$$\begin{aligned} \widetilde{\mathcal{F}}_{s_1 s_2}^{\text{SRM}} &= [\mathcal{L}_{\text{TEH}1}^s]^{-1} \cdot [\eta_0 \mathcal{L}_{s_1 p_1}] \cdot [\eta_0 \mathcal{L}_{p_1 p_1}]^{-1} \\ &\cdot [-\eta_0 \mathcal{L}_{p_1 p_2}] \cdot [\eta_0 \mathcal{L}_{s_2 p_2}]^+ \cdot [\mathcal{L}_{\text{TEH}2}^s] \end{aligned} \quad (36)$$

and the definition of $\widetilde{\mathcal{S}}_{s_1 s_1}^{\text{TEH}}$ is the same as (17). Similarly, the equation for the equivalence scattering currents on ES 2 can be written as

$$\mathbf{J}_2^s = \widetilde{\mathcal{F}}_{s_2 s_1}^{\text{SRM}} \cdot \mathbf{J}_1^s + \widetilde{\mathcal{S}}_{s_2 s_2}^{\text{TEH}} \cdot \mathbf{J}_2^i. \quad (37)$$

Finally, the new EPA equations for connected structures can be obtained by combining (35) and (37):

$$\begin{bmatrix} \mathcal{F} & -\widetilde{\mathcal{F}}_{s_1 s_2}^{\text{SRM}} \\ -\widetilde{\mathcal{F}}_{s_2 s_1}^{\text{SRM}} & \mathcal{F} \end{bmatrix} \cdot \begin{bmatrix} \mathbf{J}_1^s \\ \mathbf{J}_2^s \end{bmatrix} = \begin{bmatrix} \widetilde{\mathcal{S}}_{s_1 s_1}^{\text{TEH}} \cdot \mathbf{J}_1^i \\ \widetilde{\mathcal{S}}_{s_2 s_2}^{\text{TEH}} \cdot \mathbf{J}_2^i \end{bmatrix}. \quad (38)$$

The coupling between PEC 1 and PEC 2 is calculated directly and there is no need to use buffer region. So the final unknowns are only equivalence surface currents by using the source reconstruction method. Equation (38) is simple and well-conditioned, which is similar to original EPA equation (10).

6. Generalized Single-Source Tangential Equivalence Principle Algorithm

By combing the above single-source EPA, tangential field projection, and source reconstruction method, the generalized single-source tangential equivalence principle algorithm (GSST-EPA) can be derived. Considering the scattering of N connected objects, each object is enclosed by an equivalence surface as shown in Figure 5. Then the GSST-EPA equation can be written as

$$\begin{aligned} &\begin{bmatrix} \mathcal{F} & -\mathcal{L}_{12} & \cdots & -\mathcal{L}_{1N} \\ -\mathcal{L}_{21} & \mathcal{F} & \cdots & -\mathcal{L}_{2N} \\ \vdots & \vdots & \ddots & \vdots \\ -\mathcal{L}_{N1} & -\mathcal{L}_{N2} & \cdots & \mathcal{F} \end{bmatrix} \cdot \begin{bmatrix} \mathbf{J}_1^s \\ \mathbf{J}_2^s \\ \vdots \\ \mathbf{J}_N^s \end{bmatrix} \\ &= \begin{bmatrix} \widetilde{\mathcal{S}}_{11}^{\text{TEH}} \cdot \mathbf{J}_1^i \\ \widetilde{\mathcal{S}}_{22}^{\text{TEH}} \cdot \mathbf{J}_2^i \\ \vdots \\ \widetilde{\mathcal{S}}_{NN}^{\text{TEH}} \cdot \mathbf{J}_N^i \end{bmatrix}, \end{aligned} \quad (39)$$

where

$$\mathcal{L}_{ij} = \begin{cases} \widetilde{\mathcal{S}}_{ii}^{\text{TEH}} \widetilde{\mathcal{F}}_{ij}^{\text{TEH}}, & \text{if } i \text{ and } j \text{ are non-adjacent,} \\ \widetilde{\mathcal{F}}_{ij}^{\text{SRM}}, & \text{if } i \text{ and } j \text{ are adjacent.} \end{cases} \quad (40)$$

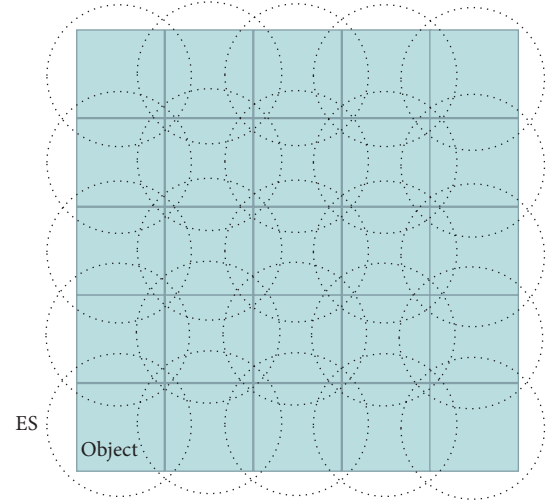


FIGURE 5: Each object is enclosed by an equivalence surface.

It should be pointed out that although the GSST-EPA can be used to solve generalized object, the GSST-EPA is much more suited for array structures because $\widetilde{\mathcal{S}}_{ii}^{\text{TEH}}$ is identical when the array element and equivalence surface are the same as each other. For the periodic array structures, $\widetilde{\mathcal{F}}_{ij}^{\text{TEH}}$ and $\widetilde{\mathcal{F}}_{ij}^{\text{SRM}}$ have the property of translation invariance which can be used to reduce the computing time and memory requirement. Therefore, the GSST-EPA is used to solve array structures in this paper.

To improve the ability of GSST-EPA to solve large-scale array structures, multilevel fast multipole algorithm (MLFMA) is applied in GSST-EPA. This is because the calculating of mutual coupling between two equivalence surfaces is divided into two cases: adjacent case and nonadjacent case; then the MLFMA in GSST-EPA is different from that in original EPA. Firstly, the adjacent case is the near interaction actually which is solved by SRM. So the matrix $[\widetilde{\mathcal{F}}_{ij}^{\text{SRM}}]$ is calculated directly and stored. Secondly, the nonadjacent case is the far interaction which is solved by translation operator. So the translation matrix $[\widetilde{\mathcal{F}}_{ij}^{\text{TEH}}]$ is implemented using MLFMA instead of MoM.

7. Numerical Results

In this part, several numerical examples are given to show the accuracy and efficiency of the GSST-EPA.

The first example is to demonstrate the accuracy of GSST-EPA. The scattering of two PEC spheres in free space is investigated. The radius of PEC sphere is 0.3 m. The distance between the centers of two spheres is 1.0 m in x -axis. Each sphere is enclosed by equivalence surface separately, which is a rectangle surface with $0.8 \times 0.8 \times 0.8 \text{ m}^3$ as shown in Figure 6. The excitation is a polarized plane wave propagating into the negative direction at 300 MHz. The curvilinear Rao-Wilton-Glisson (CRWG) function [19] is used to discretize the spheres and equivalence surfaces. This case is solved by three kinds of methods separately: MoM,

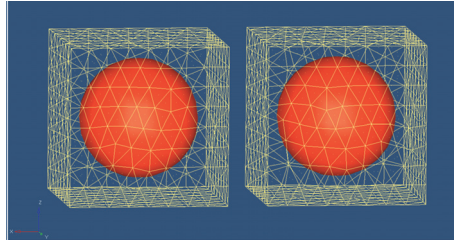


FIGURE 6: Two spheres are enclosed by two equivalence surfaces.

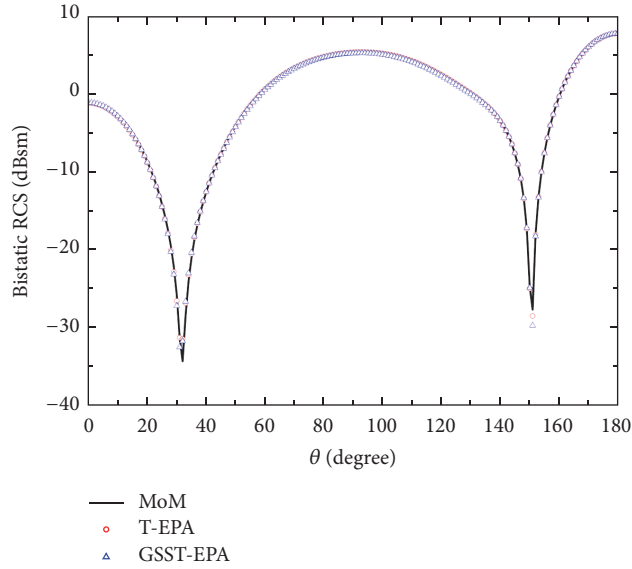


FIGURE 7: The bistatic RCS of two PEC spheres with center distance 1.0 m.

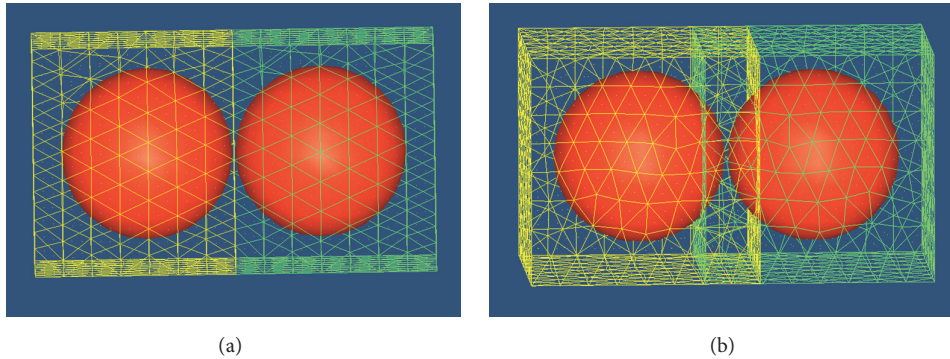


FIGURE 8: Two PEC spheres enclosed by two ES, (a) T-EPA scheme, and (b) GSST-EPA scheme.

T-EPA [10], and GSST-EPA. The bistatic Radar Cross Section (RCS) results for the HH polarization are shown in Figure 7. It can be seen that the results agree with each other very well.

In the second example, the scattering of two PEC spheres is still investigated but changing the center distance from 1.0 m to 0.605 m as shown in Figure 8. In this case, it is difficult for the T-EPA scheme [10] to solve this problem accurately, because these spheres are too close with each other as shown in Figure 8(a). Then the equivalence surfaces are very close to the spheres which makes the field hard to calculate with good

accurate. However, it is easy for the GSST-EPA to solve this case because the equivalence surfaces can intersect with each other as shown in Figure 8(b). In Figure 9, the bistatic RCS for the HH polarization of these two methods are compared with MoM. Obviously, the T-EPA result is incorrect while the GSST-EPA has good accuracy.

The third example shows a 5×5 sphere array solved by the new scheme. Each element is a dielectric-coated PEC sphere. The radius of PEC sphere is 0.2 m. The thickness of the dielectric coating is 0.1 m with $\epsilon_r = 2.2$, $\mu_r = 1.0$. The center

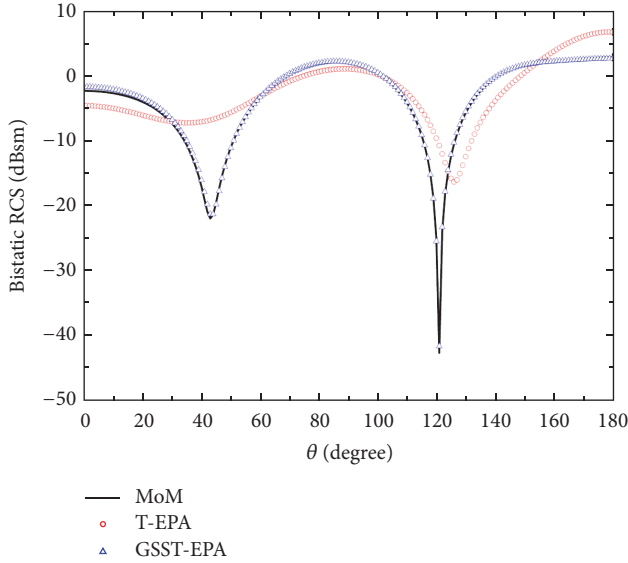


FIGURE 9: The bistatic RCS of two PEC spheres with center distance 0.605 m.

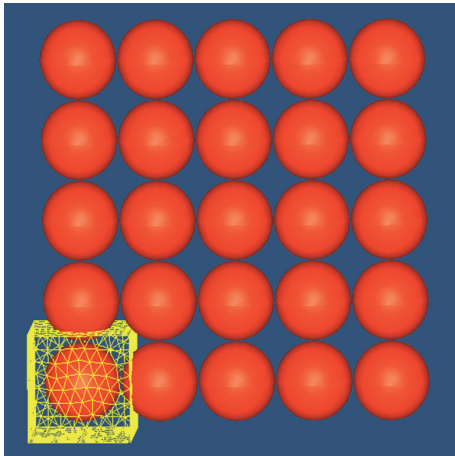


FIGURE 10: The model of a 5×5 sphere array.

distance between two spheres is 0.605 m in \hat{x} and \hat{y} directions. Each sphere is enclosed by an equivalence surface with $0.8 \times 0.8 \times 0.8 \text{ m}^3$ as shown in Figure 10. The excitation is a polarized plane wave propagating into the negative \hat{z} direction at 300 MHz. In the GSST-EPA, each sphere is solved by volume surface integral equation (VSIE), and MLFMA is also used to accelerate the solution [20]. The result of VSIE_MLFMA with block diagonal preconditioner (BDP) is given as the benchmark as shown in Figure 11. The computational results are shown in Table 1. Obviously, GSST-EPA is more efficient than VSIE_MLFMA for solving this array structure. It is necessary to mention that the memory requirement has not been reduced much although the number of unknowns has been reduced by about 60%. Because the equivalence surfaces can intersect with each other, couplings between the adjacent equivalence surfaces are calculated and stored directly. Only the coupling between the nonadjacent equivalence surfaces

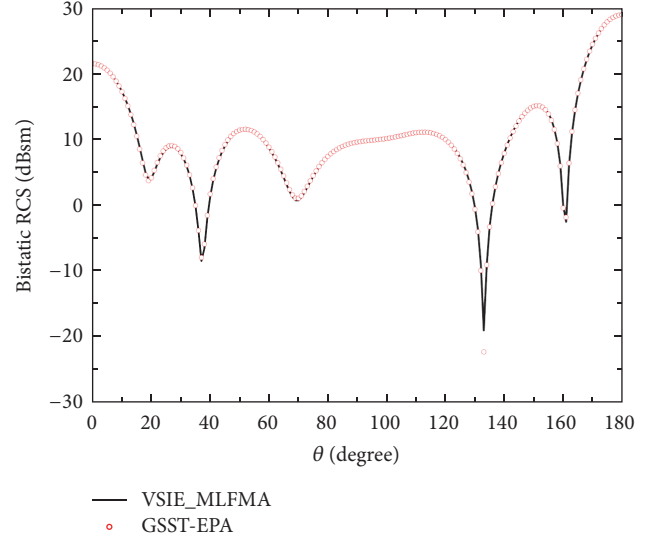


FIGURE 11: The bistatic RCS of a 5×5 sphere array; HH polarization at 300 MHz.

is calculated using MLFMA. Therefore the size of finest cube in MLFMA should be chosen twice as large as equivalence surface, which leads to the neighbor groups having a lot of unknowns.

Next, the scattering of a connected pyramid array is investigated. The dimension of a pyramid is shown in Figure 12(a) with $\epsilon_r = 2.0 - j0.04$, $\mu_r = 2.0 - j0.04$. Each pyramid is enclosed by the same rectangle equivalence surface with $9 \times 9 \times 17 \text{ cm}^3$. The distance between the centers of two elements is 7 cm which means that the elements connect with each other. The excitation is an \hat{x} polarized plane wave propagating into the negative \hat{z} direction at 1.0 GHz. The array elements are solved by VIE. The comparison of bistatic RCS for HH polarization is shown in Figure 13. It can be seen that these two methods agree with each other very well. The computational results are shown in Table 2. Compared with VIE_MLFMA, the total solution time has been reduced by more than 90% in the GSST-EPA.

Finally, to demonstrate the efficiency and capability of the proposed method, the scattering of 10×10 pyramid array is solved. The parameters of the array are the same as that in the above example, except for the number of elements. The total number of unknowns of the array elements is 105,900, while the number of unknowns on the equivalence surface is 23,400. The error converging to 0.001 only needs 6 iteration steps. The total memory requirement is 3.2 GB and total solution time is 2,501 s. If the VIE_MLFMA is used to solve the array structure, then the memory requirement is more than 16 GB. The result of bistatic RCS for the HH polarization is shown in Figure 14.

8. Conclusions

In this paper, a new scheme named GSST-EPA has been proposed to seek the scattering solution of array structures with very small distance or even connected array elements.

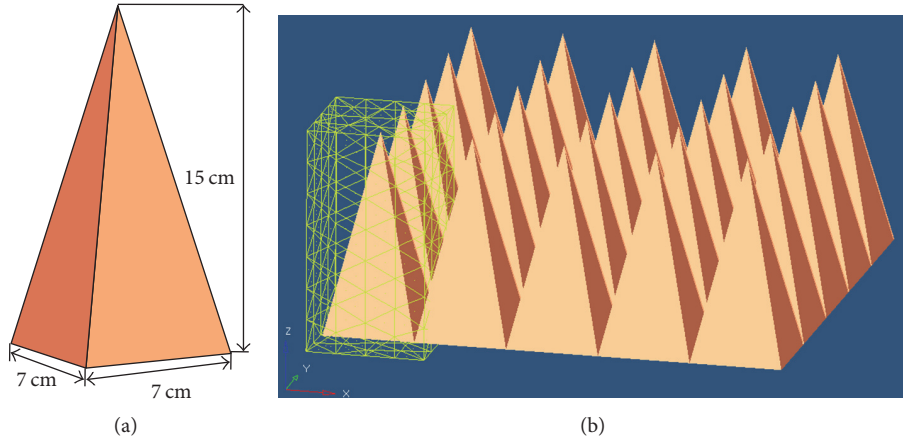


FIGURE 12: The model of pyramid array: (a) element; (b) 5×5 array and equivalence surface.

TABLE 1: The computational results of two methods.

Method	Unknowns	Memory (MB)	Iteration number (0.001)	Total time (s)
VSIE_MLFMA	47,314	2,220.6	251	4,442.4
GSST-EPA	13,050	1,888.3	22	2,421.3

TABLE 2: The comparison of computational results.

Method	Unknowns	Memory (MB)	Iteration number (0.001)	Total time (s)
VIE_MLFMA	27,121	3,285.7	11	8,112.7
GSST-EPA	5,850	422.5	5	575.9

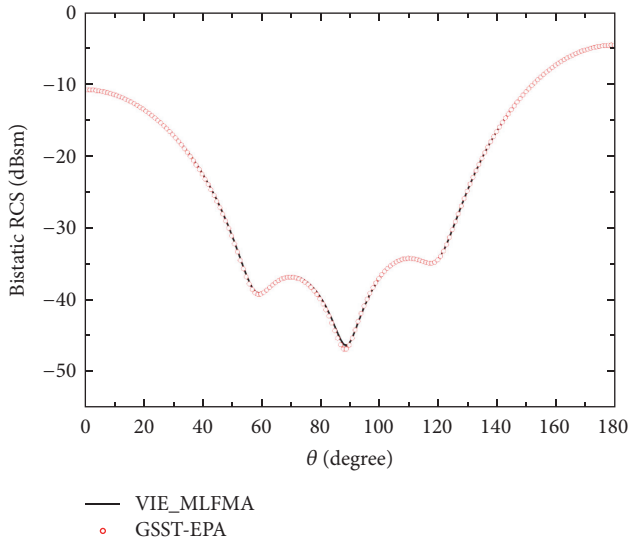


FIGURE 13: The bistatic RCS of 5×5 pyramid array; HH polarization at 1.0 GHz.

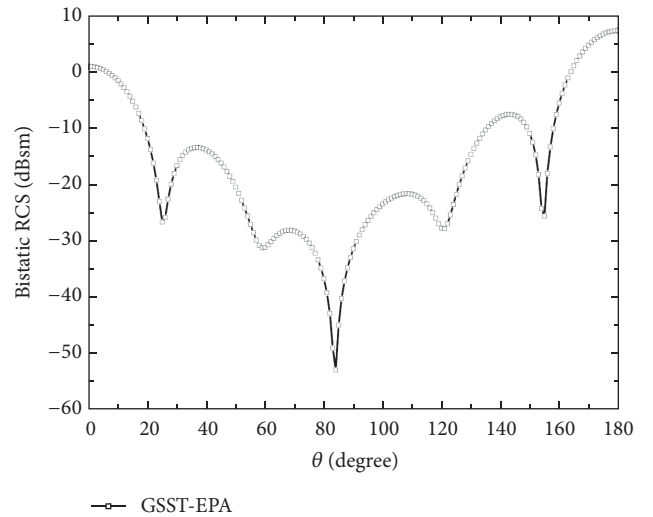


FIGURE 14: The bistatic RCS of 10×10 pyramid array; HH polarization at 1.0 GHz.

This scheme is based on the combination of single-source EPA, tangential field projection, and source reconstruction method. Compared with traditional EPA, this GSST-EPA can reduce the number of unknowns by half, improve the

accuracy, and solve the connected structures. The MLFMA is applied further to improve the ability of GSST-EPA to solve large array problems. Numerical results show that the proposed method can solve the connected structures efficiently.

Conflicts of Interest

The authors declare that there are no conflicts of interest regarding the publication of this paper.

Acknowledgments

This work is supported by National Natural Science Foundation of China (Grant no. 61501267, no. 61631012, no. 61671257, and no. 61425010), Zhejiang Provincial Natural Science Foundation of China (Grant no. LQ16F010003), and Ningbo University Discipline Project (Grant nos. XKLI4D2058 and XYL15008) and is partially sponsored by K. C. Wong Magna Fund in Ningbo University.

References

- [1] W. C. Chew and L. J. Jiang, "Overview of large-scale computing: The past, the present, and the future," *Proceedings of the IEEE*, vol. 101, no. 2, pp. 227–241, 2013.
- [2] W. B. Lu, T. J. Cui, Z. G. Qian, X. X. Yin, and W. Hong, "Accurate analysis of large-scale periodic structures using an efficient subentire-domain basis function method," *IEEE Transactions on Antennas and Propagation*, vol. 52, no. 11, pp. 3078–3085, 2004.
- [3] V. V. S. Prakash and R. Mittra, "Characteristic basis function method: a new technique for efficient solution of method of moments matrix equations," *Microwave and Optical Technology Letters*, vol. 36, no. 2, pp. 95–100, 2003.
- [4] L. Matekovits, V. A. Laza, and G. Vecchi, "Analysis of large complex structures with the synthetic-functions approach," *IEEE Transactions on Antennas and Propagation*, vol. 55, no. 9, pp. 2509–2521, 2007.
- [5] M.-K. Li, W. C. Chew, and L. J. Jiang, "A domain decomposition scheme based on equivalence theorem," *Microwave and Optical Technology Letters*, vol. 48, no. 9, pp. 1853–1857, 2006.
- [6] M. Li and W. C. Chew, "Wave-field interaction with complex structures using equivalence principle algorithm," *IEEE Transactions on Antennas and Propagation*, vol. 55, no. 1, pp. 130–138, 2007.
- [7] M.-K. Li and W. C. Chew, "Multiscale simulation of complex structures using equivalence principle algorithm with high-order field point sampling scheme," *Institute of Electrical and Electronics Engineers. Transactions on Antennas and Propagation*, vol. 56, no. 8, part 1, pp. 2389–2397, 2008.
- [8] A. M. Van De Water, B. P. De Hon, M. C. Van Beurden, A. G. Tijhuis, and P. De Maagt, "Linear embedding via Green's operators: A modeling technique for finite electromagnetic band-gap structures," *Physical Review E - Statistical, Nonlinear, and Soft Matter Physics*, vol. 72, no. 5, Article ID 056704, 2005.
- [9] S. Xiang, G. Xiao, X. Tian, and J. Mao, "Analysis of large-scale phased antenna array with generalized transition matrix," *IEEE Transactions on Antennas and Propagation*, vol. 61, no. 11, pp. 5456–5464, 2013.
- [10] P. Ylä-Oijala and M. Taskinen, "Electromagnetic scattering by large and complex structures with surface equivalence principle algorithm," *Waves in Random and Complex Media*, vol. 19, no. 1, pp. 105–125, 2009.
- [11] H. Shao, J. Hu, H. Guo, F. Ye, W. Lu, and Z. Nie, "Fast simulation of array structures using T-EPA with hierarchical LU decomposition," *IEEE Antennas and Wireless Propagation Letters*, vol. 11, pp. 1560–1563, 2012.
- [12] Z.-H. Ma, L. J. Jiang, and W. C. Chew, "Loop-tree free augmented equivalence principle algorithm for low-frequency problems," *Microwave and Optical Technology Letters*, vol. 55, no. 10, pp. 2475–2479, 2013.
- [13] Y. Shi, J. Wang, and C.-H. Liang, "A time-domain equivalence principle and its marching-on-in-degree solution," *Microwave and Optical Technology Letters*, vol. 56, no. 10, pp. 2415–2422, 2014.
- [14] T. Su, L. Du, and R. Chen, "Electromagnetic scattering for multiple PEC bodies of revolution using equivalence principle algorithm," *Institute of Electrical and Electronics Engineers. Transactions on Antennas and Propagation*, vol. 62, no. 5, pp. 2736–2744, 2014.
- [15] H. Shao, J. Hu, and W. C. Chew, "Single-source equivalence principle algorithm for the analysis of complex structures," *IEEE Antennas and Wireless Propagation Letters*, vol. 13, pp. 1255–1258, 2014.
- [16] H. Shao, J. Dong, and J. Hu, "Improving the Accuracy of Single-Source Equivalence Principle Algorithm by Using Tangential Field Projection Scheme," *Electromagnetics*, vol. 36, no. 8, pp. 534–545, 2016.
- [17] H. Shao and J. Hu, "Analysis of connected structures using equivalence principle algorithm with source reconstruction method," *Journal of Electromagnetic Waves and Applications*, vol. 30, no. 13, pp. 1740–1754, 2016.
- [18] J. M. Song and W. C. Chew, "Multilevel fast-multipole algorithm for solving combined field integral equations of electromagnetic scattering," *Microwave and Optical Technology Letters*, vol. 10, no. 1, pp. 14–19, 1995.
- [19] S. Wandzura, "Electric current basis functions for curved surfaces," *Electromagnetics*, vol. 12, no. 1, pp. 77–91, 1992.
- [20] C. C. Lu and W. C. Chew, "Electromagnetic scattering from material coated PEC objects: a hybrid volume and surface integral equation approach," in *Proceedings of the IEEE Antennas and Propagation Society International Symposium*, IEEE, pp. 2562–2565, Orlando, FL, USA, July, 1999.

Research Article

A Truncated Singular Value Decomposition Enhanced Nested Complex Source Beam Method

Lianning Song and Zaiping Nie

Department of Microwave Engineering, University of Electronic Science and Technology of China, Chengdu, Sichuan 610054, China

Correspondence should be addressed to Lianning Song; lianningsong@foxmail.com

Received 15 May 2017; Accepted 8 June 2017; Published 1 August 2017

Academic Editor: Yumao Wu

Copyright © 2017 Lianning Song and Zaiping Nie. This is an open access article distributed under the Creative Commons Attribution License, which permits unrestricted use, distribution, and reproduction in any medium, provided the original work is properly cited.

This work presents a novel matrix compression algorithm to improve the computational efficiency of the nested complex source beam (NCSB) method. The algorithm is based on the application of the truncated singular value decomposition (TSVD) to the multilevel aggregation, translation, and disaggregation operations in NCSB. In our implementation, the aggregation/disaggregation matrices are solved by the truncated far-field matching, which is based on the directional far-field radiation property of the complex source beams (CSBs). Furthermore, the translation matrices are obtained according to the beam width of CSBs. Due to the high directivity of the radiation patterns of CSBs, all the far-field related interaction matrices are low-ranked. Therefore, TSVD can be employed and a new set of equivalent sources can be constructed by a linear combination of the original CSBs. It is proved that the radiation power of the new sources is proportional to the square of the corresponding singular values. This provides a theoretical guideline to drop the insignificant singular vectors in the calculation. In doing so, the efficiency of the original NCSB method can be much improved while a reasonably good accuracy is maintained. Several numerical tests are conducted to validate the proposed method.

1. Introduction

Integral equation (IE) method has been intensively studied in the analysis of electromagnetic (EM) radiation and scattering in recent years. For a numerical solution, the IE is usually discretized into a matrix equation by the method of moments (MoM) [1]. In order to conduct large-scale simulations, a variety of numerical techniques have been developed based on MoM. These techniques are carried out efficiently either by reduction of the far-field interaction exploiting the physical or mathematical properties of the IE or by using well-designed basis/test functions to reduce the total number of unknowns.

In the first category, the multilevel fast multipole algorithm (MLFMA) [2] is widely used, where the far-field interactions can be accelerated by aggregation, translation, and disaggregation operations. Besides it, the low rank property of the MoM far-field submatrices leads to a series of matrix decomposition methods, such as the multilevel matrix decomposition algorithm (MLMDA) [3] and the adaptive cross approximation (ACA) [4, 5]. For the second category,

the higher order basis functions (HOBFB) [6], phase extracted basis functions (PE) [7, 8], characteristic basis function (CBF) [9, 10], or body of revolution (BoR) [11] MoM are proposed to reduce the number of unknowns in a given problem.

Following the first category, a complex source beam-method of moments (CSB-MoM) is recently proposed to accelerate the far-field interactions of MoM [12]. In this method, the object is divided into groups and complex source beams (CSBs) [13] are used to expand the fields of the basis functions residing in each group [14, 15]. Hence, the far-field interactions of these basis/test functions can be accounted for by their equivalent CSB expansions. Due to the directional nature of CSBs [16], the interactions usually involve only a small portion of the total CSBs. A multilevel version of this method is developed in [17] to further improve the computational efficiency. The branch cut issue of CSBs, which might degrade the accuracy in the evaluation of group interactions, can be avoided by a proper choice of the CSB parameters.

Unfortunately, in this method, the CSB expansions at any level are calculated directly from the basis functions contained in the finest level. This operation is very computationally expensive. Hence, the application of this method to electrically large problems is prohibited. To overcome this difficulty, a nested complex source beam (NCSB) method is proposed by utilizing an equivalent relationship between adjacent levels [18]. This relationship is built by treating CSBs in the child group as new sources and applying the far-field matching to get their CSB expansions in the parent group. In doing this, the computational complexity of NCSB can be reduced to $O(N \log N)$, where N is the number of unknowns. However, it should be noted that the CSBs involved in the translation process have to be determined empirically. Moreover, the aggregation and disaggregation matrices are still in a dense format.

To fully exploit the directional property of CSBs, a truncated singular value decomposition (TSVD) method is applied to compress the aggregation, translation, and disaggregation matrices of NCSB in this paper. After SVD, a set of equivalent sources can be obtained by a linear combination of the original CSBs. A theoretical proof reveals that the radiation power of the new sources is proportional to the square of the corresponding singular values. This provides a guideline for the truncation in the calculation. Thereby, the proposed method not only leads to a significant improvement of the computational efficiency but also provides a flexible compromise between accuracy and computational cost.

2. Formulations

Given a 3D perfectly electrical conducting (PEC) body defined by its surface, a MoM matrix equation can be obtained as

$$\mathbf{Z}\mathbf{I} = \mathbf{Z}_N\mathbf{I} + \mathbf{Z}_F\mathbf{I} = \mathbf{V}, \quad (1)$$

where \mathbf{I} is the unknown vector containing the expansion coefficients of the current, \mathbf{V} is the excitation vector, and \mathbf{Z} is the MoM impedance matrix. After grouping, this dense matrix can be separated into the near-field interaction part \mathbf{Z}_N and the far-field interaction counterpart \mathbf{Z}_F .

In CSB-MoM, the far-field interactions between different groups are carried out by a series of CSBs launched on a complex equivalence surface enclosing each group [14]. The far-field part of the matrix-vector product (MVP) in CSB-MoM can be represented as

$$\mathbf{Z}_F\mathbf{I} = \mathbf{Z}_{mm'}\mathbf{I}_{m'} = \sum_{p,p'=\theta,\phi} \mathbf{Y}_m^p \mathbf{T}_{L,mm'}^{pp'} \mathbf{W}_{m'}^{p'} \mathbf{I}_{m'}, \quad (2)$$

where m and m' denote the observation and source groups and L indicates the finest level (single level in CSB-MoM). $\mathbf{W}_m^{p'}$ and \mathbf{Y}_m^p are, respectively, the expansion matrix and local expansion matrix for both θ and ϕ components. The far-field matching technique can be used for constructing $\mathbf{W}_m^{p'}$ and \mathbf{Y}_m^p in electric field integral equation (EFIE), magnetic field integral equation (MFIE) [19], and PMCHWT integral

equation [20]. $\mathbf{T}_{L,mm'}^{pp'}$ is the translation matrix, of which the elements are expressed as

$$\left[\mathbf{T}_{L,mm'}^{pp'} \right]_{qq'} = \hat{\mathbf{p}}_q \cdot \overline{\overline{\mathbf{G}}} \left(\tilde{\mathbf{r}}_{L,m}^q \mid \tilde{\mathbf{r}}_{L,m'}^{q'} \right) \cdot \hat{\mathbf{p}}_{q'}, \quad (3)$$

where $\hat{\mathbf{p}}_q$ and $\hat{\mathbf{p}}_{q'}$ denote the unit vectors of q th and q' th CSB, respectively. The complex position vectors $\tilde{\mathbf{r}}_{L,m}^q$ and $\tilde{\mathbf{r}}_{L,m'}^{q'}$ are the launch points of CSBs. $\overline{\overline{\mathbf{G}}}(\tilde{\mathbf{r}}_m^q \mid \tilde{\mathbf{r}}_{m'}^{q'})$ is the dyadic Green function with complex arguments.

By using this representation, the CSB expansion coefficients for the source group m' can be expanded from the surface currents as

$$\mathbf{S}_{L,m'} = \begin{bmatrix} \mathbf{S}_{L,m'}^\theta \\ \mathbf{S}_{L,m'}^\phi \end{bmatrix} = \begin{bmatrix} \mathbf{W}_{m'}^\theta \\ \mathbf{W}_{m'}^\phi \end{bmatrix} \mathbf{I}_{m'}. \quad (4)$$

On the other hand, the CSB expansion coefficients $\mathbf{R}_{L,m'}$ for the receiving group m are translated from the transmitting group m' :

$$\mathbf{R}_{L,m'} = \mathbf{T}_{L,mm'}^{pp'} \mathbf{S}_{L,m'}. \quad (5)$$

As has been mentioned previously, the directional property of CSBs can be used to reduce the computational cost in the translation procedure. The translation window can be set based on numerical experiments for different group sizes and CSB parameters, as is done in [18].

2.1. NCSB Formulations. Motivated by the idea of MLFMA [2], CSB-MoM can be naturally extended to a multilevel version if a similar octree data structure is adopted. However, the multilevel CSB or MLCSB proposed in [17] calculates the CSB expansion coefficients for each level directly from the basis functions in the finest level. The lack of a proper mechanism of interlevel aggregation and disaggregation prohibits this method from analyzing large-unknown problems. To end this, the NCSB is proposed in [18] to introduce the aggregation and disaggregation operations between every two adjacent levels through a proper far-field matching.

In the following, we obtain the aggregation matrix in a slightly different way by further utilizing the directional property of the radiating far field of CSBs. Moreover, the symmetry is fully exploited so that only one aggregation matrix is needed for all the eight child groups of one parent group. First, a linear system is set up to build the equivalent relationship of CSBs between two adjacent levels:

$$\mathbf{Z}_l \mathbf{A}_{lc} = \mathbf{F}_{l+1,c} \quad c = 1, 2, \dots, 8, \quad (6)$$

where \mathbf{Z}_l is the matching matrix that connects the equivalent CSB sources with the far fields $\mathbf{F}_{l+1,c}$. The expression of the matching matrix is the same as the matrix used for CSB expansion with electric current type equivalent sources in CSB-MoM [12, 14]. Different from CSB-MoM of single level, the equivalent CSB sources in \mathbf{Z}_l are launched in level l , and

the far fields here are radiated by CSBs in child level $l + 1$ with both θ and ϕ components:

$$\mathbf{F}_{l+1,c} = \begin{bmatrix} \mathbf{E}_{l+1,c}^{\theta\theta} & \mathbf{E}_{l+1,c}^{\theta\phi} \\ \mathbf{E}_{l+1,c}^{\phi\theta} & \mathbf{E}_{l+1,c}^{\phi\phi} \end{bmatrix}, \quad (7)$$

where the elements in each block matrix are

$$\left[\mathbf{E}_{l+1,c}^{p'p} \right]_{q_l q_{l+1}} = \hat{P}'_{q_l} \bar{\bar{G}}(\mathbf{r}_{q_l} | \bar{\mathbf{r}}'_{q_{l+1},c}) \hat{P}_{q_{l+1}}. \quad (8)$$

It is noted that, for a parent group in the octree, there are eight different child groups at most. Hence, eight corresponding aggregation matrices are required in the calculation. However, by fully exploiting the symmetry property, we discover that only one aggregation matrix is needed and others can be easily deduced from it. In the following, the subscript c will be omitted for simplicity.

In our method, the radiating far fields on the right-hand-sides of (6) can be fast calculated by truncating CSB directional fields within the paraxial regions. Once \mathbf{Z}_l and $\mathbf{F}_{l+1,c}$ are assembled, the aggregation matrix for level l

$$\mathbf{A}_l = \begin{bmatrix} \bar{\mathbf{A}}_l^{\theta\theta} & \bar{\mathbf{A}}_l^{\theta\phi} \\ \bar{\mathbf{A}}_l^{\phi\theta} & \bar{\mathbf{A}}_l^{\phi\phi} \end{bmatrix}_{2Q_l \times 2Q_{l+1}} \quad (9)$$

can be numerically solved. Here Q_l and Q_{l+1} are the numbers of CSBs in levels l and $l + 1$. In this work, we apply the least square method to improve the stability of the solution. In

(9), the element $[\bar{\mathbf{A}}_l^{p'p''}]_{q_l q_{l+1}}$ in the block aggregation matrix is the mapping coefficient between the q_{l+1} th CSB in the child group and the q_l th CSB in its parent group. By using this relationship, the disaggregation matrix can be easily obtained from the transpose of the aggregation matrix. The CSB expansion coefficients of the parent group in level l can be obtained efficiently from its child groups in level $l + 1$ with the aggregation matrix:

$$\mathbf{S}_{l,m'} = \begin{bmatrix} \mathbf{S}_{l,m'}^{\theta} \\ \mathbf{S}_{l,m'}^{\phi} \end{bmatrix} = \sum_{n' \in \text{child}(m')} \mathbf{A}_l \mathbf{S}_{l+1,n'}. \quad (10)$$

Similar to MLFMA, the CSB expansion coefficients of a receiving group in level $l + 1$ is obtained from both of the translation in the same level and the disaggregation from its parent level l . Therefore, we have

$$\mathbf{R}_{l+1,m} = \begin{bmatrix} \mathbf{R}_{l+1,m}^{\theta} \\ \mathbf{R}_{l+1,m}^{\phi} \end{bmatrix} = \mathbf{A}_l^T \begin{bmatrix} \mathbf{R}_{l,n}^{\theta} \\ \mathbf{R}_{l,n}^{\phi} \end{bmatrix} = \mathbf{A}_l^T \mathbf{R}_{l,n}. \quad (11)$$

As has been elaborated in the above, the NCSB algorithm can be constructed in much the same way as MLFMA. However, all the operation matrices involved in NCSB are dense matrices, in contrast with the diagonal matrices in MLFMA. Improvement can be made by utilizing the unique property of CSBs. Specifically, all the CSBs are directional; that is to say, a CSB can only directionally interact with another CSB in the far-field region. Hence, the dense aggregation/disaggregation and translation matrices are usually low-ranked. To take advantage of the directional property of CSBs, TSVD will be applied to compress these matrices in the following sections.

2.2. TSVD in Aggregation/Disaggregation Process. For the aggregation matrix in (9), the SVD factorization can be applied as

$$\mathbf{A}_l = \mathbf{U}_l^A \boldsymbol{\Sigma}_l^A (\mathbf{V}_l^A)^H, \quad (12)$$

where $[\mathbf{U}_l^A]_{2Q_l \times 2Q_l}$ and $[\mathbf{V}_l^A]_{2Q_{l+1} \times 2Q_{l+1}}$ are unitary matrices and $\boldsymbol{\Sigma}_l^A = \text{diag}\{\sigma_1, \sigma_2, \dots, \sigma_{2Q_{l+1}}\}_{2Q_l \times 2Q_{l+1}}$ is a diagonal matrix whose elements are the nonnegative real singular values listed in a descending order. The columns of \mathbf{V}_l^A represent a new set of orthonormal child CSB modes in level $l + 1$, which are obtained as linear combinations of the original CSBs. Matrix \mathbf{U}_l^A defines a complete set of orthonormal parent CSB modes associated with the child modes. Diagonal matrix $\boldsymbol{\Sigma}_l^A$ maps the child modes to the corresponding parent modes with weighting of the singular values.

The physical meaning of the above SVD can be interpreted as follows. One set of the child CSBs is coupled to another set of parent CSBs, with the coupling strength governed by the corresponding singular value. Hence, after SVD, the aggregation procedure is converted from beam-to-beam coupling into mode-to-mode coupling. Furthermore, we can prove that the radiated power by each child CSB mode is proportional to the square of the singular value (see Appendix). This power-related mode provides a helpful guideline for extracting the most significant part in the aggregation matrix.

If r_l is the effective rank of \mathbf{A}_l for a prescribed threshold ϵ , the SVD decomposition in (12) can be truncated and approximated as

$$\mathbf{A}_l \approx \tilde{\mathbf{U}}_l^A \tilde{\boldsymbol{\Sigma}}_l^A (\tilde{\mathbf{V}}_l^A)^H, \quad (13)$$

where $\tilde{\boldsymbol{\Sigma}}_l^A$ is formed by the first (largest) r_l singular values in $\boldsymbol{\Sigma}_l^A$ satisfying $\sigma_{r_l+1} < \epsilon \sigma_1$. $\tilde{\mathbf{U}}_l^A$ and $\tilde{\mathbf{V}}_l^A$ denote the corresponding submatrices consisting of the first r_l columns of \mathbf{U}_l^A and \mathbf{V}_l^A , respectively. Hence, $\tilde{\mathbf{V}}_l^A$ contains all the child CSB modes having radiated power higher than $\epsilon^2 \sigma_1^2$. According to the prescribed accuracy, this reduced set of CSBs in child group suffices to represent the far field of the parent group. Since disaggregation is implemented as the transpose of aggregation, the TSVD procedure of disaggregation matrix can be implemented by fully utilizing $\tilde{\mathbf{U}}_l^A$ and $\tilde{\mathbf{V}}_l^A$ in (13).

2.3. TSVD in Translation Process. As the CSB decays rapidly in the directions orthogonal to the beam propagation axis, in the translation process, the interactions between far-field groups are carried out by CSBs whose beam axis are aligned with the line connecting the group centers. These CSBs can be easily selected by setting a conical truncation window. To avoid amount of experiments needed to determine the minimal conical angle, in this paper, we first set the truncation angle when the field of a CSB decays to -20 dB of the aforementioned prescribed accuracy times the maximum value. According to this criterion, the CSB selection matrices $\mathbf{L}_{l,mm'}$ and $\mathbf{L}_{l,mm'}$ are introduced to pick up

TABLE I: Computational statistics.

Method	Q_l (level 2-4)	Aggregation TSVD rank (level 2-3)	K_l (level 2-4)	Translation TSVD rank (level 2-4)	Aggregation & Translation Mem.	Setup time	Solving time	Total time
NCSB		—		—	19230.5 MB	511 s	3864 s	4375 s
$\epsilon = 10^{-2}$	5738/1758/682	635/509	1213/681/289	59/48/66	1429.9 MB	936 s	1178 s	2114 s
$\epsilon = 10^{-3}$		1154/730		119/131/108	3119.3 MB	958 s	1345 s	2303 s
$\epsilon = 10^{-4}$		1600/919		206/199/142	5548.7 MB	992 s	1488 s	2480 s

the most significant CSBs in the transmitting and receiving groups; namely,

$$\begin{aligned} & \left[\mathbf{T}_{l,mm'}^{pp'} \right]_{Q_l \times Q_l} \\ &= \left[\mathbf{L}_{l,mm'} \right]_{Q_l \times K_l} \left[\tilde{\mathbf{T}}_{l,mm'}^{pp'} \right]_{K_l \times K_l} \left[\mathbf{L}'_{l,mm'} \right]_{K_l \times Q_l}, \end{aligned} \quad (14)$$

where only one element in each row (column) of $\mathbf{L}'_{l,mm'}$ ($\mathbf{L}_{l,mm'}$) is 1, if the corresponding CSB is within the conical truncation window; otherwise they are set to 0.

After this truncation based on the beam width of CSBs, the dimension of the translation matrix $\tilde{\mathbf{T}}_{l,mm'}^{pp'}$ is reduced from $Q_l \times Q_l$ to $K_l \times K_l$. However, it is still rank-deficient. The TSVD procedure is then applied to this reduced translation matrix to gain further compression:

$$\tilde{\mathbf{T}}_{l,mm'}^{pp'} \approx \tilde{\mathbf{U}}_{l,mm'}^{T,pp'} \tilde{\mathbf{\Sigma}}_{l,mm'}^{T,pp'} \left[\tilde{\mathbf{V}}_{l,mm'}^{T,pp'} \right]^H, \quad (15)$$

where $\tilde{\mathbf{U}}_{l,mm'}^{T,pp'}$, $\tilde{\mathbf{\Sigma}}_{l,mm'}^{T,pp'}$, and $\tilde{\mathbf{V}}_{l,mm'}^{T,pp'}$ are defined similarly as in (13), except that the threshold is set as ϵ^2 instead of ϵ to account for the effects from both of the transmitting and receiving groups.

The proposed TSVD procedure is effective by providing new set of CSB modes based on the singular vectors. The significance in the total radiated power is governed by the descending singular values. The SVD process fully exploits the spatial window property of CSBs, which is independent of the geometry, current distribution, and types of IE. By defining an error threshold, redundant modes which contribute negligibly to the radiated power are excluded. Therefore, the aggregation, translation, and disaggregation matrices can be represented in a very compact form. Furthermore, the balance between accuracy and computational efficiency can be easily controlled by adjusting the truncation threshold.

3. Numerical Results

In this section, several numerical tests are conducted to demonstrate the efficiency and validity of the proposed method.

Firstly, the low rank property of the aggregation matrices of NCSB method is studied. Figure 1 shows the normalized singular values of the aggregation matrices for level 2 (with electrical size of 8λ and aggregating from level 3) and level 3 (with electrical size of 4λ and aggregating from level 4). The

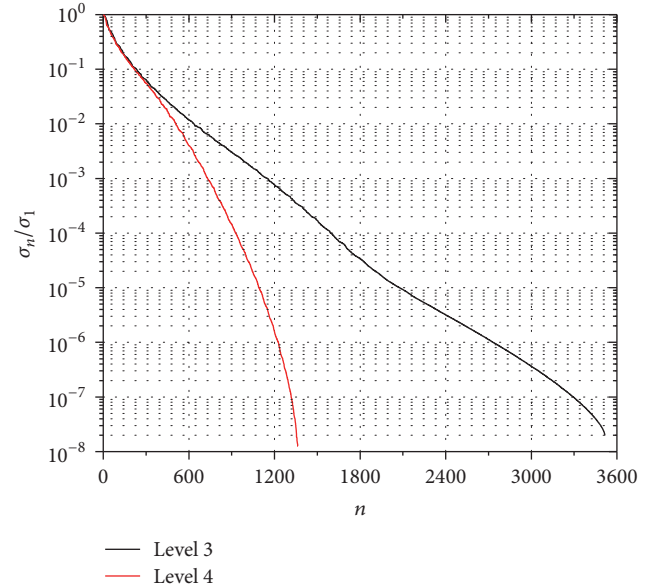


FIGURE 1: Normalized singular values of the aggregation matrix.

numbers of CSBs for levels 2, 3, and 4 are 5738, 1758, and 682, as listed in Table 1. Considering both θ and ϕ components of CSBs, the dimensions of the aggregation matrices for level 2 and level 3 are 11476×3516 and 3516×1364 , respectively. As shown in Figure 1, the singular values for both matrices decrease rapidly, indicating a quick decay of the radiated power from individual child CBS mode. Due to this fact, the aggregation matrices are truncated by thresholds of $\epsilon = 10^{-2}$, 10^{-3} , and 10^{-4} for comparison. Figure 2 depicts the relative errors of the radiated far field (an effective measure of the aggregation error) with respect to the observation angles. In particular, this relative error is defined as

$$e(\phi) = \frac{\|\mathbf{E}(\phi) - \mathbf{E}_{\text{agg}}(\phi)\|_2}{\|\mathbf{E}(\phi)\|_2} \quad (16)$$

and here $\mathbf{E}(\phi)$ is the reference field, $\mathbf{E}_{\text{agg}}(\phi)$ is the field obtained via aggregations by TSVD, and ϕ is the observation angle which is set on a azimuth circle. In Figure 2, the reference field is radiated directly by the CSBs of a group with the size of 2λ in the fourth level. Then two aggregation steps with TSVD are performed to this group until the second level. Finally, the field $\mathbf{E}_{\text{agg}}(\phi)$ is calculated by the CSBs in the second level. Figure 2 shows that the relative aggregation error can be effectively controlled by the TSVD threshold ϵ .

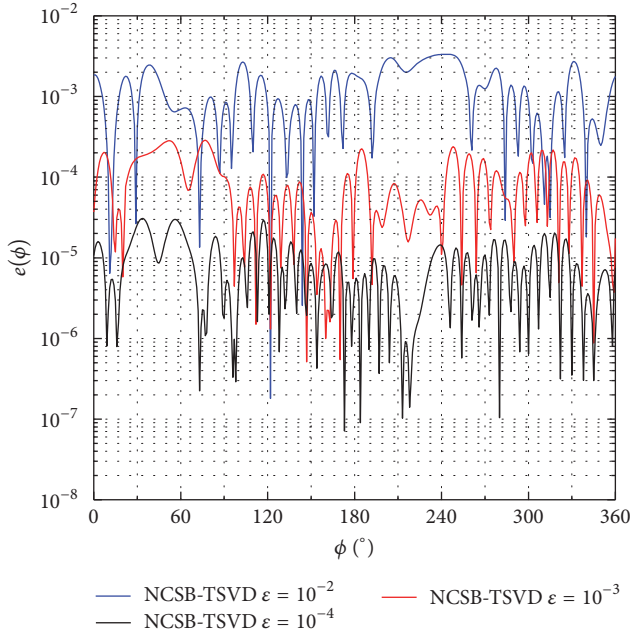


FIGURE 2: Relative aggregation errors measured by the radiated far field.

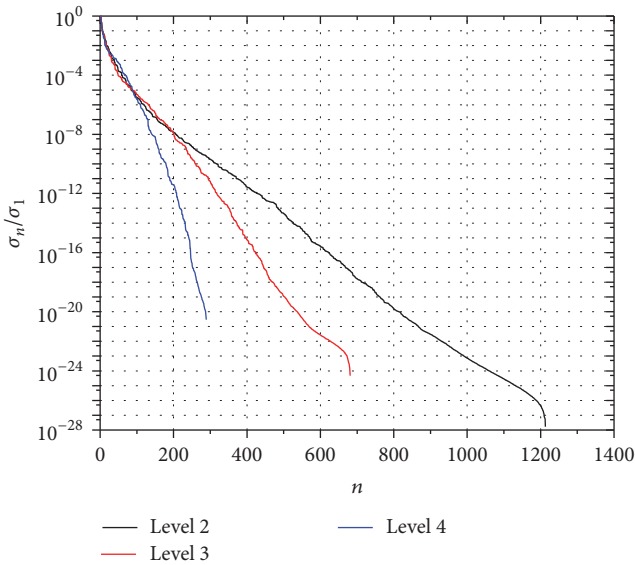


FIGURE 3: Normalized singular values of the reduced translation matrix.

Next, we investigate the TSVD based translation process. As shown in Table 1, after the aforementioned window selection, the number of CSBs for the reduced translation (K_l) drops to 1213, 681, and 289 for levels 2, 3, and 4, respectively. However, the information of the reduced translation matrices is still redundant, and the effective rank can be further compressed. Figure 3 shows the normalized singular values of the reduced translation matrices, where a rapid decrease can again be observed for individual CSB mode. As has been explained, the truncation thresholds for translation matrices

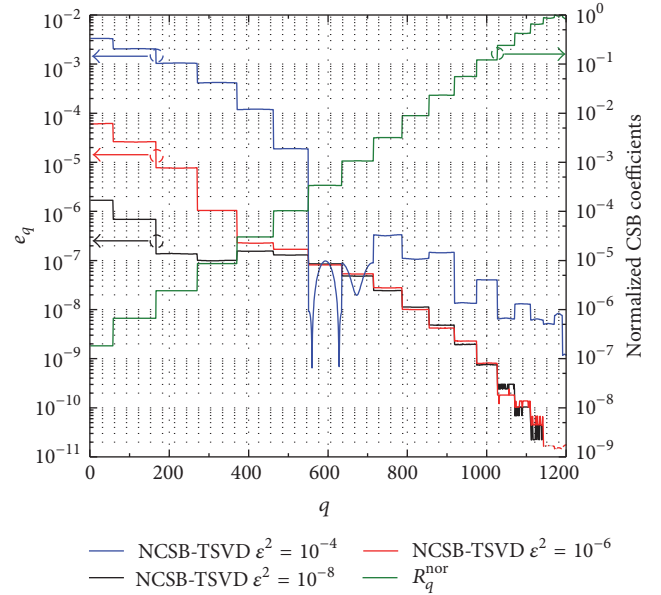


FIGURE 4: Relative translation errors.

should be set as ϵ^2 , namely, 10^{-4} , 10^{-6} , and 10^{-8} , in this example. The relative translation error

$$e_q = \frac{|R_q^{\text{tsvd}} - R_q|}{|R_q|} \quad q = 1, 2, \dots, K_l \quad (17)$$

is depicted in Figure 4, where R_q and R_q^{tsvd} are the CSB expansion coefficients in level 2, translated by the original translation and the TSVD counterpart, respectively. Even though the error is relatively higher for small indices of CSBs, the corresponding normalized expansion coefficients $R_q^{\text{nor}} = |R_q|/\max_j |R_j|$ are also relatively small. Hence, these CSBs will contribute to the total field insignificantly. In other words, TSVD maintains reasonably good translation accuracy for both the strongly coupled CSBs (with larger indices) and the weakly coupled CSBs (with smaller indices).

Finally, to demonstrate the overall performance of the proposed method, the scattering problem of a diameter 32λ sphere is presented. It is illuminated by an incident plane wave ($\theta_i = 0^\circ$, $\varphi_i = 0^\circ$) at 300 MHz and solved by combined field integral equation (CFIE). Figure 5 shows the bistatic RCS results compared with the analytical solution of Mie series from 120° to 180° . We can see a very good agreement is obtained for $\epsilon = 10^{-3}$ and $\epsilon = 10^{-4}$. Furthermore, a good agreement is still obtained for $\epsilon = 10^{-2}$. To quantify the accuracy, the RMS value of the error $E = |\delta_{\text{NCSB-TSVD}} - \delta_{\text{Mie}}|/|\delta_{\text{Mie}}|_{\text{max}}$ has been calculated, δ being the RCS (m^2). RMS errors of 0.18%, 0.0806%, and 0.0768% are found for the thresholds 10^{-2} , 10^{-3} , and 10^{-4} . At the same time, the computational efficiency can be significantly improved by the proposed method. The statistics are summarized in Table 1. It can be observed that a great computational improvement is obtained in terms of CPU time and memory consumption. It is also shown that a good compromise between accuracy and the computational efficiency can be easily achieved, by a proper choice of the truncation parameter.

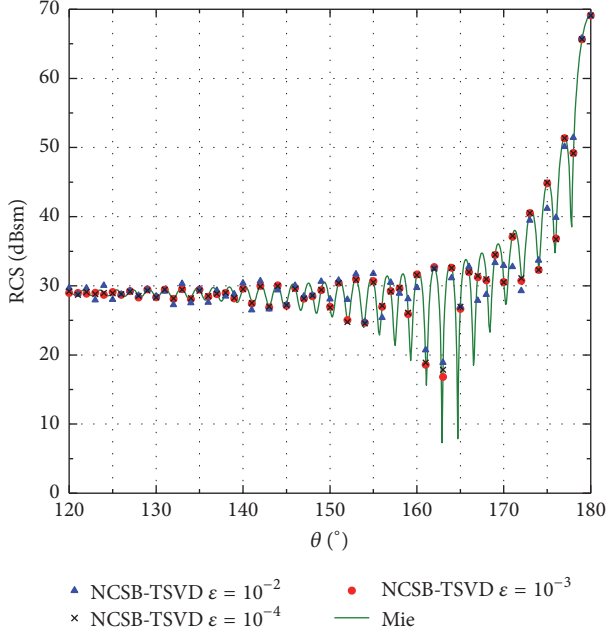


FIGURE 5: Bistatic RCS of a PEC sphere with a diameter 32λ , by NCSB-TSVD and Mie-series solution.

4. Conclusion

In this paper, we have proposed an efficient implementation of NCSB. Different from previous work, the aggregation process is first constructed by the truncated far-field matching. The dimension of the translation matrix is then reduced based on the beam width of the CSBs. Finally, TSVD is used to compress the aggregation, translation, and disaggregation matrices by fully exploiting the directional property of CSBs. It is shown that the radiated power of the new sources from SVD is proportional to the square of the corresponding singular values. This power-dependent mode provides a theoretical guideline for extracting the most significant CSB contributions in the calculation. Therefore, the desired balance between accuracy and computational efficiency can be easily controlled by adjusting the truncation threshold.

Appendix

The radiated power by the q -th CSB expansion coefficient of group m in level l can be calculated by an integral on the matching surface as:

$$\begin{aligned}
 P_m^q &= \frac{1}{2\eta} \int_s \mathbf{E}(r) \cdot \mathbf{E}^*(r) ds \\
 &= \frac{1}{2\eta} \int_s \sum_{p,p'=\theta,\phi} \left[E_{l,m}^{p'p}(r) S_q^p \right] \left[E_{l,m}^{p'p}(r) S_q^p \right]^* ds \quad (\text{A.1}) \\
 &\propto \sum_{p=\theta,\phi} S_q^p (S_q^p)^*,
 \end{aligned}$$

where $S_q^p = [\mathbf{S}_{l,m}^p]_q$. Therefore, the total radiated power can be obtained by summing up the contributions from all CSBs:

$$P_m = \sum_{q=1}^{Q_{l+1}} P_m^q \propto \sum_{q=1}^{Q_{l+1}} \sum_{p=\theta,\phi} S_q^p (S_q^p)^*, \quad (\text{A.2})$$

which can be further expressed in matrix form as:

$$P_m \propto \mathbf{S}_{l,m}^H \mathbf{S}_{l,m} \quad (\text{A.3})$$

Since the CSB expansion coefficient can be aggregated from the child groups:

$$\mathbf{S}_{l,m} = \mathbf{A}_l \mathbf{S}_{l+1,n} \quad (\text{A.4})$$

we have

$$\mathbf{S}_{l,m}^H \mathbf{S}_{l,m} = \mathbf{S}_{l+1,n}^H \mathbf{V}_l^A (\boldsymbol{\Sigma}_l^A)^2 (\mathbf{V}_l^A)^H \mathbf{S}_{l+1,n}. \quad (\text{A.5})$$

By defining the new child CSB modes as $\mathbf{S}'_{l+1,n} = (\mathbf{V}_l^A)^H \mathbf{S}_{l+1,n}$, we obtain

$$\mathbf{S}_{l,m}^H \mathbf{S}_{l,m} = \mathbf{S}'_{l+1,n}{}^H (\boldsymbol{\Sigma}_l^A)^2 \mathbf{S}'_{l+1,n}. \quad (\text{A.6})$$

Substituting (A.6) into (A.3) leads to

$$P_m \propto \mathbf{S}'_{l+1,n}{}^H (\boldsymbol{\Sigma}_l^A)^2 \mathbf{S}'_{l+1,n} \quad (\text{A.7})$$

which can be rewritten as

$$P_m \propto \sum_{q=1}^{Q_{l+1}} \sigma_i^2 \left| [\mathbf{S}'_{l+1,n}]_q \right|^2. \quad (\text{A.8})$$

This result shows that the total radiated power by CSBs is proportional to the square of singular value corresponding to the child mode.

Conflicts of Interest

The authors declare that there are no conflicts of interest regarding the publication of this paper.

Acknowledgments

This work is supported partly by the Programme of Introducing Talents of Discipline to Universities under Grant no. b07046, the National Excellent Youth Fund by NSFC no. 61425010, and the National Science Foundation of China under Grant no. 61490695.

References

- [1] R. F. Harrington and J. L. Harrington, *Field computation by moment methods*, Oxford University Press, 1996.
- [2] O. Ergül and L. Gürel, *The Multilevel Fast Multipole Algorithm (MLFMA) for Solving Large-Scale Computational Electromagnetics Problems*, John Wiley & Sons, 2014.

- [3] J. M. Rius, J. Parrón, E. Úbeda, and J. R. Mosig, "Multilevel matrix decomposition algorithm for analysis of electrically large electromagnetic problems in 3-D," *Microwave and Optical Technology Letters*, vol. 22, no. 3, pp. 177–182, 1999.
- [4] K. Zhao, M. N. Vouvakis, and J.-F. Lee, "The adaptive cross approximation algorithm for accelerated method of moments computations of EMC problems," *IEEE Transactions on Electromagnetic Compatibility*, vol. 47, no. 4, pp. 763–773, 2005.
- [5] D. Z. Ding, Y. Shi, Z. N. Jiang, and R. S. Chen, "Augmented EFIE with adaptive cross approximation algorithm for analysis of electromagnetic problems," *International Journal of Antennas and Propagation*, vol. 2013, Article ID 487276, 9 pages, 2013.
- [6] X.-M. Pan, L. Cai, and X.-Q. Sheng, "An efficient high order multilevel fast multipole algorithm for electromagnetic scattering analysis," *Progress In Electromagnetics Research*, vol. 126, pp. 85–100, 2012.
- [7] Z.-P. Nie, S. Yan, S. He, and J. Hu, "On the basis functions with traveling wave phase factor for efficient analysis of scattering from electrically large targets," *Progress In Electromagnetics Research*, vol. 85, pp. 83–114, 2008.
- [8] S. Yan, S. Ren, Z. Nie, S. He, and J. Hu, "Efficient analysis of electromagnetic scattering from electrically large complex objects by using phase-extracted basis functions," *IEEE Antennas and Propagation Magazine*, vol. 54, no. 5, pp. 88–108, 2012.
- [9] V. V. S. Prakash and R. Mittra, "Characteristic basis function method: a new technique for efficient solution of method of moments matrix equations," *Microwave and Optical Technology Letters*, vol. 36, no. 2, pp. 95–100, 2003.
- [10] H. Shao, J. Hu, W. Lu, H. Guo, and Z. Nie, "Analyzing large-scale arrays using tangential equivalence principle algorithm with characteristic basis functions," *Proceedings of the IEEE*, vol. 101, no. 2, pp. 414–422, 2013.
- [11] Y. Li, J. Hu, and Z. Nie, "Solving scattering from multiple bodies of revolution by modal characteristic basis function method with sparse matrix technique," *IEEE Antennas and Wireless Propagation Letters*, vol. 15, pp. 806–809, 2016.
- [12] K. Tap, P. H. Pathak, and R. J. Burkholder, "Complex source beam-moment method procedure for accelerating numerical integral equation solutions of radiation and scattering problems," *Institute of Electrical and Electronics Engineers. Transactions on Antennas and Propagation*, vol. 62, no. 4, part 2, pp. 2052–2062, 2014.
- [13] T. B. Hansen and G. Kaiser, "Huygens' principle for complex spheres," *Institute of Electrical and Electronics Engineers. Transactions on Antennas and Propagation*, vol. 59, no. 10, pp. 3835–3847, 2011.
- [14] K. Tap, P. H. Pathak, and R. J. Burkholder, "Exact complex source point beam expansions for electromagnetic fields," *IEEE Transactions on Antennas and Propagation*, vol. 59, no. 9, pp. 3379–3390, 2011.
- [15] E. Martini and S. Maci, "Generation of complex source point expansions from radiation integrals," *Progress in Electromagnetics Research*, vol. 152, pp. 17–31, 2015.
- [16] G. A. Deschamps, "Gaussian beam as a bundle of complex rays," *Electronics Letters*, vol. 7, no. 23, pp. 684–685, 1971.
- [17] Z. H. Fan, X. Hu, and R. S. Chen, "Multilevel Complex Source Beam Method for Electromagnetic Scattering Problems," *IEEE Antennas and Wireless Propagation Letters*, vol. 14, pp. 843–846, 2015.
- [18] K. C. Wang, Z. H. Fan, M. M. Li, and R. S. Chen, "An effective MoM solution with nested complex source beam method for electromagnetic scattering problems," *Institute of Electrical and Electronics Engineers. Transactions on Antennas and Propagation*, vol. 64, no. 6, pp. 2546–2551, 2016.
- [19] K. Tap, *Complex source point beam expansions for some electromagnetic radiation and scattering problems [Ph.D. dissertation]*, The Ohio State University, 2007.
- [20] P. F. Gu, Z. H. Fan, and R. S. Chen, "Complex source beam method for electromagnetic scattering problems of dielectric objects," *IEEE Antennas and Wireless Propagation Letters*, vol. 15, pp. 597–601, 2016.

Research Article

High Performance Computing of Complex Electromagnetic Algorithms Based on GPU/CPU Heterogeneous Platform and Its Applications to EM Scattering and Multilayered Medium Structure

Zhe Song,¹ Xing Mu,² and Hou-Xing Zhou¹

¹The State Key Laboratory of Millimeter Waves, Southeast University, Nanjing, China

²OpenLink Corp., Nanjing, China

Correspondence should be addressed to Zhe Song; zhe.song@seu.edu.cn

Received 30 April 2017; Accepted 6 June 2017; Published 30 July 2017

Academic Editor: Han Guo

Copyright © 2017 Zhe Song et al. This is an open access article distributed under the Creative Commons Attribution License, which permits unrestricted use, distribution, and reproduction in any medium, provided the original work is properly cited.

The fast and accurate numerical analysis for large-scale objects and complex structures is essential to electromagnetic simulation and design. Comparing to the exploration in EM algorithms from mathematical point of view, the computer programming realization is coordinately significant while keeping up with the development of hardware architectures. Unlike the previous parallel algorithms or those implemented by means of parallel programming on multicore CPU with OpenMP or on a cluster of computers with MPI, the new type of large-scale parallel processor based on graphics processing unit (GPU) has shown impressive ability in various scenarios of supercomputing, while its application in computational electromagnetics is especially expected. This paper introduces our recent work on high performance computing based on GPU/CPU heterogeneous platform and its application to EM scattering problems and planar multilayered medium structure, including a novel realization of OpenMP-CUDA-MLFMM, a developed ACA method and a deeply optimized CG-FFT method. With fruitful numerical examples and their obvious enhancement in efficiencies, it is convincing to keep on deeply investigating and understanding the computer hardware and their operating mechanism in the future.

1. Introduction

Demand boosting in high performance computing algorithms has been one of the most significant topics in computational electromagnetics (CEM). With the well-known merit of much fewer unknowns than finite-difference time-domain (FDTD) and finite element method (FEM), the method of moments (MoM) has been widely used in EM scattering problems of large-scale complex objects and full-wave analysis in multilayered structures during the past decades [1]. With the development in computer science and computational mathematics, many innovative algorithms have been established to accelerate the solving procedure of matrix equation. Several methods have been widely used in CEM, for example, multilevel fast multipole method (MLFMM) [2], adaptive integral method (AIM) [3, 4], fast

Fourier transform based method (p-FFT, IE-FFT) [5–7], adaptive cross approximation method (ACA) [8–10], and conjugate gradient fast Fourier transform method (CG-FFT) [11]. Some of them have been successfully implemented in commercial software. Naturally, parallelization is the obvious way to make a further enhancement to efficiency [12]. In early stage, the implementation of parallel computing was mainly based on CPU platforms, such as PC-cluster with MPI and multicore CPU workstation with OpenMP. The methodology of the parallelization based on a single PC platform is the massive use of threads while sharing the same memory. The bottleneck appears immediately as the explosive growth of communication load among threads. Therefore, the theoretical speedup when using multiple processors can be predicted by the famous Amdahl's Law [13].

TABLE 1: Detailed parameters of GPU platform.

Parameters	Fermi GF104	Kepler GK104	Kepler GK110
Compute ability	2.1	3.0	3.5
Threads/warp	32	32	32
Max warps/multiprocessor	48	64	64
Max threads/multiprocessor	1536	2048	2048
Max thread Blocks/Multiprocessor	8	16	16
32-bit registers/multiprocessor	32768	65536	65536
Max registers/thread	63	63	255
Max threads/thread block	1024	1024	1024
Max X-grid dimension	$2^{16} - 1$	$2^{32} - 1$	$2^{32} - 1$
Dynamic parallelism	×	×	√
Used in numerical algorithms	—	CG-FFT	FMM; ACA

Thanks to the upgrading in hardware architecture of GPU, it is possible to allocate much more transistors devoted to data processing, that is, arithmetic logic unit (ALU), rather than data caching or flow control [14]. This makes the GPU most involved in highly parallel, multiprocess, and many-core computing with very high memory bandwidth. The combination of GPU and CPU can be realized by the concept of heterogeneous computing, which includes other popular hardware modules, that is, field-programmable gate array (FPGA) and digital signal processing (DSP). The programming combination between GPU and CPU can fully depend on the easy-to-use language CUDA-C/PTX. To the authors' knowledge, the GPU/CPU heterogeneous platform is the most popular choice especially in CEM, such as the GPU-based FDTD [15], MLFMM [16–19], AIM [20], P-FFT [21], MoM [22, 23], and higher-order MoM [24]. In 2013, an impressive implementation of MLFMM by OpenMP-CUDA was realized on Fermi architecture (NVIDIA Tesla C2050), which achieved much higher performance than those before [16].

In this paper, our recent works on high performance computing based on GPU/CPU heterogeneous platform are introduced with the following:

- (1) A novel realization of OpenMP-CUDA-MLFMM method for EM scattering problem, in which the near-field matrix filling and the sparse matrix-vector production (MVP) are optimized, together with a warp-level parallel scheme for aggregation/disaggregation and the use of texture memory for 2D local interpolation/interpolation
- (2) A developed ACA method for EM scattering problem, in which the near-field matrix filling realizes a 100% efficiency enhancement and a thread-block-level parallel and a register-reusable schemes are applied to matrix compression and far-field MVP, respectively; also, a double-buffer technique for double precision is proposed to further enhance the efficiency of MVP computation [25]

- (3) A deeply optimized CG-FFT method for planar multilayered structure, in which the hardware instruction “*__shufl_down*” instead of shared memory was firstly used in the summation of MVP [26] and the current distribution of a large-scale flat lens was obtained efficiently.

It is worth emphasizing that the domain decomposition method (DDM) is not considered in this paper, by which means all the optimization comes from arithmetic programming. Corresponding to numerical examples, the detailed parameters of GPU platform can be found in Table 1, from which one can also discover the changes in computing ability brought by hardware's upgrading. The paper is organized as follows. With a brief introduction in numerical algorithms for MLFMM, ACA, and CG-FFT, Section 2 introduces the proposed and optimized methods from the programming point of view. Section 3 deals with the analysis of fruitful numerical examples. Section 4 presents the conclusions. Some technical terms used in this paper relating to NVIDIA GPU architectures and CUDA-C language, such as thread, threadblock, grid, warp, kernel, instruction, streaming multiprocessor (SMX), and stream processor (SP), are essential for understanding and can be found in [14].

2. Numerical Analysis of MLFMM, ACA, and CG-FFT

2.1. Principle of MLFMM and Its Optimization on GPU. As pointed out in [2], either the electric-field integral equation (EFIE) or the magnetic-field integral equation (MFIE) encounters the interior resonance at certain frequencies if exterior medium is lossless. The combined-field integral equation (CFIE) is always used to eliminate the problem, in which the matrix element can be calculated by

$$Z_{ij} = \alpha \eta \langle \vec{f}_i, K[\vec{f}_j] \rangle + (1 - \alpha) \langle \vec{f}_i, L[\vec{f}_j] \rangle, \quad (1)$$

where the EFIE and MFIE are presented as

$$\begin{aligned}
& \langle \vec{f}_i, L[\vec{f}_j] \rangle \\
&= jk\eta \int_{S_i} \vec{f}_i(\vec{r}_i) \cdot ds \int_{S_j} \left(\vec{I} + \frac{1}{k^2} \nabla \nabla \right) G(\vec{r}_i, \vec{r}'_j) \\
&\quad \cdot \vec{f}_j(\vec{r}'_j) ds', \\
& \langle \vec{f}_i, K[\vec{f}_j] \rangle = - \int_{S_i} (\vec{f}_i(\vec{r}_i) \times \hat{n}_i) \cdot ds \\
&\quad \cdot \int_{S_j} \nabla G(\vec{r}_i, \vec{r}'_j) \times \vec{f}_j(\vec{r}'_j) ds'.
\end{aligned} \tag{2}$$

By using the addition theorem of Green's function, formula (1) can be rewritten in the form named as "aggregation-translation-disaggregation" for EFIE and MFIE:

$$\begin{aligned}
& \langle \vec{f}_i, D[\vec{f}_j] \rangle \\
&= \int_E d^2 \vec{k} \vec{V}_{m'_i, j}^{S, P}(\vec{k}) \cdot \alpha_{m_i, m'_i}(\vec{k}) \cdot \vec{V}_{m'_i, i}^{F, P}(\vec{k}), \\
& \vec{V}_{m'_i, j}^{S, D}(\vec{k}) = \int_{S_j} ds' (\vec{I} - \vec{k} \vec{k}) \cdot \vec{f}_j(\vec{r}'_j) e^{-j \vec{k} \cdot \vec{r}'_{m'_i, j}}, \\
& \alpha_{m_i, m'_i}(\vec{k}) = \frac{jk\eta}{4\pi} T_B(\vec{k}, \vec{r}_{m_i, m'_i}), \\
& \vec{V}_{m_i, i}^{F, D}(\vec{k}) = \int_{S_i} ds (\vec{I} - \vec{k} \vec{k}) \cdot \vec{f}_i(\vec{r}_i) e^{-j \vec{k} \cdot \vec{r}_{m_i}}, \\
& T_B(\vec{k}, \vec{r}) \\
&\doteq \frac{k}{4\pi} \sum_{l=0}^B (-j)^{l+1} \cdot (2l+1) h_l^{(2)}(kr) P_l(\vec{k} \cdot \vec{r}),
\end{aligned} \tag{3}$$

where $D = K$ or L , $h_l^{(2)}(\cdot)$, and $P_l(\cdot)$ stand for the l -order Hankel function of the second kind and the l -order Legendre function, respectively. T_B is the truncation length and related to the diameter of the cubic in l th layer and the numerical accuracy.

Since the generation of near-field matrix is a highly intensive work in computation of MLFMM, the implementation of GPU or multi-GPU can significantly speedup the procedure even with RWG-to-RWG rather than triangle-to-triangle scheme. All the RWG functions are stored as two copies, namely, testing chain and basis chain, and each thread on GPU deals with one or more nonzero matrix elements by accessing corresponding data from the chains. This scheme can easily extend to multi-GPU case by splitting the whole task into subtasks. For example, if there are 2 GPUs, namely, GPU-0 and GPU-1, the chain can be split as $\{f_i^t\}_{i=0}^{N/2-1}$ and $\{f_i^t\}_{i=N/2}^N$, which makes each GPU has a $N/2 \times N$ sparse matrix to deal with. Considering the asynchronous launching scheme of kernel functions in CUDA, the control returns to CPU after launch immediately, which means a duty waste

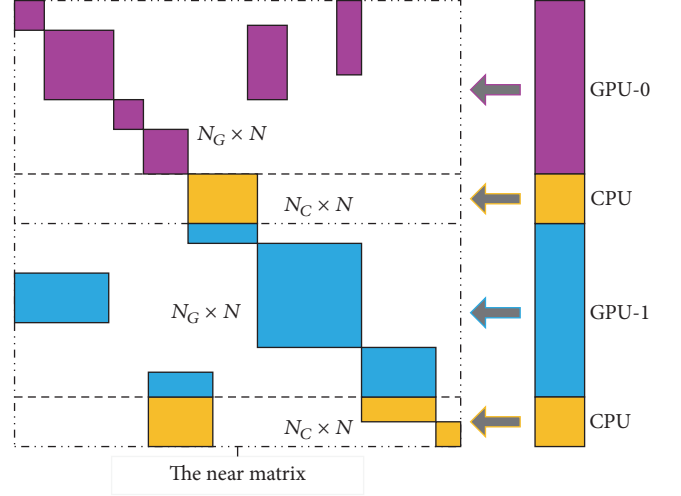


FIGURE 1: The subdivisions of the near matrix and the task assignments.

for CPU when a thread is working on GPU. Therefore, it is necessary to establish a heterogeneous scheme for coordination between CPU and GPU. For this reason, each near matrix is further divided into two parts with N_G and N_C rows, respectively, as shown in Figure 1. All the tasks can be executed concurrently while satisfying the asynchronous mechanism of GPU/CPU heterogeneous platform. This kind of subdivisions can accelerate the sparse matrix-vector productions (SpMVP). The determination of N_G and N_C cannot be easily derived from mathematics; however, the empirical value can be obtained from numerical simulation and curve fitting, in which the optimum solution can be refined by parameter scanning, as shown in Figure 2. Considering the coexistence of multicore CPU and multi-GPU, n_C and n_G stand for the number of cores in CPU and number of GPU, respectively. The sampling points were obtained from sphere scatterings with radius changing from one to six wavelengths. As a result, for the case of $n_C = 4$ and $n_G = 2$, the optimum solution of $N_C/(N/2)$ equals 0.016 and 0.083 for single and double precision, respectively.

The implementation of aggregation and disaggregation at finest level on GPU was proposed by means of allocating a thread to each spectrum point [16]. To increase the utilization of GPU on Kepler architecture (GK110) further, which has a maximum value of 32 threads in one warp, a smart scheme is designed with two steps. Firstly, all the cubes are grouped into each GPU evenly. Secondly, one warp is assigned to a certain cube, in which one thread is assigned to one or more RWG functions immediately. Taking the advantage of the hardware architecture in Kepler GK110, the shuffle instruction "`__shuffl()`" can efficiently calculate the reductive summation in register rather than shared memory [14]. Meanwhile, all the 32 threads in a warp can read the data from constant memory according to a certain spectrum point through the read-only cache by using the instruction "`__ldg()`" or "`__restrict__`".

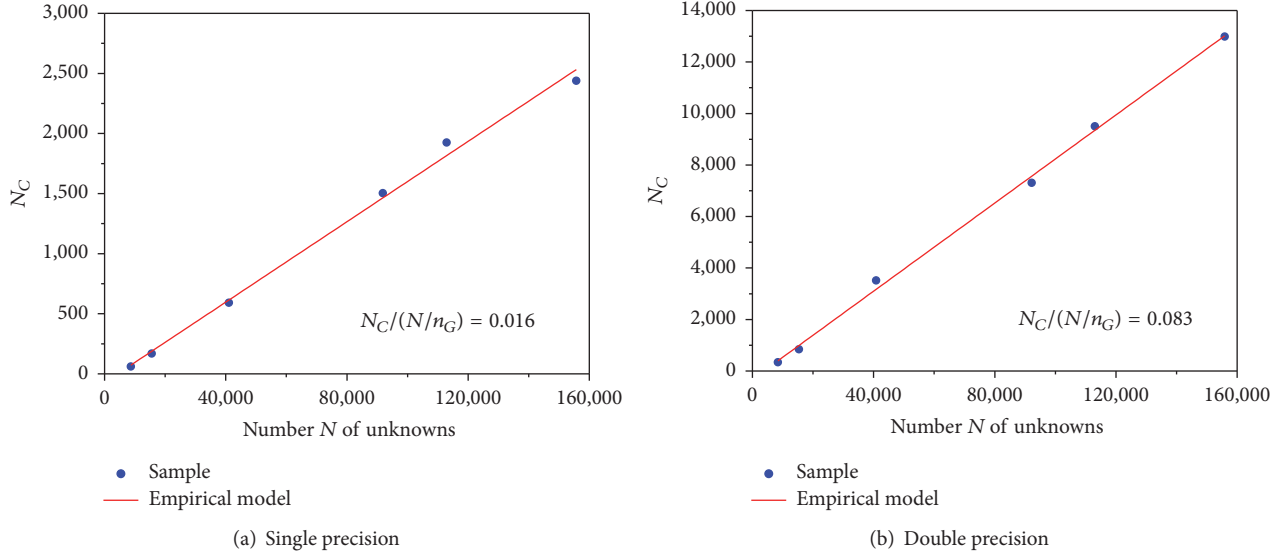


FIGURE 2: N_C as a function of N/n_G with $n_G = 2$.

Unlike the strategy of thread-based task assignment proposed for aggregation and disaggregation at coarser level [16], we make a further step in data storage by using the four times larger texture memory in Kepler than Fermi. Since the local inter-/anterpolation accesses neighboring data frequently, it had better store data in a certain pattern form looking like the geometric topology in texture memory. As is pointed out in [27], the texture cache is optimized for 2D spatial locality. Therefore, the threads in one warp reading close-set texture addresses can acquire hardware acceleration and achieve the best performance. With texture memory, the process from coarser level towards finest level can also be executed efficiently. In detail, after all the cubes at child level are grouped evenly in every device (i.e., GPU), a thread will be assigned to give a cube for a spectrum point at this level. By fetching the data from global memory, the information can be organized into a 3D CUDA array that is bound to the layer of texture memory. Then, the cube receives data disaggregated from its parent level by applying local anterpolation within texture memory. All this kind of tasks for cubes at child level can be executed concurrently and all the layers of texture memory assigned can be flushed for the subsequent requests.

2.2. Principle of ACA and Its Optimization on GPU. The ACA is a purely algebraic algorithm [8, 9], aiming at independence from the integral kernel, that is, Green's function, which makes it different from MLFMM. The main idea of ACA is based on the compressing of a rank deficient system, which corresponds to the submatrix representing interactions between two well-separated groups of RWGs. Therefore, the MVP of this kind of submatrices can be efficiently calculated by using the factorial forms [9]. In ACA, the MVP is divided into near- and far-field interactions, which leads to the same data structure as that in MLFMM, that is, the Octree structure, and forms a hierarchical representation of far-field submatrices. Hereby we use $Z_{m,n}^l$ to denote the $m \times n$

submatrix for interaction between group m and group n at the l th-level with indicating a well-separated situation. Then, it can be approximated as

$$Z_{m,n}^l \approx \tilde{Z}_{m,n}^l = U_{m,k}^l V_{k,n}^l, \quad (4)$$

$$k \approx \text{rank}(U_{m,n}^l) < \min\{m, n\} \quad (5)$$

which satisfies

$$\|Z_{m,n}^l - U_{m,k}^l V_{k,n}^l\|_F < \varepsilon_{ACA} \|Z_{m,n}^l\|_F, \quad (6)$$

where $\|\cdot\|_F$ is the Frobenius norm of a matrix and ε_{ACA} is a given threshold. The workflow of ACA can be depicted as in the following steps with initial value of $k = 1$ and $i_k = 1$.

Step 1. Generate $v^{(k)}$ as the i th row of $Z_{m,n}^l$ and update it.

$$(v^{(k)})_j \leftarrow (v^{(k)})_j - \sum_{i=1}^{k-1} (u^{(i)})_k (v^{(i)})_j. \quad (7)$$

Step 2. If $(v^{(k)})_j = 0, \forall j$, then $i_k \leftarrow i_k + 1$ and go back to Step 1; otherwise, normalize the vector with its maximum element,

$$\begin{aligned} |(v^{(k)})_{s_k}| &= \max_j \{|(v^{(k)})_j|\}, \\ (v^{(k)})_j &\leftarrow \frac{(v^{(k)})_j}{(v^{(k)})_{s_k}}, \quad \forall j. \end{aligned} \quad (8)$$

Step 3. Generate $u^{(k)}$ as the s_k th row of $Z_{m,n}^l$ and update it,

$$(u^{(k)})_j \leftarrow (u^{(k)})_j - \sum_{i=1}^{k-1} (u^{(i)})_j (v^{(i)})_{s_k}. \quad (9)$$

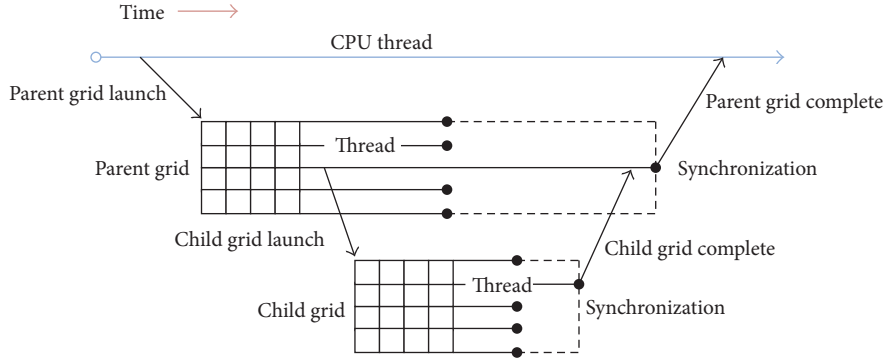


FIGURE 3: Flowchart of dynamic parallelism.

Step 4. Generate $U_{m,k}^l$ and $V_{k,n}^l$, where

$$U_{m,k}^l = [u^{(1)}, \dots, u^{(k)}],$$

$$V_{k,n}^l = \begin{bmatrix} v^{(1)} \\ \vdots \\ v^{(k)} \end{bmatrix}. \quad (10)$$

Step 5. The feedback system will keep updating by $k \leftarrow k + 1$ and $i_k \leftarrow i_k + 1$ until the condition in (5) is satisfied.

Obviously, it is convenient to employ both threadgrid and threadblock to take charge of one dimension. The total number of threads in each block is selected as 256, by means of 8 warps. The RWG functions, no matter what it is seen as, basis or test function, can be stored in shared memory during the generation of factorial form of a submatrix. Meanwhile, the submatrices U and V are stored in column- and row-major order, respectively. For the task assignment, 2^l warps perform the ACA calculation in one submatrix at the $(L - l)$ th level. However, this arrangement has no worry about insufficient blocks or logic error for $l = 0, 1, 2, 3$ until $l = 4$, because there is no synchronization mechanism between different threadblocks. In this paper, we realize one threadblock to one submatrix even at $(l \geq 4)$ by launching a child CUDA kernel function during the generation of new row or column vector [25]. The number of threads enabled in this so-called child kernel is equal to the length of the row or column vector and they calculate only one entry of the vector. It is worth emphasizing that an explicit synchronization between parent and child kernels should be adjusted in advance, which ensures that all the tasks assigned to child kernel are ultimately completed before logic and data operates on parent kernel. This treatment can be realized by the specific “dynamic parallelism” [28] in Kepler GK110 (Table 1) and a vivid flowchart is shown in Figure 3.

After the ACA operation, the MoM matrix is converted into an H -matrix that greatly reduces the storage and speeds up the MVPs. The upcoming procedure is to calculate massive

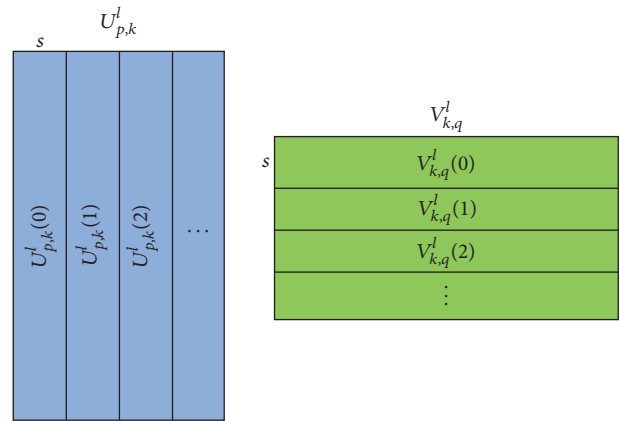


FIGURE 4: The segmentation scheme.

MVPs, which is still time consuming even though the H -matrix is used. In this paper, the batched matrix-vector productions (bMVP) are considered to deal with the massive computation [25]. The main idea of bMVP is to apply the 2D form of threadblock with $\text{dim3}(\text{pth}, \text{gridDimy})$ to calculate all the MVPs. The column in U and the row in V are performed concurrently, such that all segments (column or row) are with the same size except the last part, as shown in Figure 4. The result of $y = V_{k,n}^l(i)x$ is stored in the shared memory as an intermediate buffer and then the result of $z = U_{m,k}^l(i)y$ is accumulated into the result by reductive summation in shared memory. If we let s be equal to 256, there will be 64 threads in a group with the same ID in y -direction to do multiplication and the vector x can be reused in registers. Therefore, each threadblock can deal with 8 rows of V matrix and at most 32 threadblocks ($\text{gridDimy} = 32$) are needed to calculate the MVP.

2.3. Principle of CG-FFT, Multilayered Green's Functions, and Its Optimization on GPU. The CG-FFT [11] is one of the most classical methods with iterative procedure and many applications have been found in different areas such as algebra, signal processing, computational geometry, and CEM, especially in

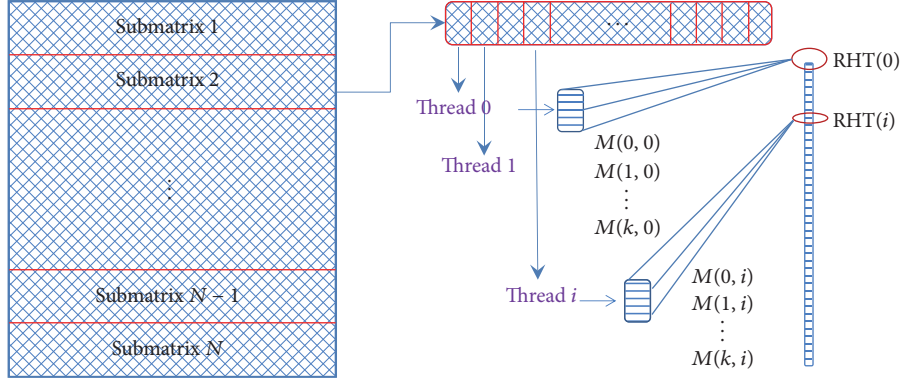


FIGURE 5: Flowchart of matrix partition for threads assignment.

MoM based algorithms [29]. The pseudocode of traditional CG-FFT can be depicted as

$$\begin{aligned}
 x &= x_0, \quad \text{initial value} \\
 r_0 &= b - Ax_0, \\
 p_0 &= s_0 = A^H r_0, \\
 \gamma_0 &= \|s_0\|_2^2 \\
 &\text{for } k = 0, 1, 2, \text{ until convergence} \\
 q_k &= Ap_k, \quad \text{MVP} \\
 \alpha_k &= \gamma_k / \|q_k\|_2^2, \\
 x_{k+1} &= x_k + \alpha_k p_k, \\
 r_{k+1} &= r_k - \alpha_k q_k, \\
 s_{k+1} &= A^H r_{k+1}, \quad \text{MVP} \\
 \gamma_{k+1} &= \|s_{k+1}\|_2^2, \\
 \beta_k &= \gamma_{k+1} / \gamma_k, \\
 p_{k+1} &= s_{k+1} + \beta_k p_k,
 \end{aligned}$$

where A^H is the conjugate transpose of matrix A and k stands for the iteration round. Obviously, the MVP operation dominates the most computation source and needs to be optimized. As we mentioned before, after a multiprocessor is assigned one or more threadblocks to execute, it will divide them into warps and each warp will be scheduled by a warp scheduler. The full efficiency can be realized when all 32 threads of a warp agree on their execution path. Considering the Kepler GK110 platform, the maximum threadblocks in one stream multiprocessor are 16 and each SMX contains 192 ALUs. An optimized parallelization can be realized by the so-called “single instruction multiple thread (SIMT)” [14]. The flowchart of this optimized CG-FFT on GPU is depicted in Figure 5, in which the “RHT” stands for right-hand term in MoM matrix equation.

As the matrix is partitioned into N submatrices with at least $(N - 1)$ of them having the same size, each submatrix can also be partitioned into pieces and each piece occupies a certain thread. Just like the realization in OpenMP-CUDA-MLFMM, the hardware instruction “__shufll()” is

used instead of the shared memory to do reductive summation. This makes the performance even more efficient than the famous CUBLAS library. That is because the shuffle instruction is more efficient and reduces the usage of shared memory with increasing the occupancy.

A brief review of dyadic Green’s functions in planar multilayered medium structure is also necessary in this part. The most important one is the mixed potential integral equation (MPIE), based on which the MoM can be established [30–35].

$$\vec{E} = -j\omega\mu_0 \left\langle \vec{G}^A; \vec{J} \right\rangle + \frac{1}{j\omega\epsilon_0} \nabla \left(\left\langle G^\Phi; \nabla' \cdot \vec{J} \right\rangle \right), \quad (11)$$

where the dyadic Green’s functions can be presented as

$$\vec{G}^A = \begin{bmatrix} G_{xx}^A & 0 & G_{xz}^A \\ 0 & G_{xx}^A & G_{yz}^A \\ G_{zx}^A & G_{zy}^A & G_{zz}^A \end{bmatrix}. \quad (12)$$

One of the most efficient ways to evaluate the Green’s functions through Sommerfeld Integral (SI) from the spectral to spatial domain is the discrete complex image method (DCIM). According to the analysis in [30], the DCIM is suitable for near-field region ($\rho \leq 0.05\lambda$) by calculating three terms, namely, the quasi-static term (G_{Q-S}), the surface wave term (G_{SWP}), and the complex image term (G_{CIM}), as shown below.

$$G(\rho) = \frac{A}{4\pi} (G_{Q-S} + G_{SWP} + G_{CIM}), \quad (13a)$$

$$G_{Q-S} = G|_{\rho \rightarrow \infty} \cdot \frac{e^{-jk_0\rho}}{\rho}, \quad (13b)$$

$$G_{SWP} = -2\pi j \sum_i^{N_{SWP}} \text{Res}_i H_0^{(2)}(k_{\rho i} \rho) k_{\rho i}, \quad (13c)$$

$$G_{CIM} = \sum_{i=1}^{N_c} a_i \frac{e^{-jk_0 r_i}}{r_i}, \quad (13d)$$

where $H_0^{(2)}$ stand for the zero-order Hankel function of the second kind and Res_i stands for the residues of surface wave

poles on the complex spectrum plane. For far-field region ($\rho \geq 0.05\lambda$), both the surface and leaky wave should be considered, together with a branch cut integral contribution, as shown below.

$$\int_{SIP} (\bullet) dk_\rho = \int_{\Gamma} (\bullet) dk_\rho - 2\pi j \cdot \left(\sum_i^{N_{SWP}} R_{k_{pi}} + \sum_j^{N_{LWP}} R_{k_{pj}} \right), \quad (14a)$$

$$\int_{\Gamma} (\bullet) dk_\rho = \int_{\Gamma} [\tilde{G}^+(k_\rho) + \tilde{G}^-(k_\rho)] \cdot H_n^{(2)}(k_\rho \rho) k_\rho dk_\rho, \quad (14b)$$

where SIP stands for the Sommerfeld integral path, N_{SWP} and N_{LWP} stand for the number of extracted surface and leaky wave poles, respectively, Γ stands for the integral path along the branch cut, and \tilde{G}^+ and \tilde{G}^- are the spectral Green's functions along the top and bottom Riemann sheets of the branch cut, respectively [30]. With accurate evaluation of all the components in dyadic Green's functions, the MPIE can be solved by MoM with RWG functions, in which the matrix element is calculated as

$$\begin{aligned} Z_{mm} &= k_0^2 \sum_{n=1}^N I_n \int_{T_m} \int_{T_n} \vec{f}_n(\vec{r}') \cdot \vec{G}^A(\vec{r} | \vec{r}') \cdot \vec{f}_m(\vec{r}) ds' ds + \sum_{n=1}^N I_n \\ &\cdot \int_{T_m} \nabla \left(\int_{T_n} G^\Phi(\vec{r} | \vec{r}') (\nabla_s' \cdot \vec{f}_n(\vec{r}')) ds' \right) \cdot \vec{f}_m(\vec{r}) ds, \end{aligned} \quad (15)$$

where \vec{f}_n and \vec{f}_m stand for the basis and testing RWG functions, respectively. The right-hand term of the MoM matrix equation will be different from radiating, transmitting to scattering cases.

3. Numerical Examples

To verify the efficiency enhancement of the proposed optimization based on GPU/CPU heterogeneous platform, this section will demonstrate fruitful numerical examples, respectively, corresponding to the OpenMP-CUDA-MLFMM, the GPU-based ACA, and the deeply optimized CG-FFT. All the programming codes are compiled in CUDA-C environment, and the hardware configuration can be found in Table 2. Similar to Section 2, the numerical results are also separated into 3 groups. The correctness of proposed methods with MLFMM and ACA have been verified by the very good agreement between bistatic RCS and standard Mie solutions of PEC spheres, which will not be demonstrated in this section.

TABLE 2: Configurations of GPU/CPU platform of numerical examples.

Parameters	MLFMM	ACA	CG-FFT
CPU	Intel	Intel	Intel Xeon
Processor #	i5 4570	i5 4570	E5420
# of cores	4	4	4
Base frequency (GHz)	3.20	3.20	2.50
GPU	NVIDIA	NVIDIA	NVIDIA
Architecture	GK110	GK110	GK104
CUDA cores	2304	2304	960
Base clock (MHz)	863	863	980
Memory Config (MB)	3072	3072	2048
Memory BW (GB/s)	288	288	144
CUDA version	6.0	7.0 RC	4.2
# of GPU	2	2	1

TABLE 3: Variables definition of time consumption.

Variables	Description
t_M	Time for near matrix generation
t_S	Time for corresponding SpMVP
t_{AF}	Time for aggregation at finest level
t_{DF}	Time for disaggregation at finest level
t_{AS}	Time for aggregation towards coarsest level
t_{DS}	Time for disaggregation towards finest level

3.1. Numerical Results of OpenMP-CUDA-MLFMM. As a benchmark result to verify the robustness of algorithms, the scattering from the PEC NASA Almond at 7 GHz for VV polarization and that from the PEC NASA Ogive at 9 GHz for HH polarization are considered. These two PEC surfaces are discretized into refined triangles with edge length of about 0.1λ , which produce 8416 and 15516 RWG unknowns, respectively. The monostatic RCS curves with the incident angle as argument are obtained by the proposed method, as shown in Figure 6. From the comparison with measurement results, very good agreement can be found. Note that the interpretations labeled as “mid VV,” “high VV,” and “VV FERM” refer to Figure 5 in [36], and those labeled as “HH,” “VV,” “HH Cicero,” and “VV Cicero” refer to Figure 9 in [36]. To demonstrate the efficiency performance of the proposed OpenMP-CUDA-MLFMM, we need to define some variables to record time consumption in different procedures, as shown in Table 3.

By sampling on different number of unknowns, an approximate curve of $(t_M; t_S)$ and $(t_{AF} + t_{DF}; t_{AS} + t_{DS})$ can be fitted in a broad range, as shown in Figure 7. It can be clearly seen that the proposed method has higher efficiency than that reported in [16] based on the same Kepler GK110 architecture. It is worth pointing out that the translation is not included because both the proposed method and that in [16] have almost the same performance in this procedure.

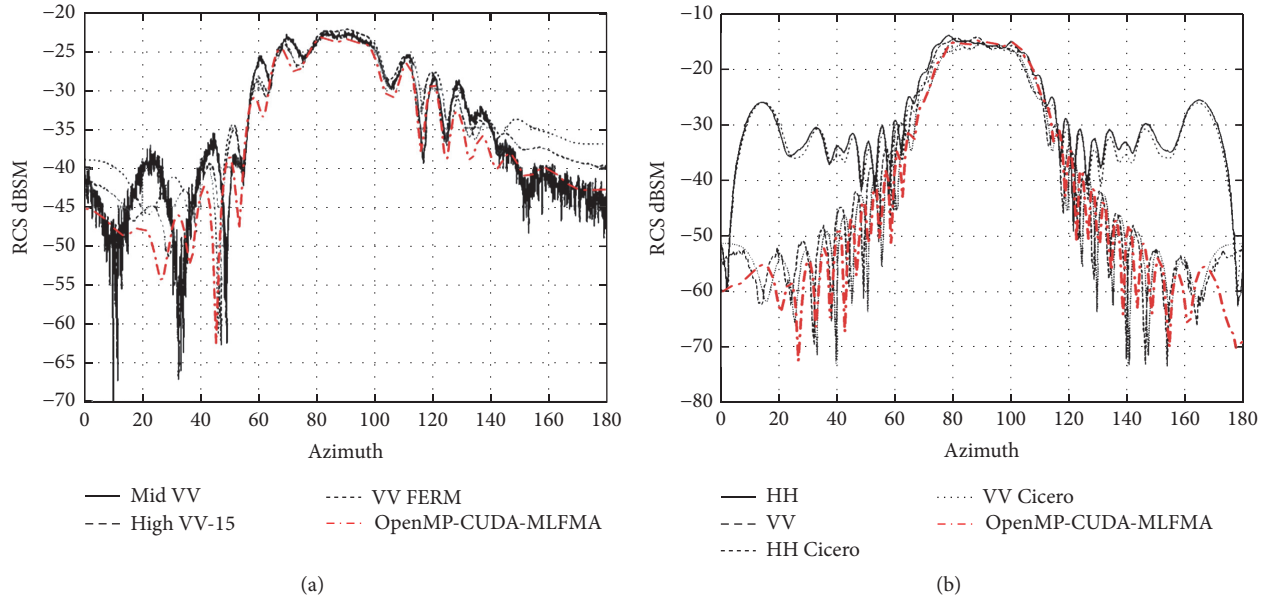


FIGURE 6: (a) The monostatic RCS at 7 GHz for VV polarization. (b) The monostatic RCS at 9 GHz for HH polarization.

3.2. Numerical Results of GPU-Based ACA. To verify the robustness of the proposed GPU-based ACA, the bistatic RCS from a rotor with four blades and a depressed cylindrical object are considered, as shown in Figure 8. Very good agreement can be seen between the proposed method and the traditional MoM on CPU. These two PEC surfaces are discretized into refined triangles with edge length of about 0.1λ , which produce 6636 and 4817 RWG unknowns, respectively.

To demonstrate the efficiency performance of the proposed GPU-based ACA, the scattering from a PEC sphere with radius of $n\lambda$ ($n = 1, 2, 3$, and 4) is considered. The number of generated RWG unknowns is 4774, 18468, 40950, and 72120, respectively. In this paper, the threshold in formula (6) is selected as $\epsilon_{ACA} = 10^{-3}$. The efficiency comparison between GPU and CPU platform in both the bMVP operations and the whole ACA scheme with single and double precision are shown in Figure 9. It can be seen that the speedup ratio of matrix compression by using ACA can achieve about 50~100 and 25~50 for single and double precision, respectively. Meanwhile, the speedup ratio of bMVP can achieve about 10~30 and 6~17 for single and double precision, respectively.

3.3. Numerical Results of Deeply Optimized CG-FFT. To validate the accuracy and efficiency of the proposed method, the quasiperiodical structures of flat lens on substrate ($\epsilon_r = 2.2$, $\mu_r = 1.0$) with a copper ground ($\sigma = 5.98 \times 10^7$ S/m) are considered, which consist of 15×15 and 33×33 Jerusalem crosses and generate 19561 and 85849 RWG unknowns, respectively, as shown in Figure 10. The flat lenses are illuminated by an orthogonal incident plane wave with polarization in the x

direction, where the incident information are $\theta = \pi$, $\varphi = 0$, $E_{0x} = 1$, and $E_{0y} = E_{0z} = 0$.

Since the MVP operation is the most time consuming part in CG-FFT, direct optimization from arithmetic programming point of view is a challenging topic and should be tested before applying to complicated structure. Therefore, both square and nonsquare matrices MVP are tested, from which a significant speedup ratio is observed comparing to the famous CUBLAS, as shown in Tables 4 and 5. For this experiment on arithmetic realization, the GPU occupancy of CUBLAS and that of the proposed method is 25% and 75%, respectively, while the usage of shared memory is 288 B and 10240 B, respectively. This can be seen as a great enhancement in hardware performance, which makes a speedup ratio of 1.4 in average on single GPU.

As is mentioned in Section 2, the right-hand term in MoM of multilayered structure is different from radiating, transmitting, and scattering cases. With an orthogonal incident wave, the right-hand term can be calculated as below.

$$V_m = -j\omega\epsilon_0 \int_{T_m} \vec{E}^{\text{inc}}(\vec{r}) \cdot \vec{f}_m(\vec{r}) ds, \quad (16)$$

$$\vec{E}^{\text{inc}}(\rho) = \vec{E}_0 e^{j(k_x x + k_y y + k_z d)} + \vec{R} e^{j(k_x x + k_y y - k_z d)},$$

where the calculation of reflection coefficient refers to [37] and d in the exponential term is the thickness of substrate. The relative error of iteration in CG-FFT for the case with 15×15 elements is shown in Figure 11 and the current distribution in centre of the case with 33×33 elements is shown in Figure 12. To enhance the efficiency further, we have realized the fast calculation of multilayered Green's functions

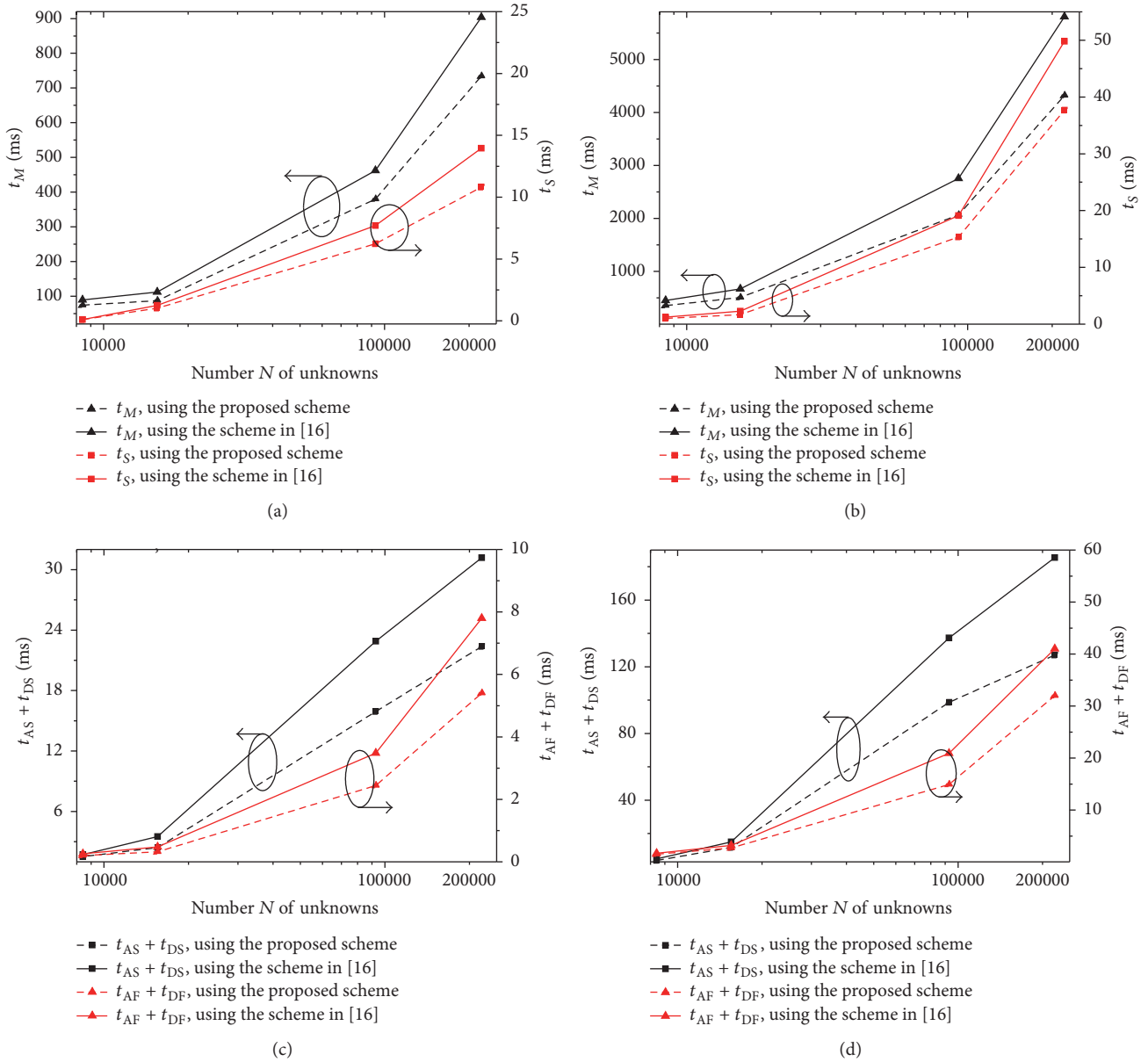


FIGURE 7: t_M and t_S as function of N with (a) single and (b) double precision; $t_{AF} + t_{DF}$ and $t_{AS} + t_{DS}$ as function of N with (c) single and (d) double precision.

on GPU/CPU heterogeneous platform [38], which will be implemented to the MPIE-MoM in future work.

4. Conclusions

In this paper, our recent works on high performance computing based on GPU/CPU heterogeneous platform and its application to EM scattering problems and planar multilayered medium structures are introduced. There are three typical applications analyzed, including a novel implementation of OpenMP-CUDA-MLFMM, a developed GPU-based ACA method, and a deeply optimized CG-FFT method.

Comparing to the MLFMM, the ACA method starts to accelerate computing with Green's functions; however, it is still worth mentioning that the data storage strategy of ACA needs to be further developed. This paper is to explain the coordination between GPU and CPU on a heterogeneous platform. In addition, the methodology of optimization through hardware instructions is also adopted. Following the trends of both parallel and distributed computing, the OpenMP-CUDA-MLFMM and ACA are realized on a 2-GPU platform. With fruitful numerical examples for the three kinds of algorithms, we can find obvious enhancement in efficiency. As the development in hardware world, it

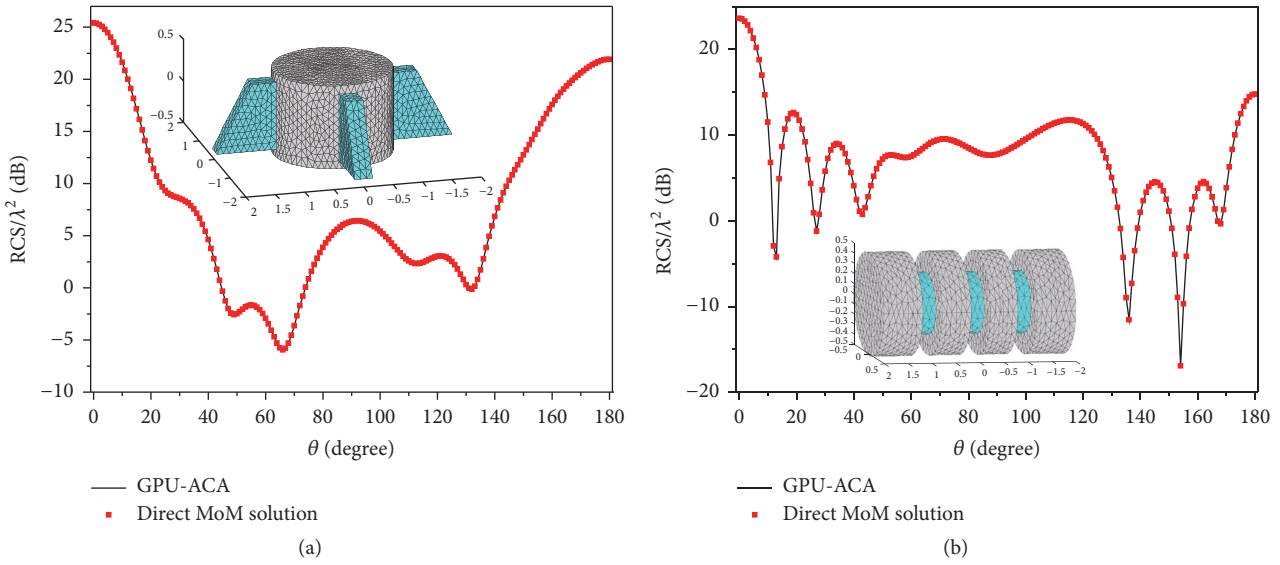


FIGURE 8: Bistatic RCS of (a) 4 blades rotor and (b) depressed cylindrical object.

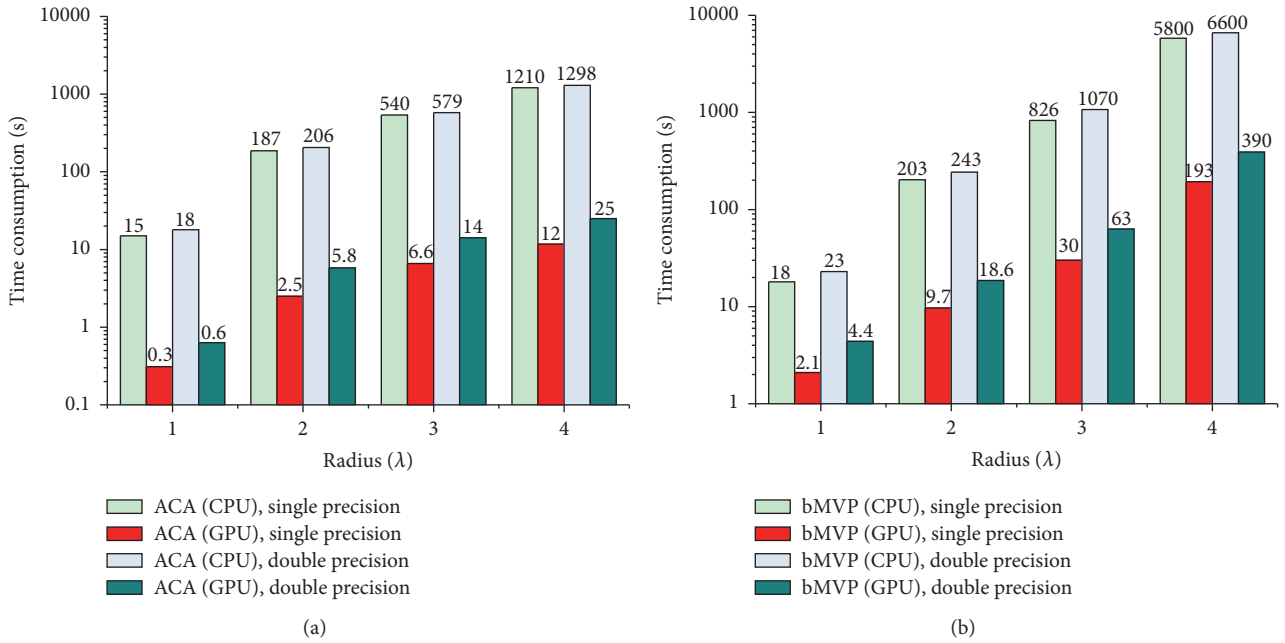


FIGURE 9: Efficiency comparison of (a) ACA and (b) bMVP.

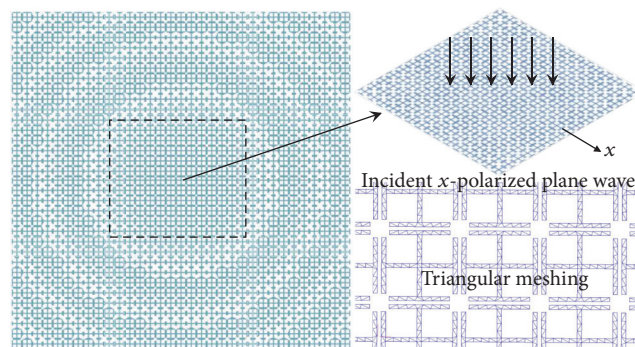


FIGURE 10: Geometry of flat lens on substrate and its meshing scheme.

TABLE 4: Comparison in MVP for square matrix.

Matrix dimension	CUBLAS (ms)	This paper (ms)
4,000	1.58	1.12
5,000	2.50	1.77
6,000	3.43	2.54
7,000	4.63	3.46
8,000	5.65	4.07
9,000	7.17	5.19
10,000	8.83	6.48
11,000	10.75	7.94
12,000	13.28	9.53

TABLE 5: Comparison in MVP for nonsquare matrix.

Matrix dimension	CUBLAS (ms)	This paper (ms)
1,700 × 9,000	1.69	1.10
1,800 × 9,000	1.58	1.17
1,900 × 9,000	1.71	1.22
2,900 × 15,000	4.28	2.95
3,000 × 15,000	4.00	2.98
3,100 × 15,000	4.69	3.16
4,900 × 25,000	11.48	8.24
5,000 × 25,000	11.19	8.44
5,200 × 25,000	11.29	8.72

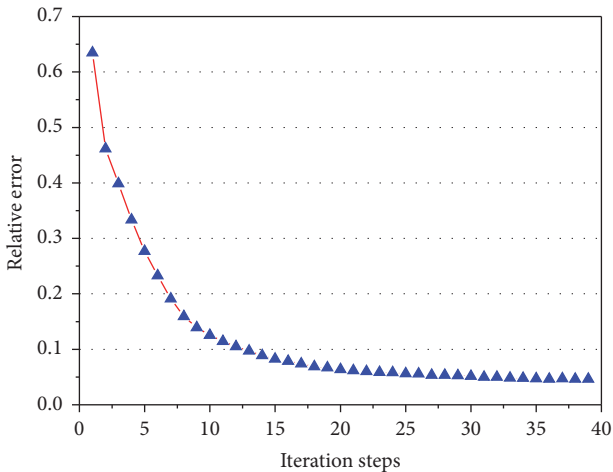


FIGURE 11: Relative error of iterations of the flat lens with 15 × 15 elements.

is worthy keeping an eye on different kinds of modules, including GPU, FPGA, and DSP. Meanwhile, it is also worthy keeping one on investigating and understanding the operating mechanism of heterogeneous computing.

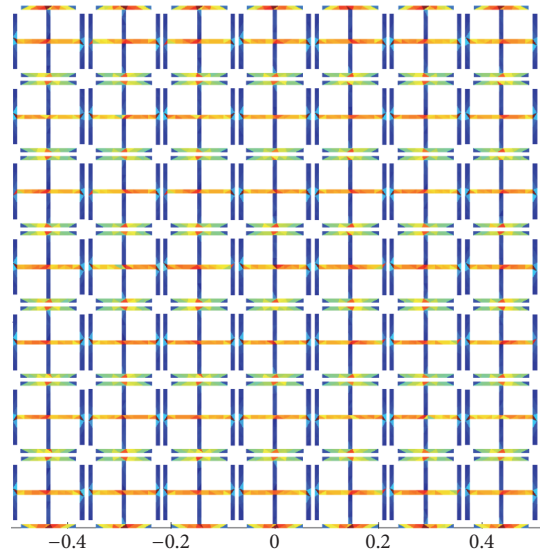


FIGURE 12: Current distribution in centre of the flat lens with 33 × 33 elements.

Disclosure

Zhe Song is now with Eindhoven University of Technology, TUE, The Netherlands.

Conflicts of Interest

The authors declare that there are no conflicts of interest regarding the publication of this paper.

Acknowledgments

This work was supported in part by the NSFC under Grants 61601121, 61401092, and 61302019.

References

- [1] W. C. Chew, J. M. Jin, E. Michielssen, and J. M. Song, *Fast and Efficient Algorithm in Computational Electromagnetics*, Artech House, Boston, USA, 2001.
- [2] J. M. Song and W. C. Chew, “Multilevel fast-multipole algorithm for solving combined field integral equations of electromagnetic scattering,” *Microwave and Optical Technology Letters*, vol. 10, no. 1, pp. 14–19, 1995.
- [3] E. Bleszynski, M. Bleszynski, and T. Jaroszewicz, “AIM: Adaptive integral method for solving large-scale electromagnetic scattering and radiation problems,” *Radio Science*, vol. 31, no. 5, pp. 1225–1251, 1996.
- [4] C.-F. Wang, F. Ling, J. Song, and J.-M. Jin, “Adaptive integral solution of combined field integral equation,” *Microwave and Optical Technology Letters*, vol. 19, no. 5, pp. 321–328, 1998.
- [5] J. R. Phillips and J. K. White, “A Precorrected-FFT method for electrostatic analysis of complicated 3-D structures,” *IEEE Transactions on Computer-Aided Design of Integrated Circuits and Systems*, vol. 16, no. 10, pp. 1059–1072, 1997.
- [6] X.-C. Nie, N. Yuan, and L.-W. Li, “Precorrected-FFT algorithm for solving combined field integral equations in electromagnetic

- scattering,” *Journal of Electromagnetic Waves and Applications*, vol. 16, no. 8, pp. 1171–1187, 2002.
- [7] S. M. Seo and J.-F. Lee, “A fast IE-FFT algorithm for solving PEC scattering problems,” *IEEE Transactions on Magnetics*, vol. 41, no. 5, pp. 1476–1479, 2005.
- [8] W. Leipzig, “A sparse matrix arithmetic based on H-matrices. Part I: introduction to Hmatrices,” *Computing*, vol. 62, no. 2, pp. 89–108, 1999.
- [9] W. Leipzig and S. Saarbrücken, “Adaptive low-rank approximation of collocation matrices,” *Computing*, vol. 70, no. 1, pp. 1–24, 2003.
- [10] A. Schroder, H.-D. Bruns, and C. Schuster, “Fast evaluation of electromagnetic fields using a parallelized adaptive cross approximation,” *IEEE Transactions on Antennas and Propagation*, vol. 62, no. 5, pp. 2818–2822, 2014.
- [11] M. F. Càtedra and E. Gago, “Spectral Domain Analysis of Conducting Patches of Arbitrary Geometry in Multilayer Media Using the CG-FFT Method,” *IEEE Transactions on Antennas and Propagation*, vol. 38, no. 10, pp. 1530–1536, 1990.
- [12] P. Pacheco, *An Introduction to Parallel Programming*, Elsevier, 2011.
- [13] D. P. Rodgers, “Improvements in multiprocessor system design,” *ACM SIGARCH Computer Architecture News*, vol. 13, no. 3, pp. 225–231, 1985.
- [14] NVIDIA corp., *CUDA, C Programming Guide Version 5.5*, 2013.
- [15] D. De Donno, A. Esposito, L. Tarricone, and L. Catarinucci, “Introduction to GPU computing and CUDA programming: a case study on FDTD,” *IEEE Antennas and Propagation Magazine*, vol. 52, no. 3, pp. 116–122, 2010.
- [16] J. Guan, S. Yan, and J.-M. Jin, “An OpenMP-CUDA implementation of multilevel fast multipole algorithm for electromagnetic simulation on multi-GPU computing systems,” *Institute of Electrical and Electronics Engineers. Transactions on Antennas and Propagation*, vol. 61, no. 7, pp. 3607–3616, 2013.
- [17] N. A. Gumerov and R. Duraiswami, “Fast multipole methods on graphics processors,” *Journal of Computational Physics*, vol. 227, no. 18, pp. 8290–8313, 2008.
- [18] K. Xu, D. Z. Ding, Z. H. Fan, and R. S. Chen, “Multilevel fast multipole algorithm enhanced by GPU parallel technique for electromagnetic scattering problems,” *Microwave and Optical Technology Letters*, vol. 52, no. 3, pp. 502–507, 2010.
- [19] M. Cwikla, J. Aronsson, and V. Okhmatovski, “Low-frequency MLFMA on graphics processors,” *IEEE Antennas and Propagation Letters*, vol. 9, pp. 8–11, 2010.
- [20] S. Li, R. Chang, A. Boag, and V. Lomakin, “Fast electromagnetic integral-equation solvers on graphics processing units,” *IEEE Antennas and Propagation Magazine*, vol. 54, no. 5, pp. 71–87, 2012.
- [21] S. Peng and C.-F. Wang, “Precorrected-FFT method on graphics processing units,” *Institute of Electrical and Electronics Engineers. Transactions on Antennas and Propagation*, vol. 61, no. 4, part 2, pp. 2099–2107, 2013.
- [22] S. Peng and Z. Nie, “Acceleration of the method of moments calculations by using graphics processing units,” *IEEE Transactions on Antennas and Propagation*, vol. 56, no. 7, pp. 2130–2133, 2008.
- [23] B. M. Kolundzija and D. P. Zoric, “Efficient evaluation of MoM matrix elements using CPU and/or GPU,” in *Proceedings of the 6th European Conference on Antennas and Propagation, EuCAP 2012*, pp. 702–706, cze, March 2012.
- [24] X. Mu, H.-X. Zhou, K. Chen, and W. Hong, “Higher order method of moments with a parallel out-of-core LU solver on GPU/CPU platform,” *Institute of Electrical and Electronics Engineers. Transactions on Antennas and Propagation*, vol. 62, no. 11, pp. 5634–5646, 2014.
- [25] X. Mu, H.-X. Zhou, Z. Song, W.-B. Kong, and W. Hong, “An implementation of the ACA on GPU platform,” in *Proceedings of the Asia-Pacific Microwave Conference, APMC 2015*, chn, December 2015.
- [26] Z. Song, Y. Zhang, X. Mu, H.-X. Zhou, and W. Hong, “Full wave analysis of millimeter wave quasi-periodical structure for antenna applications by method of moments and its conjugate gradient solution on GPU/CPU platform,” in *Proceedings of the 2015 1st IEEE International Conference on Computational Electromagnetics, ICCEM 2015*, pp. 41–42, hkg, February 2015.
- [27] NVIDIA corp., *NVIDIA’s Next Generation CUDA Compute Architecture: Kepler GK110*, 2013.
- [28] J. Marco and M. Taufer, “Performance impact of dynamic parallelism on different clustering algorithms on GPUs,” in *Proceedings of NVIDIA GPU Tech Conf*, 2014.
- [29] C.-F. Wang, F. Ling, and J.-M. Jin, “A Fast Full-Wave Analysis of Scattering and Radiation from Large Finite Arrays of Microstrip Antennas,” *IEEE Transactions on Antennas and Propagation*, vol. 46, no. 10, pp. 1467–1474, 1998.
- [30] Z. Song, H.-X. Zhou, K.-L. Zheng, J. Hu, W.-D. Li, and W. Hong, “Accurate evaluation of green’s functions for a lossy layered medium by fast extraction of surface-and leaky-wave modes,” *IEEE Antennas and Propagation Magazine*, vol. 55, no. 1, pp. 92–102, 2013.
- [31] K. A. Michalski and J. R. Mosig, “Multilayered media Green’s functions in integral equation formulations,” *IEEE Transactions on Antennas and Propagation*, vol. 45, no. 3, pp. 508–519, 1997.
- [32] W. C. Chew, *Waves and Fields in Inhomogeneous Media, ser. Electromagn. Waves Piscataway*, Waves Piscataway, IEEE Press, New York, USA, 1995.
- [33] R. E. Collin, *Field Theory of Guided Waves*, Mc-Graw Hill, New York, NY, USA, 1960.
- [34] D. G. Fang, J. J. Yang, and G. Y. Delisle, “Discrete image theory for horizontal electric dipoles in a multilayered medium,” *IEEE Proceedings H: Microwaves, Antennas and Propagation*, vol. 135, no. 5, pp. 297–303, 1988.
- [35] Y. L. Chow, J. J. Yang, and G. E. Howard, “A Closed-Form Spatial Green’s Function for the Thick Microstrip Substrate,” *IEEE Transactions on Microwave Theory and Techniques*, vol. 39, no. 3, pp. 588–592, 1991.
- [36] A. C. Woo, M. J. Schuh, M. L. Sanders, H. T. G. Wang, and J. L. Volakis, “Benchmark Radar Targets for the Validation of Computational Electromagnetics Programs,” *IEEE Antennas and Propagation Magazine*, vol. 35, no. 1, pp. 84–89, 1993.
- [37] D. Vande Ginste, E. Michielssen, F. Olyslager, and D. De Zutter, “An efficient perfectly matched layer based multilevel fast multipole algorithm for large planar microwave structures,” *IEEE Transactions on Antennas and Propagation*, vol. 54, no. 5, pp. 1538–1548, 2006.
- [38] Z. Song, “Fast and Accurate Evaluation of Multilayered Green’s Functions by Extracting Surface and Leaky Wave Poles Based on GPU/CPU Heterogeneous Platform,” in *Proceedings of the IEEE Int. Workshop on Electromagnetics. (iWEM2017)*, London, UK, 2014.

Research Article

Acceleration of Augmented EFIE Using Multilevel Complex Source Beam Method

Lianning Song, Yongpin Chen, Ming Jiang, Jun Hu, and Zaiping Nie

Department of Microwave Engineering, University of Electronic Science and Technology of China, Chengdu, Sichuan 610054, China

Correspondence should be addressed to Jun Hu; hujun@uestc.edu.cn

Received 20 April 2017; Accepted 12 June 2017; Published 13 July 2017

Academic Editor: Song Guo

Copyright © 2017 Lianning Song et al. This is an open access article distributed under the Creative Commons Attribution License, which permits unrestricted use, distribution, and reproduction in any medium, provided the original work is properly cited.

The computation of the augmented electric field integral equation (A-EFIE) is accelerated by using the multilevel complex source beam (MLCSB) method. As an effective solution of the low-frequency problem, A-EFIE includes both current and charge as unknowns to avoid the imbalance between the vector potentials and the scalar potentials in the conventional EFIE. However, dense impedance submatrices are involved in the A-EFIE system, and the computational cost becomes extremely high for problems with a large number of unknowns. As an exact solution to Maxwell's equations, the complex source beam (CSB) method can be well tailored for A-EFIE to accelerate the matrix-vector products in an iterative solver. Different from the commonly used multilevel fast multipole algorithm (MLFMA), the CSB method is free from the problem of low-frequency breakdown. In our implementation, the expansion operators of CSB are first derived for the vector potentials and the scalar potentials. Consequently, the aggregation and disaggregation operators are introduced to form a multilevel algorithm to reduce the computational complexity. The accuracy and efficiency of the proposed method are discussed in detail through a variety of numerical examples. It is observed that the numerical error of the MLCSB-AEFIE keeps constant for a broad frequency range, indicating the good stability and scalability of the proposed method.

1. Introduction

The method of moments (MoM) [1] for solving electric field integral equation (EFIE) has received intensive study in the analysis of electromagnetic (EM) radiation, scattering, and circuit problems in recent years. However, the commonly used EFIE with RWG basis function suffers from a “low-frequency breakdown” problem [2] when the frequency decreases and/or when the mesh is refined. In this situation, EFIE is dominated by the scalar potentials while the contribution from the vector potentials is overwhelmed due to the finite machine precision. Since the scalar potential term is singular, the EFIE matrix system becomes extremely ill-conditioned and results in convergence issue when the iterative solver is applied.

To address this difficulty, several methods have been proposed in the past years. A widely used remedy is the loop-tree or loop-star decomposition [3] which decouples the magneto- and electrostatic physics. However, the extraction of global loops is difficult for complex interconnecting structures, and the system matrix becomes ill-conditioned as

the frequency increases. On the other hand, the convergence issue can be improved by a Calderón preconditioner [4] when iterative solvers are applied. To avoid the involved loop searching process, alternative formulations have been proposed by separating current and charge, such as the current and charge integral equation (CCIE) [5], split potential integral equation (SPIE) [6, 7], and augmented electric field integral equation (A-EFIE) [8–11]. In the A-EFIE method, the contributions of the vector potentials and the scalar potentials are separated by adding charge as extra unknowns, where the current continuity equation is explicitly enforced. Frequency scaling is then implemented to stabilize the system equation. The resulting impedance matrix of A-EFIE has the characteristics of a saddle point matrix and is well-conditioned at low frequencies. Recently, the perturbation method is introduced to enhance the accuracy of A-EFIE at extremely low frequencies [12]. The augmented equivalence principle algorithm (A-EPA) [13] and discontinuous Galerkin (DG) method [14] are combined with the A-EFIE for domain decomposition problems.

As the number of unknowns increases, a fast algorithm has to be incorporated into the iterative solver to reduce the operation complexity of the matrix-vector product (MVP). Such fast algorithms should be low-frequency stable; for instance, the low-frequency multilevel fast multipole algorithm (LF-MLFMA) [15], the multilevel accelerated Cartesian expansion algorithm (MLACEA) [16], the multilevel adaptive cross-approximation (MLACA) algorithm [17], and fast Fourier transform (FFT) [18] are eligible candidates for such purpose. Recently, a complex source beam-method of moment (CSB-MoM) is proposed to accelerate the far-field interactions of MoM at midfrequencies [19]. The object is first divided into groups and complex source beams (CSBs) are used to expand the fields of the basis functions residing in each group [20, 21]. A multilevel version of this method is developed in [22]. To further improve the computational efficiency, a nested complex source beam (NCSB) method is proposed by utilizing an equivalent relationship between adjacent levels [23]. Since the CSBs are exact solutions of Maxwell's equations, any arbitrary EM fields can be expanded in terms of a set of CSBs [20, 24]. Therefore, this method can be extended to solve the low-frequency problems without any theoretical barriers.

This paper is organized as follows. The basis formulations of CSB-MoM and A-EFIE are briefly reviewed in Section 2. In Section 3, the CSB-MoM is integrated into the A-EFIE system to remedy the low-frequency breakdown problem. The detailed derivation of the CSB expansions for A-EFIE is first presented. The aggregation/disaggregation, translation operators for a multilevel CSB method are then discussed. Finally, numerical examples are summarized in Section 4 to demonstrate the validity and efficiency of the proposed method.

2. Theory Background

Given a 3D perfectly electrical conducting (PEC) body defined by its surface, the conventional MoM formulation can be applied to the electric field integral equation (EFIE), leading to a matrix equation of the form

$$\mathbf{Z}\mathbf{j} = \mathbf{b}, \quad (1)$$

where \mathbf{j} is the unknown vector for the surface current density, \mathbf{b} is the excitation vector, and \mathbf{Z} is the dense impedance matrix. The impedance matrix can be expressed as

$$\mathbf{Z}_{ij} = \int_{S_i} \mathbf{f}_i(\mathbf{r}) \cdot \int_{S_j} \overline{\overline{\mathbf{G}}}(\mathbf{r}, \mathbf{r}') \mathbf{f}_j(\mathbf{r}') dS', \quad (2)$$

where

$$\overline{\overline{\mathbf{G}}}(\mathbf{r}, \mathbf{r}') = \left[\overline{\overline{\mathbf{I}}} + \frac{\nabla\nabla}{k_0^2} \right] g(\mathbf{r}, \mathbf{r}') \quad (3)$$

is the dyadic Green function and $g(\mathbf{r}, \mathbf{r}') = e^{ik_0|\mathbf{r}-\mathbf{r}'|}/4\pi|\mathbf{r}-\mathbf{r}'|$ is the scalar Green function. Moreover, $\mathbf{f}_j(\mathbf{r}')$ and $\mathbf{f}_i(\mathbf{r})$ denote the RWG basis functions for expanding surface current and Galerkin testing, respectively. This equation suffers from the

low-frequency breakdown problem, because the contribution of the vector potential is swamped by that of the scalar potential at low frequencies due to the finite machine precision.

2.1. Formulation of CSB-MoM for EFIE. In CSB-MoM method, the MVP acceleration of $\mathbf{Z}\mathbf{j} = \mathbf{b}$ is achieved through a FMM-like near-field and far-field decomposition. For the far-field interactions $\mathbf{Z}_F\mathbf{j}$ between well separated groups, the MVP are carried out by a series of CSBs launched on a complex equivalence surface enclosing each group:

$$\mathbf{Z}_F\mathbf{j} = \mathbf{Z}_{mm'}\mathbf{j}_{m'} = \sum_{\varepsilon, \varepsilon'=\theta, \phi} (\mathbf{W}_m^\varepsilon)^T \mathbf{T}_{L,mm'}^{\varepsilon\varepsilon'} \mathbf{W}_{m'}^{\varepsilon'} \mathbf{j}_{m'}, \quad (4)$$

where m and m' denote the observation and source groups and L indicates the finest level (single level in CSB-MoM). $\mathbf{W}_{m'}^\varepsilon$ and $\mathbf{W}_m^{\varepsilon'}$ are the expansion matrices for both θ and ϕ components, which can be obtained by the far-field matching of basis functions in groups m and m' , respectively [19]. Superscript T stands for the transpose of the corresponding matrix. It needs to be emphasized that only θ and ϕ components are considered in CSBs, since the far-field radiation fields contain only θ and ϕ components.

By using the expansion matrices, the CSB expansion coefficients for the source group m' can be expanded from the surface currents as

$$\mathbf{s}_{L,m'} = \begin{bmatrix} \mathbf{s}_{L,m'}^\theta \\ \mathbf{s}_{L,m'}^\phi \end{bmatrix} = \begin{bmatrix} \mathbf{W}_{m'}^\theta \\ \mathbf{W}_{m'}^\phi \end{bmatrix} \mathbf{j}_{m'}. \quad (5)$$

$\mathbf{T}_{L,mm'}^{\varepsilon\varepsilon'}$ in (4) is the translation matrix, of which the elements are expressed as

$$\left[\mathbf{T}_{L,mm'}^{\varepsilon\varepsilon'} \right]_{qq'} = \hat{\varepsilon}_q \cdot \overline{\overline{\mathbf{G}}}(\tilde{\mathbf{r}}_{L,m}^q, \tilde{\mathbf{r}}_{L,m'}^{q'}) \cdot \hat{\varepsilon}_{q'}, \quad (6)$$

where $\hat{\varepsilon}_q$ and $\hat{\varepsilon}_{q'}$ denote the unit vectors of q th and q' th CSB, respectively. The complex position vectors $\tilde{\mathbf{r}}_{L,m}^q$ and $\tilde{\mathbf{r}}_{L,m'}^{q'}$ are the launch points of CSBs associated with groups m and m' . $\overline{\overline{\mathbf{G}}}(\tilde{\mathbf{r}}_{L,m}^q, \tilde{\mathbf{r}}_{L,m'}^{q'})$ is the dyadic Green function with complex arguments. The directional property of CSBs can be used to reduce the computational cost in the translation procedure.

2.2. Formulation of A-EFIE. In the augmented electric field integral equation, the surface current is discretized by the normalized RWG basis function, which is modified by removing the length of the common edge

$$\rho_i(\mathbf{r}) = \begin{cases} \frac{\mathbf{r} - \mathbf{r}_i^+}{2A_i^+}, & \mathbf{r} \in T_i^+ \\ \frac{\mathbf{r}_i^- - \mathbf{r}}{2A_i^-}, & \mathbf{r} \in T_i^- \\ 0, & \text{otherwise,} \end{cases} \quad (7)$$

where A_i^\pm are the area of triangles T_i^\pm , \mathbf{r}_i^\pm are the free vertices of the two triangles. On the other hand, the surface charge

density is approximated by the pulse function defined on each triangle, which is expressed as

$$h_i(\mathbf{r}) = \begin{cases} \frac{1}{A_i}, & \mathbf{r} \in T_i \\ 0, & \text{otherwise.} \end{cases} \quad (8)$$

Combining EFIE in (1) and the current continuity condition between current and charge, we can arrive at the A-EFIE equation

$$\begin{bmatrix} \bar{\mathbf{V}} & \bar{\mathbf{D}}^T \cdot \bar{\mathbf{P}} \\ \bar{\mathbf{D}} & k_0^2 \bar{\mathbf{I}} \end{bmatrix} \cdot \begin{bmatrix} ik_0 \mathbf{j} \\ c_0 \phi \end{bmatrix} = \begin{bmatrix} \eta_0^{-1} \mathbf{b} \\ 0 \end{bmatrix} \quad (9)$$

with

$$\bar{\mathbf{V}}_{ij} = \int_{S_i} \boldsymbol{\rho}_i(\mathbf{r}) \cdot \int_{S_j} g(\mathbf{r}, \mathbf{r}') \boldsymbol{\rho}_j(\mathbf{r}') dS' dS \quad (10)$$

$$\bar{\mathbf{P}}_{ij} = \int_{S_i} h_i(\mathbf{r}) \cdot \int_{S_j} g(\mathbf{r}, \mathbf{r}') h_j(\mathbf{r}') dS' dS \quad (11)$$

$$\mathbf{b}_i = \int_{S_i} \mathbf{f}_i(\mathbf{r}) \cdot \mathbf{E}^i dS \quad (12)$$

$$\bar{\mathbf{D}}_{ij} = \begin{cases} 1, & T_i \in S_j, \text{ the positive part} \\ -1, & T_i \in S_j, \text{ the negative part} \\ 0, & T_i \notin S_j, \end{cases} \quad (13)$$

where \mathbf{j} and ϕ denote the unknown coefficients for current and charge, k_0 and η_0 are the wave number and the wave impedance in free space, and c_0 is the light speed in free space. The dense matrix $\bar{\mathbf{V}}$ represents the vector potentials and depicts the current interactions between inner edges. On the other hand, $\bar{\mathbf{P}}$ denotes the scalar potentials, which describes charges interactions between triangles. The sparse matrix $\bar{\mathbf{D}}$ represents the relationship between edge and the triangles patch, and $\bar{\mathbf{I}}$ is the identity matrix. In the matrix system (9), the vector potential and scalar potential are balanced by using a proper frequency scaling, which is critical for low-frequency problems.

3. Implementation of MLCSB for A-EFIE

3.1. CSB Expansions for A-EFIE. Motivated by the idea of CSB expansion method for EFIE, we can derive the expansions for A-EFIE in a similar way. The inner integrals of (10) and (11) can be written as

$$\mathbf{V}_i(\mathbf{r}) = \int_{S_i} g(\mathbf{r}, \mathbf{r}') \boldsymbol{\rho}_i(\mathbf{r}') dS' \quad (14)$$

$$\mathbf{P}_j(\mathbf{r}) = \int_{S_j} g(\mathbf{r}, \mathbf{r}') h_j(\mathbf{r}') dS', \quad (15)$$

where i and j represent the i th normalized RWG basis function and the j th pulse function in group m' . The above

integral equation is equivalent to the summation of CSB vector and scalar potentials:

$$\mathbf{V}_i(\mathbf{r}) = \sum_{q=1}^Q g(\mathbf{r}, \tilde{\mathbf{r}}_q) (\hat{x} w_{q,i}^x + \hat{y} w_{q,i}^y + \hat{z} w_{q,i}^z) \quad (16)$$

$$\mathbf{P}_j(\mathbf{r}) = \sum_{q=1}^Q g(\mathbf{r}, \tilde{\mathbf{r}}_q) w_{q,j}^p, \quad (17)$$

where $\hat{x} w_{q,i}^x + \hat{y} w_{q,i}^y + \hat{z} w_{q,i}^z$ is the vector CSB weight for current i , $w_{q,j}^p$ is the weight for charge j , and Q represents the total number of beams in this discretization. Combining (16) with (14) and (17) with (15) and testing on a far-field matching point, we get

$$\begin{aligned} \hat{x} \cdot \sum_{q=1}^Q g(\mathbf{r}_t, \tilde{\mathbf{r}}_q) \hat{x} w_{q,i}^x &= \hat{x} \cdot \int_{S_i} g(\mathbf{r}_t, \mathbf{r}') \boldsymbol{\rho}_i(\mathbf{r}') dS' \\ \hat{y} \cdot \sum_{q=1}^Q g(\mathbf{r}_t, \tilde{\mathbf{r}}_q) \hat{y} w_{q,i}^y &= \hat{y} \cdot \int_{S_i} g(\mathbf{r}_t, \mathbf{r}') \boldsymbol{\rho}_i(\mathbf{r}') dS' \\ \hat{z} \cdot \sum_{q=1}^Q g(\mathbf{r}_t, \tilde{\mathbf{r}}_q) \hat{z} w_{q,i}^z &= \hat{z} \cdot \int_{S_i} g(\mathbf{r}_t, \mathbf{r}') \boldsymbol{\rho}_i(\mathbf{r}') dS' \\ \sum_{q=1}^Q g(\mathbf{r}_t, \tilde{\mathbf{r}}_q) w_{q,j}^p &= \int_{S_j} g(\mathbf{r}_t, \mathbf{r}') h_j(\mathbf{r}') dS', \end{aligned} \quad (18)$$

where \mathbf{r}_t ($t = 1, 2, \dots, Q$) is the matching point. Those linear equations can be converted into a matrix form and combined as a multiple right-hand side problem by all the current and charge basis in the group m' :

$$\mathbf{G} [\mathbf{W}_{m'}^x, \mathbf{W}_{m'}^y, \mathbf{W}_{m'}^z, \mathbf{W}_{m'}^p] = [\mathbf{V}_{m'}^x, \mathbf{V}_{m'}^y, \mathbf{V}_{m'}^z, \mathbf{P}_{m'}], \quad (19)$$

where

$$\begin{aligned} [\mathbf{G}]_{tq} &= g(\mathbf{r}_t, \tilde{\mathbf{r}}_q) \\ [\mathbf{W}_{m'}^v]_{qi} &= w_{q,i}^v \quad (v = x, y, z) \\ [\mathbf{W}_{m'}^p]_{qj} &= w_{q,j}^p \\ [\mathbf{V}_{m'}^v]_{ti} &= \hat{v}_t \cdot \int_{S_i} g(\mathbf{r}_t, \mathbf{r}') \boldsymbol{\rho}_i(\mathbf{r}') dS' \quad (v = x, y, z) \\ [\mathbf{P}_{m'}]_{tj} &= \int_{S_j} g(\mathbf{r}_t, \mathbf{r}') h_j(\mathbf{r}') dS'. \end{aligned} \quad (20)$$

By using the expansion matrices $\mathbf{W}_{m'}^x, \mathbf{W}_{m'}^y, \mathbf{W}_{m'}^z$, and $\mathbf{W}_{m'}^p$, the CSB expansion coefficients for vector potentials of group m' can be expanded from $\mathbf{j}_{m'}$ as

$$\bar{\mathbf{s}}_{L,m'}^v = [\mathbf{s}_{L,m'}^x, \mathbf{s}_{L,m'}^y, \mathbf{s}_{L,m'}^z] = [\mathbf{W}_{m'}^x, \mathbf{W}_{m'}^y, \mathbf{W}_{m'}^z] \mathbf{j}_{m'}. \quad (21)$$

Similarly, the coefficients for scalar ones are

$$\mathbf{s}_{L,m'}^p = \mathbf{W}_{m'}^p \phi_{m'}. \quad (22)$$

Hence, the far-field MVP procedure for (10) and (11) can be obtained with a similar process in (4):

$$\bar{\mathbf{V}}_{mm'} \mathbf{j}_{m'} = \sum_{v=x,y,z} (\mathbf{W}_m^v)^T \mathbf{T}_{L,mm'} \mathbf{W}_{m'}^v \mathbf{j}_{m'} \quad (23)$$

$$\bar{\mathbf{P}}_{mm'} \phi_{m'} = (\mathbf{W}_m^d)^T \mathbf{T}_{L,mm'} \mathbf{W}_{m'}^d \phi_{m'},$$

where the translation operator $\mathbf{T}_{L,mm'}$ is expressed as

$$[\mathbf{T}_{L,mm'}]_{qq'} = g(\tilde{\mathbf{r}}_{L,m}^q, \tilde{\mathbf{r}}_{L,m'}^{q'}). \quad (24)$$

It is noticed that the scalar Green function with complex arguments is used here, and the translation for the vector and scalar expansion coefficients shares the same operators.

3.2. Multilevel Algorithm of CSB for A-EFIE. So far, we have derived the CSB expansion method for A-EFIE and have presented the far-group MVP process with the help of translation operators in a single level algorithm. In the following, we will obtain the aggregation and disaggregation operators of CSB expansion coefficients for both (10) and (11), to realize a multilevel algorithm. Firstly, the vector and scalar potentials by the q_{l+1} th CSB in a group is

$$\mathbf{V}_{q_{l+1}}(\mathbf{r}) = g(\mathbf{r}, \tilde{\mathbf{r}}_{q_{l+1}}) (\hat{x}s_{q_{l+1}}^x + \hat{y}s_{q_{l+1}}^y + \hat{z}s_{q_{l+1}}^z) \quad (25)$$

$$\mathbf{P}_{q_{l+1}}(\mathbf{r}) = g(\mathbf{r}, \tilde{\mathbf{r}}_{q_{l+1}}) s_{q_{l+1}}^p$$

where $l+1$ means the $(l+1)$ th level of the octree in the multilevel algorithm. By applying the summation and testing procedures similar to (16)–(18), a linear system can be set up to obtain the equivalent relationship of CSBs between two adjacent levels:

$$\mathbf{G}_l \mathbf{A}_l = \mathbf{P}_{l+1}, \quad (26)$$

where $[\mathbf{G}_l]_{t_l q_l} = g(\mathbf{r}_{t_l}, \tilde{\mathbf{r}}_{q_l}')$ is the matching matrix in parent level l . This matching matrix connects the equivalent CSB sources to the scalar potentials \mathbf{P}_{l+1} . Different from the right-hand side in (19), the right-hand side here for each vector potential component is the same as the scalar one, which is

$$[\mathbf{P}_{l+1}]_{q_l q_{l+1}} = g(\mathbf{r}_{q_l} | \tilde{\mathbf{r}}_{q_{l+1}}'). \quad (27)$$

Once \mathbf{G}_l and \mathbf{P}_{l+1} are assembled, the aggregation matrix \mathbf{A}_l for level l can be numerically solved. By using the aggregation matrix, the CSB expansion coefficients of the parent group in level l can be obtained efficiently from its child groups in level $l+1$:

$$\begin{aligned} \bar{\mathbf{s}}_{l,m'}^v &= [\mathbf{s}_{l,m'}^x, \mathbf{s}_{l,m'}^y, \mathbf{s}_{l,m'}^z] = \sum_{n' \in \text{child}(m')} \mathbf{A}_l \bar{\mathbf{s}}_{l+1,n'}^v \\ \mathbf{s}_{l,m'}^p &= \sum_{n' \in \text{child}(m')} \mathbf{A}_l \mathbf{s}_{l+1,n'}^p. \end{aligned} \quad (28)$$

Similar to the multilevel fast multipole algorithm (MLFMA) [25], the CSB expansion coefficients of a receiving group in level $l+1$ are obtained from the translation in the same level as well as the disaggregation from its parent level l . The disaggregation matrix can be easily obtained from the transpose of the aggregation matrices.

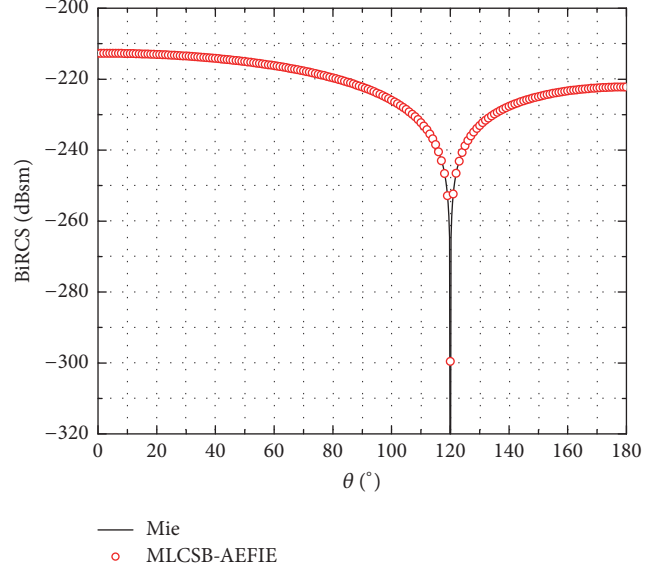


FIGURE 1: Bistatic RCS of the PEC sphere at 100 Hz, validated by the Mie series.

4. Numerical Results

In this section, the accuracy, error analysis, computational complexity, and the efficiency of the method are investigated through several numerical examples. All the examples were run on a computer of 2 processors, each with 14 cores at 2.6 GHz, 512 GB memory, and OpenMP parallelization.

4.1. Small Sphere. To show the accuracy of MLCSB-AEFIE at low frequencies, the electromagnetic scattering by a PEC sphere of 1 m radius is analyzed at 100 Hz. The sphere is discretized with 1,764 triangular patches, which corresponds to 2,646 inner edges. A three levels' MLCSB algorithm is used with a group size of $8.3 \times 10^{-8} \lambda$ at the finest level. The incident angle of a plane wave is $\theta_i = 0^\circ$, $\varphi_i = 0^\circ$, and the observed azimuth angle is fixed at $\theta_o = 0^\circ$. The residual error threshold is set to be 10^{-15} for GMRES-30. It takes 80 iteration steps to converge, with the help of the saddle point preconditioner in [9]. A good agreement of the bistatic RCS is observed in Figure 1, as compared with the analytical solution of Mie series.

4.2. Computational Complexity. To demonstrate the computational complexity of the proposed method, the plane wave scattering of a PEC cube with a side length of 0.1 m is calculated at 300 MHz. The electric size of the cube is 0.173λ . The surface of the cube is discretized into six different meshes: Mesh A, Mesh B, Mesh C, Mesh D, Mesh E, and Mesh F. The coarsest Mesh A has 1262 planar triangles and 1893 interior edges, and the average edge length is $1.05 \times 10^{-2} \lambda$. Then we refine Mesh A by halving the edge length recursively until Mesh F. Mesh F comprises 1,534,536 planar triangles and 2,301,804 interior edges, and the average edge length is $3 \times 10^{-4} \lambda$.

TABLE 1: Computational statistics of the PEC cube with different meshes at 300 MHz.

Mesh	Number of RWG	Number of triangles	Near-field Mem. (MB)	Expansion Mem. (MB)	Translation Mem. (MB)	Interpolation Mem. (MB)	Total Mem. (MB)	MVP time (s)	Iteration number	Total time (s)
A	1,893	1,262	2.7	21.5	59.1	4.2	87.5	0.15	25	4.1
B	7,992	5,328	10.2	90.7	88.6	8.4	197.9	0.6	36	22.8
C	33,330	22,220	43.5	378.3	118.2	12.6	552.6	2.2	52	118.4
D	139,002	92,668	178	1,541	147.8	16.8	1,883.6	8.7	74	655.8
E	563,292	375,528	727.9	6,245	177.36	21	7,170.4	31.2	110	3,480
F	2,301,804	1,534,536	2,932.9	25,518	206.9	25.2	28,683	120.9	174	21,232.6

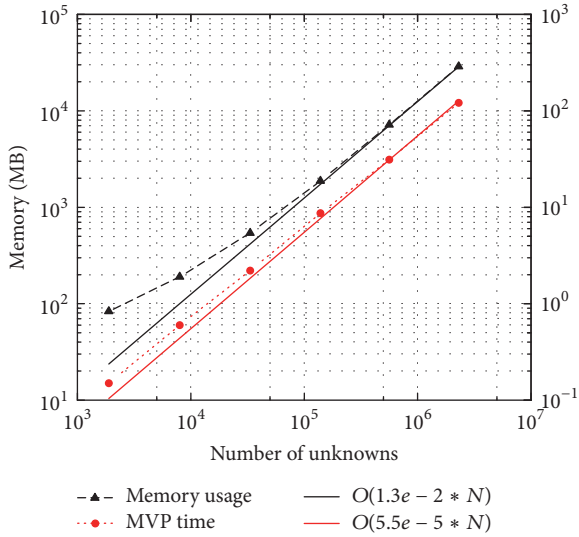


FIGURE 2: CPU time for each MVP and memory usage in the example of the PEC cube.

The CPU times for each MVP and the memory usage is plotted in Figure 2. It can be found that the computational complexity and the memory requirement of MLCB-AEFIE both scale as $O(N)$, where N are the unknown numbers. The detailed computational statistics are summarized in Table 1, and the iteration histories are shown in Figure 3 for comparison. By using the preconditioner in [9], the iteration converges quickly to 10^{-4} . A good agreement of the bistatic radar cross sections (RCS) of the five cases is demonstrated in Figure 4.

4.3. Error Analysis. In the proposed MLCB-AEFIE, the numerical error is mainly from expansion and aggregation. Since the expansion and aggregation processes are similar for the vector and scalar potentials, we only show the scalar potential case in the following. For the expansion, the relative errors related to a group with the size of 0.005 m and average discretization length of 0.001 m are studied. The relative error of expansion is defined as

$$e = \frac{|P(\mathbf{r}) - P^{\text{CSB}}(\mathbf{r})|}{|P(\mathbf{r})|}, \quad (29)$$

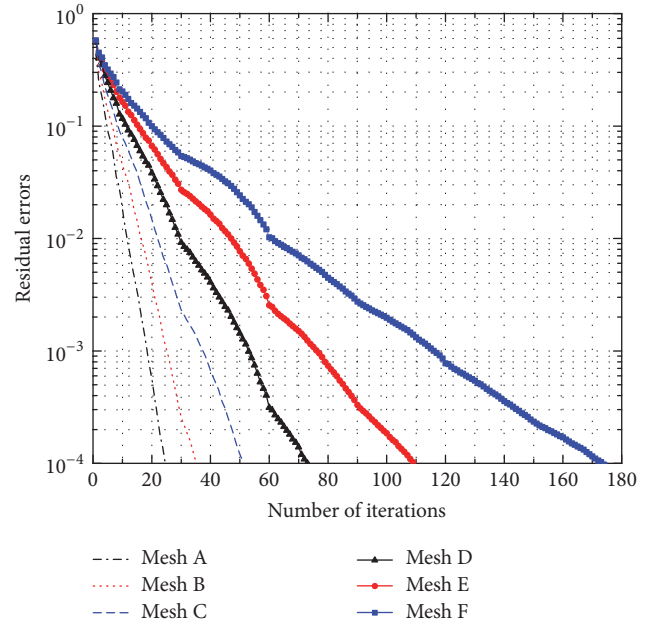


FIGURE 3: Iteration history of the PEC cube for different meshes.

where $P^{\text{CSB}}(\mathbf{r})$ is the scalar potential obtained via the expansion process in (17), $P(\mathbf{r})$ is the exact data calculated by (15), and the observation point \mathbf{r} is fixed at the center of the nearest cousin group. Figure 5 shows the relative errors e for different numbers of CSBs $Q = 30, 42, 58,$ and 82 with respect to the frequencies from 30 Hz to 300 MHz. It is noticed that the expansion errors are almost constant for the same Q in a very wide frequency range, indicating an excellent stability and scalability of the proposed method for broadband computations.

To investigate the interpolation error in the aggregation process, we compare the scalar potentials related to a group with the size of 0.005 m and the parent group with the size of 0.01 m. The scalar potentials are calculated by CSBs, while the CSB coefficients of the parent group are aggregated from the child group. The RMS relative error is shown in Figure 6, which is defined as

$$\text{RMS}(P) = \sqrt{\frac{1}{N} \sum_{i=1}^N \frac{\|P_i^{\text{CSB}}(\mathbf{r}_i) - P_{l+1}^{\text{CSB}}(\mathbf{r}_i)\|^2}{\|P_{l+1}^{\text{CSB}}(\mathbf{r}_i)\|^2}} \quad (30)$$

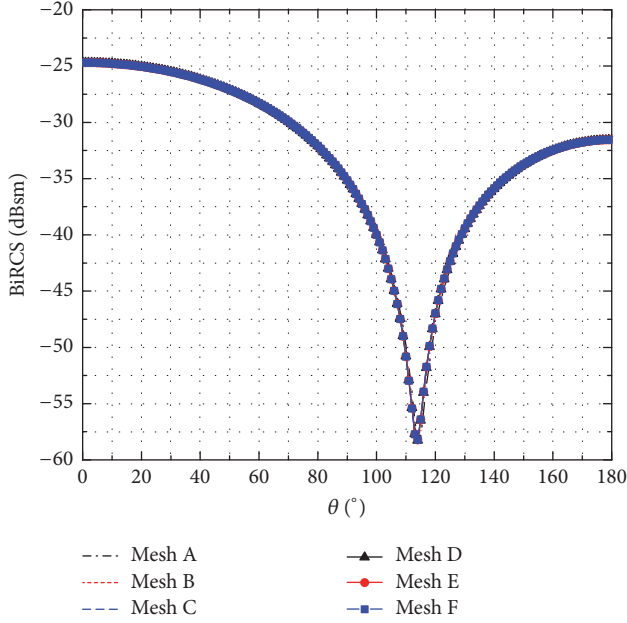


FIGURE 4: Bistatic RCS of the PEC cube with different meshes.

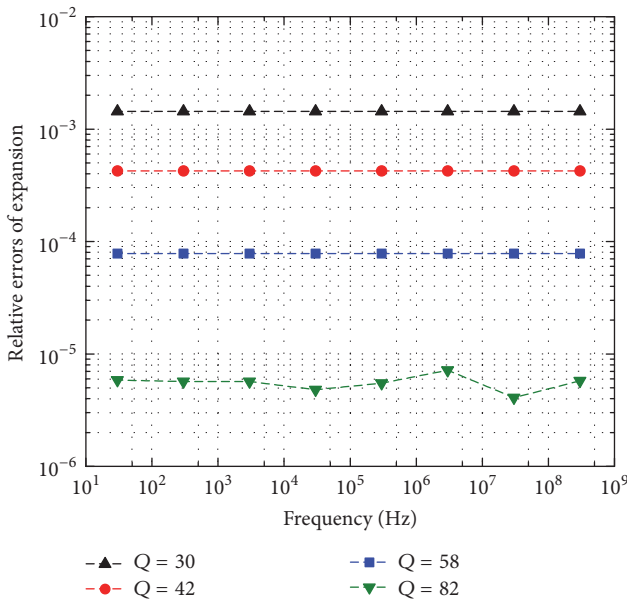


FIGURE 5: Relative errors of expansion.

and here $P_l^{\text{CSB}}(\mathbf{r}_i)$, $P_{l+1}^{\text{CSB}}(\mathbf{r}_i)$ are the scalar potentials of the parent group and the child group, respectively, and \mathbf{r}_i is set on azimuth circle centered at the parent group. Figure 6 also shows a constant accuracy level for different frequencies with the same Q .

4.4. Scattering of Multiscale Cone. The performance of the MLCSB-AEFIE for multiscale structures is evaluated by a nonuniformly meshed cone illustrated in Figure 7. The radius of the cone is 5 m at the bottom and the height is 10 m. We mesh the cone with a length of 0.1 m at the bottom and gradually reduce it to 0.001 m at the sharp point

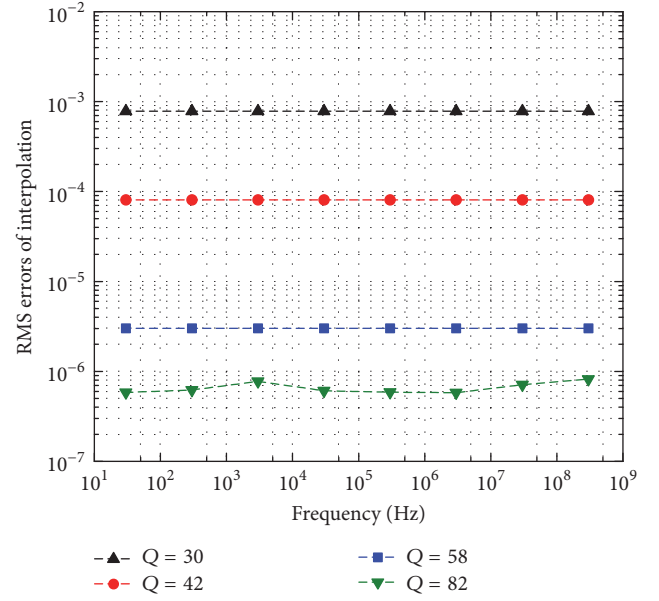


FIGURE 6: RMS errors of interpolation.

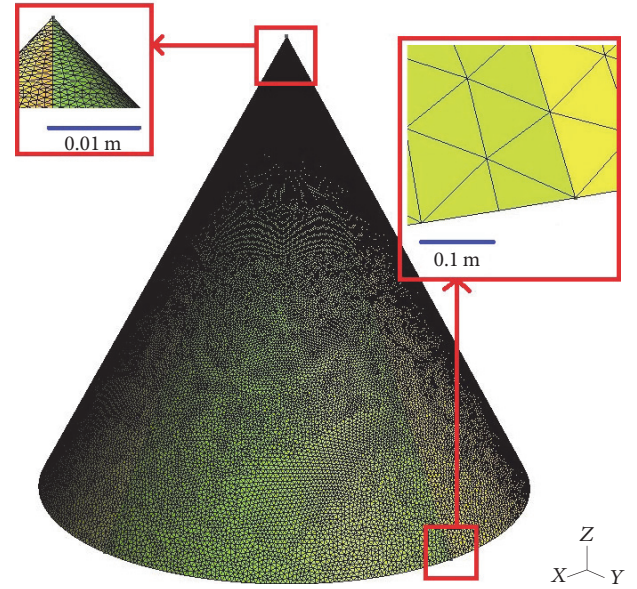


FIGURE 7: A cone of radius 5 m and height 10 m, which is meshed with average length 0.1 m at the bottom and 0.001 m at the sharp point. Mesh details are shown with reference lengths 0.1 m and 0.01 m.

point. Finally, the cone is discretized with 191,976 planar patches, and hence 287,964 interior edges. Figure 8 shows the bistatic RCS of the cone excited by a y -polarized plane wave incident from the x direction at 10 KHz and 10 MHz. In this example, MLCSB-AEFIE converges to relative residual error of 10^{-3} within 73 and 67 iterations, for 10 KHz and 10 MHz, respectively.

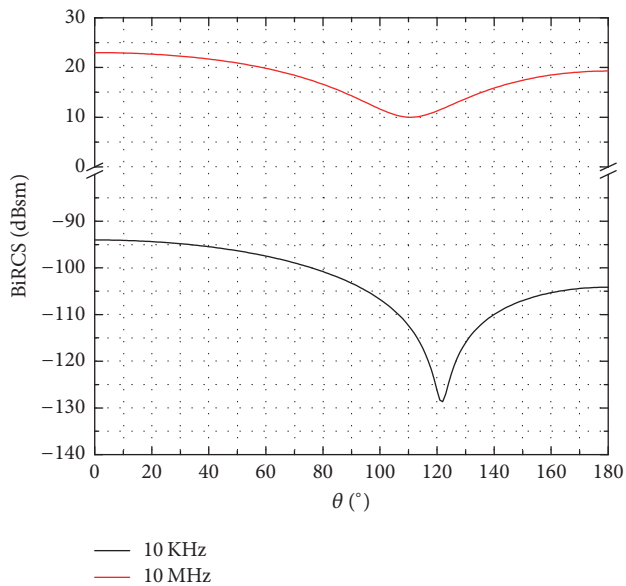


FIGURE 8: Bistatic RCS of the PEC cone at 10 KHz and 10 Mhz.

5. Conclusion

In this paper, we have proposed a MLCSB-AEFIE method for the well-known low-frequency problem. The vector and scalar potentials from the current and charge unknowns are expanded with CSBs. An aggregation matrix is obtained for the CSB expansion coefficients to form an efficient multilevel algorithm. Numerical examples have validated the good accuracy, efficiency, and scalability of the proposed method for low-frequency problems.

Conflicts of Interest

The authors declare that there are no conflicts of interest regarding the publication of this paper.

Acknowledgments

This work is supported partly by the National Excellent Youth Fund by NSFC no. 61425010, Programme of Introducing Talents of Discipline to Universities under Grant no. b07046, the Chang Jiang Scholar Project of MOE, and the National Natural Science Foundation of China under Grant no. 61490695.

References

- [1] R. F. Harrington and J. L. Harrington, *Field Computation by Moment Methods*, Oxford University Press, Oxford, UK, 1996.
- [2] Z. G. Qian and W. C. Chew, "A quantitative study on the low frequency breakdown of EFIE," *Microwave and Optical Technology Letters*, vol. 50, no. 5, pp. 1159–1162, 2008.
- [3] F. P. Andriulli, "Loop-star and loop-tree decompositions: analysis and efficient algorithms," *IEEE Transactions on Antennas and Propagation*, vol. 60, no. 5, pp. 2347–2356, 2012.
- [4] S. Yan, J.-M. Jin, and Z. Nie, "EFIE analysis of low-frequency problems with loop-star decomposition and Calderón multiplicative preconditioner," *IEEE Transactions on Antennas and Propagation*, vol. 58, no. 3, pp. 857–867, 2010.
- [5] M. Taskinen and P. Yla-Oijala, "Current and charge integral equation formulation," *IEEE Transactions on Antennas and Propagation*, vol. 54, no. 1, pp. 58–67, 2006.
- [6] D. Gope, A. Ruehli, and V. Jandhyala, "Solving low-frequency EM-CKT problems using the PEEC method," *IEEE Transactions on Advanced Packaging*, vol. 30, no. 2, pp. 313–320, 2007.
- [7] A. Das and D. Gope, "Modified SPIE formulation for low-frequency stability of electric field integral equation," in *Proceedings of the 5th IEEE Applied Electromagnetics Conference (AEMC '15)*, Guwahati, India, December 2015.
- [8] Z. G. Qian and W. C. Chew, "An augmented electric field integral equation for high-speed interconnect analysis," *Microwave and Optical Technology Letters*, vol. 50, no. 10, pp. 2658–2662, 2008.
- [9] Z.-G. Qian and W. C. Chew, "Fast full-wave surface integral equation solver for multiscale structure modeling," *IEEE Transactions on Antennas and Propagation*, vol. 57, no. 11, pp. 3594–3601, 2009.
- [10] Y. P. Chen, L. Jiang, Z.-G. Qian, and W. C. Chew, "Modeling electrically small structures in layered medium with augmented EFIE method," in *Proceedings of the IEEE International Symposium on Antennas and Propagation and USNC/URSI National Radio Science Meeting, APSURSI 2011*, pp. 3218–3221, Spokane, Wash, USA, July 2011.
- [11] Y. G. Liu, W. C. Chew, L. Jiang, and Z. Qian, "A memory saving fast A-EFIE solver for modeling low-frequency large-scale problems," *Applied Numerical Mathematics*, vol. 62, no. 6, pp. 682–698, 2012.
- [12] Z.-G. Qian and W. C. Chew, "Enhanced A-EFIE with perturbation method," *IEEE Transactions on Antennas and Propagation*, vol. 58, no. 10, pp. 3256–3264, 2010.
- [13] Z.-H. Ma, L. J. Jiang, and W. C. Chew, "Loop-tree free augmented equivalence principle algorithm for low-frequency problems," *Microwave and Optical Technology Letters*, vol. 55, no. 10, pp. 2475–2479, 2013.
- [14] K.-J. Xu, X.-M. Pan, and X.-Q. Sheng, "An augmented EFIE with discontinuous Galerkin discretization," in *Proceedings of the IEEE International Conference on Computational Electromagnetics, ICCEM 2016*, pp. 106–108, Guangzhou, China, February 2016.
- [15] J. S. Zhao and W. C. Chew, "Applying LF-MLFMA to solve complex PEC structures," *Microwave and Optical Technology Letters*, vol. 28, no. 3, pp. 155–160, 2001.
- [16] Y. Zheng, Y. Zhao, Z. Nie, and Q. Cai, "Full-wave fast solver for circuit devices modeling," *Applied Computational Electromagnetics Society Journal*, vol. 30, no. 10, pp. 1115–1121, 2015.
- [17] D. Z. Ding, Y. Shi, Z. N. Jiang, and R. S. Chen, "Augmented EFIE with adaptive cross approximation algorithm for analysis of electromagnetic problems," *International Journal of Antennas and Propagation*, vol. 2013, Article ID 487276, 9 pages, 2013.
- [18] M. M. Jia, S. Sun, and W. C. Chew, "Accelerated A-EFIE with perturbation method using fast fourier transform," in *Proceedings of the IEEE Antennas and Propagation Society International Symposium (APSURSI '14)*, pp. 2148–2149, Memphis, Tenn, USA, July 2014.
- [19] K. Tap, P. H. Pathak, and R. J. Burkholder, "Complex source beam-moment method procedure for accelerating numerical

- integral equation solutions of radiation and scattering problems,” *IEEE Transactions on Antennas and Propagation*, vol. 62, no. 4, part 2, pp. 2052–2062, 2014.
- [20] K. Tap, *Complex source point beam expansions for some electromagnetic radiation and scattering problems [Ph.D. thesis]*, The Ohio State University, Columbus, Ohio, USA, 2007.
- [21] E. Martini and S. Maci, “Generation of complex source point expansions from radiation integrals,” *Progress in Electromagnetics Research*, vol. 152, no. 3, pp. 17–31, 2015.
- [22] Z. H. Fan, X. Hu, and R. S. Chen, “Multilevel complex source beam method for electromagnetic scattering problems,” *IEEE Antennas and Wireless Propagation Letters*, vol. 14, pp. 843–846, 2015.
- [23] K. C. Wang, Z. H. Fan, M. M. Li, and R. S. Chen, “An effective MoM Solution with nested complex source beam method for electromagnetic scattering problems,” *IEEE Transactions on Antennas and Propagation*, vol. 64, no. 6, pp. 2546–2551, 2016.
- [24] T. B. Hansen and G. Kaiser, “Huygens’ principle for complex spheres,” *IEEE Transactions on Antennas and Propagation*, vol. 59, no. 10, pp. 3835–3847, 2011.
- [25] Ö. Ergül and L. Gürel, *The Multilevel Fast Multipole Algorithm (MLFMA) for Solving Large-Scale Computational Electromagnetics Problems*, John Wiley & Sons, Hoboken, NJ, USA, 2014.

Research Article

Tolerance Analysis of Antenna Array Pattern and Array Synthesis in the Presence of Excitation Errors

Ying Zhang, DanNi Zhao, Qiong Wang, ZhengBin Long, and Xiaofeng Shen

College of Electronic Engineering, University of Electronic Science and Technology of China, Chengdu, Sichuan 611731, China

Correspondence should be addressed to Xiaofeng Shen; sxf.uestc@163.com

Received 28 December 2016; Accepted 16 March 2017; Published 11 July 2017

Academic Editor: Yumao Wu

Copyright © 2017 Ying Zhang et al. This is an open access article distributed under the Creative Commons Attribution License, which permits unrestricted use, distribution, and reproduction in any medium, provided the original work is properly cited.

This paper analyzes array pattern tolerance against excitation errors. The nonprobabilistic interval analysis algorithm is used for tolerance analysis of the nonideal uniform linear array in this work. Toward this purpose, corresponding interval models of the power pattern functions are established, respectively, with the consideration of the amplitude errors, phase errors, or both simultaneously, in antenna arrays. The tolerance for the amplitude-phase error of the main function parameters including the beamwidth, sidelobe level, and the directivity is simulated by computer according to the indicators and the actual requirements. Accordingly, the worst admissible performance of an array can be evaluated, which may provide theoretical reference for optimal antenna array design. As for the problem of array synthesis in the presence of various array errors, interval analysis-convex programming (IA-CP) is presented. Simulation results show that the proposed IA-CP based synthesis technique is robust for the amplitude and phase errors.

1. Introduction

Antenna arrays are widely used for their flexibility and reliability in wireless data transmission. For array design, an important performance indicator is the radiation pattern. In real applications, excitation errors including amplitude error and phase error widely existed due to manufacturing errors. Excitation errors affect radiation pattern of arrays, which usually deteriorates performance of the designed arrays. Therefore, the effect of excitation errors on array radiation pattern should be analyzed for robust array design [1].

Traditional error analysis strategies are generally based on the statistical theory. For instance, under the assumption that the excitation errors are normally distributed, Ruze proposed analyzing the association between the radiation pattern and the random excitation errors [2]. In [3], Hsiao obtained the statistical regularities of sidelobes distributed in different regions by studying the impacts of stochastic independence and corresponding amplitude-phase errors on the sidelobe level. However, these statistical methods cannot be applied into engineering design directly as the distribution of amplitude and phase errors may be unknown.

To resolve this issue, a novel approach based on interval arithmetic (IA) was proposed in [4]. IA was originally introduced for the computation of the rounding errors when using numerical resolution strategies [5, 6]. It was then extended to deal with nonlinear equations [7] as well as optimization problems [8, 9]. Recently, this method has been successfully applied to compute the bounds of the radiation pattern when array excitation errors exist [4, 10–13]. Existing IA-based analysis methods showed satisfactory results. Nevertheless, there has been no literature considering the case where excitation amplitude and phase errors simultaneously exist.

In this paper, the excitation amplitude and phase errors are considered simultaneously to achieve the upper and lower bounds of array radiation patterns. Tolerance of array radiation pattern is analyzed by interval arithmetic (IA). Since excitation phase error has different influence on the real and imaginary parts of the radiation pattern, the optimal bounds are hard to achieve. Instead, a relaxed version bound is presented. Accordingly, the worst admissible performance of an array can be evaluated, which may provide theoretical reference for optimal antenna array design. As for the problem of array synthesis in the presence of various array errors,

a method based on interval analysis-convex programming (IA-CP) is given. Simulation results show that the IA-CP-based synthesis technique is not only robust for the amplitude and phase errors, but also suitable for large arrays.

2. Radiation Pattern Tolerance Analysis in the Presence of Excitation Amplitude and Phase Errors

2.1. Analysis Based on Interval Arithmetic. Consider a uniform linear array with N elements. Assume the real excitation amplitude and phase on the n th element are denoted by α_n and φ_n , respectively. The array factor interval is given by

$$AF^I(\theta) = \sum_{n=0}^{N-1} AF_n^I(\theta) = \sum_{n=0}^{N-1} \alpha_n^I e^{j\Theta_n^I(\theta)}, \quad (1)$$

where $\alpha_n^I = [\alpha_n^L, \alpha_n^U]$ denotes the amplitude interval. $\Theta_n^I(\theta) = nk d \sin \theta + \varphi_n^I$, where $\varphi_n^I = [\varphi_n^L, \varphi_n^U]$ denotes the phase interval. $\theta \in [-\pi/2, \pi/2]$ is the angular direction measured from boresight, $j = \sqrt{-1}$ is the unit complex number, d denotes element space, and $k = 2\pi/\lambda$ is the wavenumber.

The interval of power pattern is given by

$$P^I(\theta) = [AF_{\Re}^I(\theta)]^2 + [AF_{\Im}^I(\theta)]^2, \quad (2)$$

$$P^U(\theta) = \left(\left| \mu \{AF_{\Re}^I(\theta)\} \right| + \frac{\omega \{AF_{\Re}^I(\theta)\}}{2} \right)^2 + \left(\left| \mu \{AF_{\Im}^I(\theta)\} \right| + \frac{\omega \{AF_{\Im}^I(\theta)\}}{2} \right)^2, \quad (5a)$$

$$P^L(\theta) = \begin{cases} \left(\left| \mu \{AF_{\Re}^I(\theta)\} \right| - \frac{\omega \{AF_{\Re}^I(\theta)\}}{2} \right)^2, & 0 \notin AF_{\Re}^I, 0 \in AF_{\Im}^I \\ \left(\left| \mu \{AF_{\Im}^I(\theta)\} \right| - \frac{\omega \{AF_{\Im}^I(\theta)\}}{2} \right)^2, & 0 \in AF_{\Re}^I, 0 \notin AF_{\Im}^I \\ \left(\left| \mu \{AF_{\Re}^I(\theta)\} \right| - \frac{\omega \{AF_{\Re}^I(\theta)\}}{2} \right)^2 + \left(\left| \mu \{AF_{\Im}^I(\theta)\} \right| - \frac{\omega \{AF_{\Im}^I(\theta)\}}{2} \right)^2, & 0 \notin AF_{\Re}^I, 0 \notin AF_{\Im}^I \\ 0, & \text{otherwise,} \end{cases} \quad (5b)$$

where $\mu \{AF_{\Re}^I(\theta)\} = \sum_{n=0}^{N-1} \mu \{AF_{n,\Re}^I(\theta)\}$, $\omega \{AF_{\Re}^I(\theta)\} = \sum_{n=0}^{N-1} \omega \{AF_{n,\Re}^I(\theta)\}$, $\mu \{AF_{\Im}^I(\theta)\} = \sum_{n=0}^{N-1} \mu \{AF_{n,\Im}^I(\theta)\}$, and $\omega \{AF_{\Im}^I(\theta)\} = \sum_{n=0}^{N-1} \omega \{AF_{n,\Im}^I(\theta)\}$.

The midpoint and the interval width of $AF_{n,\Re}^I(\theta)$ and $AF_{n,\Im}^I(\theta)$ are given by

$$\mu \{AF_{n,\Re}^I(\theta)\} = \frac{1}{2} [AF_{n,\Re}^L(\theta) + AF_{n,\Re}^U(\theta)], \quad (6a)$$

$$\mu \{AF_{n,\Im}^I(\theta)\} = \frac{1}{2} [AF_{n,\Im}^L(\theta) + AF_{n,\Im}^U(\theta)],$$

$$\omega \{AF_{n,\Re}^I(\theta)\} = AF_{n,\Re}^U(\theta) - AF_{n,\Re}^L(\theta), \quad (6b)$$

$$\omega \{AF_{n,\Im}^I(\theta)\} = AF_{n,\Im}^U(\theta) - AF_{n,\Im}^L(\theta).$$

where $AF_{\Re}^I(\theta)$ and $AF_{\Im}^I(\theta)$ denote the real and imaginary part of $AF^I(\theta)$, respectively.

In the presence of amplitude and phase error, it is difficult to determine the upper and lower bound of (2), since the real and imaginary parts of power pattern are coupled with phase. Use the fact that

$$\begin{aligned} & \max \{AF_{\Re}^2(\theta) + AF_{\Im}^2(\theta)\} \\ & \leq \max \{AF_{\Re}^2(\theta)\} + \max \{AF_{\Im}^2(\theta)\}, \\ & \min \{AF_{\Re}^2(\theta) + AF_{\Im}^2(\theta)\} \\ & \geq \min \{AF_{\Re}^2(\theta)\} + \min \{AF_{\Im}^2(\theta)\}. \end{aligned} \quad (3)$$

A relaxed version of the upper and lower bound of power pattern is proposed as

$$P^U(\theta) = [AF_{\Re}^U(\theta)]^2 + [AF_{\Im}^U(\theta)]^2, \quad (4a)$$

$$P^L(\theta) = [AF_{\Re}^L(\theta)]^2 + [AF_{\Im}^L(\theta)]^2. \quad (4b)$$

Then, similar to [4], the upper and lower bounds can be expressed by the midpoint and the interval width of $AF_{\Re}^I(\theta)$ and $AF_{\Im}^I(\theta)$:

Based on the rules of interval algorithm, $AF_{n,\Re}^I(\theta)$ and $AF_{n,\Im}^I(\theta)$ can be computed as

$$AF_{n,\Re}^U(\theta) = \begin{cases} A_n^L \cos^U(\Theta_n^I), & \cos^U(\Theta_n^I) < 0, \\ A_n^U \cos^U(\Theta_n^I), & \text{otherwise} \end{cases} \quad (7a)$$

$$AF_{n,\Re}^L(\theta) = \begin{cases} A_n^L \cos^L(\Theta_n^I), & \cos^L(\Theta_n^I) > 0, \\ A_n^U \cos^L(\Theta_n^I), & \text{otherwise.} \end{cases}$$

$$AF_{n,\Im}^U(\theta) = \begin{cases} A_n^L \sin^U(\Theta_n^I), & \sin^U(\Theta_n^I) < 0, \\ A_n^U \sin^U(\Theta_n^I), & \text{otherwise} \end{cases} \quad (7b)$$

$$AF_{n,\Im}^L(\theta) = \begin{cases} A_n^L \sin^L(\Theta_n^I), & \sin^L(\Theta_n^I) > 0, \\ A_n^U \sin^L(\Theta_n^I), & \text{otherwise.} \end{cases}$$

The lower and upper bounds of $\sin(\Theta_n^I)$ and $\cos(\Theta_n^I)$ are given by

$$\cos(\Theta_n^I(\theta)) = \begin{cases} [\cos(\Theta_n^L(\theta)), \cos(\Theta_n^U(\theta))], & \frac{\partial \cos(\Theta_n^I)}{\partial \Theta_n^I} > 0, \\ [\cos(\Theta_n^U(\theta)), \cos(\Theta_n^L(\theta))], & \frac{\partial \cos(\Theta_n^I)}{\partial \Theta_n^I} < 0, \\ [\min\{\cos(\Theta_n^L(\theta)), \cos(\Theta_n^U(\theta))\}, 1], & 2i\pi \in \Theta_n^I, \\ [-1, \max\{\cos(\Theta_n^L(\theta)), \cos(\Theta_n^U(\theta))\}], & \pi + 2i\pi \in \Theta_n^I, \end{cases} \quad (8a)$$

$$\sin(\Theta_n^I(\theta)) = \begin{cases} [\sin(\Theta_n^L(\theta)), \sin(\Theta_n^U(\theta))], & \frac{\partial \sin(\Theta_n^I)}{\partial \Theta_n^I} > 0, \\ [\sin(\Theta_n^U(\theta)), \sin(\Theta_n^L(\theta))], & \frac{\partial \sin(\Theta_n^I)}{\partial \Theta_n^I} < 0, \\ [\min\{\sin(\Theta_n^L(\theta)), \sin(\Theta_n^U(\theta))\}, 1], & \frac{\pi}{2} + 2i\pi \in \Theta_n^I, \\ [-1, \max\{\sin(\Theta_n^L(\theta)), \sin(\Theta_n^U(\theta))\}], & -\frac{\pi}{2} + 2i\pi \in \Theta_n^I. \end{cases} \quad (8b)$$

3. Array Synthesis in the Presence of Array Excitation Errors

For ideal array, array synthesis has been studied in many literatures. However, array errors bring bad influence on the performance of the designed array pattern, for example, decrease of array gain and increase of sidelobe level. To avoid these problems, a solution is to take array error into account when designing the array. In [14], particle swarm optimization (PSO) technique is combined with interval arithmetic to realize array synthesis in the presence of array excitation amplitude error. However, PSO suffers from high computational loads. In this paper, array excitation in the presence of array excitation amplitude and phase errors is optimized by convex programming which can decrease computational loads.

The interval of array power pattern considering excitation amplitude and excitation phase error can be expressed as

$$P_{\alpha,\varphi}^I(\theta) = \left| \sum_{n=0}^{N-1} \alpha_n^I e^{j\Theta_n^I(\theta)} \right|^2, \quad (9)$$

where $P_{\alpha,\varphi}^I(\theta) = [P_{\alpha,\varphi}^L(\theta), P_{\alpha,\varphi}^U(\theta)]$.

To optimize the array excitation, the following cost function is constructed:

$$\alpha^{\text{opt}} = \arg \left\{ \max_{\alpha} [P_{\alpha,\varphi}^L(\theta_0)] \right\}, \quad (10a)$$

$$\text{subject to } P_{\alpha,\varphi}^U(\theta_s) \Big|_{\alpha=\alpha^{\text{opt}}} \leq M(\theta_s), \quad \theta_s \notin \Omega, \quad (10b)$$

where θ_0 denotes the look direction, Ω denotes the main-lobe region, and θ_s denotes the sidelobe region. The proposed cost function aims to maximize the lower bound of the array radiation pattern at the look direction and simultaneously guarantees that the upper bound of the array pattern in sidelobe region does not exceed a preset value.

Based on (4b), the objective function can be equivalently expressed as

$$\begin{aligned} P_{\alpha,\varphi}^L(\theta_0) &= \left(\sum_{n=0}^{N-1} \alpha_n^L \cos^L(\Theta_n(\theta_0)) \right)^2 \\ &\quad + \left(\sum_{n=0}^{N-1} \alpha_n^L \sin^L(\Theta_n(\theta_0)) \right)^2 \\ &= \left(\sum_{n=0}^{N-1} \alpha_n^L \cos(\Theta_n^U(\theta_0)) \right)^2 \\ &\quad + \left(\sum_{n=0}^{N-1} \alpha_n^L \sin(\Theta_n^L(\theta_0)) \right)^2 \\ &= \left(\sum_{n=0}^{N-1} (\alpha_n - \varepsilon_n) \cos(\Theta_n^U(\theta_0)) \right)^2 \\ &\quad + \left(\sum_{n=0}^{N-1} (\alpha_n - \varepsilon_n) \sin(\Theta_n^L(\theta_0)) \right)^2, \end{aligned} \quad (11)$$

where ε_n is the excitation amplitude error of the n th element.

Following (5a), (10b) can be expressed as

$$\begin{aligned} P_{\alpha,\varphi}^U(\theta_s) &= \left(\left| \sum_{n=0}^{N-1} \mu \{ \alpha_n^I \cos(\Theta_n^I(\theta_s)) \} \right| \right. \\ &\quad \left. + \frac{1}{2} \sum_{n=0}^{N-1} \omega \{ \alpha_n^I \cos(\Theta_n^I(\theta_s)) \} \right)^2 \\ &\quad + \left(\left| \sum_{n=0}^{N-1} \mu \{ \alpha_n^I \sin(\Theta_n^I(\theta_s)) \} \right| \right. \\ &\quad \left. + \frac{1}{2} \sum_{n=0}^{N-1} \omega \{ \alpha_n^I \sin(\Theta_n^I(\theta_s)) \} \right)^2 \leq M(\theta_s). \end{aligned} \quad (12)$$

It is observed from (11) and (12) that $P_{\alpha,\varphi}^L(\theta_0)$ and $P_{\alpha,\varphi}^U(\theta_s)$ are quadratic functions with respect to α_n . Therefore, convex programming can be used to solve (10a) and (10b).

4. Computer Simulations

4.1. IA-Based Method. A uniform linear array (ULA) with $N = 10$ half-wavelength spaced sensors is considered. The nominal amplitudes α_n ($n = 0, 1, \dots, N-1$) based on Chebyshev synthesis method are given in Table 1, which generates a power pattern with the sidelobe level -20 dB. The interval of the excitation amplitude and phase are assumed to be $\alpha_n^I = [\alpha_n - (\delta\alpha_n)\alpha_n, \alpha_n + (\delta\alpha_n)\alpha_n]$ and $\varphi_n^I = [\varphi_n - \delta\varphi_n, \varphi_n + \delta\varphi_n]$.

$Q = 5000$ array patterns $P(u)$, where $u = \sin \theta$, have been generated by randomly selecting the amplitude and phase from these intervals with uniform distribution. Figures 1–3 show all Q beams as well as the IA-computed power pattern bounds with different amplitude and phase intervals.

TABLE 1: Amplitude distribution ($N = 10$, $d = \lambda/2$; Chebyshev: $\text{SLL}_{\text{ref}} = -20$ dB).

$\alpha_0 = \alpha_9$	$\alpha_1 = \alpha_8$	$\alpha_2 = \alpha_7$	$\alpha_3 = \alpha_6$	$\alpha_4 = \alpha_5$
1.000	0.926	1.213	1.436	1.559

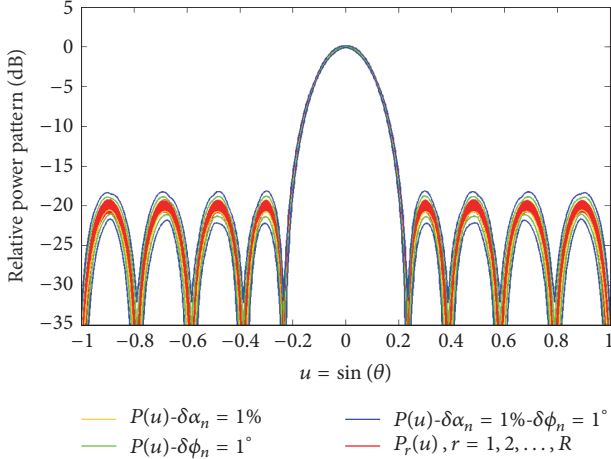


FIGURE 1: Bounds of the power pattern $P(u)$ based on IA with $\delta\alpha_n = 1\%$, $\delta\phi_n = 1^\circ$.

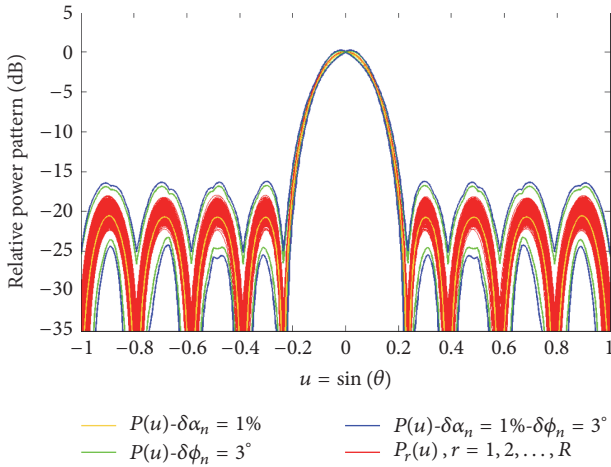


FIGURE 2: Bounds of the power pattern $P(u)$ based on IA with $\delta\alpha_n = 1\%$, $\delta\phi_n = 3^\circ$.

It can be observed from the figures that the IA-based methods which consider the amplitude or phase error only are unable to consistently give correct bounds of the power pattern. For the proposed method, the bounds are correct for all situations.

For different expected sidelobe level (ISLL_{ref}), Figures 4–6 show the derived SLL interval, main-lobe bandwidth (BW) interval, and the directivity (D) interval with different amplitude and phase intervals, respectively.

It can be concluded from these figures that synthesis of the desired array pattern becomes difficult when the excitation errors are large, since higher excitation errors lead to larger interval width, for example, for $\text{SLL}_{\text{ref}} = -25$ dB,

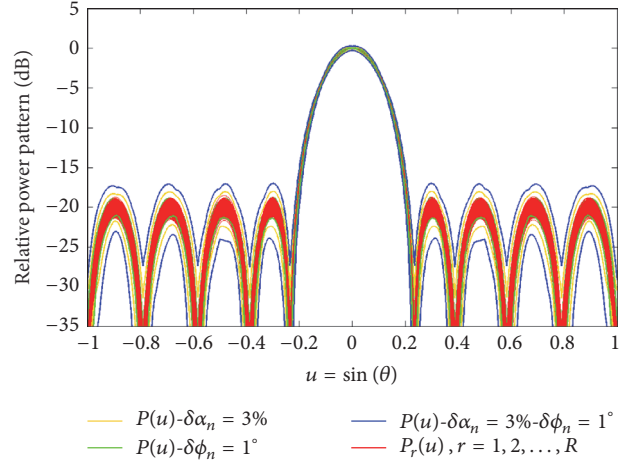


FIGURE 3: Bounds of the power pattern $P(u)$ based on IA with $\delta\alpha_n = 3\%$, $\delta\phi_n = 1^\circ$.

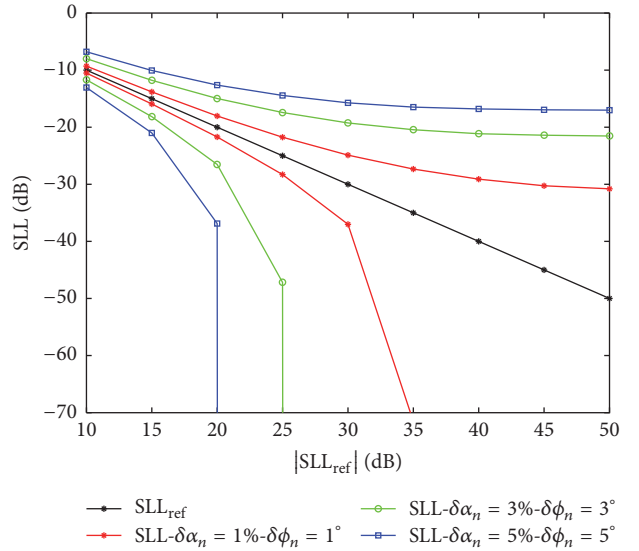
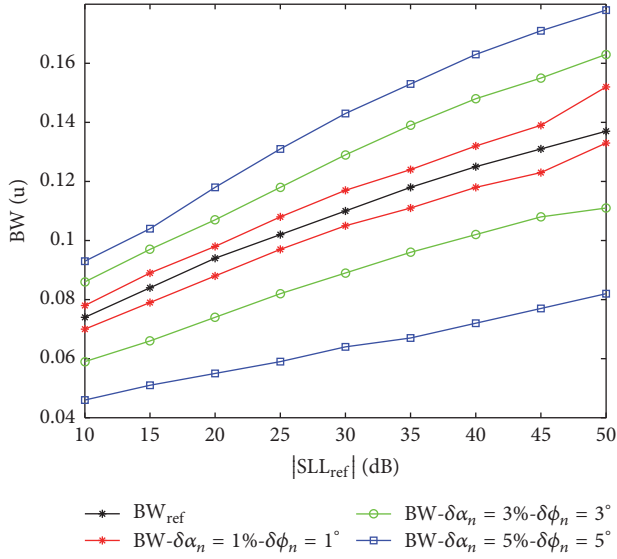
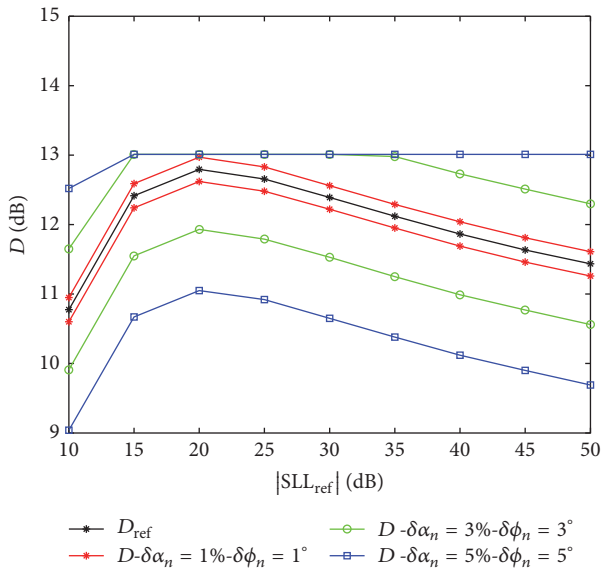


FIGURE 4: SLL interval based on IA against ISLL_{ref} .

$\omega\{\text{SLL}\}_{\delta\alpha_n=1\%,\delta\phi_n=1^\circ} = 6.54$ dB, $\omega\{\text{SLL}\}_{\delta\alpha_n=3\%,\delta\phi_n=3^\circ} = 29.75$ dB, and $\omega\{\text{SLL}\}_{\delta\alpha_n=5\%,\delta\phi_n=5^\circ} = \infty$. From Figure 4, as ISLL_{ref} increases, the upper bound of the SLL approaches a constant higher than the expected SLL, which means it is unguaranteed to achieve an array pattern with low sidelobe level in the presence of excitation error. Also, from the figure, the precision of the excitation to achieve relative satisfactory performance can be derived; for example, for $\text{ISLL}_{\text{ref}} = 20$ dB, $\delta\alpha_n = 1\%$, $\delta\phi_n = 1^\circ$ guarantees that the derived SLL is within $[-21.71, -18.03]$ dB.

4.2. IA-CP Based Array Synthesis. In this simulation, array excitation amplitude and phase errors are taken into account. The interval of the excitation amplitude and phase are assumed to be $\alpha_n^I = [\alpha_n - (\delta\alpha_n)\alpha_n, \alpha_n + (\delta\alpha_n)\alpha_n]$ and $\phi_n^I = [\phi_n - \eta, \phi_n + \eta]$. A ULA with 20 half-wavelength spaced elements is considered. The constraint of the sidelobe level $M(\theta_s)$ is set to


 FIGURE 5: BW interval based on IA against $ISLL_{ref}$.

 FIGURE 6: Directivity interval based on IA against $ISLL_{ref}$.

0 dB. Figure 7 shows the derived array excitation amplitudes with $\delta\alpha_n = 1\%$, $\eta = 1^\circ$ and $\delta\alpha_n = 3\%$, $\eta = 3^\circ$. Figures 8 and 9 show the generated array radiation patterns using the derived excitation amplitudes.

It can be observed from Figure 7 that when excitation errors become large, the derived array excitation amplitudes decrease. It is natural to see this since larger errors yield higher upper bound of array pattern. Therefore, in order to satisfy sidelobe constraint, excitation amplitudes become smaller. Figures 8 and 9 validate this conclusion. It can be observed from Figure 9 that the main-lobe gain with $\delta\alpha_n = 3\%$, $\eta = 3^\circ$ is smaller than that with $\delta\alpha_n = 1\%$, $\eta = 1^\circ$. For the two cases, the upper bounds of the radiation pattern in sidelobe region meet the constraint, that is, smaller than 0 dB.

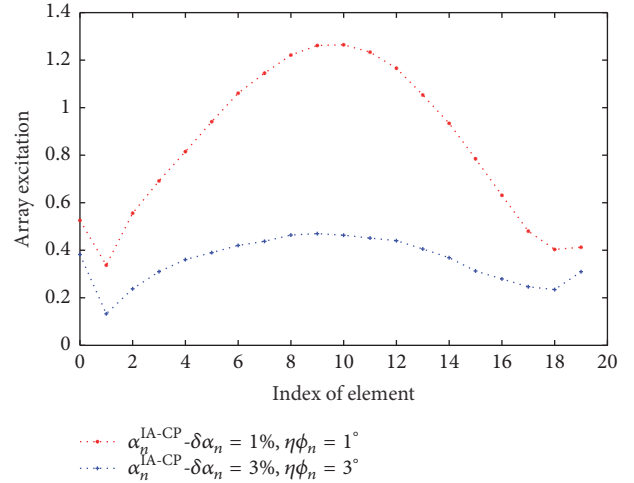
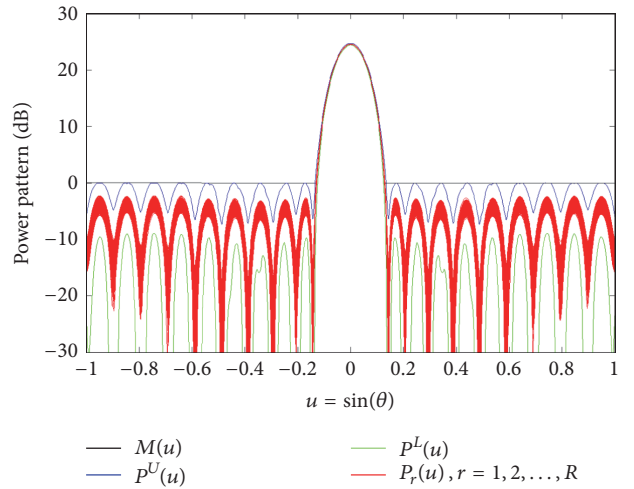
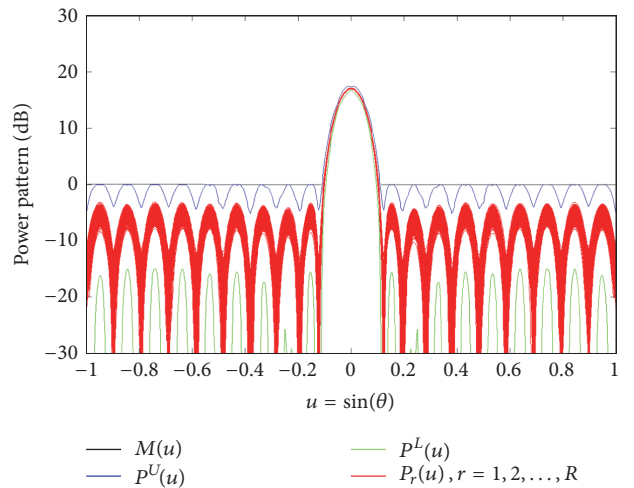


FIGURE 7: Optimized array excitation amplitudes using IA-CP method.


 FIGURE 8: Array radiation patterns using the optimized array excitation ($\delta\alpha_n = 1\%$, $\eta = 1^\circ$).

 FIGURE 9: Array radiation patterns using the optimized array excitation ($\delta\alpha_n = 3\%$, $\eta = 3^\circ$).

5. Conclusion

In this paper, a novel approach based on interval analysis has been proposed to efficiently access the impact on power pattern when random manufacturing errors are present on both the array weights and the element position. The upper and lower bounds of the corresponding radiated array pattern are deduced according to the rules of the interval arithmetic. The obtained bounds can be used to facilitate array synthesis when array weights error and elements position error are considered in real applications. Simulation results demonstrate the robustness and reliability of the deduced new bounds. Furthermore, with the derived bounds, array synthesis is realized in the presence of excitation errors.

Conflicts of Interest

The authors declare that there are no conflicts of interest regarding the publication of this paper.

References

- [1] C. A. Balanis, *Antenna Theory: Analysis and Design*, Wiley, New York, NY, USA, 3rd edition, 2005.
- [2] J. Ruze, "The effect of aperture errors on the antenna radiation pattern," *Il Nuovo Cimento*, vol. 9, no. 3, pp. 364–380, 1952.
- [3] J. K. Hsiao, "Design of error tolerance of a phased array," *Electronics Letters*, vol. 21, no. 19, pp. 834–836, 1985.
- [4] P. Rocca, L. Manica, N. Anselmi, and A. Massa, "Analysis of the pattern tolerances in linear arrays with arbitrary amplitude errors," *IEEE Antennas and Wireless Propagation Letters*, vol. 12, pp. 639–642, 2013.
- [5] N. Anselmi, L. Manica, P. Rocca, and A. Massa, "Tolerance analysis of antenna arrays through interval arithmetic," *Institute of Electrical and Electronics Engineers. Transactions on Antennas and Propagation*, vol. 61, no. 11, pp. 5496–5507, 2013.
- [6] R. E. Moore, *Interval Analysis*, Prentice-Hall, Englewood Cliffs, NJ, USA, 1966.
- [7] E. R. Hansen, "On solving systems of equations using interval arithmetic," *Mathematics of Computation*, vol. 22, pp. 374–384, 1968.
- [8] A. Neumaier, "Interval iteration for zeros of systems of equations," *BIT Numerical Mathematics*, vol. 25, no. 1, pp. 256–273, 1985.
- [9] E. Hansen, "Global optimization using interval analysis—the multidimensional case," *Numerische Mathematik*, vol. 34, no. 3, pp. 247–270, 1980.
- [10] E. Hansen and G. W. Walster, *Global Optimization Using Interval Analysis*, vol. 264, CRC Press, New York, NY, USA, 2004.
- [11] R. Boche, "Complex interval arithmetic with some applications Lockheed Missiles & Space Company," Tech. Rep. pp. 1-33, Sunnyvale, Calif, USA, 1966.
- [12] R. S. Elliott, *Antenna Theory and Design IEEE Press*, Wiley, Hoboken, NJ, USA, 2nd edition, 2003.
- [13] L. Poli, P. Rocca, N. Anselmi, and A. Massa, "Dealing with uncertainties on phase weighting of linear antenna arrays by means of interval-based tolerance analysis," *Institute of Electrical and Electronics Engineers. Transactions on Antennas and Propagation*, vol. 63, no. 7, pp. 3229–3234, 2015.
- [14] L. Manica, N. Anselmi, and P. Rocca, "Robust mask-constrained linear array synthesis through an interval-based particle SWARM optimization," *IET Microwaves, Antennas & Propagation*, vol. 7, no. 12, pp. 976–984, 2013.

Research Article

Full-Wave Analysis of the Shielding Effectiveness of Thin Graphene Sheets with the 3D Unidirectionally Collocated HIE-FDTD Method

Arne Van Londersele, Daniël De Zutter, and Dries Vande Ginste

Electromagnetics Group, Department of Information Technology-imec, Ghent University, Technologiepark Zwijnaarde 15, 9000 Gent, Belgium

Correspondence should be addressed to Arne Van Londersele; arne.vanlondersele@ugent.be

Received 29 March 2017; Accepted 22 May 2017; Published 3 July 2017

Academic Editor: Su Yan

Copyright © 2017 Arne Van Londersele et al. This is an open access article distributed under the Creative Commons Attribution License, which permits unrestricted use, distribution, and reproduction in any medium, provided the original work is properly cited.

Graphene-based electrical components are inherently multiscale, which poses a real challenge for finite-difference time-domain (FDTD) solvers due to the stringent time step upper bound. Here, a unidirectionally collocated hybrid implicit-explicit (UCHIE) FDTD method is put forward that exploits the planar structure of graphene to increase the time step by implicitizing the critical dimension. The method replaces the traditional Yee discretization by a partially collocated scheme that allows a more accurate numerical description of the material boundaries. Moreover, the UCHIE-FDTD method preserves second-order accuracy even for nonuniform discretization in the direction of collocation. The auxiliary differential equation (ADE) approach is used to implement the graphene sheet as a dispersive Drude medium. The finite grid is terminated by a uniaxial perfectly matched layer (UPML) to permit open-space simulations. Special care is taken to elaborate on the efficient implementation of the implicit update equations. The UCHIE-FDTD method is validated by computing the shielding effectiveness of a typical graphene sheet.

1. Introduction

Graphene, a carbon monolayer with honeycomb pattern, is a promising material to manufacture high-speed transistors and other switching devices thanks to its thinness, its mechanical strength, and its extraordinarily high electron mobility. Consequently, it has attracted lots of research interests, in particular with regard to the development of computational electromagnetic design tools. The finite-difference time-domain (FDTD) method is amid the most popular electromagnetic full-wave solvers. Classically, it discretizes both the electric and magnetic fields in a staggered fashion on a finite cubic grid and approximates the derivatives occurring in Maxwell's equations by second-order accurate central differences. The algorithm marches on in time by alternately updating the electric and magnetic fields with a time step that is bounded by the cell size. Hence, the thinness of graphene poses a huge computational burden on the conventional FDTD method as it invokes a dense temporal discretization.

Also, the spatial staggering gives rise to material-averaging errors near the graphene boundary.

To resolve both problems at once, the unidirectionally collocated hybrid implicit-explicit (UCHIE) FDTD method was proposed in 2D in [1] for good conductors in a multiscale environment and is extended here to 3D problems including graphene sheets. This 3D UCHIE-FDTD method implicitizes the direction perpendicular to the graphene boundary, hereby eliminating the small cell sizes from the time step limit and, consequently, speeding up the simulation. At the same time, it collocates the fields in this direction, which permits an unambiguous definition of the graphene boundary, strongly enhancing the accuracy. Furthermore, the proposed UCHIE-FDTD method wisely combines interpolations and differences as to preserve second-order accuracy even for nonuniform discretizations. Hence, different cell sizes can be adopted inside and outside the graphene sheet without any form of accuracy trade-off. In contrast to [1], where the UCHIE method was confined to a small part in the interior of

the simulation domain, open-space simulations now require the construction of a perfectly matched layer (PML) for the UCHIE method. Moreover, the dispersive properties of graphene necessitate an auxiliary differential equation (ADE) formulation of the UCHIE method. These are two important issues that will be tackled here.

In the remainder of this article, the set of continuous equations that need to be solved are first presented in Section 2, including a uniaxial PML. In Section 3, the corresponding update equations are listed. An efficient direct solver based on the twofold use of the Schur complement is next presented in Section 4. Finally, in Section 5, the proposed UCHIE-FDTD technique is validated by computing the shielding effectiveness (SE) of a practical graphene sheet illuminated by a plane wave, an electric dipole, and a magnetic dipole. Section 6 gives a short conclusion and lists some possible future research topics.

2. ADE Formulation

At microwave and THz frequencies, the conductivity of graphene is mainly attributed to intraband electron transitions. In that case, the graphene sheet is typically characterized by a Drude model with effective relative permittivity

$$\varepsilon_{r_g}(\omega) = 1 + \frac{\sigma_g/j\omega\varepsilon_0}{1 + j\omega/2\Gamma}, \quad (1)$$

where the volumetric DC conductivity of graphene is (see, e.g., [2])

$$\sigma_g = \frac{q^2 k_B T}{\pi \hbar^2 \Gamma d} \ln \left(2 \cosh \left(\frac{\mu_c}{2k_B T} \right) \right), \quad (2)$$

with q being the electron charge, \hbar the reduced Planck constant, k_B the Boltzmann constant, T the temperature, Γ the scattering rate, μ_c the chemical potential, and d the sheet thickness. The Drude model, which takes the dispersive nature of graphene into account, is incorporated into Maxwell's equations by means of an auxiliary differential equation describing the time-domain behavior of the graphene current \mathbf{J} . Thus, we are looking for the solution of

$$\begin{aligned} \mu_0 \frac{\partial \mathbf{H}}{\partial t} &= -\nabla \times \mathbf{E} \\ \varepsilon_0 \frac{\partial \mathbf{E}}{\partial t} + \mathbf{J} &= \nabla \times \mathbf{H} \\ \frac{1}{2\Gamma} \frac{\partial \mathbf{J}}{\partial t} + \mathbf{J} &= \sigma_g \mathbf{E}, \end{aligned} \quad (3)$$

with μ_0 and ε_0 being the vacuum permeability and permittivity, respectively. They constitute the vacuum wave impedance and phase velocity

$$\begin{aligned} Z_0 &= \sqrt{\frac{\mu_0}{\varepsilon_0}} \\ c_0 &= \frac{1}{\sqrt{\mu_0 \varepsilon_0}}. \end{aligned} \quad (4)$$

The substitution

$$\begin{aligned} \bar{\mathbf{E}} &= Z_0 \hat{\mathbf{E}} \\ \tau &= c_0 t \\ \hat{\sigma}_g &= Z_0 \sigma_g \end{aligned} \quad (5)$$

permits symmetrizing Maxwell's equations, yielding

$$\begin{aligned} \frac{\partial \bar{\mathbf{H}}}{\partial \tau} &= -\nabla \times \hat{\mathbf{E}} \\ \frac{\partial \hat{\mathbf{E}}}{\partial \tau} + \mathbf{J} &= \nabla \times \bar{\mathbf{H}} \\ \frac{c_0}{2\Gamma} \frac{\partial \mathbf{J}}{\partial \tau} + \mathbf{J} &= \hat{\sigma}_g \hat{\mathbf{E}}. \end{aligned} \quad (6)$$

In order to perform simulations in open space, a UPML is added [3]. Thereto, the electric and magnetic field each require one auxiliary equation to model the dispersive PML medium. Moreover, the electric field requires an additional auxiliary equation to prolong the graphene sheet inside the PML. We highlight these auxiliary unknowns by single and double bars. The final set of equations, embracing all these considerations, is

$$\begin{aligned} \kappa_{[yzx]} \frac{\partial \bar{\bar{\mathbf{H}}}}{\partial \tau} + \hat{\sigma}_{[yzx]} \bar{\bar{\mathbf{H}}} &= -\nabla \times \hat{\mathbf{E}} \\ \kappa_{[zxy]} \frac{\partial \bar{\mathbf{H}}}{\partial \tau} + \hat{\sigma}_{[zxy]} \bar{\mathbf{H}} &= \kappa_{[xyz]} \frac{\partial \bar{\bar{\mathbf{H}}}}{\partial \tau} + \hat{\sigma}_{[xyz]} \bar{\bar{\mathbf{H}}} \\ \frac{\partial \bar{\bar{\mathbf{E}}}}{\partial \tau} + \mathbf{J} &= \nabla \times \bar{\mathbf{H}} \\ \frac{c_0}{2\Gamma} \frac{\partial \mathbf{J}}{\partial \tau} + \mathbf{J} &= \hat{\sigma}_g \bar{\bar{\mathbf{E}}} \\ \kappa_{[yzx]} \frac{\partial \bar{\mathbf{E}}}{\partial \tau} + \hat{\sigma}_{[yzx]} \bar{\mathbf{E}} &= \frac{\partial \bar{\bar{\mathbf{E}}}}{\partial \tau} \\ \kappa_{[zxy]} \frac{\partial \hat{\mathbf{E}}}{\partial \tau} + \hat{\sigma}_{[zxy]} \hat{\mathbf{E}} &= \kappa_{[xyz]} \frac{\partial \bar{\bar{\mathbf{E}}}}{\partial \tau} + \hat{\sigma}_{[xyz]} \bar{\bar{\mathbf{E}}}, \end{aligned} \quad (7)$$

where a short notation was adopted for the tensors; for example,

$$\begin{aligned} \kappa_{[yzx]} &= \begin{bmatrix} \kappa_y & & \\ & \kappa_z & \\ & & \kappa_x \end{bmatrix} \\ \hat{\sigma}_{[yzx]} &= Z_0 \begin{bmatrix} \sigma_y & & \\ & \sigma_z & \\ & & \sigma_x \end{bmatrix}, \end{aligned} \quad (8)$$

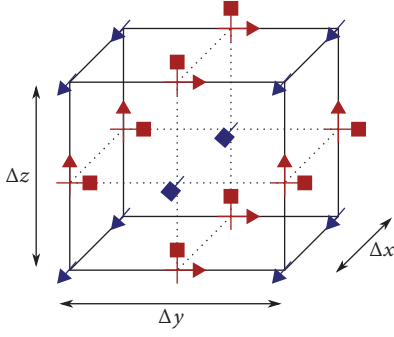


FIGURE 1: The UCHIE cell for implicitization and collocation in the x -dimension. Triangular arrows denote electric field components and square arrows magnetic field components. Blue and red markers are staggered in time.

with, for the i th PML layer,

$$\begin{aligned}\kappa_u &= 1 + (\kappa_u^{\max} - 1) \left(\frac{i}{n_{\text{pml}}} \right)^m \\ \sigma_u &= \sigma_u^{\max} \left(\frac{i}{n_{\text{pml}}} \right)^m\end{aligned}\quad (9)$$

$$u \in \{x, y, z\}.$$

This is the so-called polynomially graded PML with number of layers n_{pml} and power m . In this paper, we always choose the standard values $n_{\text{pml}} = 10$ and $m = 4$. Also, from [3], we borrow the optimal value

$$\sigma_u^{\max} = \frac{m+1}{150\pi \Delta u} \quad u \in \{x, y, z\}, \quad (10)$$

where Δu is the spatial step in the u -dimension (i.e., Δx , Δy , or Δz). The UPML is mathematically perceived as a complex stretching of the Cartesian coordinates (and the fields) ensuring impedance matching across its interface. In other words, it is a reflectionless lossy medium. The real-stretch parameter κ_u aims to absorb the evanescent waves, whereas the imaginary-stretch parameter σ_u is responsible for the absorption of the traveling waves. They are, respectively, one and zero inside the simulation region of interest, and they are polynomially graded according to (9) inside the PMLs normal to the u -dimension. In the next section, (7) is discretized, giving rise to the UCHIE-FDTD update equations.

3. Update Equations

In a nutshell, the UCHIE-FDTD method organizes the electromagnetic field components in unidirectionally collocated cells such as the one depicted in Figure 1. Unlike traditional collocated finite-difference methods, the proposed scheme ensures second-order accuracy, albeit at the cost of computationally more involved update equations. Thereto, it retains the conventional central differences, but it evaluates the Maxwell equations that contain a derivative with respect to

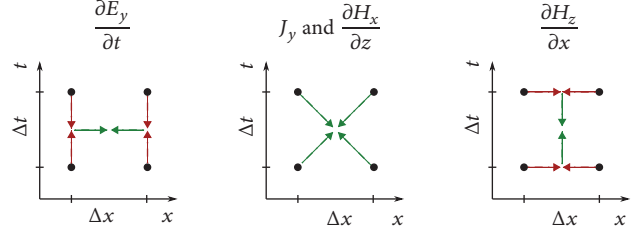


FIGURE 2: Visualization of the difference method applied to the Maxwell equation $\varepsilon \partial_t E_y + J_y = \partial_z H_x - \partial_x H_z$. The black dots represent the field samples in the (x, t) -space, the red arrows are differences, and the green arrows are interpolations. All terms are evaluated with second-order accuracy in the midpoint of the rectangle formed by the four sample points.

the direction of collocation (here the x -dimension) right in the middle between two adjacent samples in that direction by means of linear interpolations. In order to end up with a consistent update scheme, similar field interpolations are needed in time. This principle is exemplified in Figure 2. In the end, the two field components along the direction of collocation, that is, E_x and H_x , are updated explicitly, whereas the remaining four field components are updated implicitly. In line with conventional ADE schemes, the electric current components have the exact same discretization as their associated electric field components. Hence, we get the following set of explicit update equations:

$$\begin{aligned}\gamma_y^+ \bar{h}_x|_{i,j+1/2,k+1/2}^{n+1} &= \gamma_y^- \bar{h}_x|_{i,j+1/2,k+1/2}^n \\ &\quad - \frac{1}{\Delta y} \left(\hat{e}_z|_{i,j+1,k+1/2}^{n+1/2} - \hat{e}_z|_{i,j,k+1/2}^{n+1/2} \right) \\ &\quad + \frac{1}{\Delta z} \left(\hat{e}_y|_{i,j+1/2,k+1}^{n+1/2} - \hat{e}_y|_{i,j+1/2,k}^{n+1/2} \right)\end{aligned}\quad (11)$$

$$\begin{aligned}\gamma_z^+ h_x|_{i,j+1/2,k+1/2}^{n+1} &= \gamma_z^- h_x|_{i,j+1/2,k+1/2}^n \\ &\quad + \left(\gamma_x^+ \bar{h}_x|_{i,j+1/2,k+1/2}^{n+1} - \gamma_x^- \bar{h}_x|_{i,j+1/2,k+1/2}^n \right)\end{aligned}$$

for the magnetic field and

$$\begin{aligned}\left(\frac{1}{\Delta \tau} + \frac{\hat{\sigma}_g}{2\alpha^+} \right) \bar{e}_x|_{i,j,k}^{n+1} &= \left(\frac{1}{\Delta \tau} - \frac{\hat{\sigma}_g}{2\alpha^+} \right) \bar{e}_x|_{i,j,k}^n - \frac{1}{2} \left(1 + \frac{\alpha^-}{\alpha^+} \right) j_x|_{i,j,k}^n \\ &\quad + \frac{1}{\Delta y} \left(h_z|_{i,j+1/2,k}^{n+1/2} - h_z|_{i,j-1/2,k}^{n+1/2} \right) \\ &\quad - \frac{1}{\Delta z} \left(h_y|_{i,j,k+1/2}^{n+1/2} - h_y|_{i,j,k-1/2}^{n+1/2} \right)\end{aligned}$$

$$\begin{aligned}
\alpha^+ j_x|_{i,j,k}^{n+1} &= \alpha^- j_x|_{i,j,k}^n + \hat{\sigma}_g \left(\bar{\mathbf{e}}_x|_{i,j,k}^{n+1} + \bar{\mathbf{e}}_x|_{i,j,k}^n \right) \\
\gamma_y^+ \bar{\mathbf{e}}_x|_{i,j,k}^{n+1} &= \gamma_y^- \bar{\mathbf{e}}_x|_{i,j,k}^n + \frac{1}{\Delta\tau} \left(\bar{\mathbf{e}}_x|_{i,j,k}^{n+1} - \bar{\mathbf{e}}_x|_{i,j,k}^n \right) \\
\gamma_z^+ \hat{\mathbf{e}}_x|_{i,j,k}^{n+1} &= \gamma_z^- \hat{\mathbf{e}}_x|_{i,j,k}^n + \gamma_x^+ \bar{\mathbf{e}}_x|_{i,j,k}^{n+1} - \gamma_x^- \bar{\mathbf{e}}_x|_{i,j,k}^n
\end{aligned} \tag{12}$$

for the electric field. Here, we used the notation

$$\begin{aligned}
\alpha^\pm &= \frac{\epsilon_0}{\Gamma\Delta\tau} \pm 1 \\
\gamma_u^\pm &= \frac{\kappa_u}{\Delta\tau} \pm \frac{Z_0\sigma_u}{2} \quad u \in \{x, y, z\}.
\end{aligned} \tag{13}$$

There are two implicit updates (14) and (15). The PEC boundary conditions at the back of the PMLs require the exterior tangential electric fields to be zero. Consequently, for n_x cells in the x -dimension, there are $n_x - 1$ electric field and $n_x + 1$ magnetic field samples in (14)-(15). The bracket notation is used to denote diagonal matrices whose rank is $n_x - 1$ or $n_x + 1$ depending on whether they act on electric or magnetic field components, respectively.

$$\begin{aligned}
& \begin{bmatrix} [\alpha^+] & -[\hat{\sigma}_g] & 0 & 0 & 0 & 0 \\ \frac{A_1}{2} & \frac{A_1}{\Delta\tau} & 0 & 0 & D_2 & 0 \\ 0 & 0 & A_2[\gamma_x^+] & 0 & 0 & D_1 \\ 0 & -\frac{I}{\Delta\tau} & 0 & [\gamma_z^+] & 0 & 0 \\ 0 & 0 & -[\gamma_z^+] & 0 & [\gamma_y^+] & 0 \\ 0 & 0 & 0 & -[\gamma_y^+] & 0 & [\gamma_x^+] \end{bmatrix} \begin{bmatrix} \mathbf{j}_y \\ \bar{\mathbf{e}}_y \\ \bar{\mathbf{h}}_z \\ \bar{\mathbf{e}}_y \\ \mathbf{h}_z \\ \hat{\mathbf{e}}_y \end{bmatrix}_{j+1/2,k}^{n+1/2} \\
& = \begin{bmatrix} [\alpha^-] & [\hat{\sigma}_g] & 0 & 0 & 0 & 0 \\ -\frac{A_1}{2} & \frac{A_1}{\Delta\tau} & 0 & 0 & -D_2 & 0 \\ 0 & 0 & A_2[\gamma_x^-] & 0 & 0 & -D_1 \\ 0 & -\frac{I}{\Delta\tau} & 0 & [\gamma_z^-] & 0 & 0 \\ 0 & 0 & -[\gamma_z^-] & 0 & [\gamma_y^-] & 0 \\ 0 & 0 & 0 & -[\gamma_y^-] & 0 & [\gamma_x^-] \end{bmatrix} \begin{bmatrix} \mathbf{j}_y \\ \bar{\mathbf{e}}_y \\ \bar{\mathbf{h}}_z \\ \bar{\mathbf{e}}_y \\ \mathbf{h}_z \\ \hat{\mathbf{e}}_y \end{bmatrix}_{j+1/2,k}^{n-1/2} \\
& + \begin{bmatrix} 0 \\ \frac{A_1}{\Delta z} (\mathbf{h}_{x,j+1/2,k+1/2}^n - \mathbf{h}_{x,j+1/2,k-1/2}^n) \\ \frac{A_2}{\Delta y} (\hat{\mathbf{e}}_{x,j+1,k}^n - \hat{\mathbf{e}}_{x,j,k}^n) \\ 0 \\ 0 \\ 0 \end{bmatrix}
\end{aligned} \tag{14}$$

$$\begin{aligned}
& \begin{bmatrix} [\alpha^+] & -[\hat{\sigma}_g] & 0 & 0 & 0 & 0 \\ \frac{A_1}{2} & \frac{A_1}{\Delta\tau} & 0 & 0 & -D_2 & 0 \\ 0 & 0 & A_2[\gamma_z^+] & 0 & 0 & -D_1 \\ 0 & -\frac{I}{\Delta\tau} & 0 & [\gamma_x^+] & 0 & 0 \\ 0 & 0 & -[\gamma_y^+] & 0 & [\gamma_x^+] & 0 \\ 0 & 0 & 0 & -[\gamma_z^+] & 0 & [\gamma_y^+] \end{bmatrix} \begin{bmatrix} \mathbf{j}_z \\ \bar{\mathbf{e}}_z \\ \bar{\mathbf{h}}_y \\ \bar{\mathbf{e}}_z \\ \mathbf{h}_y \\ \hat{\mathbf{e}}_z \end{bmatrix}_{j,k+1/2}^{n+1/2} \\
& = \begin{bmatrix} [\alpha^-] & [\hat{\sigma}_g] & 0 & 0 & 0 & 0 \\ -\frac{A_1}{2} & \frac{A_1}{\Delta\tau} & 0 & 0 & D_2 & 0 \\ 0 & 0 & A_2[\gamma_z^-] & 0 & 0 & D_1 \\ 0 & -\frac{I}{\Delta\tau} & 0 & [\gamma_x^-] & 0 & 0 \\ 0 & 0 & -[\gamma_y^-] & 0 & [\gamma_x^-] & 0 \\ 0 & 0 & 0 & -[\gamma_z^-] & 0 & [\gamma_y^-] \end{bmatrix} \begin{bmatrix} \mathbf{j}_z \\ \bar{\mathbf{e}}_z \\ \bar{\mathbf{h}}_y \\ \bar{\mathbf{e}}_z \\ \mathbf{h}_y \\ \hat{\mathbf{e}}_z \end{bmatrix}_{j,k+1/2}^{n-1/2} \\
& - \begin{bmatrix} 0 \\ \frac{A_1}{\Delta y} (\mathbf{h}_{x,j+1/2,k+1/2}^n - \mathbf{h}_{x,j-1/2,k+1/2}^n) \\ \frac{A_2}{\Delta z} (\hat{\mathbf{e}}_{x,j,k+1}^n - \hat{\mathbf{e}}_{x,j,k}^n) \\ 0 \\ 0 \\ 0 \end{bmatrix}.
\end{aligned} \tag{15}$$

Besides, we introduced the x -interpolators

$$\begin{aligned}
A_1 &= \begin{bmatrix} 1 & & & & & \\ & 1 & & & & \\ & & \ddots & & & \\ & & & 1 & & \\ & & & & 1 & \\ & & & & & 1 \end{bmatrix}_{n_x \times (n_x - 1)} \\
A_2 &= \begin{bmatrix} 1 & & & & & \\ & 1 & & & & \\ & & \ddots & & & \\ & & & 1 & & \\ & & & & 1 & \\ & & & & & 1 \end{bmatrix}_{n_x \times (n_x + 1)},
\end{aligned} \tag{16}$$

and the x -differentiators

$$\begin{aligned}
D_1 &= \begin{bmatrix} \Delta x_1 & & & & & \\ & \ddots & & & & \\ & & \Delta x_{n_x} & & & \end{bmatrix}^{-1} \begin{bmatrix} 1 & & & & & \\ -1 & 1 & & & & \\ & & \ddots & & & \\ & & & -1 & 1 & \\ & & & & & -1 \end{bmatrix}_{n_x \times (n_x - 1)} \\
D_2 &= \begin{bmatrix} \Delta x_1 & & & & & \\ & \ddots & & & & \\ & & \Delta x_{n_x} & & & \end{bmatrix}^{-1} \begin{bmatrix} -1 & 1 & & & & \\ & \ddots & & & & \\ & & & -1 & 1 & \\ & & & & & -1 \end{bmatrix}_{n_x \times (n_x + 1)}.
\end{aligned} \tag{17}$$

As suggested by the time-indices of the field samples, the time stepping algorithm alternately performs sets of explicit

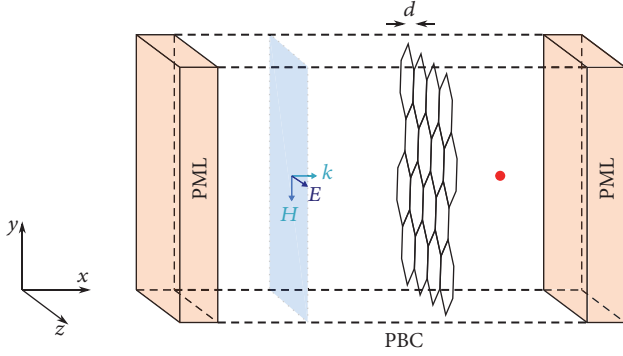


FIGURE 3: The TFSD plane (blue) excites a plane wave with nonzero components H_y and E_z which normally impinges upon a thin graphene sheet (hexagons) of thickness $d = 1$ nm. The electric field E_z is recorded a few cells behind the graphene sheet (red). Infiniteness in the y - and z -dimension is mimicked by PBCs along four of the exterior faces. The remaining two faces are covered by PMLs to absorb outgoing waves in the x -dimension.

- (2) Compute $\mathbf{p} = \mathbf{v}_1 - M_{12}M_{22}^{-1}\mathbf{v}_2$ and split this vector into two parts \mathbf{p}_1 and \mathbf{p}_2 conforming to the partitioning applied in (22).
- (3) Use forward and backward triangular sweeps to compute $[\bar{\mathbf{e}}_y, \bar{\mathbf{h}}_z] = R^T Q U^{-1} L^{-1} P C R (\mathbf{p}_2 - S_{21} S_{11}^{-1} \mathbf{p}_1)$.
- (4) Compute $\mathbf{j}_y = S_{11}^{-1} (\mathbf{p}_1 - S_{12} [\bar{\mathbf{e}}_y, \bar{\mathbf{h}}_z])$.
- (5) Compute $[\bar{\mathbf{e}}_y, \bar{\mathbf{h}}_z, \hat{\mathbf{e}}_y] = M_{22}^{-1} (\mathbf{v}_2 - M_{21} [\mathbf{j}_y, \bar{\mathbf{e}}_y, \bar{\mathbf{h}}_z])$.

For clarity, we omitted the transposition superscripts above, because it should be quite clear that all occurring vectors are column vectors. Note that some matrix products can be computed prior to time stepping. Compared to the conventional HIE-FDTD method [5], the proposed UCHIE-FDTD method requires the inversion of two pentadiagonal matrices of rank $2n_x$ instead of two tridiagonal matrices of rank n_x . Hence, the improved accuracy of the UCHIE-FDTD method comes at a slightly higher computational cost.

5. Numerical Examples

5.1. SE for a Plane Wave. The graphene sheet under investigation has $d = 1$ nm, $T = 300$ K, $\mu_c = 0.05$ eV, and $\Gamma = 0.5$ THz. Hence, according to (2), the sheet has a DC conductivity $\sigma_g = 6.7$ S/ μm . In order to validate the stability and accuracy of the proposed unidirectionally collocated HIE-FDTD method, the shielding effectiveness is determined for normal plane-wave incidence on an infinite graphene sheet. Thereto, a similar configuration as the one in [6, 7] is adopted and depicted in Figure 3. A plane wave is generated by a total-field scattered-field (TFSD) surface placed at one side of the graphene sheet, whereas the transmitted field $E_{z_g}(t)$ is recorded in one point at the other side of the sheet. The source is a differentiated Gaussian pulse with bandwidth $b = 0.55$ THz, temporal width $t_w = 2/\pi b$, and delay $t_d = 6t_w$. The spatial invariance in the y - and z -dimension is fulfilled by imposing periodic boundary conditions (PBCs). Both the

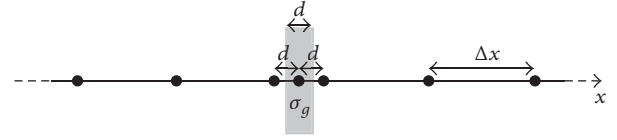


FIGURE 4: Discretization along the x -axis. The vacuum part of the grid is uniformly discretized with step $\Delta x \approx 27$ μm . The graphene sheet is approximated by two small UCHIE cells of size $d = 1$ nm. The graphene conductivity $\sigma_g = 6.7$ S/ μm is solely assigned to the single discretization point enclosed by these two small cells and does not need to be averaged as is the case for the conventional Yee grid.

transmitted and the back-scattered plane waves are absorbed by UPMLs with $\kappa_x^{\text{max}} = 1$. The overall grid is uniformly discretized with steps $\Delta x = \Delta y = \Delta z \approx 27$ μm , whereas the graphene sheet is locally resolved by two small cells of size d along the x -axis as depicted in Figure 4. The time step equals the Courant limit in the yz -plane, more specifically

$$\Delta \tau = \frac{1}{\sqrt{1/\Delta y^2 + 1/\Delta z^2}} \approx 19 \mu\text{m}, \quad (29)$$

which is about 19,000 times larger than the time step that would have been used by the classical FDTD method. The recorder is placed 136 μm beyond the graphene sheet. The simulation performs 10,000 iterations. An auxiliary simulation uses the same configuration but replaces the graphene sheet by a vacuum layer as to record the reference field $E_{z_0}(t)$. The time-domain data are then Fourier transformed and their ratio determines the shielding effectiveness

$$\text{SE}_{\text{num}}(\omega) = 20 \log_{10} \left| \frac{\mathcal{F}[E_{z_0}(t)]}{\mathcal{F}[E_{z_g}(t)]} \right|. \quad (30)$$

The analytical solution for the SE is known to be

$$\text{SE}_{\text{ana}}(\omega) = 20 \log_{10} \left| \frac{1 - r^2 e^{-jk_g 2d}}{1 - r^2} e^{jk_g d} \right|, \quad (31)$$

with r being the Fresnel reflection coefficient of a single vacuum-graphene interface

$$r = \frac{1 - \sqrt{\epsilon_{r_g}}}{1 + \sqrt{\epsilon_{r_g}}}, \quad (32)$$

and wave number

$$k_g = \frac{\omega}{c_0} \sqrt{\epsilon_{r_g}}. \quad (33)$$

Recall that the effective relative permittivity of the graphene sheet ϵ_{r_g} was defined previously in (1). The resulting SEs are plotted in Figure 5. Despite the enormous refinement ratio of 27,000, the analytical and numerical curves are indistinguishable, confirming the accuracy of the UCHIE-FDTD method. The shielding is mainly ascribed to reflections from the two interfaces rather than to the skin effect. At 0.5 THz, the skin depth, hereby meaning the thickness that the graphene sheet should have to reduce the amplitude of a plane wave by 63%, is 360 nm and this value increases towards DC.

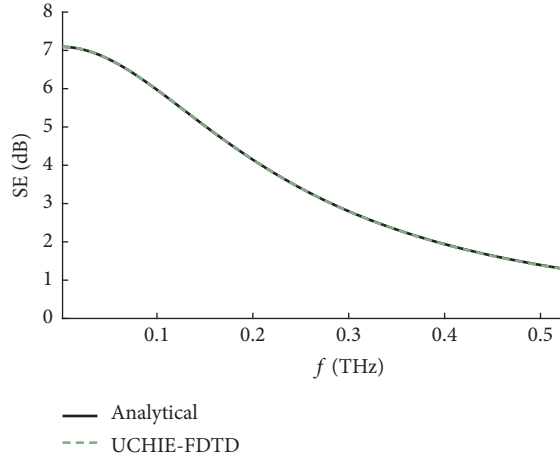


FIGURE 5: Shielding effectiveness of the 1 nm graphene sheet illuminated by a normally incident plane wave.

5.2. SE for an E- and H-Dipole. A similar simulation is repeated but this time a dipole of length Δz is excited, at a distance $d_s = 409 \mu\text{m}$ from the left side of the graphene sheet. All six exterior faces of the grid are covered by UPMLs, this time with $\kappa_x^{\text{max}} = \kappa_y^{\text{max}} = \kappa_z^{\text{max}} = 10$ in order to absorb the evanescent waves radiated by the dipole source as well as the evanescent waves inside the graphene sheet. Indeed, the graphene sheet extends inside the PMLs in order to exclude reflections from its outer edges, such that we are again modeling an infinite graphene sheet. For the E-dipole, the SE is again determined by recording E_z and taking the ratio defined in (30), whereas, for the H-dipole, the dual definition of the SE is adopted where E_z is replaced by H_z . The recorded fields are plotted in Figure 6 together with the plane-wave data from Section 5.1. The resulting SEs for both the E- and the H-dipole are shown in Figure 7. Below 0.12 THz, which corresponds to $k_0 d_s < 1$, the graphene sheet experiences the reactive near field of the dipole. For this frequency range, the wave impedances of the E- and H-dipole are approximately $Z_E = Z_0/k_0 d_s > Z_0$ and $Z_H = Z_0 k_0 d_s < Z_0$, respectively. The graphene sheet behaves like a classical good conductor at low frequencies. As such, it has a very low wave impedance. Consequently, the E-dipole experiences a higher contrast resulting in more reflections, whereas the H-dipole does the opposite. This is exactly what we observe in Figure 7: at low frequencies, the E-dipole is better shielded by the graphene sheet due to strong reflections, whereas the H-dipole does not even notice the graphene sheet because their wave impedances have the same order of magnitude. At higher frequencies, both dipoles are electrically further removed from the graphene sheet and, consequently, they resemble a plane wave as demonstrated by the convergence of the three curves in Figure 7.

6. Conclusion

A novel HIE-FDTD method is proposed that features collocation in the direction of implicitization. This technique, combined with the ADE formalism to incorporate Drude

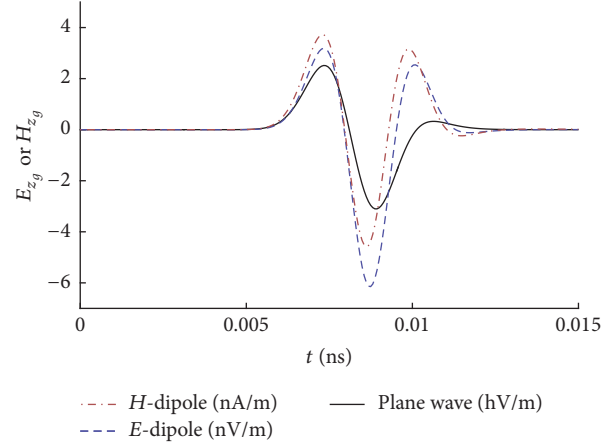


FIGURE 6: Fields recorded in the observation point behind the graphene sheet. Only a small part of the total simulated time (0.6428 ns) is shown.

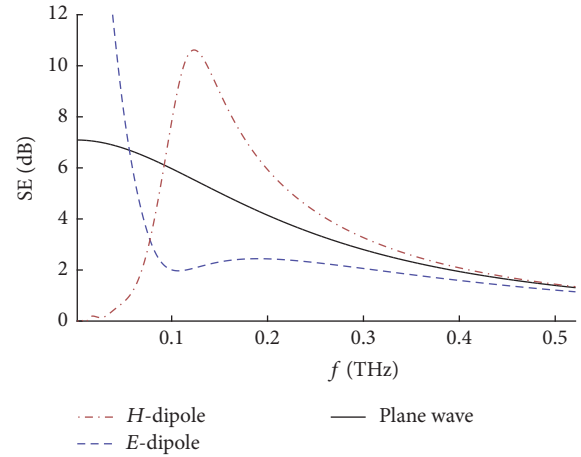


FIGURE 7: Shielding effectiveness of the 1 nm graphene sheet illuminated by a small E- and H-dipole.

media, is demonstrated to accurately capture the multi-scale and dispersive intricacies of graphene sheets in the microwave and THz regime. At higher frequencies such as the near infrared, the contributions from both the intraband and interband interactions to the overall conductivity of the graphene sheet should be taken into account as was done in [7] by means of Padé fitting. Future work focuses on the extension to gyrotropic graphene sheets in the presence of a biasing magnetic field, which is preferably treated with a fully collocated FDTD method such as the one described in [8]. However, an intensive study is required to reduce the computational cost of the occurring matrix inversion, which will be critical for the success of this approach. Also, it should be possible to combine the presented UCHIE-FDTD method with classical Yee-FDTD by means of a correct generalization to three dimensions of the interface condition derived in [1].

Conflicts of Interest

The authors declare that there are no conflicts of interest regarding the publication of this paper.

References

- [1] A. Van Londersele, D. De Zutter, and D. Vande Ginste, "A new hybrid implicit-explicit FDTD method for local subgridding in multiscale 2-D TE scattering problems," *IEEE Transactions on Antennas and Propagation*, vol. 64, no. 8, pp. 3509–3520, 2016.
- [2] D. L. Sounas and C. Caloz, "Gyrotropy and nonreciprocity of graphene for microwave applications," *IEEE Transactions on Microwave Theory and Techniques*, vol. 60, no. 4, pp. 901–914, 2012.
- [3] S. D. Gedney, "An anisotropic perfectly matched layer-absorbing medium for the truncation of FDTD lattices," *IEEE Transactions on Antennas and Propagation*, vol. 44, no. 12, pp. 1630–1639, 1996.
- [4] D. S. Bernstein, *Matrix Mathematics: Theory, Facts, and Formulas*, Princeton University Press, Princeton, NJ, USA, 2009.
- [5] J. Chen and J. Wang, "A three-dimensional semi-implicit FDTD scheme for calculation of shielding effectiveness of enclosure with thin slots," *IEEE Transactions on Electromagnetic Compatibility*, vol. 49, no. 2, pp. 354–360, 2007.
- [6] M. L. Zhai, H. L. Peng, X. H. Wang, X. Wang, Z. Chen, and W. Y. Yin, "The conformal HIE-FDTD method for simulating tunable graphene-based couplers for THz applications," *IEEE Transactions on Terahertz Science and Technology*, vol. 5, no. 3, pp. 368–376, 2015.
- [7] J. Chen, J. Li, and Q. H. Liu, "Designing graphene-based absorber by using HIE-FDTD method," *IEEE Transactions on Antennas and Propagation*, vol. 65, no. 4, pp. 1896–1902, 2017.
- [8] W. Tierens and D. De Zutter, "An unconditionally stable time-domain discretization on cartesian meshes for the simulation of nonuniform magnetized cold plasma," *Journal of Computational Physics*, vol. 231, no. 15, pp. 5144–5156, 2012.

Research Article

Numerical Simulations of the Lunar Penetrating Radar and Investigations of the Geological Structures of the Lunar Regolith Layer at the Chang'E 3 Landing Site

Chunyu Ding,^{1,2,3} Yan Su,^{1,2} Shuguo Xing,^{1,2} Shun Dai,^{1,2} Yuan Xiao,^{1,2,3} Jianqing Feng,^{1,2} Danqing Liu,⁴ and Chunlai Li^{1,2}

¹Key Laboratory of Lunar and Deep Space Exploration, Chinese Academy of Sciences, Beijing 100012, China

²National Astronomical Observatories, Chinese Academy of Sciences, Beijing 100012, China

³University of Chinese Academy of Sciences, Beijing 100049, China

⁴Renmin University of China, Beijing 100872, China

Correspondence should be addressed to Yan Su; suyan@nao.cas.cn

Received 21 December 2016; Revised 12 March 2017; Accepted 3 April 2017; Published 23 May 2017

Academic Editor: Han Guo

Copyright © 2017 Chunyu Ding et al. This is an open access article distributed under the Creative Commons Attribution License, which permits unrestricted use, distribution, and reproduction in any medium, provided the original work is properly cited.

In the process of lunar exploration, and specifically when studying lunar surface structure and thickness, the established lunar regolith model is usually a uniform and ideal structural model, which is not well-suited to describe the real structure of the lunar regolith layer. The present study aims to explain the geological structural information contained in the channel 2 LPR (lunar penetrating radar) data. In this paper, the random medium theory and Apollo drilling core data are used to construct a modeling method based on discrete heterogeneous random media, and the simulation data are processed and collected by the electromagnetic numerical method FDTD (finite-difference time domain). When comparing the LPR data with the simulated data, the heterogeneous random medium model is more consistent with the actual distribution of the media in the lunar regolith layer. It is indicated that the interior structure of the lunar regolith layer at the landing site is not a pure lunar regolith medium but rather a regolith-rock mixture, with rocks of different sizes and shapes. Finally, several reasons are given to explain the formation of the geological structures of the lunar regolith layer at the Chang'E 3 landing site, as well as the possible geological stratification structure.

1. Introduction

The exploration of the internal structure of moon has been ongoing since the first time a human being landed on the surface of the moon in the 1960s. According to the analysis of seismic data, the internal structure of the moon can be roughly divided into a lunar crust, lunar mantle, and lunar nucleus. The thickness of the outermost lunar shell is approximately 60~65 km, the top 1~2 km of which mainly consists of lunar regolith and rock fragments [1]. On December 2, 2013, China successfully launched the Chang'E 3 spacecraft to explore the moon. The LPR was one of the important payloads on the Chang'E 3. As a high-resolution lunar surface penetrating radar, LPR consists of two channels.

The first channel is centered at a 60 MHz frequency and has a meter-level resolution in simulated lunar rock material. It is used to detect the subsurface lunar structures along the path of the Yutu rover. The second channel is centered at a 500 MHz frequency, with a resolution of less than 30 cm in the simulated lunar regolith, and it is used to detect the internal structure of the lunar regolith and its thickness. ALSE (Apollo Lunar Sounder Experiment), LRS (Lunar Radar Sounder), and LPR are all surface penetration radars, which are usually used to detect subsurface lunar structures. However, the LPR resolution is significantly higher than that of either ALSE or LRS. Especially for the detection of lunar regolith, the resolution of ALSE and LRS does not have sufficient detection accuracy, and the deepest drilling depth of an experiment

TABLE 1: Basic parameters of lunar penetrating radar.

LPR parameters	Ch. 1	Ch. 2
Center frequency (MHz)	60	500
Pulse emission voltage (V)	1000	400
Bandwidth (MHz)	40–80	250–750
Sampling interval (ns)	2.5	0.3125
Range resolution	Meter level	<30 cm
Detection depth (m)	≥ 100 m	≤ 30 m

with a sample return is 294.5 cm from Apollo 17 [2]. However, it is obvious that the above drilling depths cannot reach the bottom of the lunar regolith layer in the lunar maria, where the average layer depth is approximately 5 m [3]. Therefore, the LPR data are valuable for the study of the internal structure of the lunar regolith. Furthermore, the core diameter from the Apollo borehole is no more than 4 cm, which means that no data, other than that of lunar penetrating radar, can directly verify that there exist rock fragments with diameters larger than 4 cm in the lunar regolith.

The study of the internal structure or thickness of the lunar regolith requires theoretical modeling, regardless of whether active radar detection or passive microwave radiometer detection is used. For instance, Shkuratov and Bondarenko [3] established a simplified ideal uniform lunar regolith structure model to obtain the first map of the distribution of lunar regolith thickness on the front side of the moon using the data of the Arecibo Astronomical Observatory's 70 cm-wavelength ground-based radar in combination with the iron and titanium abundances of the front side of the lunar surface. Lan and Zhang [4] assumed that the lunar regolith layer is a uniform medium in their study of the thickness of the lunar regolith using microwaves. Fa and Jin [5] assumed that the lunar regolith layer has a uniform distribution of dense particle media to simulate the bright temperature of the multichannel lunar surface radiation. Meng et al. [6] assumed that the permittivity of the lunar regolith follows changes in depth, established a nonisotropic lunar model, and analyzed lunar thickness, frequency, and other effects on the bright temperature. Using the same assumption as Meng et al., Chen et al. [7] established two-layer and three-layer models. In Chen et al.'s studies, the lunar surface structure was simulated using GprMax, and its waveform characteristics were analyzed.

However, the LPR data show that the internal structure of the lunar regolith is very complex and the above modeling method is too ideal, so it is difficult to describe the real structure of the lunar regolith. Therefore, here, we employ the random medium model theory, Apollo drilling sample data, and geomorphologic images to establish a heterogeneous random medium model of the lunar regolith layer. Then, the FDTD numerical method is used to simulate the propagation of the electromagnetic wave in the model. The result of the echoes is obtained and compared with the LPR data.

2. Lunar Penetrating Radar (LPR)

LPR is a surface penetrating radar with a carrier frequency in the nanosecond pulse time domain whose working principle [8] is as follows: the transmitter antenna emits an electromagnetic wave into the lunar subsurface; when the propagating electromagnetic wave meets a heterogeneous medium, layered interface, or other buried object, phenomena such as reflection, diffraction, and scattering occur; the receiving antenna receives echo signals, such as reflections and scatterings; by analyzing and processing the received echo signals, we will obtain information about the geological structure of the lunar regolith along the road of Yutu rover. The basic parameters of the LPR are shown in Table 1.

The echo signals are mainly affected by the electromagnetic wave propagation velocity v , seen in (1), and the attenuation α , seen in (2), in the Yutu rover detection process.

$$\alpha = \omega \left[\frac{\mu\epsilon_r}{2} \left(\sqrt{1 + \left(\frac{\sigma}{\omega\epsilon_r} \right)^2} - 1 \right) \right]^{1/2}, \quad (1)$$

$$v = c \left\{ \frac{\epsilon_r}{2\epsilon_0} \left[\left(\sqrt{1 + \left(\frac{\sigma}{\omega\epsilon_r} \right)^2} + 1 \right) \right] \right\}^{-1/2}, \quad (2)$$

where ω is the angular frequency, c is the speed of light in free space, μ is the permeability, ϵ_r is the permittivity, and σ is the electrical conductivity. The loss tangent, $\tan \delta = \sigma/\omega\epsilon_r$, reflects the loss of energy when propagating through the lunar regolith.

3. The Heterogeneous Random Medium Model of the Lunar Regolith Layer

As shown in Figure 1, there is a random distribution of lunar rocks of different sizes on the lunar surface. Therefore, it is inferred that there exist a large number of small-scale and irregularly distributed media, such as basalt grains and breccias, under the lunar surface. The radar echo signal is affected by these small-scale media during the detection process, which is probably the reason for the confusing radar gram. These small-scale media distributions can be considered as random processes to study the characteristics of their permittivity. The technique of random medium modeling is applied to the seismic numerical simulation [9–11].

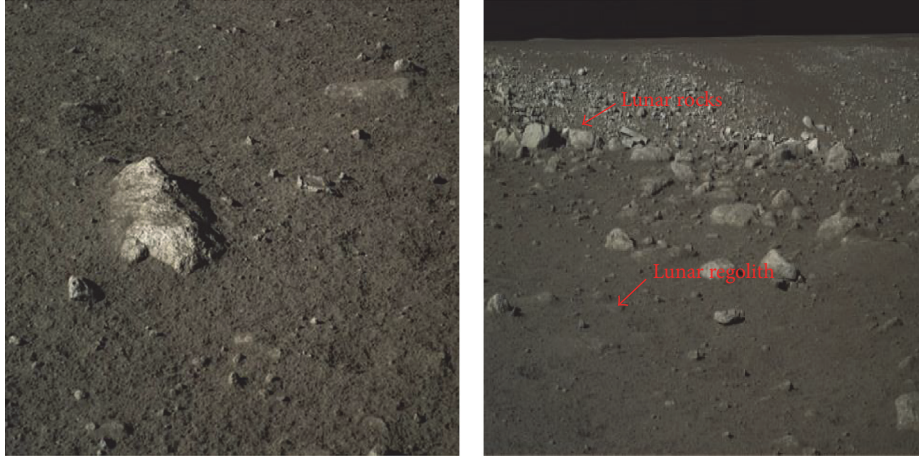


FIGURE 1: The photos were taken by the panoramic camera on the Yutu rover.

On the assumption of stationary random processes, the permittivity of the random medium model is expressed by

$$\varepsilon(x, z) = \varepsilon_m + \delta(x, z) \varepsilon_f(x, z), \quad (3)$$

where ε_m is the mean permittivity of the background, $\delta(x, z)$ is the standard deviation, and $\varepsilon_f(x, z)$ is a small-scale random perturbation whose spatial distribution is subject to

$$\phi(x, z) = \exp \left\{ - \left[\left(\frac{x \cos \theta + z \sin \theta}{a} \right)^2 + \left(\frac{-x \sin \theta + z \cos \theta}{b} \right)^2 \right]^{1/(1+r)} \right\}, \quad (4)$$

where $\phi(x, z)$ is the autocorrelation function; parameters a and b are the horizontal and vertical autocorrelation lengths, respectively; θ is the autocorrelation angle; and r is the roughness factor at the microscale. When $r = 0$, (4) is the Gaussian autocorrelation function. When $r = 1$, (4) is the exponential autocorrelation function. When $0 < r < 1$, (4) is a hybrid autocorrelation function [12].

The algorithm of the established discrete random medium model is as follows.

Step 1. The power spectra density function, $\Phi(k_x, k_z)$, of the spatial random perturbation function, $\varepsilon_f(x, z)$, was calculated from (4) and is defined as

$$\Phi(k_x, k_z) = \sum_{x=0}^{M-1} \sum_{z=0}^{N-1} \phi(x, z) e^{-j2\pi(k_x x/M + k_z z/N)}. \quad (5)$$

Step 2. We used a random phase function $\varphi(k_x, k_z)$, which is an independent and evenly distributed two-dimensional random sequence on the interval $[0, 2\pi)$, to calculate the random power spectra function $W(k_x, k_z)$, which is defined as

$$W(k_x, k_z) = \sqrt{\Phi(k_x, k_z)} \cdot e^{j\varphi(k_x, k_z)}. \quad (6)$$

Step 3. We obtained the spatial perturbation function of the random medium, $\varepsilon_f(x, z)$, by using the inverse Fourier transform of the random power spectra function.

$$\varepsilon_f(x, z) = \frac{1}{MN} \sum_{k_x=0}^{M-1} \sum_{k_z=0}^{N-1} W(k_x, k_z) e^{j2\pi(k_x x/M + k_z z/N)}. \quad (7)$$

Step 4. The spatial perturbation function was normalized. Moreover, we substitute (7) into (3) to achieve a discrete heterogeneous random medium model.

The lunar regolith layer medium should be composed of a lunar regolith and rock mixture at the Chang'E 3 landing site area, which is shown in Figure 2. This type of lunar geological structure can be called a regolith-rocks mixture. Hence, the random medium theory modeling method is used to describe the geological structure of a regolith-rocks mixture. According to previous knowledge from the Apollo samples, the lunar regolith is mainly composed of mineral and rock fragments, breccia debris, all kinds of glass material, meteorite fragments, and so forth, with a permittivity in the range of 2.3 to 3.5 and loss tangent in the range of 0.005~0.009. The mare region is mainly composed of basalt, with a permittivity in the range of 6.6 to 8.6 and a loss tangent in the range of 0.009~0.016 [13]. Therefore, we assume that the dielectric properties of the random medium model of the lunar regolith range from 2.3 to 8.6 and the loss tangent ranges from 0.005 to 0.016. A set of autocorrelation lengths, a and b , equal to 0.05 m, 0.1 m, 0.2 m, and 0.3 m, are chosen to establish four discrete heterogeneous random medium models with different characteristics, which are shown in Figure 3. The model size is 5 m \times 5 m and the length of the discrete step is 0.01 m. The channel 2 antenna, which is mounted on the bottom of the Yutu rover, is 0.3 m away from the lunar surface. Hence, we set the antenna height as 0.3 m off the lunar surface in the model. The first layer is the vacuum layer, with a permittivity of 1 and a depth of 0.3 m. The second layer is the heterogeneous random medium of the lunar regolith layer with a background permittivity of 4.8, autocorrelation angle of 0, roughness factor of 0, and model standard deviation of

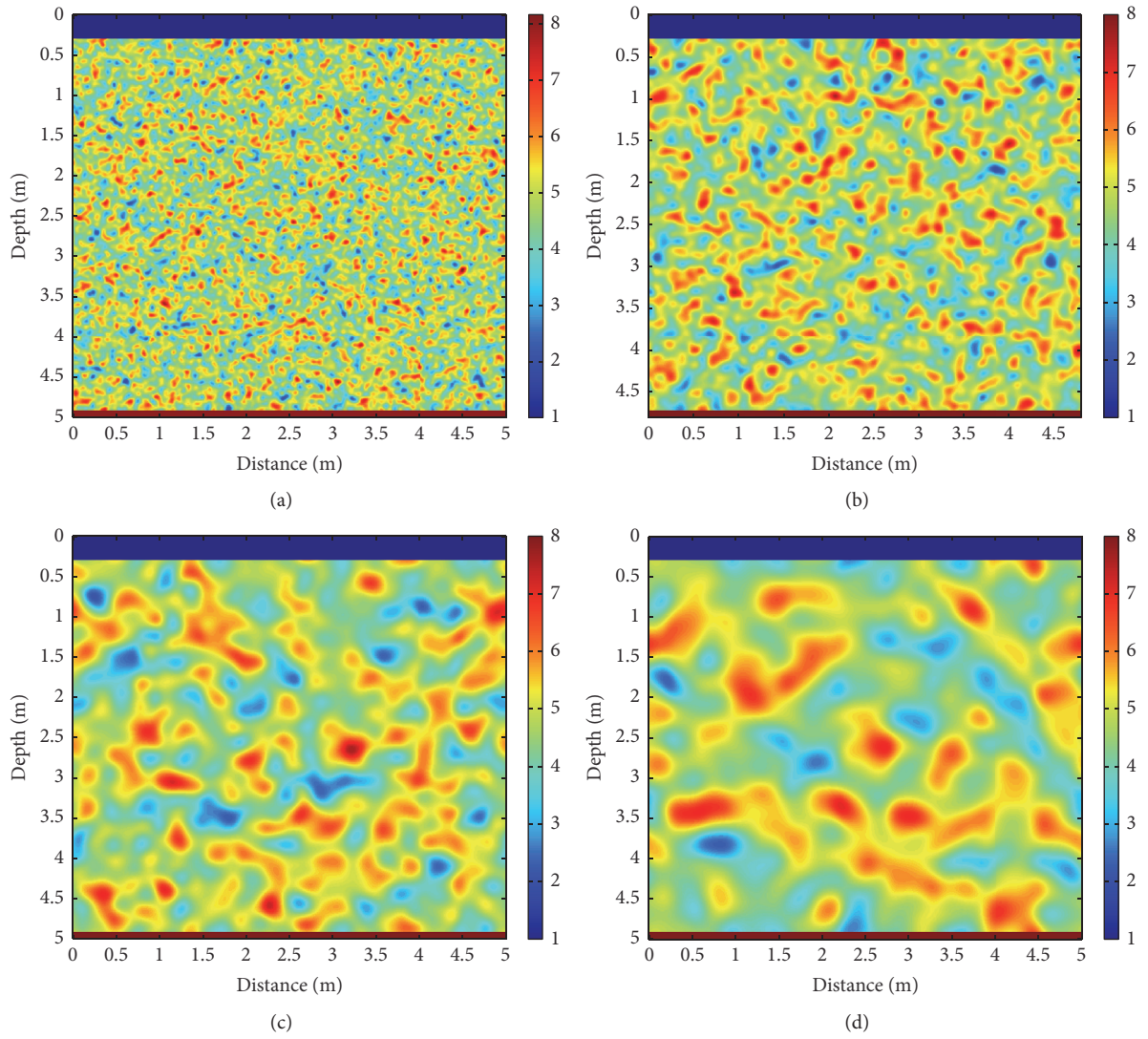


FIGURE 2: The discrete heterogeneous medium models, (a), (b), (c), and (d), with different autocorrelation lengths of 0.05 m, 0.1 m, 0.2 m, and 0.3 m, respectively.

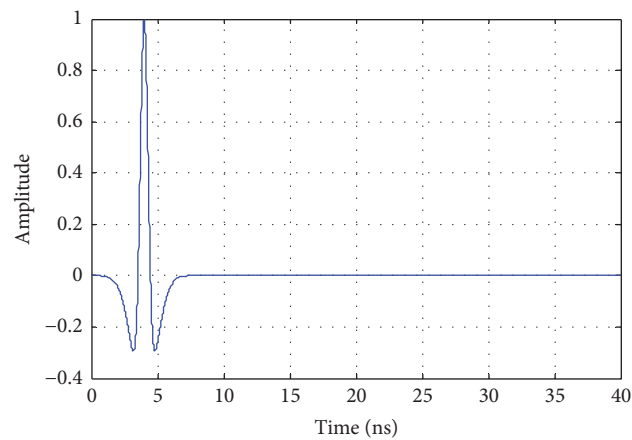


FIGURE 3: UWB Ricker pulse waveform.

0.85. The third layer serves as a reference layer with a permittivity of 8 and a depth of 0.1 m. The autocorrelation length describes the scale of the random medium in the horizontal and vertical directions, which is manifested in the size of the rock fragments distributed randomly in the model, as shown in Figure 3. With an increase of the autocorrelation length, the size of the rocks increases and the number of rocks decreases. That is, the distribution of the real medium in the lunar regolith layer can be described effectively by selecting the appropriate parameters.

4. The Numerical Simulation of LPR Channel 2

4.1. *The Selection of the Radiation Pulse Source.* The radar radiation pulse source waveform is taken from [8], which can be calculated by UWB Ricker. Equation (8) [14] is defined as

$$E_{\text{excit}}(\tau) = \frac{\phi_{\eta} \exp[-\pi^2 \phi_{\eta}^2 (\tau - \tau_0)^2] - \phi_{\lambda} \exp[-\pi^2 \phi_{\lambda}^2 (\tau - \tau_0)^2]}{\phi_{\eta} - \phi_{\lambda}} \quad (8)$$

We substituted the parameters of the LPR into (8), where $\phi_{\eta} = 750$ MHz, $\phi_{\lambda} = 250$ MHz, and time τ_0 is 4 ns. Then, we can obtain the radiation pulse source waveform shown in Figure 3.

4.2. *The Numerical Method of the 2D-FDTD.* The differential Maxwell equations in the time domain are given by

$$\nabla \times H = \varepsilon \frac{\partial E}{\partial t} + \sigma E, \quad (9a)$$

$$\nabla \times E = -\mu \frac{\partial H}{\partial t} - \sigma H, \quad (9b)$$

where H is the magnetic field strength and E is the electric field strength. ε , μ , and σ are the dielectric permittivity, permeability, and conductivity, respectively. Considering only the two-dimensional TM mode [15], all of the electric fields are transverse electric fields for the y coordinates, and (9a) and (9b) contain only the directional components of H_x , H_z , and E_y . In the Cartesian coordinate system, the 2D-FDTD differential iterative equations in the TM mode are defined as

$$H_x^{n+1/2}(i, j) = \frac{2\mu_x(i, j) - \Delta t \sigma_x(i, j)}{2\mu_x(i, j) + \Delta t \sigma_x(i, j)} \times H_x^{n-1/2}(i, j) + \frac{2\Delta t}{2\mu_x(i, j) + \Delta t \sigma_x(i, j)} \left(\frac{E_y^n(i, j+1) - E_y^n(i, j)}{\Delta z} \right), \quad (10a)$$

$$H_z^{n+1/2}(i, j) = \frac{2\mu_z(i, j) - \Delta t \sigma_z(i, j)}{2\mu_z(i, j) + \Delta t \sigma_z(i, j)} \times H_z^{n-1/2}(i, j) - \frac{2\Delta t}{2\mu_z(i, j) + \Delta t \sigma_z(i, j)} \left(\frac{E_y^n(i+1, j) - E_y^n(i, j)}{\Delta x} \right), \quad (10b)$$

$$E_y^{n+1}(i, j) = \frac{2\varepsilon_y(i, j) - \Delta t \sigma_y(i, j)}{2\varepsilon_y(i, j) + \Delta t \sigma_y(i, j)} \times E_y^n(i, j) + \frac{2\Delta t}{2\varepsilon_y(i, j) + \Delta t \sigma_y(i, j)} \left(\frac{H_x^{n+1/2}(i, j) - H_x^{n+1/2}(i-1, j)}{\Delta z} - \frac{H_z^{n+1/2}(i, j) - H_z^{n+1/2}(i, j-1)}{\Delta x} \right). \quad (10c)$$

Moreover, in order to avoid the dispersion of the electromagnetic wave caused by the numerical calculation, it is necessary to satisfy the following conditional formula (see (11)) when the discrete interval parameters Δt , Δx , and Δz approach zero.

$$\Delta t \leq \sqrt{\frac{\mu\varepsilon}{(1/\Delta x^2 + 1/\Delta z^2)}}. \quad (11)$$

4.3. *Numerical Simulation of the Models.* This section will make use of the 2D-FDTD numerical method to simulate the heterogeneous random medium models (a), (b), (c), and (d), which are established in Figure 2. As a comparison, the second layer in Figure 2(a) is replaced by homogeneous media with a permittivity of 3 and loss tangent of 0.005. Before the simulation, we need to set the parameters of the simulation model. The transmitter and receiver are set in the same position as the point source. The simulation time window is set to 80 ns. The discrete grid spacing is set to 0.01 m. A data trace is detected with every movement of 0.043 m in the horizontal direction. The separation distance is in accordance with the real situation when the LPR probed the lunar surface. The simulated horizontal direction of the model is 5 m, such that it receives 116 data traces. The discrete time step is set to 0.02 ns, according to (11). Due to the limited memory of the computer, a PML (Perfectly Matched Layer) is used as the electromagnetic absorption boundary condition [16], which simulates the propagation of electromagnetic waves in free infinite space.

The simulation result of the model (a) was calculated by 2D-FDTD, shown as both the A-Scan and B-Scan in Figure 4. In the figure, the direct and coupling waves of the radargram are clearly shown, but the reflected echoes of the buried objects are not clearly displayed. The A-Scan waveforms were plotted from a trace of the B-Scan data, and it was found that the amplitudes of the direct and coupling wave reflected signals were much larger than those of the reflected signals from the lunar buried objects.

The main objective of this data processing is to analyze the reflection signal of the objects in the lunar regolith layer. For this reason, the amplitudes of the reflected signals of the direct and coupling waves can be suppressed by the threshold in (12) to relatively increase the amplitude of the reflection signal of the lunar buried objects.

$$\text{Amplitude}(i, j) = \begin{cases} \text{threshold}, & \text{if } |\text{Amplitude}(i, j)| > \text{threshold}, \\ \text{Amplitude}(i, j), & \text{else.} \end{cases} \quad (12)$$

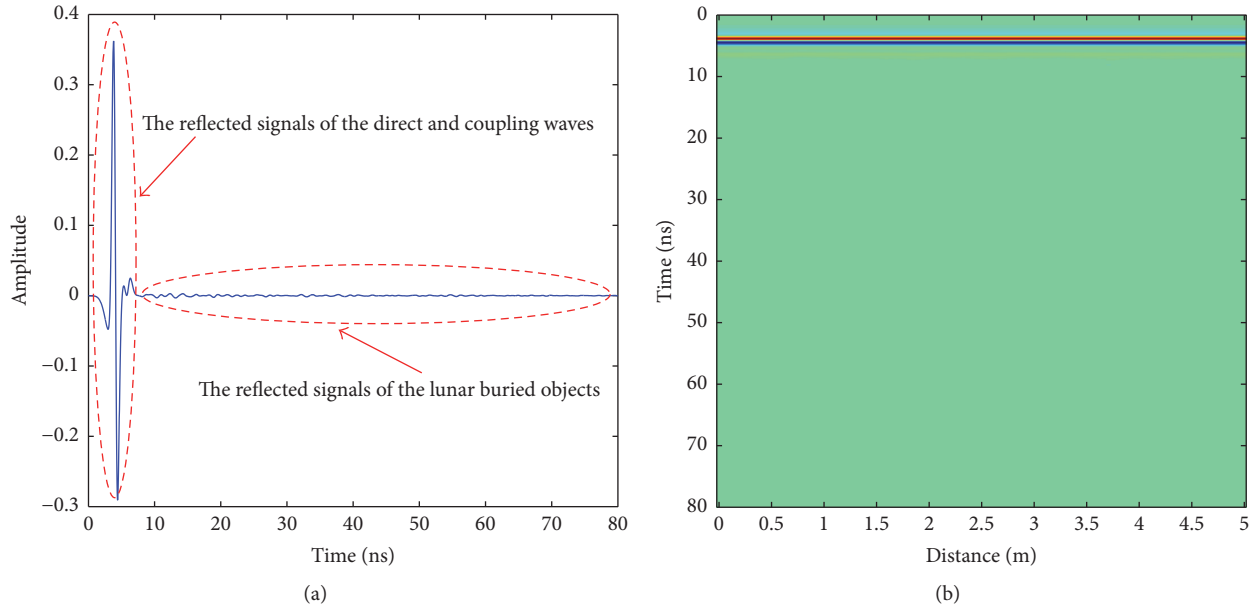


FIGURE 4: The simulation result of the random media model (a). The A-Scan of the simulated data is shown in (a). The B-Scan of the simulated data is shown in (b).

The amplitude threshold is set to 0.003 for each radar gram which are the simulation results of the models (a), (b), (c), and (d) and the homogeneous media. We plotted both the A-Scan and B-Scan simulation results, shown in Figure 5.

The time delay of the lunar surface is 7.91 ns, as calculated in Figure 5. The reference layer echoes cannot be found from simulation results of models (a) and (b) because the radargrams are so cluttered, but they can be gradually found when they become more distinct, in models (c) and (d), from the homogeneous media, in which the time delays are 75.58 ns, 72.39 ns, and 61.29 ns, respectively. On the one hand, as the autocorrelation length decreases, the complexity of the model increases. The position of the echo signals of the reference layer is delayed because it is obscured by other signals and cannot be visually distinguished. On the other hand, when the autocorrelation length increases and the multiplied reflected echoes among the rock fragments are diminished, the amplitude of the reflected echoes of the buried targets in the lunar regolith layer model is gradually weakened, and the reference layer gradually becomes distinct. Moreover, this simulated experiment can also explain why the LPR did not find clear layers below the lunar surface at the Chang'E 3 landing site. The details of the investigation of the geological information of the lunar regolith layer will be elaborated in the following chapters.

5. Comparison between the LPR Data and Simulated Data

The LPR began work at 10:50:32 (UTC) on December 15, 2013, and ran until 14:16:56 (UTC) on January 15, 2014, when it stopped working due to a mechanical problem after a total

of 277 minutes of work on the lunar surface [17]. Channel 2 received 2351 valid data traces during that working period. The probe distance is approximately 114 m along the path of the Yutu rover on the moon. Part of the LPR data at the landing site in the Mare Imbrium is shown in Figure 6. Meanwhile, we compared the LPR data with the simulated data calculated from the lunar regolith models by FDTD.

By comparing the LPR data and the simulation data, it is found that the echo characteristics of the two radargrams are similar. To quantify the degree of similarity of the two radargrams, the Bhattacharyya distance is used to analyze the two datasets in this paper. The method used to calculate the Bhattacharyya distance is defined as follows:

$$D_{\text{dist}}(p_{\text{meas}}, q_{\text{simul}}) = -\ln \left(\sum \sqrt{p_{\text{meas}} \cdot q_{\text{simul}}} \right), \quad (13)$$

where p_{meas} and q_{simul} are the LPR data and simulation data, respectively. The results of the Bhattacharyya distances of models (a), (b), (c), and (d) and the homogeneous model are 0.5829, 0.7798, 0.1165, 0.1216, and 0.1045, respectively. It is clear that model (b) is the most similar to the LPR data among those results. This means that the heterogeneous random medium model (b) effectively corresponds to the interior structural characteristics of the lunar regolith. Hence, we can infer that the lunar regolith layer is not a purely regolith medium but rather has a distribution of a large number of rock fragments of uneven sizes and different shapes, and the diameters of the rock fragments are approximately 20 cm. In addition, there are continuously reflected echo signals at 24 ns, which may be a stratified structure in the lunar regolith layer or an echo signal of a continuous block of rocks.

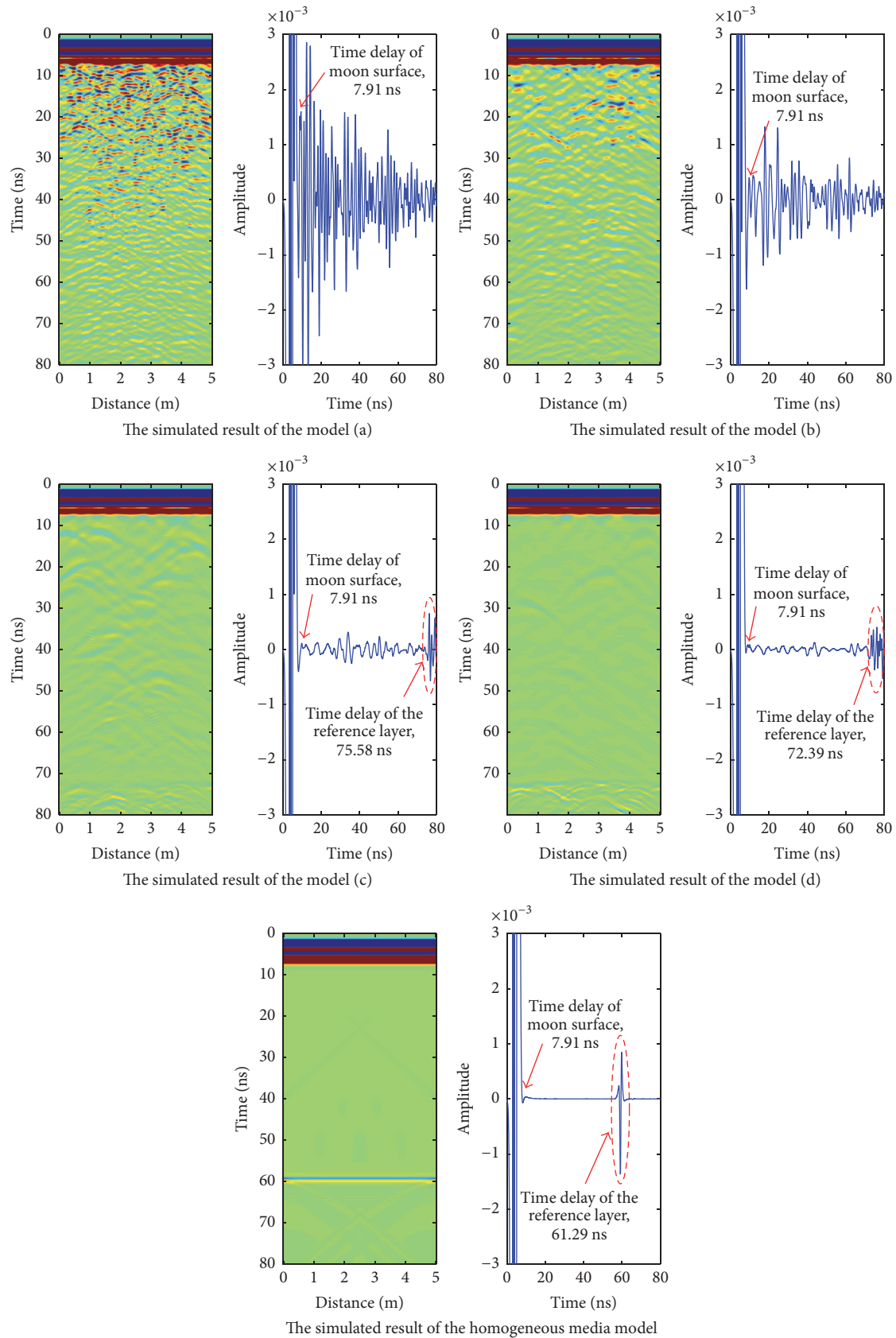


FIGURE 5: The A-Scan and B-Scan simulation results of the models (a), (b), (c), and (d) and the homogeneous media with the amplitude threshold at 0.003.

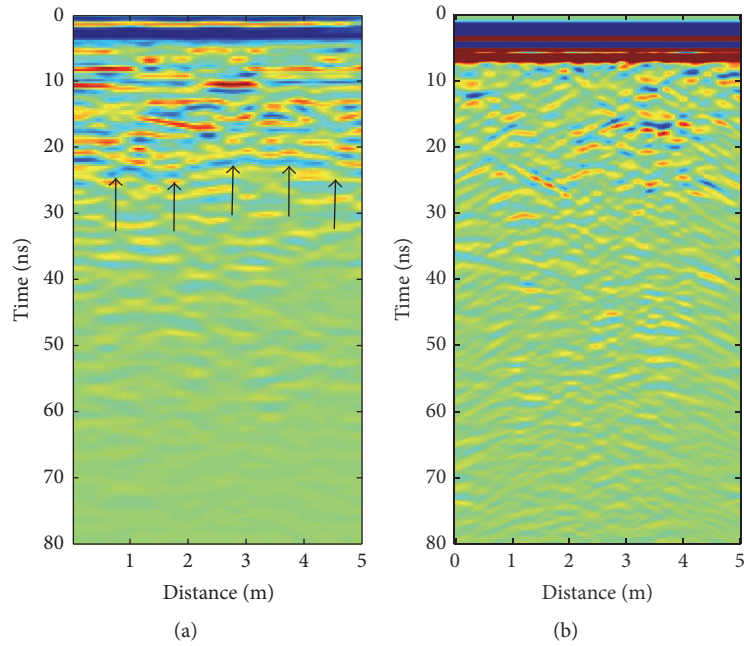


FIGURE 6: B-Scan of the LPR data (a) and the simulated data (b) of the heterogeneous random medium model (b).

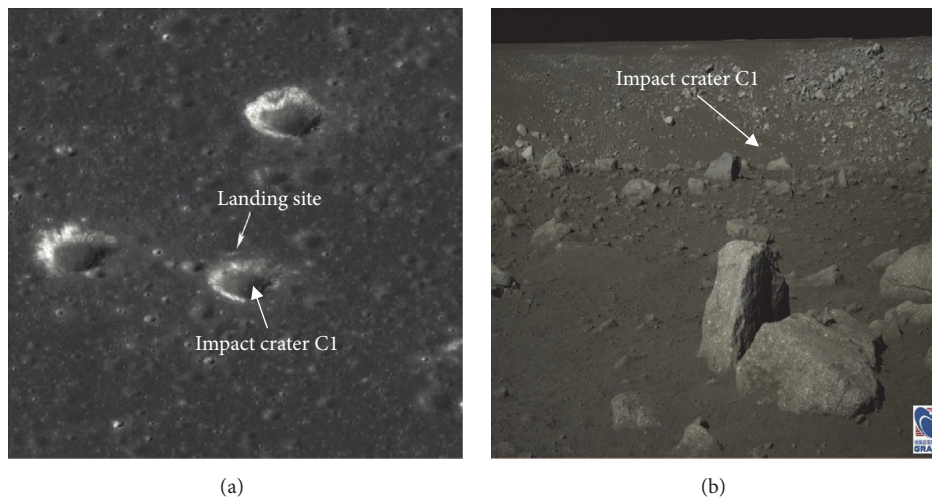


FIGURE 7: Chang'E 3 landing site and the topography of the impact crater C1. (a) is from Arizona State University, and (b) is from the Science and Application Center for Moon and Deep Space Exploration.

6. The Interior Structure of the Lunar Regolith at the Chang'E 3 Landing Site

The Chang'E 3 landed near the young crater C1, which has a diameter of approximately 450 m [18, 19]. The landing position was approximately 50 m from the edge of the impact crater. It can be seen in Figures 1 and 7 that the lunar surface is scattered with a large number of rock fragments of different sizes. At the impact edge, the distribution of rock fragments is even denser. These rocks originate from the lunar crater formation process. When the meteorite crashed on the lunar surface, the bedrock was contacted, squeezed, and crushed. This process formed an ejecta blanket and dug out material from

deeper sections of the lunar surface. Some rocks were gasified or melted by the high temperatures, forming new material. The broken rock fragments were also formed because the meteorite impact process involves a massive transfer of mechanical energy to heat energy. Therefore, the large-scale materials sputtering over the original lunar regolith layer formed an ejecta layer, which could also be called a new lunar regolith layer, including a large number of new materials formed by the high temperature, such as impact breccias, glass, and metal, and broken rock blocks.

Xiao et al. [18] used a diameter-frequency method to estimate the geological age of the landing site (impact crater C1) at a minimum model age of 27 million years (My) and a

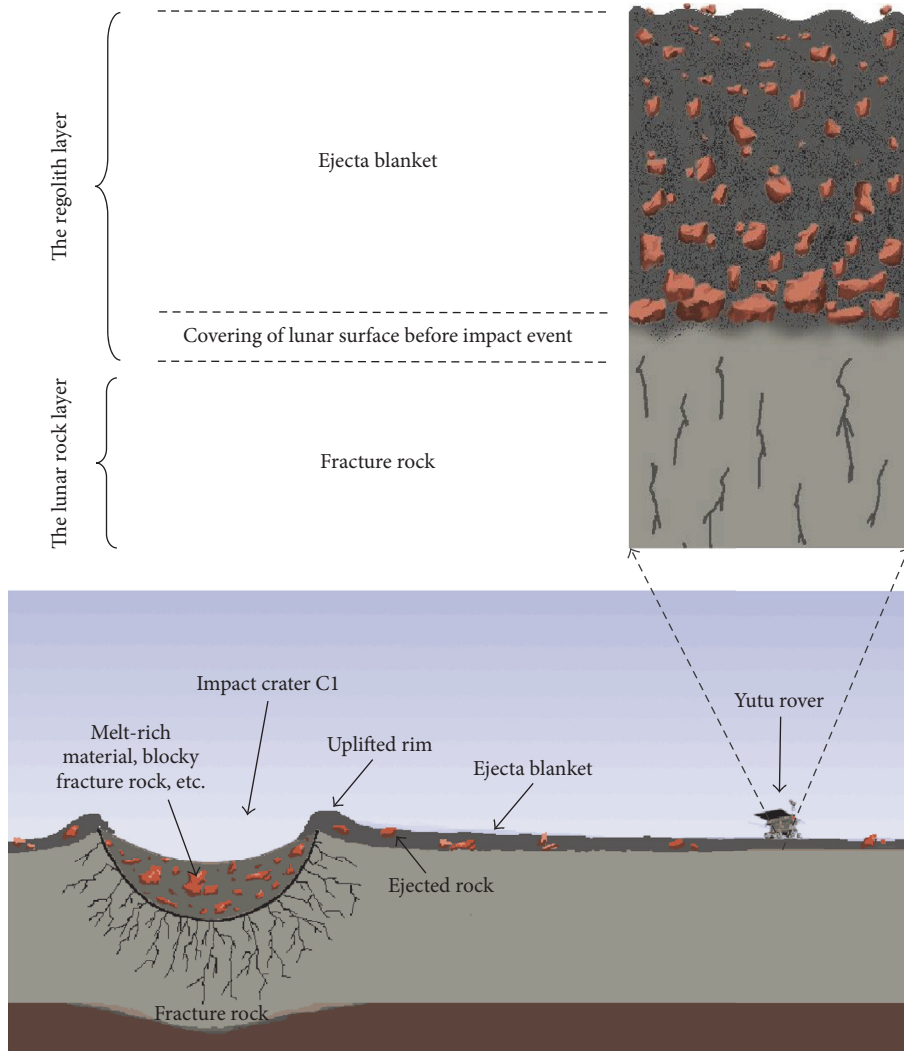


FIGURE 8: The diagram of the interior structure of the lunar regolith layer at the Chang'E 3 landing site.

maximum model age of 80 million years (My). This indicates that the geological structure is very young, the lunar regolith is immature, and the internal structure is rock-like. Basilevsky et al. [20] compared the photographs taken by the Lunokhod and Yutu rovers, which indicated that there exist rock blocks with diameters of dozens of centimeters across the lunar surface. In other words, it can be inferred that the interior of the lunar regolith also contains similar scales of rocks. This is consistent with one of the conclusions of the current study, namely, that the interior of the lunar regolith is a regolith-rock mixture.

Based on the above studies, the subsurface geological structures of the Chang'E 3 landing site are probably divided into a lunar regolith layer and a lunar rock layer, as shown in Figure 8. The lunar regolith layer includes the materials of the ejecta blanket and the original lunar regolith layer. We did not include the lunar dust layer because the boundary between the lunar dust layer and lunar regolith layer is difficult to define in this dataset. Because the geological structure of the Chang'E 3 landing site is very young, with immature lunar

regolith and more internal stones, it is easy to misidentify the continuous echoes produced by a number of adjacent lunar rocks as a layered structure in the radargram. According to the statistics of the Apollo samples, as the sampling depth increases, the average diameter of the rocks in the lunar regolith layer increases slightly. In general, lunar rock size is related to maturity. The higher the maturity level, the smaller the diameter of lunar rocks. The maturity is related to the time of exposure on lunar surface [21]. It can be seen that the maturity of the lunar regolith is low at the landing site; the distribution of the interior rocks is irregular, and the geological structure is young at the Chang'E 3 landing site. Therefore, one possible structure is a fractured rock layer that transitions to the bedrock layer below the lunar regolith layer.

The specific depth of the lunar regolith layer is not determined because the simulation results show that, within a certain range, as the number of rocks increases, the electromagnetic wave propagation in that medium will produce multiple reflections and scattering, which makes the radar echoes too complicated. Thus, an accurate depth of the lunar regolith

is difficult to determine by LPR. In fact, the boundary between the lunar regolith layer and the lunar rock layer is not clear [22]. Rather, it is a gradual structure from top to bottom, which makes it difficult for radar to distinguish interior layers.

7. Conclusion and Discussion

Based on the theory of the random medium model, the Apollo drilling samples data, and the real lunar surface at the Chang'E 3 landing site, the model of a heterogeneous random medium is established. By using the FDTD numerical method, electromagnetic wave propagation is simulated and the resulting radar echoes are obtained. Comparing the LPR data and the simulated data, the following conclusions are obtained:

- (1) The lunar model of a heterogeneous random medium is more consistent with the real structure of the lunar regolith than other theoretical models of the lunar regolith layer used in the preceding literature.
- (2) The radar echoes become more complicated as the number of rocks increases, within a certain range. Thus, the accurate depth and interior structure of the lunar regolith are difficult to determine by LPR.
- (3) The interior of the lunar regolith is not a purely uniform medium but has a distribution of regolith-rock mixture media with different rock sizes and shapes. The diameter of the rock fragments is approximately 20 cm in the lunar regolith layer, which is larger than the 4 cm diameter of the sample from the Apollo mission.
- (4) The site produces clear layered echoes at approximately 24 ns in the LPR data, shown in Figure 6. These layered echoes can be interpreted as stratified structures in the interior of the lunar regolith or as a large number of small-scale lunar rocks that produce overlapping radar echo signals.

The future Chang'E 5 program will be equipped with a lunar regolith radar sounder, which will have a higher detection resolution and working frequency than the LPR. Therefore, further studies of the application of the heterogeneous random medium method in lunar regolith modeling will be helpful to interpret the lunar radar data and better understand the real distribution characteristics and structures of the lunar regolith. In addition, the traditional homogeneous multireflection filtering method [23] has been difficult to use to filter the multiple reflection electromagnetic waves of the radar echoes in the lunar regolith layer. Using statistical methods, it is possible to establish a multireflection filtering method based on the random medium theory, which may be a breakthrough for solving complicated filtering problems.

Conflicts of Interest

The authors declare that they have no conflicts of interest.

Acknowledgments

The authors thank the Ground Application System of Lunar Exploration, NAOC, for providing the lunar penetrating radar data. This work was supported by NAOC through Grant no. Y734061V01 and the National Natural Science Foundation of China (Grant no. 41403054).

References

- [1] Z. Y. Ouyang, *Introduction of Lunar Sciences*, China Aerospace Publishing House, Beijing, China, 2005.
- [2] O. E. Berg, F. F. Richardson, and H. Burton, "Apollo 17 preliminary science report," Tech. Rep. 16, NASA SP-330, 1973.
- [3] Y. G. Shkuratov and N. V. Bondarenko, "Regolith layer thickness mapping of the moon by radar and optical data," *Icarus*, vol. 149, no. 2, pp. 329–338, 2001.
- [4] A.-L. Lan and S.-W. Zhang, "Study on the thickness of lunar regolith with microwave radiometer," *Remote Sensing Technology And Application*, vol. 03, pp. 154–158, 2004.
- [5] W. Fa and Jin Y., "Simulation of Multiple-Channels radiance brightness temperature on lunar surface and inversion of lunar regolith layer thickness," *Progress in Natural Science*, vol. 01, pp. 86–94, 2006.
- [6] Z.-G. Meng, S.-B. Chen, and C. Liu et al., "Simulation on passive microwave radiative transfer in inhomogeneous lunar regolith," *Journal of Jinlin University (Earth Science Edition)*, vol. 06, pp. 1070–1074, 2008.
- [7] S. Chen, F. Zha, and Y. Lian et al., "Forward modelling of the lunar regolith layer using radar detection based on FDTD," *Earth Science Frontiers*, vol. 21, no. 6, pp. 88–91, 2014.
- [8] G.-Y. Fang, B. Zhou, Y.-C. Ji et al., "Lunar penetrating radar onboard the Chang'e-3 mission," *Research in Astronomy and Astrophysics*, vol. 14, no. 12, pp. 1607–1622, 2014.
- [9] L. Ikelle, S. Yung, and F. Daube, "2-D random media with ellipsoidal autocorrelation functions," *Geophysics*, vol. 58, no. 9, pp. 1359–1372, 1993.
- [10] S. C. N. Ergintav, "Modeling of multi-scale media in discrete form," *Journal of Seismic Exploration*, vol. 6, no. 1, pp. 77–96, 1997.
- [11] X. Xi and Y. Yao, "Simulations of random medium model and intermixed random medium," *Earth Science—Journal of China University of Geosciences*, vol. 27, no. 1, pp. 67–71, 2002.
- [12] Z. Jiang, Z. Zeng, J. Li, F. Liu, and W. Li, "Simulation and analysis of GPR signal based on stochastic media model with an ellipsoidal autocorrelation function," *Journal of Applied Geophysics*, vol. 99, pp. 91–97, 2013.
- [13] G. H. Heiken, Vaniman D. T., and B. M. French, *Lunar Source-Book: A Users Guide to the Moon*, New York, NY, USA Cambridge University Press, 1999.
- [14] S. Yu, "Wide-band Ricker wavelet," *OGP*, vol. 31, no. 05, pp. 605–615, 1996.
- [15] A. Z. Elsherbeni, *The Finite-Difference Time-Domain Method for Electromagnetics with MATLAB Simulations*, SciTec Publishing, Inc, Raleigh, NC, USA, 2006, 2-32.
- [16] J.-P. Berenger, "A perfectly matched layer for the absorption of electromagnetic waves," *Journal of Computational Physics*, vol. 114, no. 2, pp. 185–200, 1994.
- [17] Y. Su, G.-Y. Fang, J.-Q. Feng et al., "Data processing and initial results of Chang'e-3 lunar penetrating radar," *Research in Astronomy and Astrophysics*, vol. 14, no. 12, pp. 1623–1632, 2014.

- [18] L. Xiao, P. Zhu, G. Fang et al., "A young multilayered terrane of the northern Mare Imbrium revealed by Chang'E-3 mission," *Science*, vol. 347, no. 6227, pp. 1226–1229, 2015.
- [19] J. Zhang, W. Yang, S. Hu et al., "Volcanic history of the Imbrium basin: a close-up view from the lunar rover Yutu," *Proceedings of the National Academy of Sciences of the United States of America*, vol. 112, no. 17, pp. 5342–5347, 2015.
- [20] A. T. Basilevsky, A. M. Abdrakhimov, J. W. Head, C. M. Pieters, Y. Wu, and L. Xiao, "Geologic characteristics of the Luna 17/Lunokhod 1 and Chang'E-3/Yutu landing sites, Northwest Mare Imbrium of the Moon," *Planetary and Space Science*, vol. 117, pp. 385–400, 2015.
- [21] B. B. Wilcox, M. S. Robinson, P. C. Thomas, and B. R. Hawke, "Constraints on the depth and variability of the lunar regolith," *Meteoritics and Planetary Science*, vol. 40, no. 5, pp. 695–710, 2005.
- [22] J. Feng, Y. Su, and C. Ding et al., "Dielectric properties estimation of the lunar regolith at CE-3 landing site using lunar penetrating radar data," *Icarus*, vol. 284, pp. 424–430, 2017.
- [23] S. Caorsi and M. Stasolla, "GPR data enhancement via multiple reflections' filtering," *International Journal of RF and Microwave Computer-Aided Engineering*, vol. 23, no. 4, pp. 417–422, 2013.

Research Article

A Robust Method to Suppress Jamming for GNSS Array Antenna Based on Reconstruction of Sample Covariance Matrix

Yanyun Gong, Ling Wang, Rugui Yao, and Zhaolin Zhang

School of Electronics and Information, Northwestern Polytechnical University, Xi'an 710072, China

Correspondence should be addressed to Ling Wang; lingwang@nwpu.edu.cn

Received 27 October 2016; Revised 5 January 2017; Accepted 23 January 2017; Published 12 March 2017

Academic Editor: Huapeng Zhao

Copyright © 2017 Yanyun Gong et al. This is an open access article distributed under the Creative Commons Attribution License, which permits unrestricted use, distribution, and reproduction in any medium, provided the original work is properly cited.

The Global Navigation Satellite System (GNSS) receiver is vulnerable to active jamming, which results in imprecise positioning. Therefore, antijamming performance of the receiver is always the key to studies of satellite navigation system. In antijamming application of satellite navigation system, if active jamming is received from array antenna main-lobe, main-lobe distortion happens when the adaptive filtering algorithm forms main-lobe nulling. A robust method to suppress jamming for satellite navigation by reconstructing sample covariance matrix without main-lobe nulling is proposed in this paper. No nulling is formed while suppressing the main-lobe jamming, which avoids main-lobe direction distortion. Meanwhile, along with adaptive pattern control (APC), the adaptive pattern of array antenna approaches the pattern without jamming so as to receive the matching navigation signal. Theoretical analysis and numerical simulation prove that this method suppresses jamming without main-beam distortion. Furthermore, the output SINR will not decrease with the main-lobe distortion by this method, which improves the antijamming performance.

1. Introduction

Satellite navigation system takes advantage of navigating satellites for positioning and navigation [1]. It plays a vital role in transportation management, time service, search and rescue, and geodesy due to its globalized and full-time duration as well as precision [2–6]. Nowadays, GNSS service includes Chinese Beidou Navigation Satellite System (BDS), American Global Positioning System (GPS), and Russian's GLONASS [7].

As the navigation satellites operate on the orbit of 20200 km far away from the Earth surface, the signal emitted by them that is finally received by the GNSS user becomes quite weak [8, 9]. Under this circumstance, navigation signal is vulnerable to active jamming, which leads to the loss of navigation signal. Therefore, the antijamming performance is a prerequisite for the navigation system.

Adaptive spatial filtering technology is one of the main antijamming techniques for GNSS as well as a major branch of adaptive array signal processing [10]. Embedding GPS antijamming technology based on power inversion algorithm

is proposed which does not require a prior information of navigation signal nor array arrangement [11]. GPS antijamming methods based on spatial time adaptive processing (STAP) increase the tapping of signal's time domain so that the antijamming performance is improved [12]. An enhanced short-time Fourier transform (STFT) jamming mitigation system is proposed in [13] which employs several windows to increase time-frequency plane resolution.

However, the above-listed methods do not constrain the receiving of useful navigation satellite signal, while only nulling the jamming signal. Therefore, it is not guaranteed that the pattern's main-lobe points to the direction of satellite signal, which posts negative influence on the receiving navigation signal [14]. A robust antijamming algorithm is proposed under this circumstance. Relevant documents take advantage of minimum variance distortionless response (MVDR) to suppress jamming on GPS. This algorithm constrains the antenna pattern and improves the antijamming performance [15]. Then multiple constrained minimum variance-spatial temporal adaptive processing (MCMV-STAP) was proposed in [16] to enhance the desired

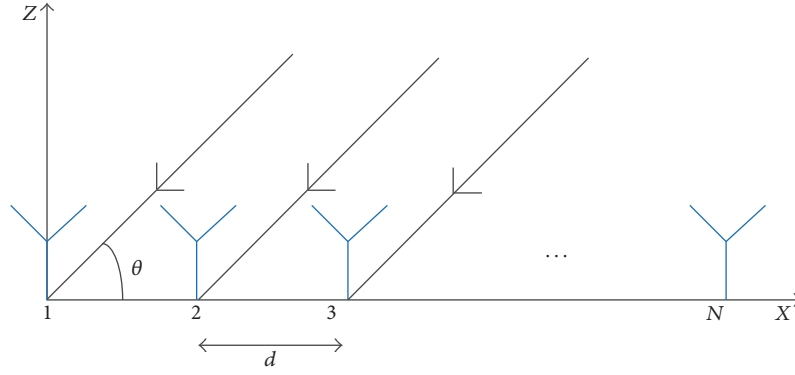


FIGURE 1: The linear antenna array geometry.

satellite signals and suppress jamming, which can broaden the width of nulls and provide approximately flat gains in other directions.

However, this useful algorithm still forms nulling when active jamming exists in the pattern's main-lobe, which leads to increased distortion and decreased SINR. Thus, the receiver cannot use navigation signal for positioning [17].

A robust method to suppress jamming for satellite navigation by reconstructing sample covariance matrix is proposed in this paper. In this method, adaptive beamforming and antijamming are achieved by combining APC with linearly constrained minimum variance (LCMV) beamformer [18–20]. In proposed method, sample covariance matrix is decomposed first; then jamming components of main-lobe are distinguished by the correlation of eigenvector and desired signal steering vector. The main-lobe jamming eigenvectors are calculated by the correlation between main-lobe jamming eigenvectors and desired signal steering vector. The sampling covariance matrix is reconstructed to eliminate the influence of the main-lobe jamming component on the pattern. Eigen-projection matrix can be constructed after eigenvector of main-lobe jamming is acquired so as to eliminate main-lobe jamming components; thus, main-lobe jamming is suppressed. When suppressing all jamming, the pattern only forms nulling in the side-lobe. Then APC is processed to constrain the weight of the LCMV beamformer so that adaptive pattern approaches the pattern without jamming further.

When the main-lobe jamming is suppressed, the proposed method does not form nulling in the main-lobe jamming direction, so that the beam direction will not be offset due to the main-lobe antijamming. This ensures that the beam will point to the navigation satellite still.

Therefore, the output SINR of the satellite navigation signal received by the antenna array in the direction of the navigation satellite is higher than that of other methods relatively. The output SINR is guaranteed, it will be easier to calculate the satellite navigation signal after suppressing the jamming for the GNSS receiver. Under the premise of satisfying the tracking sensitivity of satellite navigation receiver, the proposed algorithm in this paper can suppress more jamming than other algorithms.

Theoretical analysis and numerical simulation prove that the direction of the pattern is not offset by the suppression of main-lobe jamming. The output SINR of satellite navigation signal will not decrease due to the directional offset of the pattern, and the output SINR is only related to the intensity of the input jamming signal, which will be helpful for the navigation receiver to process the navigation signal.

This paper is organized as follows. The array model and signal's mathematic model are provided in Section 2. The details of the proposed method as well as theoretical analysis on reconstruction of covariance matrix and APC are developed in Section 3. Simulations are carried out, which include analysis on the adaptive pattern and the output SINR in Section 4. Section 5 shows the conclusion.

2. Problem Formulation

2.1. Signal Model. Suppose an N -element uniform linear array which is shown in Figure 1, d is the distance between array elements, and all the array elements are homogeneous and isotropic.

There is a far-field desired signal and P narrowband jamming signals incident as plane wave (wavelength λ) [21]. The desired signal and the jamming-signal angles of arrival are θ_0 and θ_j ($j = 1, 2, \dots, P$); then the signal received by the array can be expressed as

$$\mathbf{X}(k) = \mathbf{A}\mathbf{S}(k) + \mathbf{n}(k), \quad (1)$$

where $\mathbf{X}(k)$ refers to the matrix of array received data,

$$\mathbf{X}(k) = [\mathbf{x}_1(k), \mathbf{x}_2(k), \dots, \mathbf{x}_N(k)], \quad (2)$$

and \mathbf{A} refers to array steering vector, which is merely relevant to signal incidence angle and can be expressed as

$$\mathbf{A} = [\mathbf{a}(\theta_0), \mathbf{a}(\theta_1), \dots, \mathbf{a}(\theta_P)]^T. \quad (3)$$

In (3),

$$\mathbf{a}(\theta_k) = [1, e^{j\beta_k}, \dots, e^{j(N-1)\beta_k}]^T, \quad (k = 0, 1, \dots, P) \quad (4)$$

which is the array steering vector corresponding to the signal source; meanwhile, $\beta_k = (2\pi/\lambda)d \sin \theta_k$.

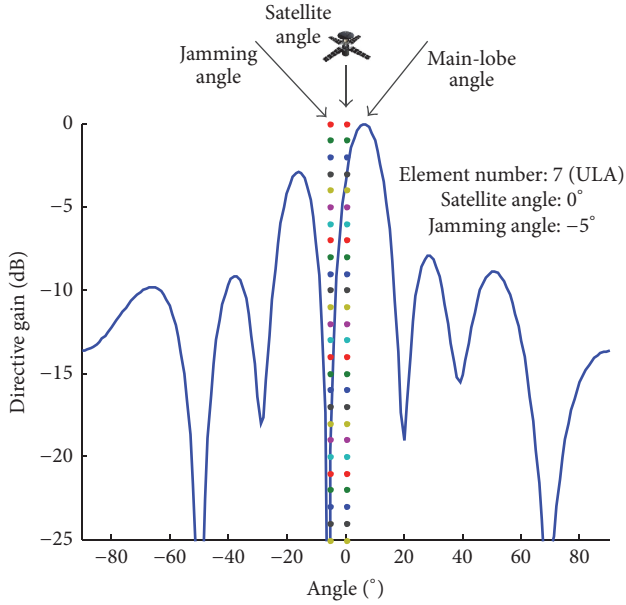


FIGURE 2: Effect of main-lobe jamming on satellite signal reception.

$\mathbf{n}(k)$ in (1) stands for noise matrix and $\mathbf{S}(k)$ for signal matrix; the latter one includes the navigation signal $\mathbf{s}_0(k)$ and the jamming signal $\mathbf{s}_j(k)$. So $\mathbf{X}(k)$ can be expressed as

$$\mathbf{X}(k) = \mathbf{a}(\theta_0) \mathbf{s}_0(k) + \sum_{j=1}^P \mathbf{a}(\theta_j) \mathbf{s}_j(k) + \mathbf{n}(k), \quad (5)$$

and sample covariance matrix can be reached as

$$\mathbf{R}_X = E[\mathbf{X}(t) \mathbf{X}^H(t)], \quad (6)$$

where $E[*]$ and $(*)^H$ denote the expectation operator, respectively, and conjugate transpose.

2.2. The LCMV Beamformer. The gain constraint by the LCMV beamformer in the expected signal direction is 1 (unit constraint), and the array output power is minimized, in which jamming and noise decrease is suppressed [22]. Weight vector of LCMV beamformer can be reached by this equation

$$\begin{aligned} \min_{\mathbf{W}} \quad & \mathbf{W}^H \mathbf{R}_X \mathbf{W}, \\ \text{s.t.} \quad & \mathbf{W}^H \mathbf{C} = \mathbf{F}^H, \end{aligned} \quad (7)$$

in which \mathbf{C} is the constraint matrix and \mathbf{F} is the corresponding response constraint vector. The weight vector of LCMV beamformer can be expressed as

$$\mathbf{W}_{\text{LCMV}} = \mathbf{R}_X^{-1} \mathbf{C} (\mathbf{C}^H \mathbf{R}_X^{-1} \mathbf{C})^{-1} \mathbf{F}, \quad (8)$$

in which \mathbf{W}_{LCMV} is the weight vector of LCMV beamformer [23].

When LCMV beamformer is utilized to suppress main-lobe jamming -5 degrees, its pattern is shown in Figure 2. The main-lobe already distorts from the expected angle of

the satellite signal when suppressing this jamming signal. The output SINR decreases; meanwhile, the nulling position is not precise.

Therefore, in the application of satellite navigation anti-jamming, both the performance of the interference suppression algorithm and the pattern distortion lead to the loss of positioning function of the receiver prematurely. In the process of suppressing the main-lobe jamming, the pattern distortion also seriously affects the reception of satellite navigation signals. The output SINR of satellite navigation signal is affected by the input jamming-signal intensity and the directional pattern offset. When the output signal to noise ratio of the array is decreased, the performance of the anti-jamming degrades. This paper focuses on the avoidance of pattern distortion in GNSS anti-jamming, so that the output signal is only affected by the input jamming intensity.

3. Proposed Method

This section proposes a new anti-jamming method by overcoming the shortcoming of LCMV beamformer in GNSS anti-jamming in Section 2. This method can deal with the distortion of pattern direction when suppressing main-lobe jamming. The adaptive pattern approaches the pattern without jamming so as to effectively receive navigation signal.

Since the navigation signal received by the antenna array is weak in power, this signal can be deemed to be composed of jamming and noise. So sample covariance matrix can be considered to be made up of jamming-and-noise covariance matrix. It meets the requirements of robust beamforming. Therefore, to prevent pattern distortion, coping with main-lobe jamming is the only step to be paid attention to. The detailed process is described as follows.

3.1. Covariance Matrix Reconstruction. The eigen-decomposition of a sample covariance matrix can be expressed as

$$\mathbf{R}_X = \sum_{i=1}^N \lambda_i \boldsymbol{\tau}_i \boldsymbol{\tau}_i^H = \boldsymbol{\Gamma}_s \boldsymbol{\Lambda}_s \boldsymbol{\Gamma}_s^H + \boldsymbol{\Gamma}_n \boldsymbol{\Lambda}_n \boldsymbol{\Gamma}_n^H, \quad (9)$$

where $\lambda_1 \geq \lambda_2 \geq \dots \geq \lambda_p \geq \lambda_{p+1} = \dots = \lambda_N = \sigma_n^2$ refers to descending-order eigenvalue of \mathbf{R}_X . $\boldsymbol{\Gamma}_s = [\boldsymbol{\tau}_1, \dots, \boldsymbol{\tau}_p]$ and $\boldsymbol{\Gamma}_n = [\boldsymbol{\tau}_{p+1}, \dots, \boldsymbol{\tau}_N]$ are signal-and-jamming subspace and noise subspace, respectively, among which $\boldsymbol{\tau}_i$ is the eigenvector corresponding to λ_i . $\boldsymbol{\Lambda}_s = \text{diag}\{\lambda_1, \dots, \lambda_p\}$ and $\boldsymbol{\Lambda}_n = \text{diag}\{\lambda_{p+1}, \dots, \lambda_N\}$ are the diagonal matrices of $\boldsymbol{\Gamma}_s$ and $\boldsymbol{\Gamma}_n$, respectively [24].

Eigenvalue and eigenvector of the main-lobe jamming signal can be achieved by the correlation of decomposed sample covariance matrix and steering vector of signal's incidence angle [25]. The correlation coefficient equation between \mathbf{a}_1 and \mathbf{a}_2 is

$$\text{cor}(\mathbf{a}_1, \mathbf{a}_2) = \frac{|\mathbf{a}_1^H \mathbf{a}_2|}{\|\mathbf{a}_1\| \|\mathbf{a}_2\|}. \quad (10)$$

The correlation coefficient between steering vector of incidence signal $\mathbf{a}(\theta_s)$ and eigenvectors of various-angle jamming $\boldsymbol{\Gamma}_s = [\boldsymbol{\tau}_1, \dots, \boldsymbol{\tau}_p]$ can also be achieved by (10).

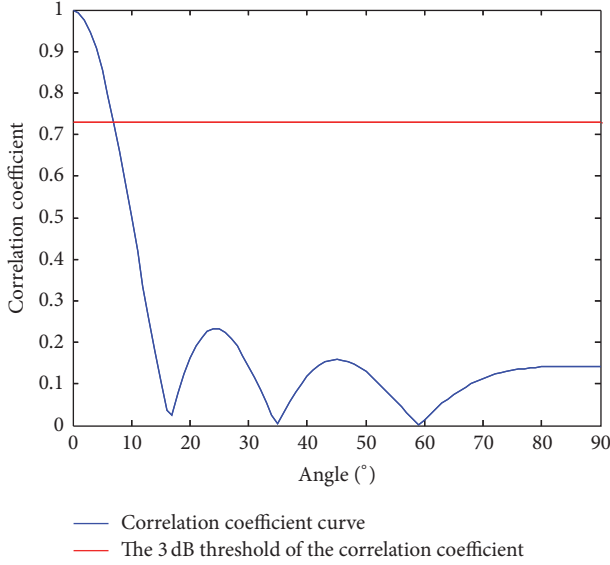


FIGURE 3: Correlation coefficient between various-angle steering vector and 0 degree steering vector.

Figure 3 shows the curve of correlation coefficient between various-angle steering vectors and the steering vector at 0 degrees based on the seven-element ULA structure.

This figure shows that the correlation coefficient curve descends as the angle increases. Taking advantage of this character, this paper assumes an interval of correlation coefficient $(\varepsilon, 1)$, among which ε can be reached by array-element structure.

The constant value in Figure 3 is the corresponding coefficient of main-lobe boundary angle reached by the seven-element uniform linear array. Main-lobe width can be defined as the 3 dB bandwidth. Eigenvector in this range can be deemed as main-lobe eigenvector of jamming eigenvector.

Therefore, it can be assumed that this steering vector is the one corresponding to main-lobe jamming when the steering vector of incident signal and coefficient of jamming eigenvector are within the interval $(\varepsilon, 1)$. This process can be expressed as

$$\varepsilon \leq \text{cor}(\boldsymbol{\tau}_i, \mathbf{a}(\theta_s)) \leq 1, \quad (\boldsymbol{\tau}_i \in \boldsymbol{\Gamma}_s), \quad (11)$$

among which $\boldsymbol{\Gamma}_s = [\boldsymbol{\tau}_1, \dots, \boldsymbol{\tau}_P]$ is the eigenvector of the various-angle jamming, and

$$\text{cor}(\boldsymbol{\tau}_i, \mathbf{a}(\theta_s)) = \frac{\|\boldsymbol{\tau}_i^H \mathbf{a}(\theta_s)\|}{\|\boldsymbol{\tau}_i\| \|\mathbf{a}(\theta_s)\|}. \quad (12)$$

Eigenvector and eigenvalue of main-lobe jamming $\hat{\boldsymbol{\tau}}_i$ and $\hat{\lambda}_i$ can be decided by (11).

Eigenvalue analysis tells that the array response of adaptive beamformer can be expressed as the difference of no jamming response and jamming beam response [26]

$$\mathbf{F}(\theta) = \frac{\mu}{\sigma_n^2} \left\{ \mathbf{a}^H(\theta_s) \mathbf{a}(\theta) - \sum_{i=1}^N \frac{\lambda_i - \sigma_n^2}{\lambda_i} [\boldsymbol{\tau}_i \mathbf{a}(\theta_s)] \boldsymbol{\tau}_i^H \mathbf{a}(\theta) \right\}, \quad (13)$$

in which $\mathbf{F}(\theta)$ is the array response of adaptive beamformer, and

$$\mu = \frac{1}{\mathbf{a}^H(\theta_s) \hat{\mathbf{R}}^{-1} \mathbf{a}(\theta_s)}. \quad (14)$$

Meanwhile, the noise power can be estimated by the mean of $N - P$ smaller eigenvalues, which can be expressed as

$$\sigma_n^2 = \frac{\lambda_{P+1} + \dots + \lambda_N}{N - P}. \quad (15)$$

Generally speaking, jamming power is considerably greater than the noise power. Therefore, as the eigenvalue corresponding to jamming signal, λ_i overwhelms σ_n^2 . So this equation is derived

$$\frac{\lambda_i - \sigma_n^2}{\lambda_i} \approx 1, \quad i \in (1, \dots, P). \quad (16)$$

That is how the adaptive array response forms nulling in the jamming direction for jamming suppression [18]. It does not form the nulling when λ_i corresponds to noise eigenvalue.

$\hat{\lambda}_i$ contains all power of the main-lobe jamming. If the eigenvalue of the main-lobe jamming is reduced to the noise power, the adaptive weight vector will not form a nulling in the main-lobe jamming direction when the adaptive weight vector is calculated.

Therefore, when eigenvalue of main-lobe jamming $\hat{\lambda}_i$ is replaced by the mean of noise eigenvalue, which results in that the eigenvalue of main-lobe jamming decreases to background noise, the replaced expression is

$$\hat{\lambda}_i = \sigma_n^2 = \frac{\lambda_{P+1} + \dots + \lambda_N}{N - P}. \quad (17)$$

In order to deal with noise in the adaptive algorithm, Λ_n is also replaced by the average value of noise. The reconstructed eigenvalue matrix of Λ_n can be expressed as

$$\hat{\Lambda} = \text{diag} \{ \lambda_1, \dots, \hat{\lambda}_i, \dots, \lambda_P, \sigma_n^2, \dots, \sigma_n^2 \}. \quad (18)$$

The steering vector matrix makes no change, so the reconstructed sample covariance matrix $\tilde{\mathbf{R}}_r$ can be expressed as

$$\tilde{\mathbf{R}}_r = \boldsymbol{\Gamma} \hat{\Lambda} \boldsymbol{\Gamma}^H, \quad (19)$$

where $\boldsymbol{\Gamma} = [\boldsymbol{\Gamma}_s, \boldsymbol{\Gamma}_n]$ and $\tilde{\mathbf{R}}_r$ excludes main-lobe jamming components. LCMV beamforming adaptive weight value can be calculated as

$$\tilde{\mathbf{W}}_{\text{LCMV}} = \tilde{\mathbf{R}}_r^{-1} \mathbf{C} (\mathbf{C}^H \tilde{\mathbf{R}}_r^{-1} \mathbf{C})^{-1} \mathbf{F}. \quad (20)$$

Adaptive array antenna pattern produces no jamming nulling in main-lobe while suppressing main-lobe jamming.

3.2. Adaptive Pattern Control. The weight value of LCMV beamformer computed from the reconstructed jamming-and-noise covariance matrix forms no nulling when suppressing main-lobe jamming and no pattern distortion appears. However, mistakes still appear in adaptive aerial pattern because of other elements. Under this circumstance, APC can be utilized to achieve the pattern without jamming so as to make adaptive management more robust.

When experiment data contains merely independent white noise, the array covariance matrix is the unit matrix multiplied by the noise power. Then the weight vector without jamming of LCMV can be expressed as

$$\mathbf{W}_q = \mathbf{C}(\mathbf{C}^H\mathbf{C})^{-1}\mathbf{F}. \quad (21)$$

In order to adjust adaptive pattern to the pattern without jamming, The weight vector \mathbf{W}_q without jamming of the LCMV is constrained to be $\bar{\mathbf{W}}_q$, which meets the constraint $\mathbf{W}^H\mathbf{C} = \mathbf{H}^H$ and approaches the weight vector without jamming \mathbf{W}_q . $\bar{\mathbf{W}}_q$ is considered to be the solution to the following constrained least squares fitting:

$$\begin{aligned} \bar{\mathbf{W}}_q = \arg \min \quad & \left\{ (\bar{\mathbf{W}} - \mathbf{W}_q)^H (\bar{\mathbf{W}} - \mathbf{W}_q) \right\}, \\ \text{s.t.} \quad & \bar{\mathbf{W}}\mathbf{C} = \mathbf{F}^H, \end{aligned} \quad (22)$$

where $\mathbf{W}_q^H \mathbf{a}(\theta_0) = 1$.

After Lagrange multiplier method is utilized to solve the following expression, the revised weight vector without jamming $\bar{\mathbf{W}}_q$ is

$$\bar{\mathbf{W}}_q = [\mathbf{I} - \mathbf{C}(\mathbf{C}^H\mathbf{C})^{-1}\mathbf{C}] \mathbf{W}_q + \mathbf{C}(\mathbf{C}^H\mathbf{C})^{-1}\mathbf{F}. \quad (23)$$

Supposing \mathbf{Z} is the block matrix of constraint matrix \mathbf{C} and $\mathbf{Z}\mathbf{C} = \mathbf{0}$, so

$$\bar{\mathbf{W}}_q = \mathbf{Z}^H(\mathbf{Z}\mathbf{Z}^H)^{-1}\mathbf{Z}\mathbf{W}_q + \mathbf{C}(\mathbf{C}^H\mathbf{C})^{-1}\mathbf{F}; \quad (24)$$

if $\mathbf{W}_Z = \mathbf{Z}^H(\mathbf{Z}\mathbf{Z}^H)^{-1}\mathbf{W}_0$, let $\bar{\mathbf{C}} = [\mathbf{C}, \mathbf{W}_Z]$ and $\bar{\mathbf{F}} = \left[\begin{smallmatrix} \mathbf{F} \\ \|\mathbf{W}_Z\|^2 \end{smallmatrix} \right]$.

So the revised the weight vector without jamming $\bar{\mathbf{W}}_q$ becomes $\bar{\mathbf{W}}_q = \bar{\mathbf{C}}(\bar{\mathbf{C}}^H\bar{\mathbf{C}})^{-1}\bar{\mathbf{F}}$.

Finally, according to formula (8), the LCMV weight vector can be revised as

$$\widehat{\mathbf{W}}_{\text{LCMV}} = \tilde{\mathbf{R}}_r^{-1}\bar{\mathbf{C}}(\bar{\mathbf{C}}^H\tilde{\mathbf{R}}_r^{-1}\bar{\mathbf{C}})^{-1}\bar{\mathbf{F}}. \quad (25)$$

3.3. Array Antenna Output. Eigen-projection matrix can be constructed after the eigenvector of main-lobe jamming is acquired so as to eliminate main-lobe jamming components. Eigenvector of main-lobe jamming $\hat{\boldsymbol{\tau}}_i$ is the prerequisite for this construction.

$$\mathbf{B} = \mathbf{I} - \hat{\boldsymbol{\tau}}_i(\hat{\boldsymbol{\tau}}_i^H\hat{\boldsymbol{\tau}}_i)^{-1}\hat{\boldsymbol{\tau}}_i^H, \quad (26)$$

in which \mathbf{B} is the eigen-projection matrix.

The eigen-projection matrix can be utilized for pretreatment of echo data \mathbf{X} in order to eliminate main-lobe jamming part in the signal.

$$\mathbf{X}_b = \mathbf{B}\mathbf{X}, \quad (27)$$

where \mathbf{X}_b refers to the output of the pretreatment, made up of navigation signal, jamming signal, and noise. Equation (27) can get rid of main-lobe jamming but not side-lobe one. This data requires adaptive weight treatment,

$$\mathbf{Y} = \widehat{\mathbf{W}}_{\text{LCMV}}^H\mathbf{B}\mathbf{X}. \quad (28)$$

After that, remaining side-lobe jamming is suppressed. Until then jamming on array output signal is completely under control, and no main-lobe nulling appears. Therefore, a relatively higher output SINR is acquired.

The flowchart of the proposed method is shown in the green frame in Figure 4.

The jamming suppression processing steps are shown as follows:

- (1) The sample covariance matrix of signals received by the array antenna is decomposed and the correlation is calculated. So the main-lobe jamming eigenvector $\hat{\boldsymbol{\tau}}_i$ is calculated.
- (2) Reconstructed sample covariance matrix $\tilde{\mathbf{R}}_r$ excludes main-lobe jamming components, eliminating the effect of main-lobe jamming on pattern. At the same time, eigen-projection matrix \mathbf{B} can be constructed after the eigenvector of the main-lobe jamming is acquired so as to eliminate the main-lobe jamming components and the main-lobe jamming can be suppressed.
- (3) Use LCMV to calculate antijamming weight value $\widehat{\mathbf{W}}_{\text{LCMV}}$. Since $\tilde{\mathbf{R}}_r$ does not contain the main-lobe jamming component, the pattern corresponding to $\widehat{\mathbf{W}}_{\text{LCMV}}$ does not form nulls at the main-lobe jamming.
- (4) Use APC to make beam pattern approach the pattern without jamming, calculating the final beamformer weight value $\widehat{\mathbf{W}}_{\text{LCMV}}$.
- (5) Calculate beamforming output $\mathbf{Y} = \widehat{\mathbf{W}}_{\text{LCMV}}^H\mathbf{B}\mathbf{X}$. The adaptive pattern not only suppresses the jamming but also does not form a nulling in the main-lobe jamming.

4. Simulation Analysis

In this section, five experiments are listed to illustrate the performance of this robust method for jamming suppression. GPS navigation signals are all on frequency point L1 and the input SNR is -20 dB [27].

This paper is written with these assumptions: jamming comes from point source. Geometrical aperture is far less than the aerial-radiation distance. Signal received by array is plane wave. Transmission medium is equivalently isotropic

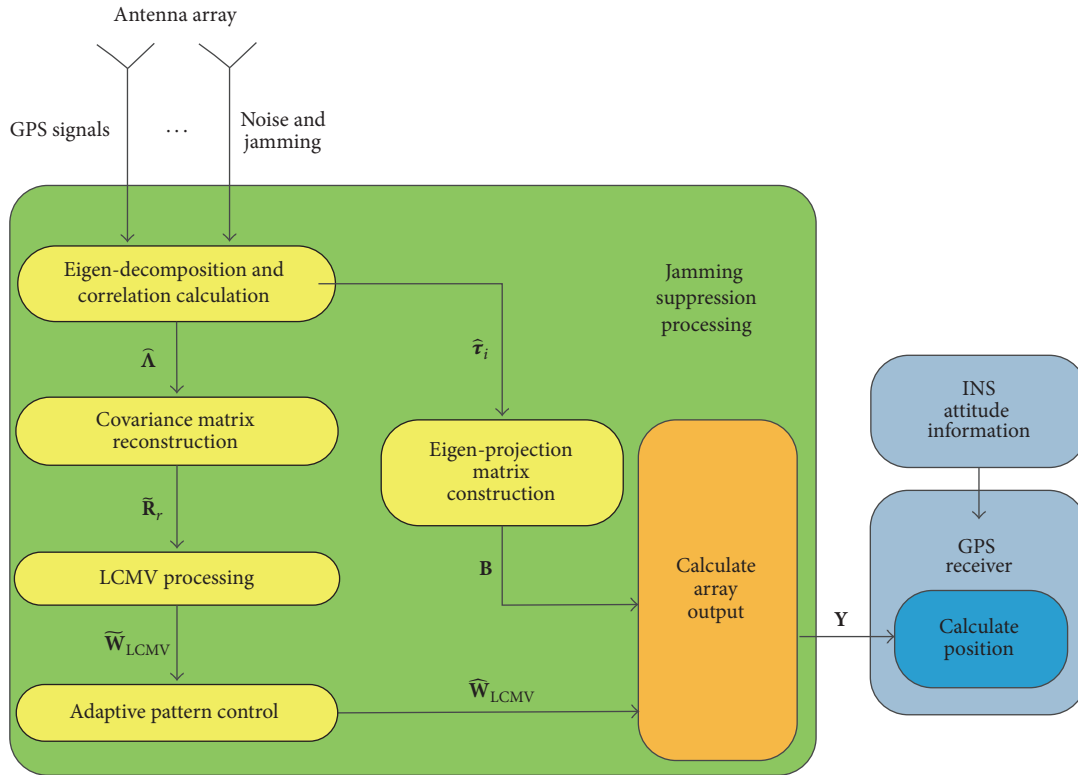


FIGURE 4: The flowchart of the proposed method.

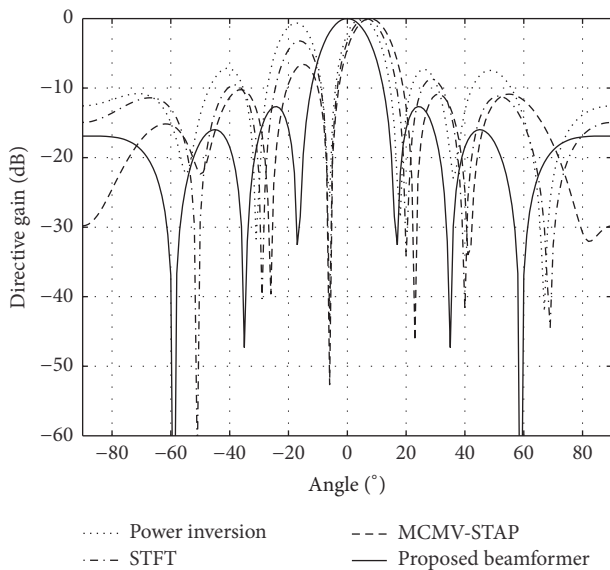


FIGURE 5: The array antenna pattern of antijamming for different method: the angle of arrival of the satellite signal is 0 degrees and the angle of arrival of jamming signal is -6 degrees.

and uniform all around. The zero-mean noise is robust, random, and of no relation with expected signal.

Power inversion algorithm is utilized for performance comparison, in which STFT algorithm (based on space-frequency structure) and MCMV-STAP algorithm (based on

space-time structure) are the two parts [28]. The number of snapshots is 500 throughout the simulation, and all results are the mean of 100 Monte Carlo experiment.

Table 1 shows angles of navigation signal-and-jamming signal. Each scenario of the simulation chooses satellite and jamming signals of different (incidence) angles.

4.1. Influence of Jamming-Signal Incidence Angle on Adaptive Pattern. In this simulation experiment, antenna array uses uniform linear array (ULA) with seven-array elements, with half wavelength width as the distance between array elements.

Figure 5 takes the first scene in Table 1 for simulation: presuming that incidence angle of satellite signal is 0 degrees. Jamming signal has an incidence angle of -6 degrees and an ISR of 50 dB and produces main-lobe jamming to seven-array antenna. So the algorithm in this paper forms no main-lobe nulling, while the other three algorithms form nulling at -6 degrees. As a result, algorithms of minimum power, STFT, and MCMV-STAP lead to deviation of beam direction: 6 degrees for the first but more on side-lobe and 8 degrees for the last but less on side-lobe. Since no jamming nulling exists in this paper's algorithm, main-lobe does not distort, and the pattern approaches the pattern without jamming as a whole.

Figure 6 shows the simulation in the second scene of Table 1: presuming that incidence angle of satellite signal is 0 degrees. Incidence angles of jamming signal are -6 degrees and 12 degrees with an ISR of 50 dB. Although the algorithms of minimum power, STFT, and MCMV-STAP can precisely produce nulling in jamming position, beam direction already

TABLE 1: Satellite and Jamming Scenarios.

Signal	Angle	Scenario 1	Scenario 2	Scenario 3	Scenario 4	Scenario 5	Scenario 6	Scenario 7
Satellite	0 degrees	•	•	•				
Satellite	-20 degrees				•			
Satellite	20 degrees					•		
Satellite	70 degrees						•	
Satellite	10 degrees							•
Satellite	-25 degrees							•
Satellite	40 degrees							•
Jamming	-6 degrees	•	•	•				
Jamming	12 degrees		•	•				
Jamming	40 degrees			•				
Jamming	-14 degrees				•			•
Jamming	12 degrees				•			
Jamming	24 degrees					•		•
Jamming	-22 degrees					•		•
Jamming	72 degrees						•	
Jamming	0 degrees						•	
Jamming	-60 degrees							•

• indicates the selected satellite signal or jamming signal.

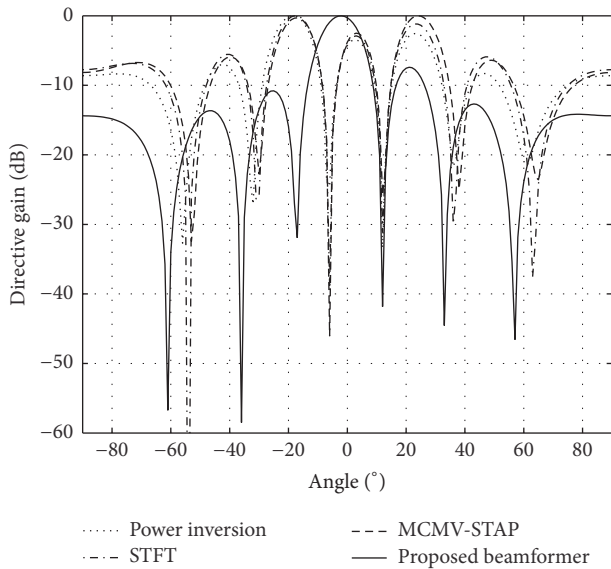


FIGURE 6: The array antenna pattern of antijamming for different method: the angle of arrival of the satellite signal is 0 degrees and the angles of arrival of jamming signals are -6 degrees and 12 degrees.

distorts terribly. The pattern's 0-degree gain is 3 dB less than the pattern without jamming, which results in lower output SINR of satellite signal. The method proposed in this paper produces no jamming nulling at -6 degrees. And 12-degree jamming, producing 2-degree main-lobe deviation because of 12-degree nulling, belongs to side-lobe and produces nulling. However, gain of the pattern without jamming, which has a lower side-lobe, is merely 0.3 dB less than one of 0-degree pattern.

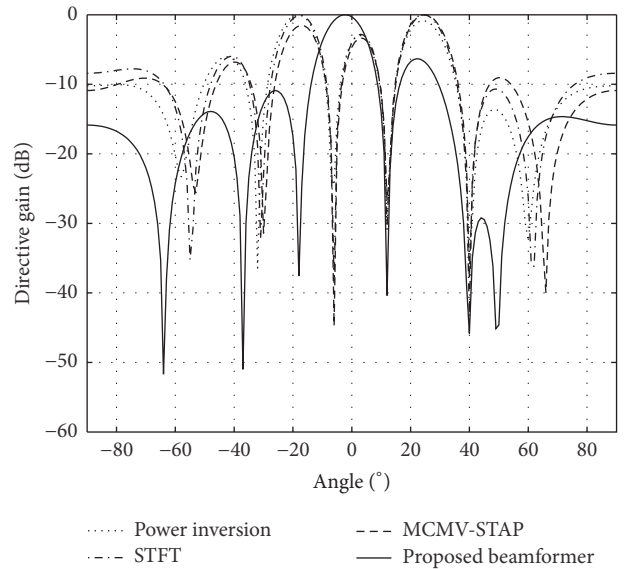


FIGURE 7: The array antenna pattern of antijamming for different method: the angle of arrival of the satellite signal is 0 degrees and the angles of arrival of jamming signals are -6 degrees, 12 degrees, and 40 degrees.

Figure 7 shows the simulation in the third scene of Table 1: presuming that incidence angle of satellite signal is 0 degrees. Incidence angles of jamming signal are -6 degrees, 12 degrees, and 40 degrees with an ISR of 40 dB. The algorithms of minimum power, STFT, and MCMV-STAP can precisely produce nulling in jamming position, but the deviation of beam direction is bigger than the proposed method. And pattern's 0-degree gain is 4.7 dB less than the pattern

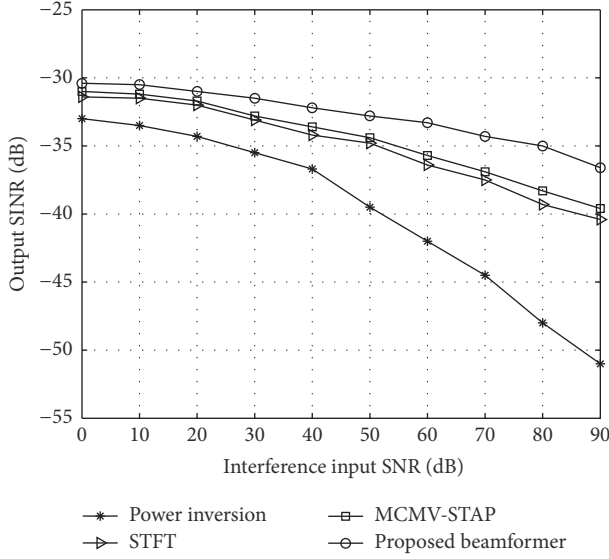


FIGURE 8: The output SINR of different method when suppress jamming; the angle of arrival of the satellite signal is 0 degrees and the angle of arrival of jamming signal is -6 degrees.

without jamming, and pattern's 0-degree gain deteriorates even further. The method proposed in this paper produces jamming nulling at 12 degrees and 40 degrees. However, gain of the pattern without jamming, which has a lower side-lobe, is merely 0.3 dB less than one of 0-degree pattern also.

Figures 5, 6, and 7 verify the validity of the method proposed in this paper. No nulling or deviation of beam direction appears when suppressing main-lobe jamming. This provides a solid guarantee for effectively receiving navigation signal since output SINR of navigation signal does not decrease because of beam-direction deviation.

4.2. Influence of Jamming-Signal Intensity on Output SINR of Satellite Signal. In this simulation experiment, seven-array-element antennas are evenly distributed with a distance of half wavelength width to each other, and ISR of jamming signal increases from 0 dB to 90 dB. Influence of jamming-signal intensity on output SINR of satellite signal is analyzed under this circumstance.

Output SINR of navigation signal can be expressed as

$$\text{SINR} = \frac{\widehat{\mathbf{W}}_{\text{LCMV}}^H \mathbf{R}_s \widehat{\mathbf{W}}_{\text{LCMV}}}{\widehat{\mathbf{W}}_{\text{LCMV}}^H (\mathbf{R}_i + \mathbf{R}_n) \widehat{\mathbf{W}}_{\text{LCMV}}}, \quad (29)$$

among which \mathbf{R}_s refers to sample covariance matrix and $\mathbf{R}_i + \mathbf{R}_n$ refers to jamming-and-noise sample covariance matrix [29].

Figure 8 shows the simulation of the first scene in Table 1. Although the beam of minimum power algorithm in Figure 5 deviates 6 degrees, its output SINR curve is the worst because of its higher side-lobe electrical level. In the 0 dB to 40 dB interval, STFT algorithm and MCMV-STAP algorithm's performance is close. Yet MCMV-STAP one performs better than STFT one between 40 dB and 90 dB. The reason is that

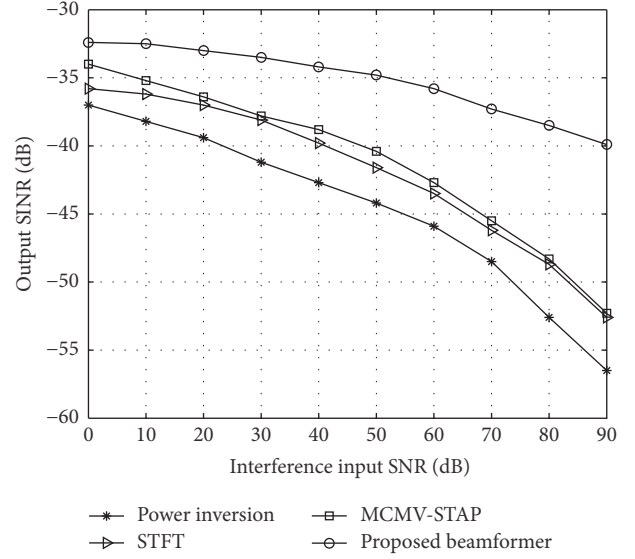


FIGURE 9: The output SINR of different method when suppress jamming; the angle of arrival of the satellite signal is 0 degrees and the angles of arrival of jamming signals are -6 degrees and 12 degrees.

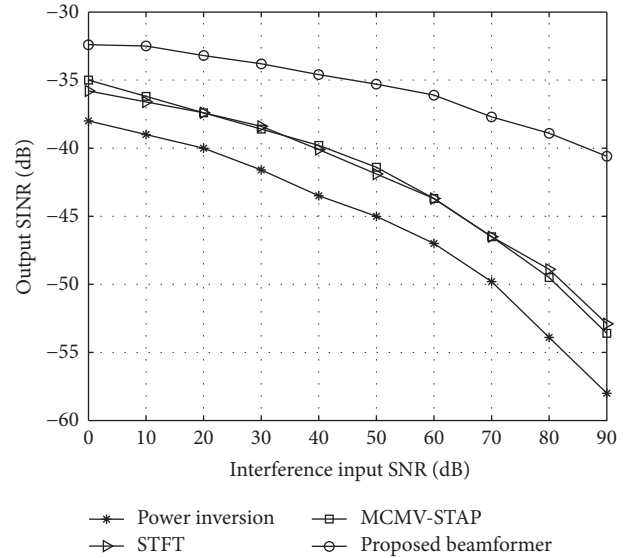


FIGURE 10: The output SINR of different method when suppress jamming; the angle of arrival of the satellite signal is 0 degrees and the angles of arrival of jamming signals are -6 degrees, 12 degrees, and 40 degrees.

MCMV-STAP algorithm utilizes multibeam as well as space-time structure so that it constrains direction of navigation signal. The method proposed in this paper produces the best performance curve, since the pattern does not distort when suppressing main-lobe jamming.

Figure 9 shows the simulation of the second scene in Table 1, and Figure 10 shows the simulation in the third scene in Table 1. Apparently, the output SINR of navigation

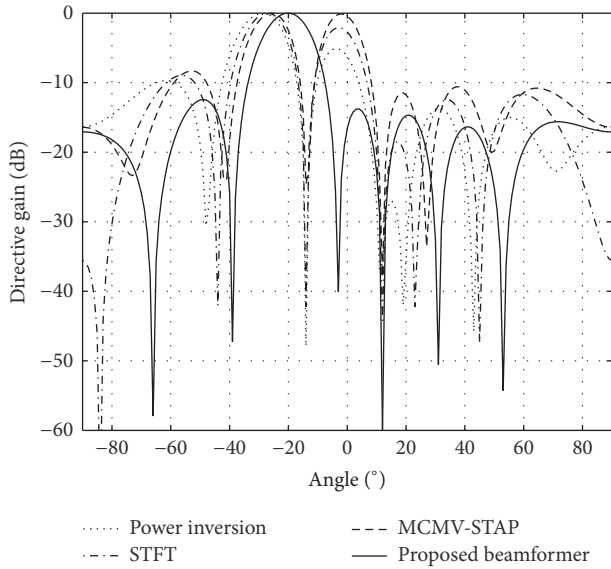


FIGURE 11: The array antenna pattern of antijamming for different method: the angle of arrival of the satellite signal is -20 degrees and the angles of arrival of jamming signals are -14 degrees and 12 degrees.

is the worst when minimum power algorithm imposes no constraint on direction of navigation signal. Having treated information about frequency domain, STFT algorithm performs equally with MCMV-STAP one in terms of output SINR. Under this circumstance, the method proposed in this paper has the best performance curve of output SINR during jamming suppression.

4.3. Influence of Jamming Signal with Various Incidence Angles on Pattern. This section focuses on influence of jamming signal with various incidence angles on the pattern. In this section, a seven-array-element ULA is evenly distributed with a distance of half wavelength width from each other. But ISR of jamming signal is a constant value of 50 dB.

Figure 11 shows the simulation of the fourth scene in Table 1: incidence signal of navigation signal is -20 degrees and ones of jamming signals are -14 degrees and 12 degrees. Algorithms of STFT and MCMV-STAP form two sets of jamming nulling and beam-direction deviation. The method proposed in this paper produces nulling at 12 -degree jamming but not at -14 -degree main-lobe jamming. The main-lobe direction does not distort.

Figure 12 shows the simulation of the fifth scene in Table 1: incidence signal of navigation signal is 20 degrees and ones of jamming signals are 24 degrees and -22 degrees. Algorithms of STFT and MCMV-STAP form two sets of jamming nulling and beam-direction deviation. The method proposed in this paper produces nulling at -22 -degree jamming but not at 24 -degree main-lobe jamming. Main-lobe direction does not distort.

Figure 13 shows the simulation of the sixth scenario in Table 1: incidence signal of navigation signal is 70 degrees and ones of jamming signals are 72 degrees and 0 degrees.

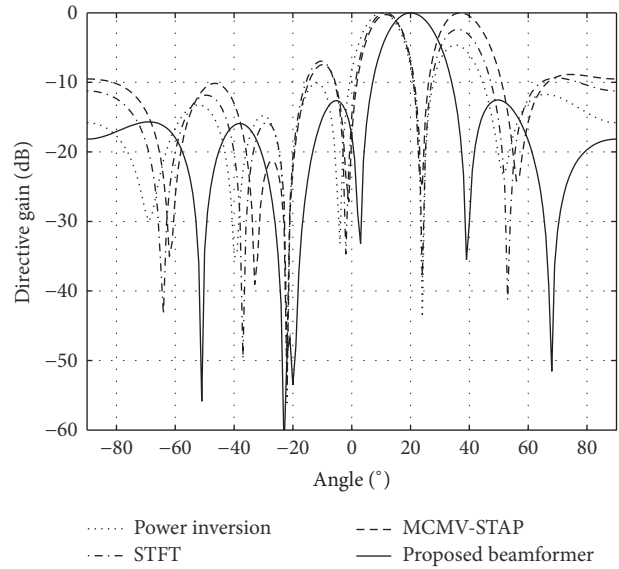


FIGURE 12: The array antenna pattern of antijamming for different method: the angle of arrival of the satellite signal is 20 degrees and the angles of arrival of jamming signals are 24 degrees and -22 degrees.

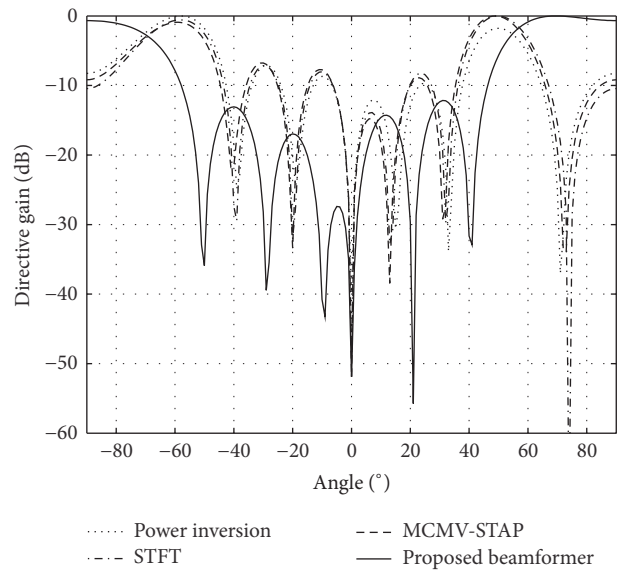


FIGURE 13: The array antenna pattern of antijamming for different method: the angle of arrival of the satellite signal is 70 degrees and the angles of arrival of jamming signals are 72 degrees and 0 degrees.

Algorithms of STFT and MCMV-STAP form two sets of jamming nulling and beam-direction deviation. The method proposed in this paper produces nulling at 0 -degree jamming but not at 72 -degree main-lobe jamming. The main-lobe direction does not distort.

4.4. Influence of Jamming Signal among Multisatellite Navigation Signal on Pattern. This subsection simulates the seventh scenario in Table 1: incidence angles of navigation signals are

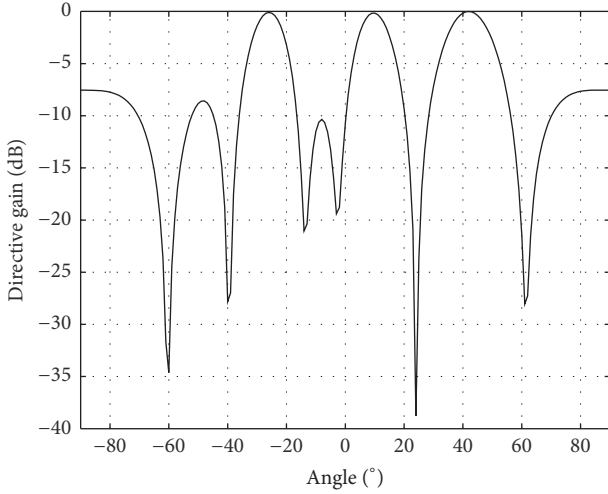


FIGURE 14: The array antenna pattern of the proposed method: the angles of arrival of the satellite signal are 10 degrees, -25 degrees, and 40 degrees and the angles of arrival of jamming signals are -14 degrees, -22 degrees, -60 degrees, and 24 degrees.

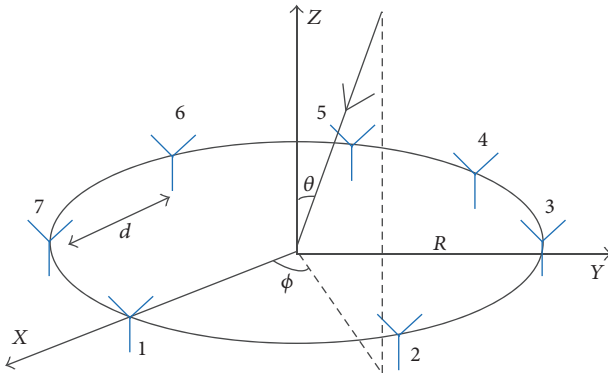


FIGURE 15: The seven-sensor uniform circular array geometry.

-25 degrees, 10 degrees, and 40 degrees. Ones of jamming signals are -60 degrees, -22 degrees, -14 degrees, and 24 degrees, among which the second one is at the main-lobe. LCMV beamformer produces three beams, pointing at incidence angles of three navigation signals relatively.

In Figure 14, seven-array-element aeriels are evenly distributed with a distance of half wavelength width from each other, and ISR of jamming signal is 40 dB, fixed. Jamming nulling only appears in adaptive pattern at -60 degrees, -14 degrees, and 24 degrees, yet none at -22-degree main-lobe jamming. Furthermore, pattern direction does not distort, which is in favor of effectively receiving navigation signal.

4.5. Influence of Jamming Signal on a Seven-Sensor Uniform Circular Array Pattern. The method proposed in this paper is applied in the seven-sensor uniform circular array pattern (Figure 15): seven-array elements are evenly distributed on the circle with half wavelength (the array-element' distance is d) as radius R . Signal incidence angle is (θ, ϕ) ; the former

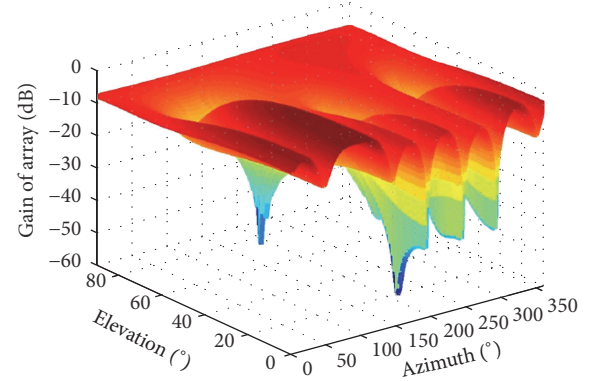


FIGURE 16: Beams and nulls 3D pattern of the proposed method according to the scenario in Table 2 and Jamming Scenario in Section 4.5.

one refers to azimuth and the latter to pitching angle [30]. So corresponding steering vector can be expressed as

$$a(\theta, \phi) = \begin{bmatrix} \exp\left[\frac{j2\pi R \sin \theta \cos(\phi - \gamma_0)}{\lambda}\right] \\ \exp\left[\frac{j2\pi R \sin \theta \cos(\phi - \gamma_1)}{\lambda}\right] \\ \vdots \\ \exp\left[\frac{j2\pi R \sin \theta \cos(\phi - \gamma_{M-1})}{\lambda}\right] \end{bmatrix} \quad (30)$$

among which $\gamma_m = 2\pi m/N$ ($m = 0, 1, \dots, 6$).

In order to verify the validity of this method in real condition, the simulation in this subsection is implemented at 11 o'clock on 14 April, 2016, at 40°N, 108.45°E. Table 2 shows the actual position of GPS satellite.

The following Jamming Scenario shows the parameters of jamming with respect to satellite's coordinate position in Table 2:

Four-CW jamming

Azimuth = 81, 146, 201, 342

Elevation = 17, 67, 15, 48

The results of simulation by this method are shown by Figures 16 and 17; the former one is three-dimensional (3D) antenna pattern and the latter one shows two-dimensional (2D) direction and pitching angle. Meanwhile, Figure 17 illustrates positions of navigation signal and jamming: jamming 1 and jamming 2 are at main-lobe but form no nulling, while jamming 3 and jamming 4 form precise nulling. Navigation signals are at respective beam main-lobe, where no deviation appears. This conforms to the result of theoretical analysis.

5. Conclusion

On the basis of reconstructing sample covariance matrix, this paper proposes a method to suppress jamming on satellite navigation. No main-lobe nulling is formed by the proposed

TABLE 2: Azimuth and elevation angles of visible satellites.

PRN	Az (degree)	El (degree)	Sky plot
1	24	5	
4	98	10	
10	170	19	
12	221	6	
14	320	10	
18	112	39	
22	99	35	
25	270	62	
32	312	81	
33	58	52	

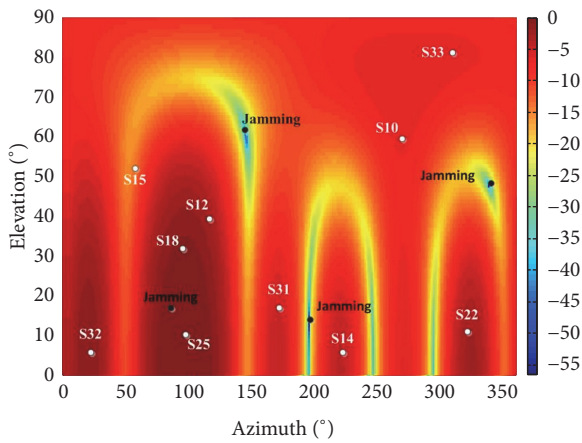


FIGURE 17: Beams and nulls 2D pattern of the proposed method according to the scenario in Table 2 and Jamming Scenario in Section 4.5.

method. Combined with APC, the adaptive pattern of array antenna approaches the pattern without jamming so as to receive the matching navigation signal.

This proposed method suppresses the jamming by constructing eigenvector matrix, because of the sampling covariance matrix reconstruction. The main-lobe jamming does not null. This pattern always accurately points to the direction of navigation satellite. The pattern accurately formed deep nulling at the side-lobe jamming. Compared with other methods, it has the highest output SINR. This is helpful for the navigation receiver to solve the navigation signal and can effectively improve the navigation system antijamming capacity.

Numerical simulation and case study results in this paper show that the pattern always precisely points to the direction of navigation satellite during jamming suppression. Deep nulling is achieved only on the position of side-lobe jamming. The proposed method has the highest output SINR compared with other methods. This is beneficial to the navigation signal receiving as well as improving the antijamming performance of the GNSS receiver.

Competing Interests

We declare that there is no conflict of interests regarding the publication of this paper.

Acknowledgments

This work has been supported by the National Natural Science Foundation of China (nos. 61271416, 61301093, and 61501376) and Fundamental Research Funds for the Central Universities (no. 3102016ZY020).

References

- [1] T. Marathe, S. Daneshmand, and G. Lachapelle, "Assessment of measurement distortions in GNSS antenna array space-time processing," *International Journal of Antennas and Propagation*, vol. 2016, Article ID 2154763, 17 pages, 2016.
- [2] G. Galati, R. Dellago, and F. Lanari, "Global navigation satellite system in an integrated air traffic management constellation," *IEE Proceedings—Radar, Sonar and Navigation*, vol. 144, no. 3, pp. 156–162, 1997.
- [3] J. H. Blakey, "Navigating towards the future: transitioning from terrestrial radio navigation to satellite navigation and airborne surveillance," *IEEE Aerospace and Electronic Systems Magazine*, vol. 21, no. 5, pp. 17–21, 2006.
- [4] A. Emmanuele, F. Zanier, G. Boccolini, and M. Luise, "Spread-spectrum continuous-phase-modulated signals for satellite navigation," *IEEE Transactions on Aerospace and Electronic Systems*, vol. 48, no. 4, pp. 3234–3249, 2012.
- [5] A. R. Lopez, "GPS landing system reference antenna," *IEEE Antennas and Propagation Magazine*, vol. 52, no. 1, pp. 104–113, 2010.
- [6] C. J. Wullems, "A spoofing detection method for civilian L1 GPS and the E1-B galileo safety of life service," *IEEE Transactions on Aerospace and Electronic Systems*, vol. 48, no. 4, pp. 2849–2864, 2012.
- [7] W. Wang, Q. Du, R. Wu, and J. Liang, "Interference suppression with flat gain constraint for satellite navigation systems," *IET Radar, Sonar and Navigation*, vol. 9, no. 7, pp. 852–856, 2015.
- [8] R. L. Fante and J. J. Vaccaro, "Wideband cancellation of interference in a GPS receive array," *IEEE Transactions on Aerospace and Electronic Systems*, vol. 36, no. 2, pp. 549–564, 2000.

- [9] W. L. Myrick, M. D. Zoltowski, and J. S. Goldstein, "Low-sample performance of reduced-rank power minimization based jammer suppression for GPS," in *Proceedings of the IEEE 6th International Symposium on Spread Spectrum Techniques and Applications (ISSSTA '00)*, pp. 93–97, September 2000.
- [10] W. Sun and M. G. Amin, "A self-coherence anti-jamming GPS receiver," *IEEE Transactions on Signal Processing*, vol. 53, no. 10, pp. 3910–3915, 2005.
- [11] W. L. Myrick, G. J. Scott, and M. D. Zoltowski, "Low complexity anti-jam space-time processing for GPS," in *Proceedings of the IEEE International Conference on Acoustics, Speech, and Signal Processing*, pp. 2233–2236, Salt Lake City, Utah, USA, May 2001.
- [12] M.-J. Yu, "INS/GPS integration system using adaptive filter for estimating measurement noise variance," *IEEE Transactions on Aerospace and Electronic Systems*, vol. 48, no. 2, pp. 1786–1792, 2012.
- [13] M. J. Rezaei, M. Abedi, and M. R. Mosavi, "New GPS anti-jamming system based on multiple short-time Fourier transform," *IET Radar, Sonar and Navigation*, vol. 10, no. 4, pp. 807–815, 2016.
- [14] B. Motella, S. Savasta, D. Margaria, and F. Dovis, "Method for assessing the interference impact on GNSS receivers," *IEEE Transactions on Aerospace and Electronic Systems*, vol. 47, no. 2, pp. 1416–1432, 2011.
- [15] A. Khabbazibasmenj, S. A. Vorobyov, and A. Hassanien, "Robust adaptive beamforming based on steering vector estimation with as little as possible prior information," *IEEE Transactions on Signal Processing*, vol. 60, no. 6, pp. 2974–2987, 2012.
- [16] J. Zhuang and A. Manikas, "Interference cancellation beamforming robust to pointing errors," *IET Signal Processing*, vol. 7, no. 2, pp. 120–127, 2013.
- [17] O. G. Vendik and D. S. Kozlov, "Phased antenna array with a side-lobe cancellation for suppression of jamming," *IEEE Antennas and Wireless Propagation Letters*, vol. 11, pp. 648–650, 2012.
- [18] X. Yang, P. Yin, T. Zeng, and T. K. Sarkar, "Applying auxiliary array to suppress mainlobe interference for ground-based radar," *IEEE Antennas and Wireless Propagation Letters*, vol. 12, pp. 433–436, 2013.
- [19] Q. Li, W. Wang, D. Xu, and X. Wang, "A robust anti-jamming navigation receiver with antenna array and GPS/SINS," *IEEE Communications Letters*, vol. 18, no. 3, pp. 467–470, 2014.
- [20] C. Rosetti and C. Carnebianca, "NAVSAT: a global satellite based navigation system," *IEEE Aerospace and Electronic Systems Magazine*, vol. 2, no. 12, pp. 15–22, 1987.
- [21] Y. Li, S. Gu, and N. Zheng, "MIMO radar transmit beam pattern design for DOA estimation with sidelobe suppression," *International Journal of Antennas and Propagation*, vol. 2016, Article ID 1512843, 10 pages, 2016.
- [22] S. Daneshmand, A. J. Jahromi, A. Broumandan, and G. Lachapelle, "GNSS space-time interference mitigation and attitude determination in the presence of interference signals," *Sensors*, vol. 15, no. 6, pp. 12180–12204, 2015.
- [23] S. Daneshmand, N. Sokhandan, M. Zaeri-Amirani, and G. Lachapelle, "Precise calibration of a GNSS antenna array for adaptive beamforming applications," *Sensors*, vol. 14, no. 6, pp. 9669–9691, 2014.
- [24] B. Bonet, I. Alcantarilla, D. Flament, C. Rodríguez, and N. Zarraoa, "The benefits of multi-constellation GNSS: reaching up even to single constellation GNSS users," in *Proceedings of the 22nd International Technical Meeting of The Satellite Division of the Institute of Navigation (ION GNSS '09)*, pp. 1268–1280, Savannah, Ga, USA, September 2009.
- [25] H. Dai, X. Wang, Y. Li, Y. Liu, and S. Xiao, "Main-lobe jamming suppression method of using spatial polarization characteristics of antennas," *IEEE Transactions on Aerospace and Electronic Systems*, vol. 48, no. 3, pp. 2167–2179, 2012.
- [26] M. R. Mosavi and F. Shafiee, "Narrowband interference suppression for GPS navigation using neural networks," *GPS Solutions*, vol. 20, no. 3, pp. 341–351, 2016.
- [27] R. L. Fante and J. J. Vacarro, "Cancellation of jammers and jammer multipath in a GPS receiver," *IEEE Aerospace and Electronic Systems Magazine*, vol. 13, no. 11, pp. 25–28, 1998.
- [28] M. Meurer, A. Konovaltsev, M. Cuntz, and C. Hättich, "Robust joint multi-antenna spoofing detection and attitude estimation using direction assisted multiple hypotheses RAIM," in *Proceedings of the 25th International Technical Meeting of the Satellite Division of the Institute of Navigation (ION GNSS '12)*, pp. 3007–3016, ION, Nashville, Tenn, USA, September 2012.
- [29] A. J. O'Brien and I. J. Gupta, "Comparison of output SINR and receiver C/N₀ for GNSS adaptive antennas," *IEEE Transactions on Aerospace and Electronic Systems*, vol. 45, no. 4, pp. 1630–1640, 2009.
- [30] K. Yang, Z. Zhao, and Q. H. Liu, "Fast pencil beam pattern synthesis of large unequally spaced antenna arrays," *IEEE Transaction on Antennas and Propagation*, vol. 61, no. 2, pp. 627–634, 2013.

Research Article

High Precise Scattering Centers Models for Cone-Shaped Targets Based on Induced Currents

Qi-Feng Li,¹ Kun-Yi Guo,¹ Xin-Qing Sheng,¹ and Tian-Shu Liu²

¹Center for Electromagnetic Simulation, School of Information and Electronics, Beijing Institute of Technology, Beijing, China

²Science and Technology on Special System Simulation Laboratory, Beijing Simulation Center, Beijing 100854, China

Correspondence should be addressed to Kun-Yi Guo; guokunyi@bit.edu.cn

Received 6 November 2016; Accepted 28 December 2016; Published 7 March 2017

Academic Editor: Yumao Wu

Copyright © 2017 Qi-Feng Li et al. This is an open access article distributed under the Creative Commons Attribution License, which permits unrestricted use, distribution, and reproduction in any medium, provided the original work is properly cited.

Based on induced currents of cone-shaped targets, the high precise scattering center model is derived in this paper. The distribution characteristics of the induced currents and their relationships with the attributes of scattering centers are investigated in detail; the high precise scattering center model is obtained. In order to validate the scattering center model, numerical simulations of two cone-shaped targets are presented, and the accuracies of the models are validated through comparing the range profiles simulated by the models with those by a full-wave numerical method. The validation results demonstrate that this model is superior to the existing model in precisely characterizing the scattering centers induced by creeping waves.

1. Introduction

Scattered fields of radar targets at sufficiently high frequencies can be approximated as the sum of scattered fields from individual scattering sources, and these scattering sources are generally called scattering centers [1]. The term of scattering center has been expanded for now. Scattering phenomena under cases of lower frequency, creeping waves, for example, can also be described in terms of scattering centers and these scattering centers are also significant scattering components in some conditions [2, 3]. The characteristics of radar returns from a target are primarily determined by the attributes of its scattering centers, such as locations and scattering amplitudes, and their dependencies on aspect angle, frequency, and polarization [4]. Therefore, parametric scattering center models that concisely and precisely characterize radar returns have gained considerable attention in many radar applications, such as automatic target recognition (ATR) [5, 6] and radar image interpretation [7, 8].

Parametric scattering center model is the combination of a series of analytical functions that describe the changes of location and scattering amplitude of scattering centers with frequency and aspect angle of line of sight (LOS) of radar. The existing scattering center models for monostatic

radar configuration include the damped exponential model [9, 10], the geometrical theory of diffraction (GTD) based model [11, 12], the attributed scattering center model [13–15], and the sliding scattering center model [16]. These scattering center models are all developed for scattering problems of high frequency, such as specular reflection by large-scale smooth surface or diffraction by large-scale straight edge. The precision of these models is greatly challenged for describing the scattering problem of lower frequency, such as diffraction by small-scale edges and rescattered waves of creeping waves and travelling waves on smooth surface. And even worse, there are no generalized analytical solutions for these kinds of scattering problems.

To tackle this problem, the models of the induced currents on the target are built at first; then the scattering center model is derived by the electric field integral expression based on the current model. The modelling of the induced currents on the target is easier than the scattering center modelling, for the precise numerical results of currents can be acquired by full-wave numerical computation. The well validated full-wave numerical method, namely, the hybrid finite element-boundary integral-multilevel fast multipole algorithm (FE-BI-MLFMA) [17–20] is used in this paper. It is found that for cone-shaped target, its scattering characteristics are mainly

determined by one-dimensional (1D) currents on the lines in the plane constructed by the LOS and the rotational axis of the cone. Therefore, the modelling of the induced currents on the target is greatly simplified.

Based on the built model of the 1D currents, the relationship between the characteristics of currents and the attributes of scattering centers is investigated; the formation processes of scattering centers by its contributing currents are analyzed. It is found that one parameter of current models is sometimes related to several scattering centers, and vice versa. In other words, the coupling of multiple scattering sources has been included in the current model. Moreover, the scattering phenomena of creeping waves are also included in the current model, and the corresponding scattering center can be easily acquired based on the current model. In order to validate the presented method, numerical simulations of two cone-shaped targets are investigated in detail, and the accuracies of the built models are validated through comparing the range profiles (RPs) simulated by the models with the real RPs of the two targets computed by FE-BI-MLFMA, as well as the RPs simulated by the attributed scattering center model obtained by traditional method.

The remainder of the paper is organized as follows: Section 2 presents the modelling of the induced currents on a blunt-nosed cone target. Section 3 presents the derived scattering center model based on the current model. Section 4 presents the validation of the built scattering center models. Finally, Section 5 provides the conclusions of this paper.

2. Parametric Expressions of Scattering Centers

The induced currents on a cone-shaped target are investigated in this section. The cone-shaped target is a perfect electric conductor (PEC). The geometry of the cone and the relative position of the target and radar are shown in Figure 1. The body-fixed Cartesian coordinate system (x, y, z) is used to describe the geometry, its origin is at the bottom center of the target, and the rotationally symmetric axis of the cone is located along the z -axis, as shown in Figure 1. The geometrical parameters of the target are set as $R = 0.732$ m, $r = 0.061$ m, $h = 3.721$ m, and $\alpha = 10.4^\circ$. The radar parameters are set as follows: the frequency range is $f = 1\sim 2$ GHz, with sampling interval of $\Delta f = 12.5$ MHz.

Suppose that the distance between the radar and the target satisfies the far-field condition ($R_0 > 2L^2/\lambda$, where R_0 is the distance between the radar and the target and L is the size of the target). In far-field condition, the incident wave can be taken as plane wave; then the induced currents on the target illuminated by the plane waves from the monostatic radar are computed by FE-BI-MLFMA. The characteristics of currents on the flank and the bottom are investigated separately in the following.

2.1. Characteristics of Induced Currents on the Flank. As the cone is a rotationally symmetrical object, the change of the LOS in azimuth angle (denoted by ϕ) does not affect the characteristics of induced currents. Therefore, without loss

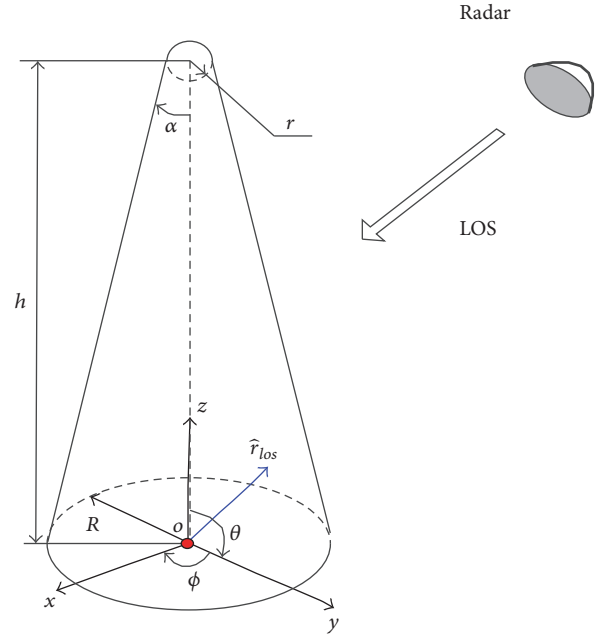


FIGURE 1: The geometry of the cone-shaped target and the radar.

of generality, we set the change of LOS to be in the xoz plane, and the elevation angle of the LOS is denoted by θ . Then, the wave vector of incident wave can be expressed as $\vec{k}_i = (2\pi/\lambda)(-\cos\theta\hat{z} - \sin\theta\hat{x})$.

When the incident electric field is under vertical polarization, the magnetic field can be expressed as $\vec{H}_i = -H_m\hat{\phi} = -H_m\hat{y}$. The induced currents on the cone are presented in Figure 2, where the used parameters of the incident waves are $f = 1$ GHz, $\theta = 8^\circ$. Figure 2(a) shows the amplitude of the induced currents and Figure 2(b)L1 is the intersection line of the flank of the cone with the plane constructed by the axis of cone and the direction of the incident electric field, and L2 is the intersection line of the flank with the plane constructed by the axis of cone and the direction of the incident magnetic field. In our geometry setting, the generatrix in xoz plane of lit region is L1 and the generatrix in $yo z$ is L2.

As shown in Figure 2(a), the maximal values of currents are on L1 and the minimal values of currents are on L2. The conclusion agrees with the analytical results based on physical optics method (PO) [21–24]. The normals of the flank on L1 and L2 are $\hat{n}_{L1} = \cos\alpha\hat{x} + \sin\alpha\hat{z}$ and $\hat{n}_{L2} = \cos\alpha\hat{y} + \sin\alpha\hat{z}$. Based on PO, induced current can be approximately expressed as $\mathbf{J} = 2\hat{n} \times \mathbf{H}_i$, so the currents on L1 and L2 can be derived as $\mathbf{J}_{L1} = 2H_m(-\cos\alpha\hat{z} + \sin\alpha\hat{x})$ and $\mathbf{J}_{L2} = 2H_m(\sin\alpha\hat{x})$. The incident electric field is generally set as 1 V/m in computation; then the incident magnetic field is $H_m = 1/Z$, where Z is the wave impedance of free space.

Optical currents on L1 computed by PO method are compared with the values computed by FE-BI-MLFMA (called full-wave currents for short), as presented in Figure 3 ($\theta = 8^\circ$). Figure 3(a) shows the amplitude (A/m²) of the currents, and Figure 3(b) shows the unwrapped phase (rad)

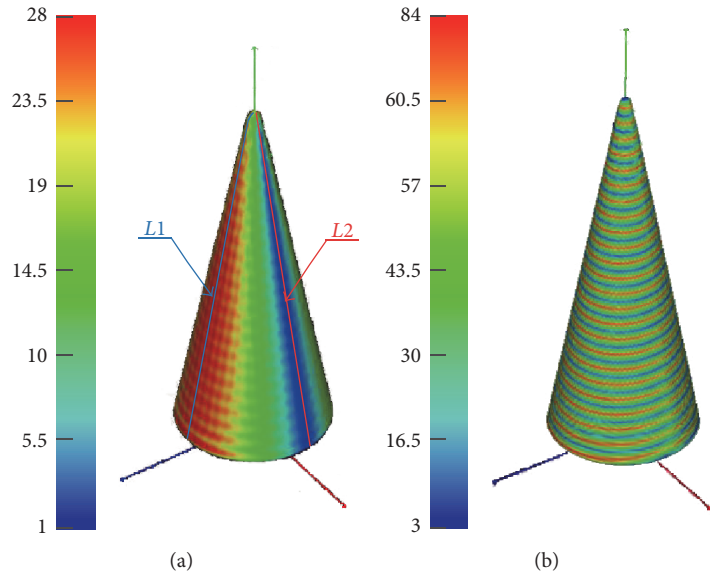


FIGURE 2: Induced currents on the flank of the cone. (a) Amplitude; (b) phase.

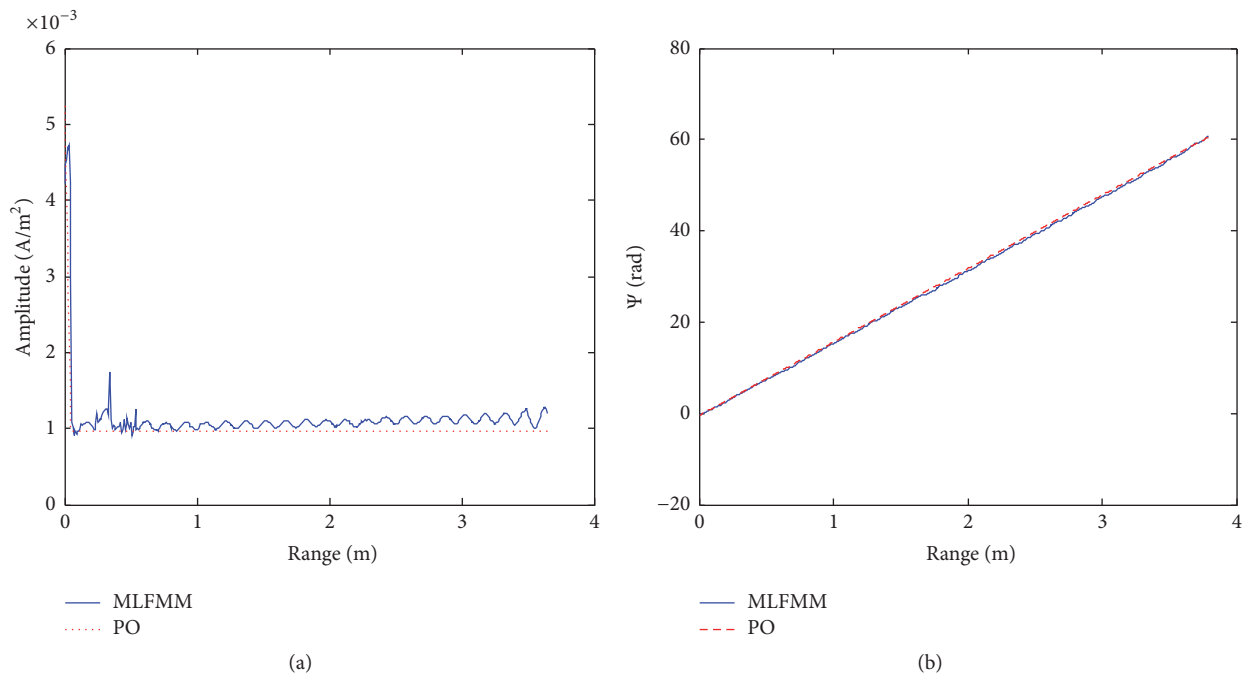


FIGURE 3: Amplitude and phase of the currents on $L1$. (a) Amplitude; (b) unwrapped phase.

of the currents. The range of horizontal axis indicates the distance between a point on $L1$ and the top of the cone

Figure 3(a) shows that there are significant differences between the optical currents and the full-wave currents. The full-wave currents along $L1$ are more complex than that of the optical currents. Near the two ends of $L1$, the amplitude of the full-wave currents is obviously larger than that of the optical currents. Within the internal region of $L1$, the amplitude fluctuates as a combination form of periodicity and linearity.

Figure 3(b) shows that the two results agree well with each other, and the phase of induced current linearly changes along $L1$.

The generatrix in xoz plane in shadow region is denoted by $L1'$. The induced currents on $L1'$ are shown in Figure 4. The fluctuation feature and the values of the induced currents on $L1'$ are similar to the case of $L1$, which means the scattering components of creeping waves are the denominated scattering contributions when the elevation angle of the LOS is

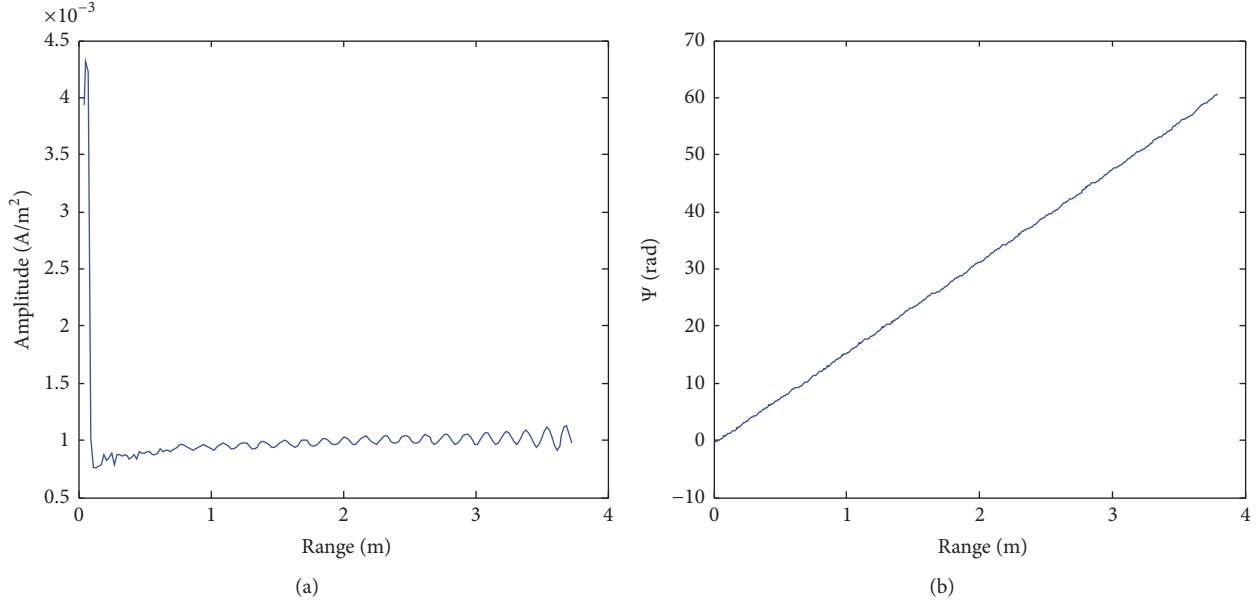


FIGURE 4: Amplitude and phase of the induced currents on $L1'$ in shadow region. (a) Amplitude; (b) unwrapped phase.

small ($\theta = 8^\circ < \alpha$). The range of horizontal axis indicates the distance between a point on $L1'$ and the top of the cone.

Based on the characteristics of the induced currents on $L1$ and $L1'$ under different LOSs, the full-wave currents are described by the following expressions:

$$J(\rho, f, \theta) = A_m(\rho, f, \theta) \exp(j\phi_m(\rho, f, \theta)) \quad (1)$$

$$A_m(\rho, f, \theta) = a_{m1} \cdot \sin[a_{m2}(\theta)f\rho + a_{m3}(\theta)\rho + a_{m4}(\theta)f + a_{m5}(\theta)] + a_{m6}\rho + a_{m7} \quad (2)$$

$$\phi_m(\rho, f, \theta) = a_{m8}(\theta)f\rho + a_{m9}(\theta)\rho, \quad (3)$$

where (1) describes the complex value of induced current; its amplitude and phase are indicated by A_m and ϕ_m . Equation (2) is proposed according to the amplitude characteristics of the induced currents on $L1$ and $L1'$ under different LOSs. Equation (3) is proposed according to the phase characteristics of the induced currents on $L1$ and $L1'$. ρ indicates the position of the current element on $L1$ ($m = 1$) or $L1'$ ($m = 2$). $A_m(\cdot)$ and $\phi_m(\cdot)$ are the amplitude and the phase of the currents, respectively. a_{mn} ($n = 1, 2, \dots, 9$) indicates the parameters to be estimated. a_{m1} is irrelevant to frequency, but a_{m2} , a_{m3} , a_{m4} , a_{m5} , a_{m8} , and a_{m9} are linear-circular correlated with θ .

To show characteristics of the currents on the whole conical surface, we slice the cone along line $L1$ and unfold the flank to a fan surface, as shown in Figure 5. The currents on the fan and the bottom are shown in Figure 6. The half-angle of the fan is $\gamma = \pi R/l$, where l is the outer radius of the fan.

Based on PO method, the two-dimensional currents can be expressed as $\mathbf{J}(\rho, \beta) = 2\hat{n}(\beta) \times \mathbf{H}^i = 2H_m(\sin \alpha \hat{x} -$

$\cos \alpha \cos((\beta/\gamma)\pi)\hat{z})$, where (ρ, β) is the coordinates of the individual current on the fan. The component of $\mathbf{J}(\rho, \beta)$ along vertical direction ($\hat{v} = -\cos \alpha \hat{z} + \sin \alpha \hat{x}$) can be expressed as (4). Therefore, the change of currents with β can be described by the currents on $L1$ and the dependant function $F(\beta)$.

$$J_v(\rho, \beta) = J_v(\rho, 0) F(\beta) \quad (4)$$

$$F(\beta) = \left(\cos^2 \alpha \cos\left(\frac{\beta}{\gamma}\pi\right) + \sin^2 \alpha \right). \quad (5)$$

Equations (4) and (5) describe the fact that the change of induced currents with β can be expressed by the currents on $L1$ and the dependent function $F(\cdot)$.

2.2. Characteristics of Induced Currents on the Bottom. Similarly, the induced currents on the bottom are investigated here. The amplitudes and phases of induced currents on the bottom are presented in Figures 7(a) and 7(b), respectively. The parameters of the incident waves are the same as those of Figure 2. The line in xoz plane along $+x$ axis is denoted by $I1$, the line in xoz plane along $-x$ axis is denoted by $I1'$, and the line in yoz plane along $+y$ axis is denoted by $I2$. The maximal values of currents are on $I1$ and the minimal values of currents are on $I2$. The scattering field from the bottom is mainly contributed by the currents on $I1$ and $I1'$.

The currents on $I1$ are presented in Figure 8. The range of horizontal axis indicates the distance between a point on $I1$ and the point on the curved edge. From Figure 8(a), it can be seen that the amplitude of full-wave currents fluctuates as a combination form of periodicity and linearity. From Figure 8(b), it can be seen that the phase of induced current changes linearly along $I1$. The characteristics of the currents on $I1'$ are similar to $I1$.

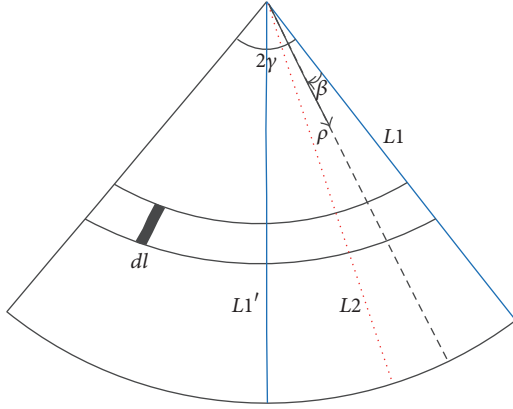


FIGURE 5: Unfolded fan.

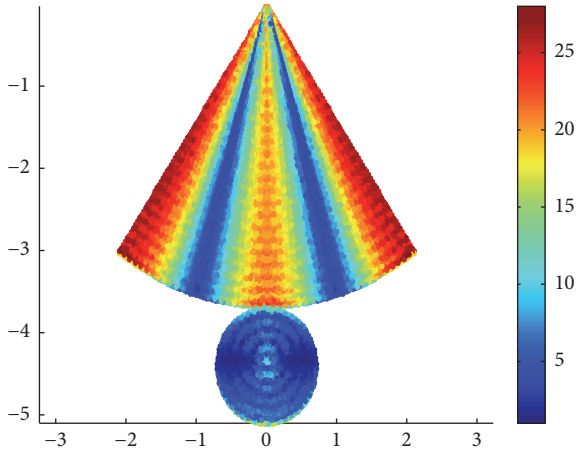


FIGURE 6: Currents on the fan and the bottom.

These characteristics of the currents on the bottom are similar to the case of currents on the flank. Therefore, the currents on the bottom are also described by the expression of (1), only with different parameters. The currents on $I1$ and $I1'$ are indicated by the case of $m = 3$. Similarly, the two-dimensional currents on the bottom are also expressed by (4).

2.3. Estimation of the Current Model Parameters. The coefficients in the presented formula, $a_{m1} \sim a_{m9}$, are estimated through matching the currents computed by the model with the currents computed by FE-BI-MLFMA. The used method for optimal estimation is genetic algorithm (GA) [25–28]. The currents on the flank computed by the model with estimated parameters (the simulated currents for short) are presented in Figures 9(a) and 10(a). For comparison, the currents computed by FE-BI-MLFMA (the real currents for short) are presented in Figures 9(b) and 10(b). The used parameters in computation are $f = 1 \sim 2$ GHz and $\Delta f = 0.125$ GHz, $\theta = 8^\circ$. The range of horizontal axis indicates the distance between a point on $L1$ and the top of the cone.

The errors between the simulated currents and the real currents are examined: the correlation coefficient of the amplitudes is 92.81% and the root mean square error (RMSE) is 6.01×10^{-5} V/m²; the correlation coefficient of the unwrapped phases is 98.72% and the RMSE is 2.99 rad.

Other cases of incident angle ($\theta = 1^\circ \sim 10^\circ$) are also investigated. The parameters of currents are estimated with the same method. The errors between the simulated currents and the real currents are the correlation coefficient of the amplitudes is larger than 90% and the RMSE is less than 10^{-4} V/m²; the correlation coefficient of the unwrapped phases is larger than 95% and the RMSE is less than 4 rad.

3. Approach of Scattering Center Modelling

There are two classical methods for scattering center modelling. Scattering centers can be extracted directly from radar images by peak or pattern detection, or they can be described by parametric models and the unknown parameters of the model then be acquired through optimal estimation. The second method is not limited by radar resolutions and could provide more precise and elaborate descriptions of scattering centers, yet it is under the strict precondition of the accuracy and application scope of parametric model. The commonly used parametric models are proposed according to the solutions of several simple targets based on the physical optics method (PO) or geometrical theory of diffraction (GTD). Due to limitations of these asymptotic methods, the existing parametric models fail in some cases, for example, creep waves. In this paper, the parametric model is derived from the induced currents which are computed by a full-wave numerical method. All the scattering contributes are included in the derived model.

Based on the electric field integral expression under the far-field condition in the free space [29], the scattered field can be expressed as

$$E_v^s = -j\omega\mu N_v = -jkZN_v, \quad (6)$$

where Z is wave impedance of free space, N_v is the component of the vector \mathbf{N} along \hat{v} direction.

$$\mathbf{N} = \frac{e^{-jkr}}{4\pi r} \int \mathbf{J}(\mathbf{r}') e^{jk\mathbf{r}' \cdot \hat{r}} dS', \quad (7)$$

where $\hat{r} = \sin\theta \cos\phi \hat{x} + \sin\theta \sin\phi \hat{y} + \cos\theta \hat{z}$ and $\mathbf{r}' = \rho \sin\alpha \cos((\beta/\gamma)\pi) \hat{x} + \rho \sin\alpha \sin((\beta/\gamma)\pi) \hat{y} + (h - \rho \cos\alpha) \hat{z}$.

Substituting (4) into (7), we can derive the results of the currents in lit region ($\beta = 0 \sim \gamma$).

$$N_v = \frac{e^{-jkr}}{4\pi r} \int_l \int_0^\gamma J_v(\rho, 0) F(\beta) \cdot \exp \left\{ jk \left[\cos\theta (h - \rho \cos\alpha) + \rho \sin\theta \sin\alpha \cos\left(\frac{\beta}{\gamma}\pi\right) \right] \right\} \rho d\rho d\beta. \quad (8)$$

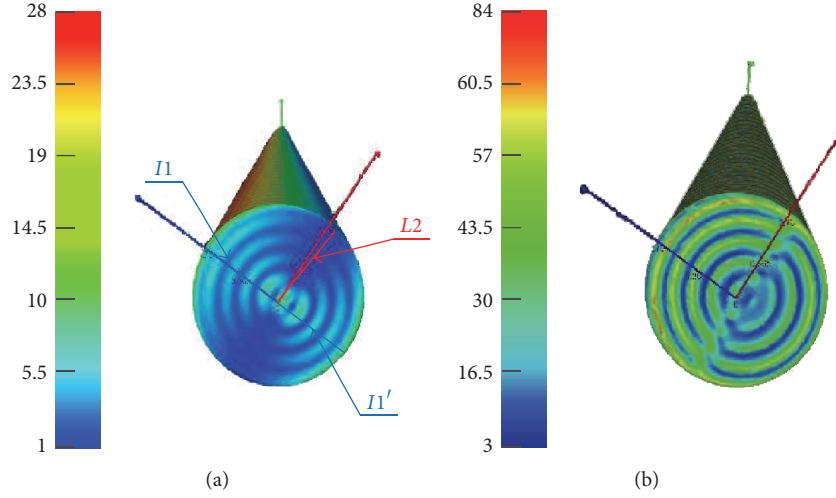


FIGURE 7: Currents on the bottom. (a) Amplitude; (b) phase.

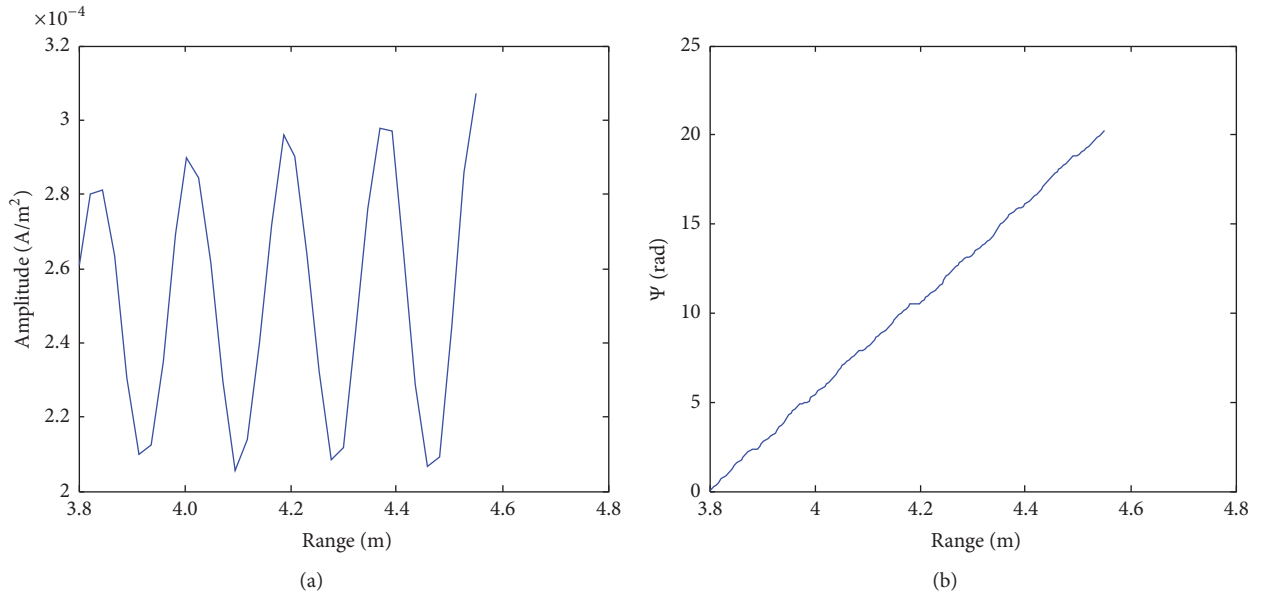


FIGURE 8: Currents on I1. (a) Amplitude; (b) unwrapped phase.

The integral part related to β can be derived based on the principle of stationary phase [30], as follows:

$$G(\rho) = \int_0^\gamma F(\beta) \exp \left\{ jk\rho \sin \theta \sin \alpha \cos \left(\frac{\beta}{\gamma} \pi \right) \right\} d\beta \quad (9)$$

$$\approx \sqrt{\frac{2\pi}{jk\rho \sin \theta \sin \alpha}} \exp \{ jk\rho \sin \theta \sin \alpha \}.$$

Then, the scattered field can be expressed as

$$E_v^s = -jkZ \frac{e^{-jkr}}{4\pi r} \int_I J_v(\rho, 0) \cdot \exp \{ jk \cos \theta (h - \rho \cos \alpha) \} G(\rho) \rho d\rho = -jkZ \quad (10)$$

$$\cdot \frac{e^{-jkr}}{4\pi r} \int_I J_v(\rho, 0) \exp \{ -jkr' \cdot \hat{r} \} V\rho^{1/2} d\rho,$$

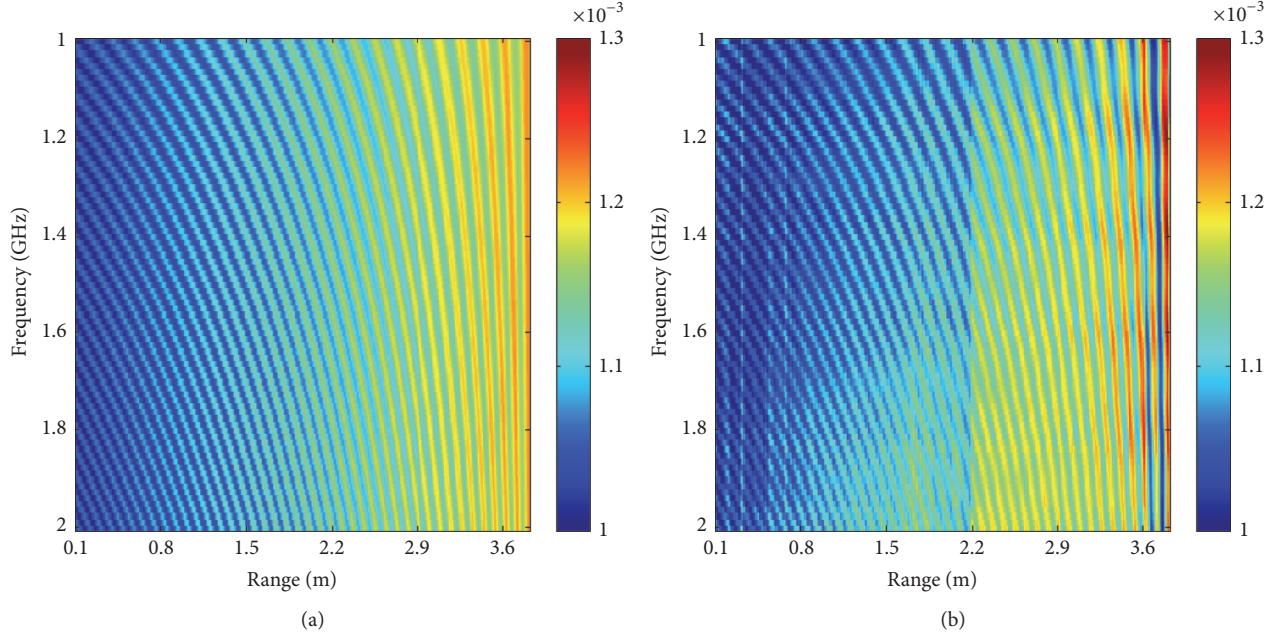


FIGURE 9: Amplitudes of the currents. (a) Simulated currents; (b) real currents.

where $V = \sqrt{2\pi/jk \sin \theta \sin \alpha}$ and \mathbf{r}' is the location vectors of currents on $L1$.

From (10) we can see that the characteristics of the scattering fields from the flank in lit region are mainly determined by the currents on $L1$. Similarly, the characteristics of the scattering fields from the flank in shadow region are mainly determined by the currents on $L1'$, and the characteristics of the scattering fields from the bottom are mainly determined by the currents on $I1$ and $I1'$. The total fields are the supposition of the three components, as given below.

$$E_v^s = \sum_{m=1}^3 E_m(a_{1m}, \dots, a_{9m}), \quad (11)$$

where E_1 indicates the electric field induced by the currents in lit region; E_2 indicates the electric field induced by the currents in shadow region; E_3 indicates the electric field induced by the currents on the bottom.

Based on (1) and (10), we can derive the analytic expression of the scattering center model at VV polarization. VV means the incident wave and reflected wave are all in vertical polarization. The analysis of the scattering centers corresponding to the currents on $L1$ is provided. The analysis processes are similar for the cases of $L1'$, $I1$, and $I1'$, so the repeated contents are ignored here.

Substituting the expressions of currents on $L1$, $L1'$, $I1$, and $I1'$ into (10), we can derive the total scattering fields, as given by (A.1) in the Appendix. Then through the regular computation of the integral along ρ in (A.1), we can get 5 exponential terms as shown in (12); the five functions are the

five corresponding parametric models of scattering centers contributed by the currents on $L1$.

$$\begin{aligned}
 pSC_1 &= e^{j[(a_{13}+a_{19})l+a_{15}]l} \left(\frac{a_{11}l}{2(a_{12}+a_{18})f-2k\mathbf{r}'\cdot\hat{\mathbf{r}}} \right. \\
 &\quad \left. + \frac{a_{11}}{2j(a_{12}+a_{18}-k\mathbf{r}'\cdot\hat{\mathbf{r}})^2 f^2} \right) e^{j[(a_{12}+a_{18})l-k\mathbf{r}'\cdot\hat{\mathbf{r}}+a_{14}]f} \\
 pSC_2 &= e^{-j[(a_{13}-a_{19})l+a_{15}]l} \left(\frac{a_{11}l}{2(a_{12}-a_{18})f+2k\mathbf{r}'\cdot\hat{\mathbf{r}}} \right. \\
 &\quad \left. - \frac{a_{11}}{2j(a_{12}-a_{18}+k\mathbf{r}'\cdot\hat{\mathbf{r}})^2 f^2} \right) \\
 &\quad \cdot e^{-j[(a_{12}-a_{18})l+k\mathbf{r}'\cdot\hat{\mathbf{r}}+a_{14}]f} \\
 pSC_3 &= e^{ja_{15}} \frac{a_{11}}{2j(a_{12}+a_{18}-k\mathbf{r}'\cdot\hat{\mathbf{r}})^2 f^2} e^{ja_{14}f} \\
 pSC_4 &= -e^{-ja_{15}} \frac{a_{11}}{2j(a_{12}-a_{18}+k\mathbf{r}'\cdot\hat{\mathbf{r}})^2 f^2} e^{-ja_{14}f} \\
 pSC_5 &= \frac{e^{ja_{19}l}}{j(a_{18}f-k\mathbf{r}'\cdot\hat{\mathbf{r}})} \left(-la_{17}-l^2 a_{16} \right. \\
 &\quad \left. + \frac{a_{17}+2la_{16}}{j(a_{18}f-k\mathbf{r}'\cdot\hat{\mathbf{r}})} - \frac{2a_{16}}{j(a_{18}-k\mathbf{r}'\cdot\hat{\mathbf{r}})f^2} \right) \\
 &\quad \cdot e^{j(a_{18}lf-k\mathbf{r}'\cdot\hat{\mathbf{r}})}.
 \end{aligned} \quad (12)$$

TABLE I: Associations between the current model parameters and scattering centers parameters.

Scattering center	Position	Amplitude
SC ₁	$a_{12}, a_{14}, a_{18}, a_{22}, a_{24}, a_{28}$	$a_{11}, a_{12}, a_{13}, a_{15}, a_{18}, a_{19}, a_{21}, a_{22}, a_{23}, a_{25}, a_{28}, a_{29}$
SC ₂	a_{18}	$a_{16}, a_{17}, a_{18}, a_{19}$
SC ₃	a_{28}	$a_{26}, a_{27}, a_{28}, a_{29}$
SC ₄	a_{32}, a_{34}, a_{38}	$a_{31}, a_{32}, a_{33}, a_{35}, a_{38}, a_{39}$

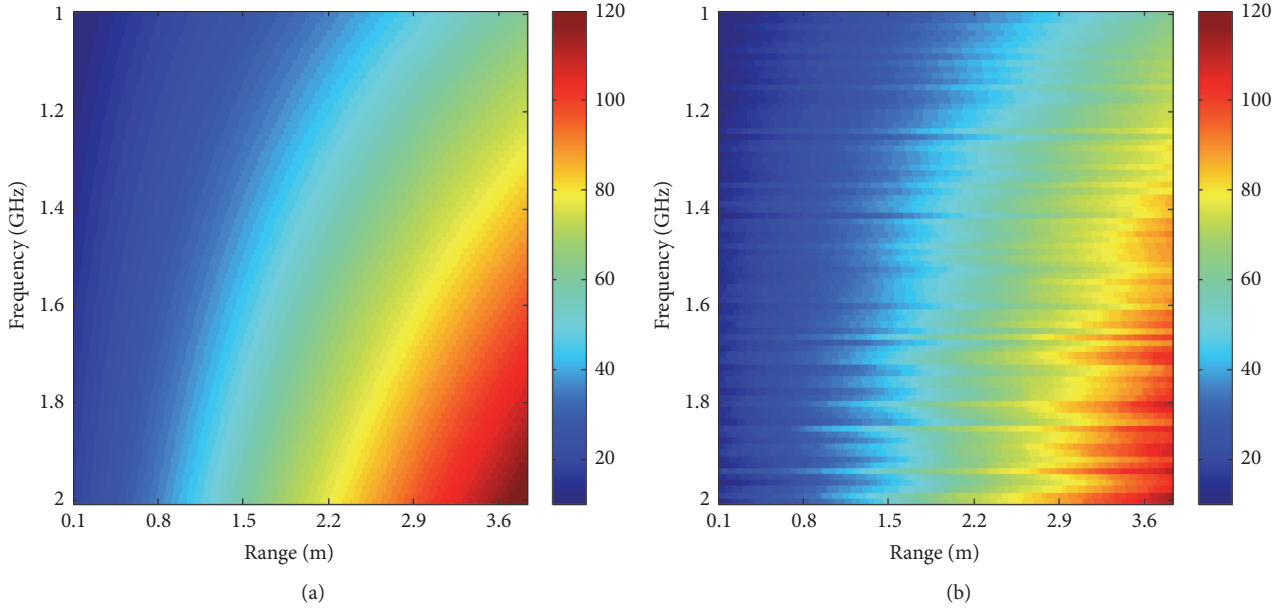


FIGURE 10: Unwrapped phases of the currents. (a) Simulated currents; (b) real currents.

According to the numerical results of the parameters, the components, pSC_1 , pSC_3 , and pSC_4 , whose amplitudes are quite small compared with the others, can be ignored in the following analysis. The components, pSC_2 and pSC_5 , include the contributions of four scattering centers. The four dominated scattering centers, denoted by SC₁, SC₂, SC₃, and SC₄, are illustrated in Figure 11. The relationship of the parameters of the model with the amplitudes and locations of scattering centers is listed in Table I.

SC₁ locates at the top of the cone, which is mainly contributed by the components pSC_2 of $L1$ and $L1'$; SC₂ locates at edges of the bottom in lit region, which is mainly contributed by the components pSC_5 of $L1$ and $I1$; SC₃ locates at edges of the bottom in shadow region, which is mainly contributed by the components pSC_5 of $L1'$ and $I1'$; SC₄ locates outside the geometry of the cone, which is mainly contributed by the components pSC_2 of $I1$ and $I1'$, that is, the creeping waves in the shadow region.

4. Validation of the Model

According to the principle of RP, the intensity and position of the peak reflect to a certain extent the scattering amplitude and downrange location of the corresponding scattering center. The accuracy of the derived scattering center model is

validated through comparing the RP simulated by the model (the simulated RP for short) and the data simulated by the scattered fields computed by FE-BI-MLFMA (the real RP for short). Two cone-shaped targets are investigated here. The geometry of target I is the same as the case of Figure 1. The radiuses of bottom disks and spherical tops of target II are the same as target I. The height of target II is $h = 5.4$ m. Two cases with different parameters setting are investigated.

Case 1 ($\theta = 0$, $\phi = 0$, $f = 1\sim 2$ GHz, $\Delta f = 0.125$ GHz). The simulated RP and the real RP are presented in Figure 12(a). For demonstration of the superiority of this model, the RP obtained by the attributed scattering center model through traditional method are also compared with the simulated RP, as presented in Figure 12(b). The errors of amplitude and locations of the scattering centers are listed in Table 2.

The comparison results demonstrate that the simulated RPs by this model agree well with the real RP. Superior to the exiting model, the scattering center SC₄ induced by creeping waves is precisely characterized by this model.

Case 2 ($\theta = 0\sim 10^\circ$, $\Delta\theta = 0.1^\circ$, $\phi = 0$, $f = 1\sim 2$ GHz, $\Delta f = 0.125$ GHz). The two-dimensional image of the RPs under the continuously changed θ (the RP history for short) is investigated. The simulated RP history and the real RP

TABLE 2: Errors of amplitude and locations of the scattering centers.

Case 1	Position errors			Amplitude errors		
Parameters	SC ₁	SC ₂	SC ₃	SC ₁	SC ₂	SC ₃
Current model	0.19λ	0.13λ	0.03λ	0.14 dB	0.02 dB	0.04 dB
Attributed scattering center model	0.19λ	0.13λ	Fail	0.15 dB	0.04 dB	Fail

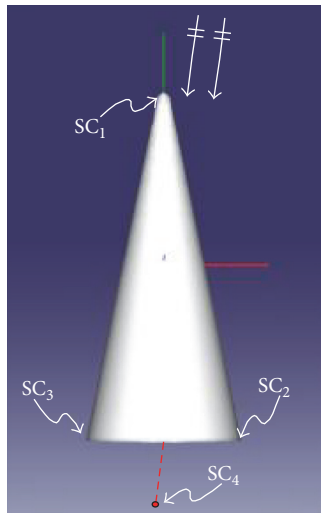


FIGURE 11: Positions of four dominated scattering centers on the target.

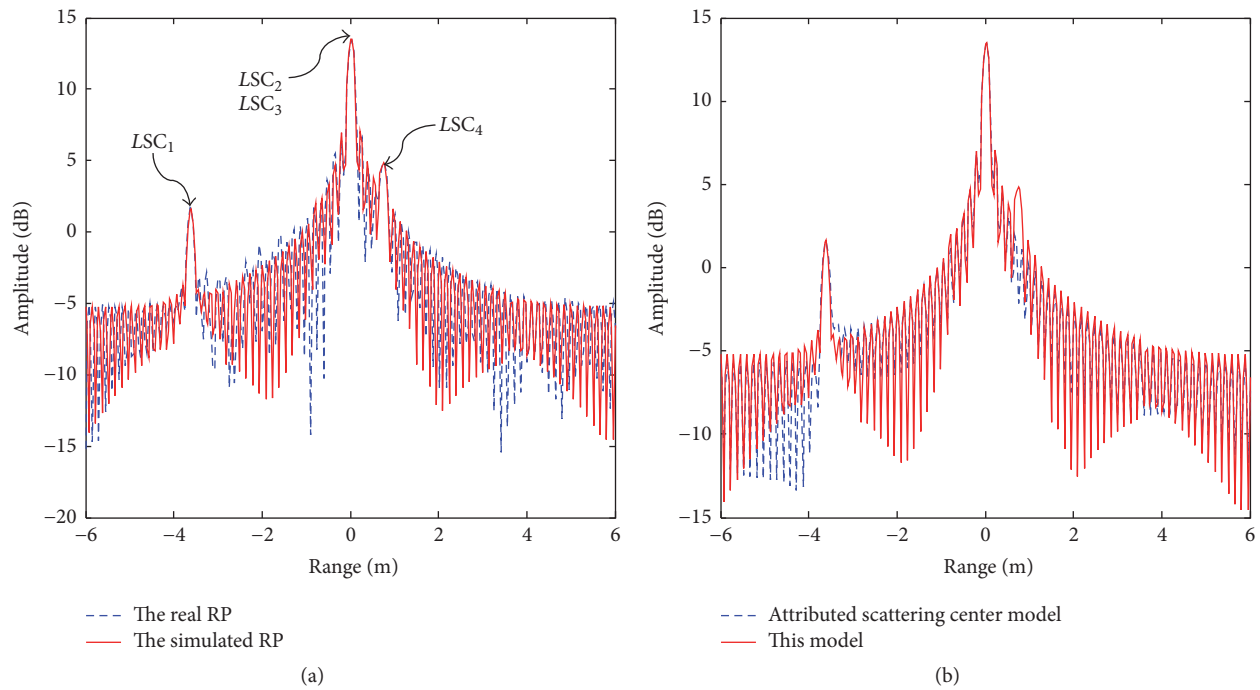


FIGURE 12: Comparison with the RP. (a) Comparison of the simulated RP with the real RP; (b) comparison of the RP obtained by the attributed scattering center model with the simulated RP by this model.

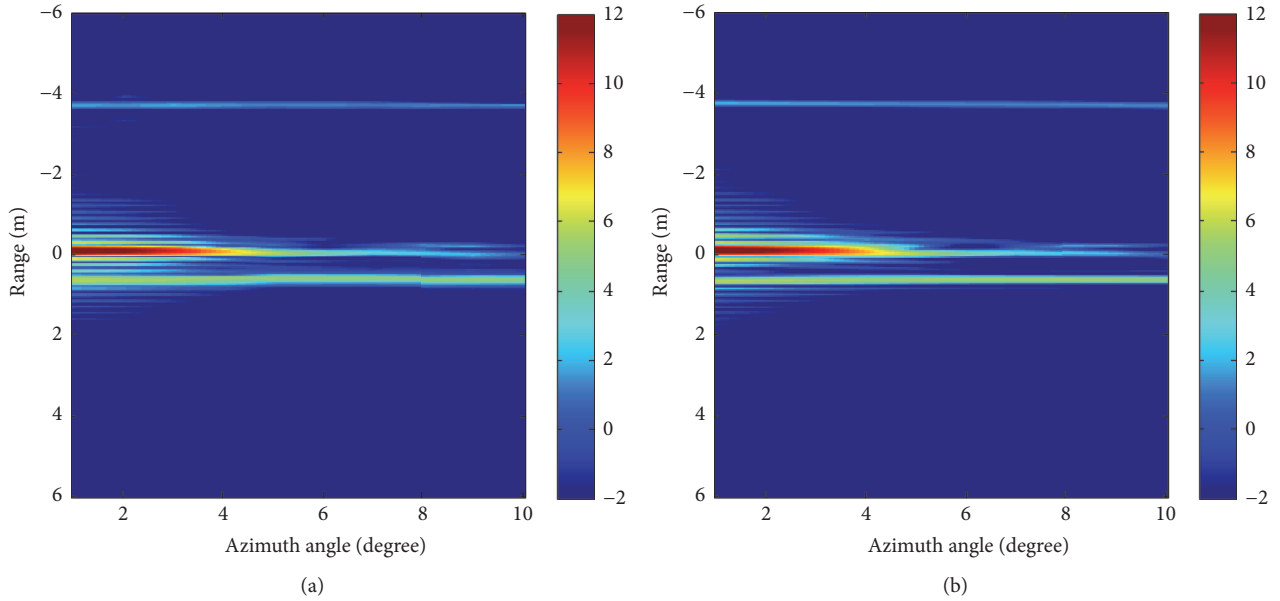


FIGURE 13: RP history of target I. (a) Simulated RP history of target I; (b) real RP history of target I.

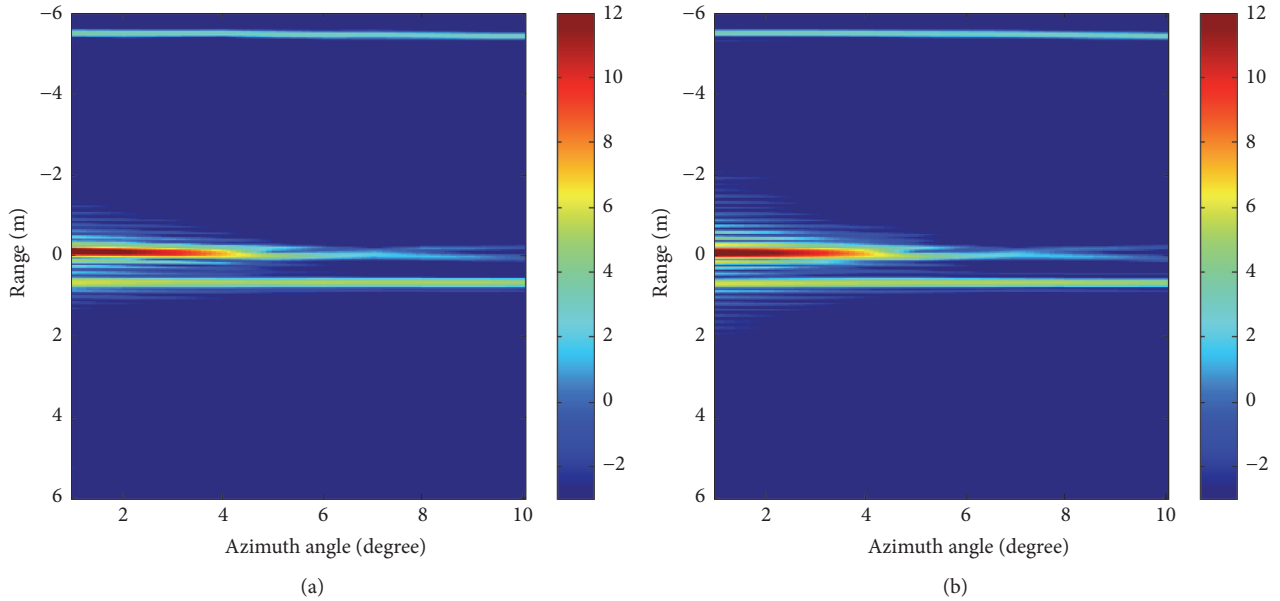


FIGURE 14: RP history of target II. (a) Simulated RP history of target II; (b) real RP history of target II.

history of target I are presented in Figures 13(a) and 13(b). The correlation coefficient of the two images is 86.3%. The RMSE is 2.56 dB.

The simulated RP history and the real RP history of target II are presented in Figures 14(a) and 14(b). The correlation coefficient of the two images is 88.7%. The RMSE is 2.21 dB.

From the images of the RP history of two targets, it can be seen that the simulated results by this model agree well with the results obtained by the full-wave method. The four dominated scattering centers under different aspect angle of LOS

are all precisely characterized. When θ is within half conical angle, the SC_4 induced by creeping waves in shadow region is a dominated scattering center; its intensity is even larger than the SC_2 and SC_3 on the edges. Therefore, in these cases, SC_4 should be considered in scattering center modelling.

5. Conclusions

The induced currents on cone-shaped targets are investigated in detail in this paper. It is found that scattering characteristics

of the cone-shaped targets are mainly determined by one-dimensional currents on the lines in the plane constructed by the LOS and the rotational axis of the cone. The parametric model of the currents on the lines is built based on their distribution characteristics. Based on the induced currents computed by FE-BI-MLFMA, the parameters of the model are estimated using GA. Then, based on the current model, the scattering center model is derived according to electric field integral expression under far-field condition. This model is suitable for cone-shaped targets with different cone angle and height and can precisely describe scattered waves under arbitrary incident directions.

The precision of this model is validated by the RPs under different aspect angles of LOS. The RPs simulated

by this model agree well with the RP simulated by the scattered fields computed by FE-BI-MLFMA. The location errors of scattering centers are less than half wavelength, the amplitude errors are less than 1dB. The comparison results between this model and the attributed scattering center model show that this model is of higher accuracy, especially in describing the scattering centers contributed by creeping waves.

Appendix

Substitute (1), (2), and (3) into (10); then the electric field can be expressed as

$$E_1 = -jkZV \frac{e^{-jkr}}{4\pi r} \left(\int_l^0 a_{11}\rho \sin(a_{12}f\rho + a_{13}\rho + a_{14}f + a_{15}) \cdot \exp(j(a_{18}f\rho + a_{19}\rho - k\mathbf{r}' \cdot \hat{r})) d\rho \right. \\ \left. + \int_l^0 a_{16}\rho^2 \exp(j(a_{18}f\rho + a_{19}\rho - k\mathbf{r}' \cdot \hat{r})) d\rho + \int_l^0 a_{17}\rho \exp(j(a_{18}f\rho + a_{19}\rho - k\mathbf{r}' \cdot \hat{r})) d\rho \right) = -jkZV \frac{e^{-jkr}}{4\pi r} (A_1 \\ + A_2 + A_3) \quad (\text{A.1})$$

$$A_1 = \int_l^0 a_{11}\rho \sin(a_{12}f\rho + a_{13}\rho + a_{14}f + a_{15}) \cdot \exp(j(a_{18}f\rho + a_{19}\rho - k\mathbf{r}' \cdot \hat{r})) d\rho = \frac{a_{11}(l+1)}{2} \\ \cdot \exp\left(j\left(\left(a_{12} + a_{18}\right)fl + a_{14}f + \left(a_{13} + a_{19}\right)l - k\mathbf{r}' \cdot \hat{r} + a_{15}\right)\right) - \frac{a_{11}(l+1)}{2} \\ \cdot \exp\left(-j\left(\left(a_{12} - a_{18}\right)fl + a_{14}f + \left(a_{13} - a_{19}\right)l + k\mathbf{r}' \cdot \hat{r} + a_{15}\right)\right) \quad (\text{A.2})$$

$$A_2 = \int_l^0 a_{17}\rho \exp(j(a_{18}f\rho + a_{19}\rho - k\mathbf{r}' \cdot \hat{r})) d\rho = a_{17}(l+1) \cdot \exp(j(a_{18}fl + a_{19}l - k\mathbf{r}' \cdot \hat{r})) \quad (\text{A.3})$$

$$A_3 = \int_l^0 a_{16}\rho^2 \exp(j(a_{18}f\rho + a_{19}\rho - k\mathbf{r}' \cdot \hat{r})) d\rho = a_{17}(l^2 + 2l + 1) \cdot \exp(j(a_{18}fl + a_{19}l - k\mathbf{r}' \cdot \hat{r})). \quad (\text{A.4})$$

Competing Interests

The authors declare that there is no competing interests regarding the publication of this paper.

Acknowledgments

This work was supported by the National Natural Science Foundation of China (Grants nos. 61471041, 61421001, and 61671059).

References

- [1] J. B. Keller, "Geometrical theory of diffraction," *Journal of the Optical Society of America*, vol. 52, no. 2, pp. 116–130, 1962.
- [2] Q.-Y. Qu, K.-Y. Guo, and X.-Q. Sheng, "Scattering centers induced by creeping waves on streamlined cone-shaped targets in bistatic mode," *IEEE Antennas and Wireless Propagation Letters*, vol. 14, pp. 462–465, 2015.

- [3] M. McClure, R. C. Qiu, and L. Carin, "On the superresolution identification of observables from swept-frequency scattering data," *IEEE Transactions on Antennas and Propagation*, vol. 45, no. 4, pp. 631–641, 1997.
- [4] M. A. Koets and R. L. Moses, "Feature extraction using attributed scattering center models on SAR imagery," in *Algorithms for Synthetic Aperture Radar Imagery VI*, vol. 3721 of *Proceedings of SPIE*, Orlando, Fla, USA, August 1999.
- [5] S. Liu, R. Zhan, J. Zhang, and Z. Zhuang, "Radar automatic target recognition based on sequential vanishing component analysis," *Progress in Electromagnetics Research*, vol. 145, pp. 241–250, 2014.
- [6] Y. He, S. Y. He, Y. H. Zhang, G. J. Wen, D. F. Yu, and G. Q. Zhu, "A forward approach to establish parametric scattering center models for known complex radar targets applied to SAR ATR," *IEEE Transactions on Antennas and Propagation*, vol. 62, no. 12, pp. 6192–6205, 2014.
- [7] H.-C. Chiang, R. L. Moses, and L. C. Potter, "Model-based classification of radar images," *IEEE Transactions on Information Theory*, vol. 46, no. 5, pp. 1842–1854, 2000.

- [8] X. Zhang, J. Qin, and G. Li, "SAR target classification using bayesian compressive sensing with scattering centers features," *Progress in Electromagnetics Research*, vol. 136, pp. 385–407, 2013.
- [9] M. P. Hurst, "Scattering center analysis via prony's method," *IEEE Transactions on Antennas and Propagation*, vol. 35, no. 8, pp. 986–988, 1987.
- [10] J. J. Sacchini, W. M. Steedly, and R. L. Moses, "Two-dimensional prony modeling and parameter estimation," *IEEE Transactions on Signal Processing*, vol. 41, no. 11, pp. 3127–3137, 1993.
- [11] L. C. Potter, D.-M. Chiang, R. Carriere, and M. J. Gerry, "A GTD-based parametric model for radar scattering," *IEEE Transactions on Antennas and Propagation*, vol. 43, no. 10, pp. 1058–1067, 1995.
- [12] X. Yan, J.-M. Hu, G. Zhao, J. Zhang, and J. Wan, "A new parameter estimation method for GTD model based on modified compressed sensing," *Progress in Electromagnetics Research*, vol. 141, pp. 553–575, 2013.
- [13] R. Carrière and R. L. Moses, "High resolution radar target modeling using a modified prony estimator," *IEEE Transactions on Antennas and Propagation*, vol. 40, no. 1, pp. 13–18, 1992.
- [14] L. C. Potter and R. L. Moses, "Attributed scattering centers for SAR ATR," *IEEE Transactions on Image Processing*, vol. 6, no. 1, pp. 79–91, 1997.
- [15] M. J. Gerry, L. C. Potter, I. J. Gupta, and A. D. Van Merwe, "A parametric model for synthetic aperture radar measurements," *IEEE Transactions on Antennas and Propagation*, vol. 47, no. 7, pp. 1179–1188, 1999.
- [16] K.-Y. Guo, Q.-F. Li, X.-Q. Sheng, and M. Gashinova, "Sliding scattering center model for extended streamlined targets," *Progress in Electromagnetics Research*, vol. 139, pp. 499–516, 2013.
- [17] X.-Q. Sheng, J.-M. Jin, J. Song, C.-C. Lu, and W. C. Chew, "On the formulation of hybrid finite-element and boundary-integral methods for 3-D scattering," *IEEE Transactions on Antennas and Propagation*, vol. 46, no. 3, pp. 303–311, 1998.
- [18] X. Q. Sheng, J.-M. Jin, J. Song, W. C. Chew, and C.-C. Lu, "Solution of combined-field integral equation using multilevel fast multipole algorithm for scattering by homogeneous bodies," *IEEE Transactions on Antennas and Propagation*, vol. 46, no. 11, pp. 1718–1726, 1998.
- [19] X.-Q. S. Edward, K.-N. Yung, C. H. Chan et al., "Scattering from a large body with cracks and cavities by the fast and accurate finite-element boundary-integral method," *IEEE Transactions on Antennas and Propagation*, vol. 48, no. 8, pp. 1153–1160, 2000.
- [20] R. F. Harrington, *Field Computation by Moment*, John Wiley & Sons, New York, NY, USA, 1993.
- [21] W. B. Gordon, "High frequency approximations to the physical optics scattering integral," *IEEE Transactions on Antennas and Propagation*, vol. 42, no. 3, pp. 427–432, 1994.
- [22] Y. M. Wu, L. J. Jiang, and W. C. Chew, "An efficient method for computing highly oscillatory physical optics integral," *Progress in Electromagnetics Research*, vol. 127, pp. 211–257, 2012.
- [23] C. Corbel, C. Bourlier, N. Pinel, and J. Chauveau, "Rough surface RCS measurements and simulations using the physical optics approximation," *IEEE Transactions on Antennas and Propagation*, vol. 61, no. 10, pp. 5155–5165, 2013.
- [24] U. d'Elia, G. Pelosi, C. Pichot, S. Selleri, and M. Zoppi, "A physical optics approach to the analysis of large frequency selective radomes," *Progress in Electromagnetics Research*, vol. 138, pp. 537–553, 2013.
- [25] Q. Li, E. J. Rothwell, K.-M. Chen, and D. P. Nyquist, "Scattering center analysis of radar targets using fitting scheme and genetic algorithm," *IEEE Transactions on Antennas and Propagation*, vol. 44, no. 2, pp. 198–207, 1996.
- [26] E. J. Hughes and M. Leyland, "Using multiple genetic algorithms to generate radar point-scatterer models," *IEEE Transactions on Evolutionary Computation*, vol. 4, no. 2, pp. 147–163, 2000.
- [27] T. S. Sijher and A. A. Kishk, "Antenna modeling by infinitesimal dipoles using genetic algorithms," *Progress in Electromagnetics Research*, vol. 52, pp. 225–254, 2005.
- [28] Z.-Q. Meng, "Autonomous genetic algorithm for functional optimization," *Progress in Electromagnetics Research*, vol. 72, pp. 253–268, 2007.
- [29] X.-Q. Sheng and W. Song, *Essentials of Computational Electromagnetics*, John Wiley & Sons, New York, NY, USA, 2012.
- [30] G. Franceschetti and R. Lanari, *Synthetic Aperture Radar Processing*, CRC Press, Boca Raton, Fla, USA, 1999.